Measurement of the mixing parameters of neutral charm mesons and search for indirect CP violation with $D^0 \to K^0_S \pi^+ \pi^-$ decays at LHCb

A thesis submitted to The University of Manchester

for the degree of

Doctor of Philosophy

(PhD)

in the Faculty of Engineering and Physical Sciences

Stefanie Reichert (M. Sc.)
born 2 February 1988 in Heilbronn, Germany

Particle Physics Group
The School of Physics and Astronomy
2015

Contents

Final word count: 38,277

List of Figures

List of Tables

Abstract

Name of the university: The University of Manchester
Candidate name: Stefanie Reichert
Degree title: Doctor of Philosophy (PhD)
Thesis title: Measurement of the mixing parameters of neutral charm mesons and search for indirect *CP* violation with $D^0 \to K^0_S\pi^+\pi^-$ decays at LHCb
Submission date: 16 December 2015

The hadronic decay $D^0 \to K^0_S\pi^+\pi^-$ provides direct access to the measurement of the mixing parameters of the neutral charm meson system and allows to test for indirect *CP* violation. Mixing is a time-dependent phenomenon for which the time evolution of the transition amplitude of a D^0 ($\overline{D}^0$) decay to the final state $K^0_S\pi^+\pi^-$ has to be considered. The parameters driving those time-dependent oscillations are $x \equiv (m_1 - m_2)/\Gamma$ and $y \equiv (\Gamma_1 - \Gamma_2)/(2\Gamma)$. The *CP* violation parameters $|q/p|$ and $\phi = \arg(q, p)$ describe the superposition of the flavour eigenstates D^0 and $\overline{D}^0$ and of the physical eigenstates D_1 and D_2, $|D_{1,2}\rangle = p|D^0\rangle \pm q|\overline{D}^0\rangle$. By measuring the time- and phase-space dependent distribution of $D^0 \to K^0_S\pi^+\pi^-$ decays, the mixing parameters can be extracted and a search for indirect *CP* violation can be performed. This thesis reports a measurement of the mixing parameters and the preparations of a measurement of the *CP* violation parameters on data collected with the LHCb experiment in 2011 and 2012, corresponding to an integrated luminosity of $3\,\text{fb}^{-1}$. The D^0 and $\overline{D}^0$ mesons are required to originate from a semileptonic decay of a B meson. The parameters of interest are extracted from a fit in D^0 decay time and the Dalitz variables, $m^2(K^0_S\pi^-)$ and $m^2(K^0_S\pi^+)$. The phase-space distribution of $D^0 \to K^0_S\pi^+\pi^-$ decays is modelled by expressing the three-body decay as a succession of two-body decays. The decay amplitude of a D^0 or $\overline{D}^0$ meson into $K^0_S\pi^\pm\pi^\mp$ final state is a superposition of all possible intermediate resonances and the single resonances interfere with each other across the phase-space. The blinded D^0-$\overline{D}^0$ mixing parameters are found to be

$$x = (-4.76 \pm 0.22_{\text{stat.}} \pm 0.05_{\text{syst.}} + 0.08_{\text{model}})\%,$$
$$y = (-4.13 \pm 0.19_{\text{stat.}} \pm 0.07_{\text{syst.}} + 0.05_{\text{model}})\%,$$

where the uncertainties are statistical, systematic and model-dependent.

Declaration

The University of Manchester
PhD by published work candidate declaration

Candidate name: Stefanie Reichert
Faculty: Engineering and Physical Sciences
Thesis title: Measurement of the mixing parameters of neutral charm mesons and search for indirect *CP* violation with $D^0 \to K^0_S \pi^+ \pi^-$ decays at LHCb

Declaration to be completed by the candidate:

This work represents the combined efforts of the LHCb collaboration. Hence, parts of the content has been published elsewhere and/or presented to several audiences. I hereby declare that, subject to the above comment, the submission is my own original work undertaken while being at the University of Manchester and that no portion of the work referred to in this thesis has been submitted in support of an application for another degree or qualification of this or any other university or other institute of learning.

Date and signature

Copyright

[1] see http://documents.manchester.ac.uk/DocuInfo.aspx?DocID=487
[2] see http://www.manchester.ac.uk/library/aboutus/regulations

Wenn es gut ist, wird es schön sein und ein Leben lang passieren.
Wenn es böse ist, dann beißt es und du wirst es schnell verlieren.
Wenn es gut ist, wird es da sein, wann immer du es brauchst.
Wenn es böse ist, dann beißt es und dein Herz gibt langsam auf.

- Olli Schulz

Für all diejenigen, die mein Leben bereichern und für diejenigen, die nicht mehr hier sind.
Ihr fehlt.

Acknowledgements

Traditions, traditions...

Madame Mim: *Now, first of all, if you don't mind, I'll make the rules.*
Archimedes the Owl: *Rules indeed! G'ha-ha-ha! Why, she only wants rules so she can break them.*
Madame Mim: *I'll take care of you later, feather-brain. Now, rule one: no mineral or vegetable, only animals. Rule two: no make-believe things like, uh, oh, pink dragons and stuff. Now, rule three: no disappearing.*
Merlin: *Rule four: no cheating.*

From *The sword in the stone*

While working on this PhD thesis, I wished more than once to have Merlin's and Madame Mim's magical powers. Somtimes, I was so busy that being a stone, which is lying on the ground doing nothing, was tempting. Having a pink dragon in the office sounded so much more exciting than fixing problems in the code. Disappearing to a cabin in the Swedish woods crossed my mind from time to time and I've seriously considered[3] using a random number generator to obtain results for the mixing and *CP* violation parameters when I had written the thesis, but was somehow lacking results due to a moody fitter.

Somehow, everything worked out in the end - as it always does. This would not have been possible without my supervisor Chris Parkes, my co-supervisor Marco Gersabeck, my advisor George Lafferty and Jolanta Brodzicka. Thank you for your advice, discussions and time. Thanks to Marco and Chris for the great feedback on my thesis, even if I sent you something last minute. Special thanks go to Marco for offering me to borrow his *The Wire* box set because apparently I can't receive my PhD without having seen *The Wire*, which is fair enough. I would also like to thank Marco for the significant amounts of chocolate, cake, coffee and whisky over the years he shared with us. A big thank you goes to Mike Sokoloff for never running out of ideas and starting to become pragmatic towards the end of my PhD. Thanks to Liang Sun, the GooFit whisperer, who saved me more than once. Mark Williams deserves a special thank you for agreeing to join the analysis, putting up the fight with GooFit and most of all for giving feedback. You will be a hell of a supervisor! Thanks for all the encouragement! Jordi Garra Ticó, thank you for the brainstorming sessions whenever I was completely stuck. Thanks to Yasmine Amhis for great advice on career and life in general. Another thank you goes to Manuel Schiller for reading my thesis even after he saw the page count! Many thanks to Sabah Salih for fixing problems with the GPU, especially in the last week before submission deadline.

[3] Disclaimer: Not really.

Acknowledgements

Many thanks go to Yvonne Peters and Christos Touramanis for a surprisingly pleasant viva, and to my family and colleagues for two fantastic PhD hats.

For financial support, I would like to thank the University of Manchester and STFC.

Thanks to my office mates over the years, for introducing me to the concept of rubber duck programming or being my rubber duck from time to time, for the coffee and beer breaks, the plush animals and the good laughs we shared. And many thanks to all other colleagues who made work so much fun and brought cake along.

For the countless coffee breaks, the tiny potato statement, the pizza vending machine excursion and so much more, thanks to Adam. To Laura for accepting me as wedding cupcake tester and the evenings where we completely missed the movie because we were chatting too much. Milena for the sometimes more than needed 'everything sucks let's whine about it' breaks. Sarah for the mini vacations at Bains des Pâquis. The German connection for the Game of Thrones sessions - they and you will be missed. All the friends I met along the way - in kindergarden, at school, at university, and somewhere in between. Dani and Julian and our apple tree, which hopefully will grow apples one day. Carina, for blackmailing me with tea, cookies and Gilmore Girls sessions. Helena for our great friendship and proving me right when I thought be would be very close friends the first time we met. Jule for always being there and being an amazing friend. Micha for his ability to learn and his stubbornness, which caused so many funny memories. Ulli for her special kind of humour and for introducing me to so many great movies. Sören for making me an American Football addict. Dan-Nha for lovely tea breaks every time I come back to Berlin. All the others I forgot to mention because my brain is a mess after writing this thesis.

A thank you with capital letters goes to my family for their love and support, especially to my parents and my brother for keeping me sane over the years. I know this was quite difficult at times. Clemens, thank you for our life together - the past, present and future - and for convincing me that we can manage everything as long as it is us against the rest of the world.

Und jetzt noch ein Nachsatz, damit hier wenigstens was steht, das jeder in meiner Familie versteht: Meine Lieben, ihr seid wunderbar. Danke für gute und nicht ganz so gute Ratschläge, fürs Anstrengendsein, fürs Liebhaben, fürs Ehrlichsein, fürs Kopfgeraderücken, fürs Mitfühlen, fürs Dasein und für Lustigsein. Kurz, fürs Familiesein. Ich hätte es deutlich schlimmer erwischen können.

The soundtrack of my PhD

Luckily, the soundtrack of my PhD consisted of a wider selection of songs compared to the playlist I listed to when writing my master thesis[4]. Apart from listening to the insanely funny radio show by Olli Schulz and Jan Böhmermann, the following songs made my life so much better.

Olli Schulz - Halt die Fresse, krieg 'n Kind
Kettcar - Die Ausfahrt zum Haus deiner Eltern
Thees Uhlmann - Und Jay-Z singt uns ein Lied
+44 - When your heart stops beating
Beatsteaks - Let me in
Gloria - Eigenes Berlin
Of Monsters and Men - Empire
Miss Platnum - Glück und Benzin
Christine and the Queens - Christine
Joris - Herz über Kopf
Mariah Carey - All I want for Christmas is you (yep, I'm being serious here)
Kings of Leon - Use somebody
Sportfreude Stiller - Laut anhör'n
The Wombats - Let's dance to Joy Division
Fallout Boy - Sugar we're going down swinging
Clueso - Chicago
Fleetwood Mac - Second hand news
Angels and Airwaves - The adventure
Turbonegro - All my friends are dead
Bad Religion - The surface of me
Sage Francis - Sun vs. moon
Muse - Super massive black hole
Queens of the Stone Age - Little sister
No Use for a name - For Fiona
Jimmy Eat World - Bleeding America
Motion City Soundtrack - Capital H
Yellowcard - Ocean Avenue

[4] Adele - Skyfall, Paul Kalkbrenner - Sky and sand

The author

Education

Primary education

- Primary school
  Staufeneckschule, Salach, Germany
  09/1994 - 07/1998

- High school, Zeugnis der allgemeinen Hochschulreife (Abitur), Grade: 1.4
  Erich Kästner Gymnasium, Eislingen/Fils, Germany
  09/1998 - 06/2007

Higher education

Humboldt University of Berlin, Berlin, Germany

- Bachelor of Science, B. Sc. Degree Grade: 1.8
  10/2007 - 09/2010, Department of Physics
  Thesis Topic: *On the determination of leptonic branching fractions of τ leptons at the BaBar experiment*
  Advisor: Prof. Dr. Heiko Lacker
  Thesis Grade: 1.0

- Master of Science, M. Sc. Degree Grade: 1.1
  10/2010 - 12/2012, Department of Physics
  Thesis Topic: *Measurement of the partial branching fraction $\Delta\mathcal{B}(B \to X_u \ell \nu_\ell)$ with the BaBar experiment using the lepton energy E_ℓ and the momentum transfer q^2*
  Advisor: Prof. Dr. Heiko Lacker
  Thesis Grade: 1.1

The University of Manchester, Manchester, United Kingdom

- Doctor of Philosophy
  01/2013 - 12/2015 PhD, The School of Physics and Astronomy
  Thesis Topic: *Measurement of the mixing parameters of neutral charm mesons and search for indirect CP violation with $D^0 \to K^0_S \pi^+ \pi^-$ decays at LHCb*
  Advisor: Prof. Christopher Parkes

1. Introduction

The Standard Model of Particle Physics provides a theory of the elementary particles and their interactions. The well-known nuclear matter particles, namely the proton and neutron, consist of three valence quarks, which are either two up-quarks and one down-quark or two down-quarks and one up-quark. The Standard Model contains overall twelve spin-$\frac{1}{2}$ particles (fermions), namely six leptons (electron, muon, tau and three neutrinos with corresponding flavour) and six quarks (up, down, charm, strange, top, and bottom quark) and their corresponding anti-particles.

The interactions between these particles are caused by the electromagnetic, weak, strong and gravitational forces, where the contribution from the latter is negligible. The strong force binds quarks in hadrons, which can be either mesons consisting of a quark-antiquark pair or baryons containing three quarks. Recently, tetra- and pentaquark states have been observed. This thesis concerns decays of the D^0 meson, which has a valence quark content of an anti-up quark and a charm quark.

In the Standard Model, neutral mesons may be subject to mixing whereby a meson transitions into its own anti-meson. The interpretation of an experimental observation in 1960 [1] required that neutral kaons $K^0 = (d\bar{s})$ oscillate in $\overline{K}^0 = (\bar{d}s)$ and vice versa. In the beauty sector, mixing between $B^0 = (d\bar{b})$ and $\overline{B}^0 = (\bar{d}b)$ mesons was observed in 1987 at the Argus experiment [2] and in 2006 at CDF between $B_s^0 = (s\bar{b})$ and $\overline{B}_s^0 = (\bar{s}b)$ mesons [3]. First evidence of mixing in the charm sector was reported by BaBar and Belle in 2007 [4, 5].

Oscillations between D^0 and $\overline{D}^0$ mesons are described by the mixing parameters x and y, which are expected to be $\sim \mathcal{O}(10^{-3})$ in the Standard Model [6]. Compared to mixing in the kaon and beauty sectors, charm mixing is highly suppressed and therefore experimentally challenging. If a particle and its anti-particle behave differently under a charge-parity transformation (CP), this phenomenon is called CP violation. CP violation is classified into three types: CP violation in decay (direct CP violation), CP violation in mixing, and CP violation in the interference of mixing and decay. The latter two types are denoted as indirect CP violation. In direct CP violation, the amplitudes of a decay into a final state, *e.g.* $D^0 \to \pi^+\pi^-$, and of the charge-conjugated decay, *e.g.* $\overline{D}^0 \to \pi^-\pi^+$, differ. CP violation in mixing occurs if the mass eigenstates D_1 and D_2 do not coincide with the CP eigenstates or if the phase between the mass and flavour eigenstates is non-zero. In the neutral charm sector, the flavour eigenstates are a linear superposition of the mass eigenstates $|D_{1,2}\rangle = p|D^0\rangle \pm q|\overline{D}^0\rangle$ with complex normalisation coefficients q and p.

Early calculations of CP violation in the Standard Model predicted indirect CP violation to be $\leq 10^{-5}$ [6]. However, more recent theoretical calculations [7] find sizable effects from the corrections from the leading Heavy Quark Expansion (HQE) [8] on the limit resulting in a less stringent prediction. Calculations allowing physics beyond the Standard Model yield mixing parameters of $\sim \mathcal{O}(10^{-2})$ and expect indirect CP at a level of $\sim \mathcal{O}(10^{-3})$. If significantly enhanced mixing parameters or levels of indirect CP violation are observed, a clear indication

for physics beyond the Standard Model is found. Currently, no evidence for *CP* violation in the charm sector has been observed [9].
The parameter q/p, which governs indirect *CP* violation, and the mixing parameters are directly accessible through $D^0 \to K^0_S\pi^+\pi^-$ decays. In this thesis, $D^0 \to K^0_S\pi^+\pi^-$ decays are exploited to measure the mixing parameters by performing a time- and model-dependent amplitude analysis. In addition, preparations for a search of indirect *CP* violation are undertaken. The analysed LHCb data correspond to an integrated luminosity of $3\,\text{fb}^{-1}$ recorded at centre-of-mass energies of 7 TeV in 2011 and at 8 TeV in 2012. The D^0 mesons are required to originate from semileptonic B decays, which grants access to a broad range of D^0 lifetimes.
This thesis is structured as follows. The theoretical background of the Standard Model with focus on mixing and *CP* violation is given in Chapter 2. The Large Hadron Collider and the LHCb experiment are introduced in Chapter 3 and the foreseen upgrade of LHCb is detailed in Chapter 4. Furthermore, the author's work on data processing algorithms for the future vertex detector are presented in this chapter. An overview of the analysis method is given in Chapter 5. Information on the recorded and simulated datasets can be found in Chapter 6. The selection of $D^0 \to K^0_S\pi^+\pi^-$ decays originating from semileptonic B decays is detailed in Chapters 7 and 8. The treatment of remaining background candidates is outlined in Chapter 9. The measurement of acceptance and resolution effects is detailed in Chapter 10. The amplitude fit, which is used to extract x, y and possibly q/p is introduced in Chapter 11 and its validation is summarised in Chapter 12. Chapter 13 discusses systematic uncertainties and cross checks while Chapter 14 reports the final results on the mixing parameters. A conclusion is drawn in Chapter 15. In this document, natural units with $\hbar = c = 1$ are used and charge conjugation is implied except where explicitly indicated otherwise.

2. Theory

The measurement of the $D^0 - \overline{D}^0$ mixing parameters x and y and of the indirect *CP* violation parameters $|q/p|$ and $\phi = \arg(q, p)$ are interpreted in the theoretical framework of the Standard Model of Particle Physics. The Standard Model describes three out of the four fundamental forces causing interactions between particles: the electromagnetic, weak and strong forces omitting gravity.

In this chapter, the principles of the Standard Model are outlined followed by a discussion of neutral meson mixing in the charm sector and the concepts of *CP* violation. An overview of the current experimental landscape is given to allow the reader to put the measurements undertaken in this thesis into context.

2.1. The Standard Model of Particle Physics

The Standard Model of Particle Physics [10] is a relativistic quantum field theory parametrisable by the gauge group $\mathrm{SU(3)_C} \times \mathrm{SU(2)_L} \times \mathrm{U(1)_Y}$ representing the strong, weak and electromagnetic interactions mediated via gauge bosons. The theory of strong interaction between quarks carrying the quantum number colour is described by the $\mathrm{SU(3)_C}$ gauge group whereas the gauge group $\mathrm{SU(2)_L} \times \mathrm{U(1)_Y}$ describes the unification of electromagnetic and weak interactions. The gauge groups of the Standard Model are labeled to point out which quantum number characterises the associated interaction or in case of $SU(2)_L$ that the weak interaction couples only to left-handed fermions. Quantum chromodynamics is described by the quantum number colour C due to the fact that the quark flavours and gluons are states carrying colour charge. The gauge group $\mathrm{SU(2)_L} \times \mathrm{U(1)_Y}$ represents the electroweak interaction with the weak hypercharge Y.

At low energies, the $\mathrm{SU(2)_L} \times \mathrm{U(1)_Y}$ symmetry is broken spontaneously to the symmetry of the electromagnetic interactions $\mathrm{U(1)_{em.}}$, which leads to the mass generation of the gauge bosons (see Chapt. 2.1.1.1).

Electroweak and strong force act between particles through the exchange of quanta of the corresponding fields. These quanta are the gauge bosons carrying spin 1 [11]. The gauge groups of degree n have $n^2 - 1$ generators, *e.g.* the gauge group $\mathrm{SU(2)_L}$ is of degree $n = 2$ and therefore has 3 generators. The generators are associated with the corresponding field quanta of the gauge group, *i.e.* for $\mathrm{SU(2)_L}$, three generators lead to the creation of gauge bosons. The gauge bosons mediating the electromagnetic and strong interaction are massless and neutral gauge bosons, the photon γ and the gluon g, respectively. In the case of the weak interactions, three types of massive gauge bosons - the Z and $W^{\pm}$ bosons - act as force carriers.

2.1.1. Electroweak theory

The weak transition current acts under parity transformation like a vector minus axial vector $(V-A)$. Left- and right-handed chiral spinor fields e_L and e_R, respectively, are introduced. These fields are given for the electron by

$$e_L \equiv P_L\psi = \frac{1-\gamma_5}{2}\psi \;\text{ and }\; e_R \equiv P_R\psi = \frac{1+\gamma_5}{2}\psi, \tag{2.1}$$

and are eigenstates of the helicity operator. ψ denotes the spinor field and $\gamma^5 = i\gamma^0\gamma^1\gamma^2\gamma^3$ is given in the Dirac representation. An overview of the fields of the Standard Model and their gauge quantum numbers is given in Table 2.1. These fields are classified as quark and lepton fields with the quark doublets Q_L^i and singlets u_R^i, d_R^i as well as lepton doublets L_L^i and singlets e_R^i. The index L and R of the fields stands for left- and right-handed fields, respectively.

Table 2.1.: *The elementary fields of the Standard Model and their corresponding properties: the electric charge Q, the weak isospin T, its third component T_3 and the weak hypercharge $Y = 2(Q - T_3)$.*

Fields of the Standard Model				Q	T	T_3	Y
$Q_L^i =$	$\begin{pmatrix} u \\ d \end{pmatrix}_L$	$\begin{pmatrix} c \\ s \end{pmatrix}_L$	$\begin{pmatrix} t \\ b \end{pmatrix}_L$	$\begin{matrix} +2/3 \\ -1/3 \end{matrix}$	$1/2$	$\begin{matrix} +1/2 \\ -1/2 \end{matrix}$	$+1/3$
$u_R^i =$	u_R	c_R	t_R	$+2/3$	0	0	$+4/3$
$d_R^i =$	d_R	s_R	b_R	$-1/3$	0	0	$-2/3$
$L_L^i =$	$\begin{pmatrix} \nu_e \\ e \end{pmatrix}_L$	$\begin{pmatrix} \nu_\mu \\ \mu \end{pmatrix}_L$	$\begin{pmatrix} \nu_\tau \\ \tau \end{pmatrix}_L$	$\begin{matrix} 0 \\ -1 \end{matrix}$	$1/2$	$\begin{matrix} +1/2 \\ -1/2 \end{matrix}$	-1
$\overline{\nu}_R^i =$	$\overline{\nu}_R^e$	$\overline{\nu}_R^\mu$	$\overline{\nu}_R^\tau$	0	0	0	0
$e_R^i =$	e_R	μ_R	τ_R	-1	0	0	-2

The theory of the electroweak interaction, also known as Glashow-Salam-Weinberg (GSW) theory [12–14], is the unification of the electromagnetic and weak interaction described by the $\mathrm{SU(2)_L} \times \mathrm{U(1)_Y}$ gauge group.
The dynamics of elementary particles under the influence of the electroweak interaction can be derived from the electromagnetic Lagrangian of a free fermion field $\mathcal{L}_0$ by considering the effects of local phase transformations and accounting for weak currents. The Lagrangian of a free fermion field is given by

$$\mathcal{L}_0 = i\bar{\psi}\gamma_\mu\partial^\mu\psi - m\bar{\psi}\psi, \tag{2.2}$$

where the first term describes the kinematics and the second the mass of the free fermion field. Under a local gauge transformation at a space-point x

$$\psi(x) \rightarrow \psi'(x) = e^{i\alpha(x)}\psi(x), \tag{2.3}$$

the free fermion Lagrangian $\mathcal{L}_0$ is not gauge invariant. By replacing ∂_μ with the covariant derivate D_μ

$$D_\mu \equiv \partial_\mu - ieA_\mu \quad \text{where} \quad A_\mu \rightarrow A'_\mu = A_\mu + \frac{1}{e}\partial_\mu\alpha, \tag{2.4}$$

the free fermion Lagrangian is rendered invariant under local gauge transformations

$$\mathcal{L}_0 \rightarrow \mathcal{L'}_0 = i\bar{\psi}\gamma_\mu D^\mu\psi - m\bar{\psi}\psi \tag{2.5}$$

$$= \bar{\psi}(i\gamma_\mu\partial^\mu - m)\psi + e\bar{\psi}\gamma^\mu A_\mu\psi. \tag{2.6}$$

The demand of local gauge-invariance introduces the gauge field A_μ, which can be interpreted physically as the field of the photon. This interpretation requires the addition of the kinetic term of the gauge field A_μ to the Lagrangian $\mathcal{L'}_0$ yielding the Lagrangian of QED

$$\mathcal{L}_{\text{QED}} = \bar{\psi}(i\gamma_\mu\partial^\mu - m)\psi + e\bar{\psi}\gamma^\mu A_\mu\psi - \frac{1}{4}F_{\mu\nu}F^{\mu\nu}. \tag{2.7}$$

The first term of the QED Lagrangian represents the kinetic and mass terms of the spinor field ψ, whereas the second term describes the interaction of the spinor field with the photon field A_μ whose kinetic energy is expressed in the term $-\frac{1}{4}F_{\mu\nu}F^{\mu\nu}$ with the field strength tensor $F_{\mu\nu} = \partial_\mu A_\nu - \partial_\nu A_\mu$.
The pure QED Lagrangian is then expanded to the Lagrangian of the electroweak interaction. The gauge group of the weak interaction is an $\mathrm{SU(2)_L}$ group with generators T_i with $i = 1, 2, 3$. The generators of the $\mathrm{SU(2)_L}$ group fulfill the commutator relation $[T_i, T_j] = i\epsilon_{ijk}T_k$ and thus do not commute, where the gauge group is non-abelian. The gauge group of weak interactions introduces a three-component weak isospin current, which couples to the vector fields $\vec{W}_\mu = (W^1_\mu, W^2_\mu, W^3_\mu)$. The generator Y of $\mathrm{U(1)_Y}$, corresponding to the weak hypercharge, gives rise to a current coupling to a vector field B_μ.

Under the $SU(2)_L \times U(1)_Y$ gauge transformation, the left- and right-handed spinor fields transform as

$$L^i_L \rightarrow {L^i_L}' = e^{i\vec{\alpha}(x)\vec{T} + i\beta(x)Y}L^i_L \quad \text{and} \quad e^i_R \rightarrow {e^i_R}' = e^{i\beta(x)Y}e^i_R. \tag{2.8}$$

Introducing a covariant derivative, gauge invariance of the Lagrangian is ensured and requires the addition of terms for the vector fields $\vec{W}_\mu$ and B_μ describing the kinetic energy as well as the self-coupling for the $\vec{W}_\mu$ fields. The Lagrangian of the GSW theory for the fields summarised in Table 2.1 is given by

$$\begin{aligned}\mathcal{L}_{\mathrm{GSW}} =& \bar{L}_L^i \gamma^\mu \left[i\partial_\mu - g\frac{\vec{\tau}}{2}\vec{W}_\mu - g'\frac{Y}{2}B_\mu \right] L_L^i \\ &+ \bar{e}_R^i \gamma^\mu \left[i\partial_\mu - g'\frac{Y}{2}B_\mu \right] e_R^i - \frac{1}{4}B_{\mu\nu}B^{\mu\nu} - \frac{1}{4}\vec{W}_{\mu\nu}\vec{W}^{\mu\nu},\end{aligned} \tag{2.9}$$

with the field strength tensors $B_{\mu\nu} \equiv \partial_\mu B_\nu - \partial_\nu B_\mu$ and $\vec{W}_{\mu\nu} \equiv \partial_\mu \vec{W}_\nu - \partial_\nu \vec{W}_\mu - g\vec{W}_\mu \times \vec{W}_\nu$. The Pauli matrices are $\vec{\tau} = (\tau_1, \tau_2, \tau_3)$ and g, g' denote the coupling strengths for $\vec{W}_\mu$ and B_μ, respectively.

The linear combination of the vector fields W_μ^1 and W_μ^2 leads to the physical fields $W_\mu^\pm$, which are given by $W_\mu^\pm = \frac{1}{\sqrt{2}}\left(W_\mu^1 \mp iW_\mu^2\right)$ describing the massive $W^\pm$ bosons. The two remaining neutral fields B_μ and W_μ^3 mix and form the following physical states representing the photon γ and the Z boson fields

$$\begin{aligned} A_\mu &= B_\mu \cos\theta_W + W_\mu^3 \sin\theta_W && \text{massless} \quad \gamma, \\ Z_\mu &= -B_\mu \sin\theta_W + W_\mu^3 \cos\theta_W && \text{massive} \quad Z, \end{aligned} \tag{2.10}$$

with the Weinberg angle θ_W defined by the masses of the $W^\pm$ and Z bosons as $\cos\theta_W = M_W/M_Z$.

2.1.1.1. Brout-Englert-Higgs mechanism

Adding mass terms to the Lagrangian $\mathcal{L}_{\mathrm{GSW}}$ would violate gauge invariance, but the masses of the gauge bosons can be generated through spontaneous symmetry breaking while gauge invariance still holds. This mechanism is known as the Brout-Englert-Higgs mechanism [15, 16]. A gauge-invariant Lagrangian including the so-called Higgs potential, $V(\phi) = \mu^2\phi^\dagger\phi + \lambda(\phi^\dagger\phi)^2$, with $\lambda > 0$ and $\mu^2 < 0$,

$$\mathcal{L}_{\mathrm{H}} = \left(i\partial_\mu\phi - g\frac{\vec{\tau}}{2}\vec{W}_\mu\phi - g'\frac{Y}{2}B_\mu\phi \right)^\dagger \left(i\partial^\mu\phi - g\frac{\vec{\tau}}{2}\vec{W}^\mu\phi - g'\frac{Y}{2}B^\mu\phi \right) - V(\phi), \tag{2.11}$$

is added to the GSW Lagrangian with the isospin doublet ϕ, which has a weak hypercharge of $Y = 1$

$$\phi = \begin{pmatrix} \phi^+ \\ \phi^0 \end{pmatrix} = \frac{1}{\sqrt{2}} \begin{pmatrix} \phi_1 + i\phi_2 \\ \phi_3 + i\phi_4 \end{pmatrix}. \tag{2.12}$$

The scalar ground state ϕ_{G} of the Higgs potential is obtained by minimisation of $V(\phi)$ leading to

$$\phi_{\mathrm{G}} = \pm\sqrt{\frac{-\mu^2}{2\lambda}} = \pm v, \tag{2.13}$$

and a possible choice of the four-vector ground state ϕ_G^0 is

$$\phi_1 = \phi_2 = \phi_4 = 0, \quad \phi_3 = \pm v. \tag{2.14}$$

The ground state ϕ_G^0 is then expanded around its minimum to

$$\phi(x) = \frac{1}{\sqrt{2}} \begin{pmatrix} 0 \\ v + \eta(x) \end{pmatrix}, \tag{2.15}$$

and the field $\phi(x)$ is substituted into the Lagrangian $\mathcal{L}_{\mathrm{H}}$. The expected mass terms produced are, *e.g.* $\propto W_\mu^+ W^{-\mu}$, and by comparison with the terms in the Lagrangian, the boson masses are identified. For example, the relevant part of Eqn. 2.11 with $Y = 1$ for ϕ

$$\left(-g\frac{\vec{\tau}}{2}\vec{W}_\mu\phi - \frac{g'}{2}B_\mu\phi\right)^\dagger \left(-g\frac{\vec{\tau}}{2}\vec{W}^\mu\phi - \frac{g'}{2}B^\mu\phi\right), \tag{2.16}$$

$$= \frac{1}{2}v^2g^2\left[(W_\mu^1)^2 + (W_\mu^2)^2\right] + \frac{1}{8}v^2(g'B_\mu - gW_\mu^3)(g'B^\mu - gW^{3\mu}), \tag{2.17}$$

$$= (\frac{1}{2}vg)^2 W_\mu^+ W^{-\mu} + \frac{1}{8}v^2(W_\mu^3, B_\mu) \begin{pmatrix} g^2 & -gg' \\ -gg' & g'^2 \end{pmatrix} \begin{pmatrix} W^{3\mu} \\ B^\mu \end{pmatrix}, \tag{2.18}$$

$$= (\frac{1}{2}vg)^2 W_\mu^+ W^{-\mu} + \frac{1}{8}v^2\left[gW_\mu^3 - g'B_\mu\right]^2 + 0\left[g'W_\mu^3 + gB_\mu\right]^2. \tag{2.19}$$

The expected mass term of a $W^\pm$ boson is $M_W^2 W_\mu^+ W^{-\mu}$ and a comparison with the term $\propto W_\mu^+ W^{-\mu}$ in Eqn. 2.19 yields the mass of the $W^\pm$ boson $M_W = \frac{1}{2}gv$. To obtain the masses of the Z boson and the photon, the second and third terms in Eqn. 2.19 need to be compared to $\frac{1}{2}M_Z^2 Z_\mu^2 + \frac{1}{2}M_A^2 A_\mu^2$ leading to

$$A_\mu = \frac{g'W_\mu^3 + gB_\mu}{\sqrt{g^2 + g'^2}}, \quad M_A \equiv M_\gamma = 0, \tag{2.20}$$

$$Z_\mu = \frac{gW_\mu^3 - g'B_\mu}{\sqrt{g^2 + g'^2}}, \quad M_Z = \frac{1}{2}v\sqrt{g^2 + g'^2}. \tag{2.21}$$

From Eqn. 2.10, it follows

$$g\sin\theta_W = g'\cos\theta_W. \tag{2.22}$$

The Higgs mechanism leads to the prediction of a physically observable boson, which is the so-called Higgs boson. In September 2012, the ATLAS and CMS collaborations published the observation of a particle compatible with the production and decay of the Standard Model Higgs boson [17, 18], the LHC Run 1 best mass measurement is $125.09 \pm 0.21_{\mathrm{stat.}} \pm 0.11_{\mathrm{syst.}}$ GeV [19].

A gauge-invariant Yukawa term describing the coupling between the Higgs and the fermion fields is added to the electroweak Lagrangian to generate fermion masses. For example, the Yukawa Lagrangian for electron and electron neutrino is given by

$$\mathcal{L}^{f}_{\text{Yukawa}} = - G_e \left[(\overline{\nu}_e, \overline{e})_L \begin{pmatrix} \phi^+ \\ \phi^0 \end{pmatrix} e_R + \overline{e}_R (\phi^-, \overline{\phi}^0) \begin{pmatrix} \nu_e \\ e \end{pmatrix}_L \right]. \tag{2.23}$$

After breaking the symmetry spontaneously by substituting ϕ by $\phi(x)$ (see Eqn. 2.15), the Lagrangian $\mathcal{L}^{f}_{\text{Yukawa}}$ becomes

$$\mathcal{L}^{f}_{\text{Yukawa}} = - \frac{G_e}{\sqrt{2}} v (\overline{e}_L e_R + \overline{e}_R e_L) - \frac{G_e}{\sqrt{2}} h (\overline{e}_L e_R + \overline{e}_R e_L). \tag{2.24}$$

The Yukawa coupling G_e is then chosen such that the electron mass is generated. The generated mass terms depend on the strength of the Yukawa coupling

$$m_e = \frac{G_e v}{\sqrt{2}}. \tag{2.25}$$

In the Standard Model, neutrinos are massless particles but experiments with atmospheric, solar, accelerator and reactor neutrinos have shown that neutrinos undergo oscillations [20–22], which requires them to have a non-zero mass. In 2015, the Nobel prize for physics was awarded to Takaaki Kajita and Arthur B. McDonald for their contribution to the discovery of neutrino oscillations, which shows that neutrinos have mass, at Super-Kamiokande [23] and the Sudbury Neutrino Observatory [24, 25].

In the quark sector, the Higgs doublet has to be modified to allow the mass generation of up-type quarks but the formalism follows the mass generation of leptons closely. The modified Higgs doublet is given by

$$\phi_c = -i\tau_2 \phi^* = \begin{pmatrix} -\overline{\phi}^0 \\ \phi^- \end{pmatrix}. \tag{2.26}$$

For example, the gauge-invariant term, which is added to the GSW Lagrangian for u and d quarks is given by

$$\mathcal{L}^{q}_{\text{Yukawa}} = - G_d (\overline{u}, \overline{d})_L \begin{pmatrix} \phi^+ \\ \phi^0 \end{pmatrix} d_R - G_u (\overline{u}, \overline{d})_L \begin{pmatrix} -\overline{\phi}^0 \\ \phi^- \end{pmatrix} u_R + h.c., \tag{2.27}$$

where $h.c.$ stands for the hermitian conjugate. Thus, similarly to the lepton masses, the quark masses are

$$m_u = \frac{G_u v}{\sqrt{2}}, \tag{2.28}$$

$$m_d = \frac{G_d v}{\sqrt{2}}. \tag{2.29}$$

2.1.1.2. Quark-mixing matrix

In the Standard Model, the masses and mixings of quarks both arise from the Yukawa interactions with the Higgs field. As described in Chapt. 2.1.1.1, the quark masses are generated by spontaneous symmetry breaking. Experimental results indicate that the mass eigenstates of quarks are not consistent with their flavour eigenstates. For instance, the flavour eigenstates (d', s', b') of the down-type quarks are linear combinations of the mass eigenstates (d, s, b). By expressing the Lagrangian in terms of the quark mass eigenstates instead of the flavour eigenstates, the couplings between up- and down-type quarks are given by the elements of the quark-mixing or Cabibbo-Kobayashi-Maskawa (CKM) matrix V_{CKM} [26, 27]

$$\begin{pmatrix} d' \\ s' \\ b' \end{pmatrix} = V_{\mathrm{CKM}} \begin{pmatrix} d \\ s \\ b \end{pmatrix} = \begin{pmatrix} V_{ud} & V_{us} & V_{ub} \\ V_{cd} & V_{cs} & V_{cb} \\ V_{td} & V_{ts} & V_{tb} \end{pmatrix} \begin{pmatrix} d \\ s \\ b \end{pmatrix} \quad \text{with} \quad V_{\mathrm{CKM}}^{\dagger} V_{\mathrm{CKM}} = 1. \tag{2.30}$$

Consequently, the matrix elements of the CKM matrix V_{ij} describe the coupling strength of the flavour-changing weak current between up- and down-type quarks mediated by $W^{\pm}$ bosons. In the Standard Model, decays that change the quark flavours and are mediated by Z bosons are forbidden at tree level. These flavour-changing neutral currents may occur beyond tree level but are highly suppressed by the GIM mechanism [28]. For a two generation system, *e.g.* consisting of (up, down) and (charm, strange) quarks, the flavour-changing neutral current amplitudes cancel out, indeed this was used to predict the existence of the charm quark in 1970 [28]. The CKM matrix can be parametrised by three rotation angles $\theta_{12}, \theta_{13}, \theta_{23}$ and a *CP*-violating phase δ as follows [11]

$$V_{\mathrm{CKM}} = \begin{pmatrix} c_{12}c_{13} & s_{12}c_{13} & s_{13}e^{-i\delta} \\ -s_{12}c_{23} - c_{12}s_{23}s_{13}e^{i\delta} & c_{12}c_{23} - s_{12}s_{23}s_{13}e^{i\delta} & s_{23}c_{13} \\ s_{12}s_{23} - c_{12}c_{23}s_{13}e^{i\delta} & -c_{12}s_{23} - s_{12}c_{23}s_{13}e^{i\delta} & c_{23}c_{13} \end{pmatrix}, \tag{2.31}$$

where the notation $s_{ij} = \sin\theta_{ij}$ and $c_{ij} = \cos\theta_{ij}$ is used.

From experimental results, it is known that the rotation angles fulfill a certain hierarchy $s_{13} < s_{23} < s_{12} < 1$. The Wolfenstein parametrisation [29] utilises this hierarchy by expanding s_{ij} in terms of λ resulting in

$$\begin{aligned} s_{12} = \lambda = \frac{|V_{us}|}{\sqrt{|V_{ud}|^2 + |V_{us}|^2}}, \quad s_{23} = A\lambda^2 = \lambda \left| \frac{V_{cb}}{V_{us}} \right|, \\ s_{13}e^{i\delta} = V_{ub}^{*} = A\lambda^3(\rho + i\eta) = \frac{A\lambda^3(\bar{\rho} + i\bar{\eta})\sqrt{1 - A^2\lambda^4}}{\sqrt{1-\lambda^2}\,[1 - A^2\lambda^4(\bar{\rho} + i\bar{\eta})]}. \end{aligned} \tag{2.32}$$

Hence, the CKM matrix in the Wolfenstein parametrisation is given by

$$V_{\mathrm{CKM}} = \begin{pmatrix} 1-\lambda^2/2 & \lambda & A\lambda^3(\rho - i\eta + i\eta\lambda^2/2) \\ -\lambda & 1-\lambda^2/2 - i\eta A\lambda^4 & A\lambda^2(1+i\eta\lambda^2) \\ A\lambda^3(1-\rho-i\eta) & -A\lambda^2 & 1 \end{pmatrix} + \mathcal{O}(\lambda^5), \quad (2.33)$$

where the real part of the CKM matrix has been expanded to $\mathcal{O}(\lambda^3)$ and the imaginary part up to $\mathcal{O}(\lambda^5)$. *CP* violation enters through the terms $\propto i\eta$ in V_{td}, V_{cs}, V_{ub} and V_{cb}.

2.1.2. Quantum chromodynamics

Quantum chromodynamics or the strong interaction is described by a non-abelian $SU(3)_{\mathrm{C}}$ gauge group with the quantum number colour C. The non-commuting generators T_a are the so-called Gell-Mann matrices fulfilling the commutation relation, $[T_a, T_b] = if_{abc}T_c$, where f_{abc} are completely antisymmetric structure constants. The gauge bosons, gluons, couple to the colour fields q_1, q_2, q_3 where the index denotes the colour charges. The free Lagrangian of a colour field q_j is given by

$$\mathcal{L}_0 = i\bar{q}_j\gamma_\mu\partial^\mu q_j - m\bar{q}_j q_j \quad \text{with} \quad j = 1,2,3. \quad (2.34)$$

In the following, the quark field q will denote one of the three colour fields q_j. Under a local $SU(3)_{\mathrm{C}}$ gauge transformation

$$q(x) \to q(x)' = e^{i\alpha_a(x)T_a} q(x) \quad \text{with} \quad a = 1, ..., 8, \quad (2.35)$$

the Lagrangian $\mathcal{L}_0$ is not invariant. Gauge invariance is ensured by introducing a covariant derivative analogously to the consideration of the $\mathrm{U(1)_Y}$ gauge group

$$D_\mu \equiv \partial_\mu + igT_a G_\mu^a \quad \text{where} \quad G_\mu^a \to G_\mu^a - \frac{1}{g}\partial_\mu\alpha_a - f_{abc}\alpha_b G_\mu^c. \quad (2.36)$$

where the gauge fields G_μ^a represent the fields corresponding to the massless gluons. Adding the kinetic term for the gauge fields, the gauge invariant QCD Lagrangian for a colour field q is given by

$$\mathcal{L}_{\mathrm{QCD}} = \bar{q}\left(i\gamma^\mu\partial_\mu - m\right)q - g\left(\bar{q}\gamma^\mu T_a q\right)G_\mu^a - \frac{1}{4}G_{\mu\nu}^a G_a^{\mu\nu}, \quad (2.37)$$

with $G_{\mu\nu}^a \equiv \partial_\mu G_\nu^a - \partial_\nu G_\mu^a - g f_{abc} G_\mu^b G_\nu^c$. In contrast to the electroweak interaction (see Chapt. 2.1.1), no experimental evidence for the violation of the symmetry under charge parity transformations has been observed. QCD does allow a violation of *CP* symmetry and it is not understood why *CP* should be conserved in QCD; this is known as the strong *CP* problem.

2.1.3. Open questions of the Standard Model

As mentioned in the previous section, the Standard Model does not give answers to all experimentally observed puzzles. For example, no evidence for *CP* violation in strong interaction has been observed (strong *CP* problem) and it is not understood why quarks are confined. In 2014, the LHCb Collaboration reported the quantum numbers of the tetraquark particle $Z(4430)$ [30], which had been discovered by Belle in 2007 [31]. A pentaquark state [32] was discovered by the LHCb Collaboration in 2015 and one open question is whether other bound quark states with *e.g.* a molecule-like structure exist. It is also not known where the asymmetry between matter and anti-matter in the early stages of the universe comes from or what particles constitute dark matter. As discussed previously, neutrinos are subject to oscillations and hence they have a non-zero mass. It is not yet known if neutrinos are Majorana or Dirac particles, *i.e.* whether or not they are their own anti-particles, and what the mass hierarchy of the ν_e, ν_μ and ν_τ states is.

2.2. Neutral Charm Mixing

In the neutral D meson system, transitions between D^0 and $\overline{D}^0$ mesons are enabled by processes changing the flavour quantum number F by $|\Delta F| = 2$ as illustrated in Fig. 2.1. The contribution of these short-distance effects to the mixing probability is suppressed in the charm sector. The internal $i = d, s, b$ quark loops contribute with factors $\propto V_{ci}^* V_{ui}$ to the amplitude of the diagram shown in Fig. 2.1. The factor $V_{ci}^* V_{ui}$ is $\propto \lambda^5$ and hence negligible. Since the mass difference between the d and s is relatively small, the diagram is suppressed by the GIM mechanism [28]. In addition, mixing between D^0 and $\overline{D}^0$ mesons occurs via long range hadronic interactions where for example the D^0 meson decays into a state, which is accessible by both flavour eigenstates such as $\pi^+\pi^-$ or K^+K^-. Through recombination, a $\overline{D}^0$ is created as illustrated in Fig. 2.2. In the following section, the phenomenon of neutral meson mixing [33] are discussed for the neutral D meson system.

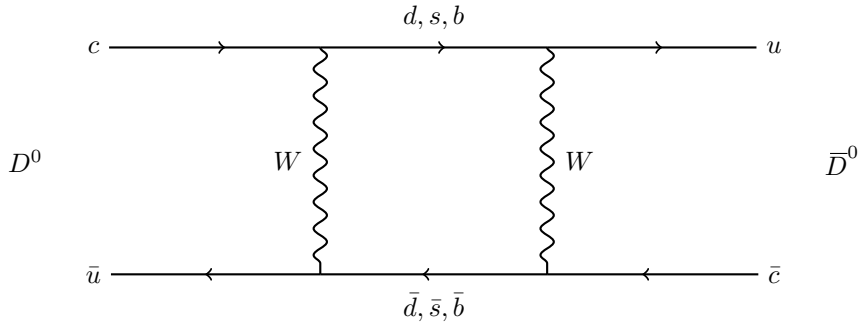

Figure 2.1.: *Box diagram for $D^0 - \overline{D}^0$ transitions via the exchange of intermediate quarks. Another box diagram with the $W^\pm$, (d, s, b) lines rotated by 90° exists.*

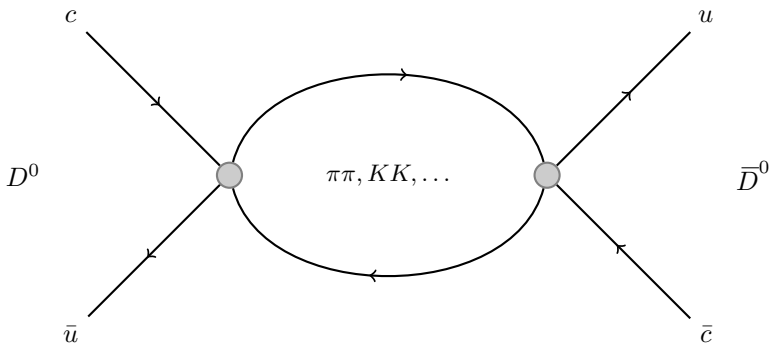

Figure 2.2.: *Diagram for $D^0 - \overline{D}^0$ transitions via long range hadronic interactions.*

Starting from the Schrödinger equation

$$i\hbar\frac{d}{dt}|\psi\rangle = \mathcal{H}|\psi\rangle \quad \text{for a generic state} \quad |\psi\rangle = \begin{pmatrix} |a(t)\rangle \\ |b(t)\rangle \end{pmatrix}, \tag{2.38}$$

$D^0 - \overline{D}^0$ oscillations are described by the effective Hamiltonian $\mathcal{H} = \mathbf{M} - i\mathbf{\Gamma}$ with the Hermitian mass $\mathbf{M}$ and decay $\mathbf{\Gamma}$ matrices

$$\mathbf{M} = \frac{1}{2}(\mathcal{H} + \mathcal{H}^\dagger) = \mathbf{M}^\dagger, \tag{2.39}$$

$$\mathbf{\Gamma} = i(\mathcal{H} - \mathcal{H}^\dagger) = \mathbf{\Gamma}^\dagger. \tag{2.40}$$

The effective Hamiltonian can be expressed as

$$\mathcal{H} = \begin{pmatrix} M_{11} - i\Gamma_{11}/2 & M_{12} - i\Gamma_{12}/2 \\ M_{21} - i\Gamma_{21}/2 & M_{22} - i\Gamma_{22}/2 \end{pmatrix}, \tag{2.41}$$

and under the assumption of *CPT* invariance, the diagonal elements of the mass and decay matrix are $M_{11} = M_{22} \equiv M$ and $\Gamma_{11} = \Gamma_{22} \equiv \Gamma$. In general, the flavour eigenstates $|D^0\rangle$ and $|\overline{D}^0\rangle$ do not coincide with the physical eigenstates $|D_1\rangle$ and $|D_2\rangle$ with masses $m_{1,2}$ and decay widths $\Gamma_{1,2}$ of the effective Hamiltonian $\mathcal{H}$

$$\mathcal{H}|D_{1,2}\rangle = \lambda_{1,2}|D_{1,2}\rangle \quad \text{with} \quad \lambda_{1,2} \equiv m_{1,2} - i\Gamma_{1,2}/2. \tag{2.42}$$

The physical eigenstates are written as linear combination of the flavour eigenstates

$$|D_{1,2}\rangle = p|D^0\rangle \pm q|\overline{D}^0\rangle, \tag{2.43}$$

with coefficients $q, p \in \mathbb{C}$ satisfying the normalisation condition $|q^2| + |p^2| = 1$ and D_1 is defined

to be *CP*-even. The diagonalisation of the effective Hamiltonian $\mathcal{H}$ yields the eigenvalues

$$\lambda_{1,2} = \mathcal{H}_{11} \pm \sqrt{\mathcal{H}_{12}\mathcal{H}_{21}} = \mathcal{H}_{11} \pm \frac{q}{p}\mathcal{H}_{12} \quad \text{with} \quad \frac{q}{p} = \sqrt{\frac{\mathcal{H}_{21}}{\mathcal{H}_{12}}}. \tag{2.44}$$

The phase convention of q and p is chosen such that, in the limit of *CP* symmetry,

$$CP|D^0\rangle = +|\overline{D}^0\rangle. \tag{2.45}$$

In this convention, the eigenstates of the *CP* operator only coincide with the Hamiltonian eigenstates if $q = p$, so *CP* conservation leads to $q/p = +1$. The time-evolution of the physical eigenstates is then

$$|D_{1,2}(t)\rangle = e^{-i\lambda_{1,2}t}|D_{1,2}(0)\rangle, \tag{2.46}$$

$$= e^{-im_{1,2}t}e^{-\frac{\Gamma_{1,2}}{2}t}|D_{1,2}(0)\rangle. \tag{2.47}$$

Introducing the mixing parameters

$$x = \frac{m_1 - m_2}{\Gamma}, \tag{2.48}$$

$$y = \frac{\Gamma_1 - \Gamma_2}{2\Gamma}, \tag{2.49}$$

with the averaged values of mass $m = (m_1 + m_2)/2$ and decay width $\Gamma = (\Gamma_1 + \Gamma_2)/2$, Eqn. 2.46 is written as

$$|D_{1,2}(t)\rangle = e^{-imt}e^{-\frac{\Gamma}{2}t}e^{\mp(y+ix)\frac{\Gamma}{2}t}|D_{1,2}(0)\rangle, \tag{2.50}$$

$$\equiv e_{1,2}(t)|D_{1,2}(0)\rangle. \tag{2.51}$$

From Eqn. 2.43 and Eqn. 2.50 follows the time evolution of the flavour eigenstates

$$|D^0(t)\rangle = \frac{e_1(t) + e_2(t)}{2}|D^0\rangle + \frac{q}{p}\frac{e_1(t) - e_2(t)}{2}|\overline{D}^0\rangle, \tag{2.52}$$

$$|\overline{D}^0(t)\rangle = \frac{e_1(t) + e_2(t)}{2}|\overline{D}^0\rangle + \frac{p}{q}\frac{e_1(t) - e_2(t)}{2}|D^0\rangle. \tag{2.53}$$

Thus, the time-dependent amplitudes of a $|D^0\rangle$ and $|\overline{D}^0\rangle$ decaying into a common final state f are

$$\langle f|\mathcal{H}|D^0(t)\rangle = \langle f|\mathcal{H}\frac{e_1(t) + e_2(t)}{2}|D^0\rangle + \langle f|\mathcal{H}\frac{q}{p}\frac{e_1(t) - e_2(t)}{2}|\overline{D}^0\rangle, \tag{2.54}$$

$$\langle f|\mathcal{H}|\overline{D}^0(t)\rangle = \langle f|\mathcal{H}\ \frac{e_1(t) + e_2(t)}{2}|\overline{D}^0\rangle + \langle f|\mathcal{H}\frac{p}{q}\frac{e_1(t) - e_2(t)}{2}|D^0\rangle. \tag{2.55}$$

With the definitions of

$$\mathcal{A}_f \equiv \langle f|\mathcal{H}|D^0\rangle, \tag{2.56}$$
$$\bar{\mathcal{A}}_f \equiv \langle f|\mathcal{H}|\overline{D}^0\rangle, \tag{2.57}$$

Eqn. 2.54 is rewritten as

$$\mathcal{A}_f(t) \equiv \langle f|\mathcal{H}|D^0(t)\rangle = \frac{e_1(t)+e_2(t)}{2}\mathcal{A}_f + \frac{q}{p}\frac{e_1(t)-e_2(t)}{2}\bar{\mathcal{A}}_f, \tag{2.58}$$
$$\bar{\mathcal{A}}_f(t) \equiv \langle f|\mathcal{H}|\overline{D}^0(t)\rangle = \frac{e_1(t)+e_2(t)}{2}\bar{\mathcal{A}}_f + \frac{p}{q}\frac{e_1(t)-e_2(t)}{2}\mathcal{A}_f. \tag{2.59}$$

To simplify the discussion, the time-dependent amplitudes $\mathcal{A}_f(t)$ and $\bar{\mathcal{A}}_f(t)$ are split into a time- and a phase-space dependent part

$$\begin{aligned}\mathcal{A}_f(t) &= \frac{1}{2}e_1(t)\left(\mathcal{A}_f + \frac{q}{p}\bar{\mathcal{A}}_f\right) + \frac{1}{2}e_2(t)\left(\mathcal{A}_f - \frac{q}{p}\bar{\mathcal{A}}_f\right) \qquad (2.60)\\ &\equiv \frac{1}{2}e_1(t)A_1 + \frac{1}{2}e_2(t)A_2,\\ \bar{\mathcal{A}}_f(t) &= \frac{1}{2}e_1(t)\left(\bar{\mathcal{A}}_f + \frac{p}{q}\mathcal{A}_f\right) + \frac{1}{2}e_2(t)\left(\bar{\mathcal{A}}_f - \frac{p}{q}\mathcal{A}_f\right) \qquad (2.61)\\ &\equiv \frac{1}{2}e_1(t)\bar{A}_1 + \frac{1}{2}e_2(t)\bar{A}_2.\end{aligned}$$

In most publications, the above notation is used, with the amplitudes being denoted as $A_{1,2}$. A different but equivalent notation is used in this analysis, where $A \equiv \mathcal{A}_f$, and $B \equiv \bar{\mathcal{A}}_f$, giving the forms

$$\mathcal{A}_f(t) = \frac{1}{2}e_1(t)\left(A + \frac{q}{p}B\right) + \frac{1}{2}e_2(t)\left(A - \frac{q}{p}B\right), \tag{2.62}$$
$$\bar{\mathcal{A}}_f(t) = \frac{1}{2}e_1(t)\left(B + \frac{p}{q}A\right) + \frac{1}{2}e_2(t)\left(B - \frac{p}{q}A\right). \tag{2.63}$$

The squared amplitude $|\mathcal{A}_f(t)|^2$ is then

$$|\mathcal{A}_f(t)|^2 = \left|\frac{1}{2}e_1(t)\left(A + \frac{q}{p}B\right) + \frac{1}{2}e_2(t)\left(A - \frac{q}{p}B\right)\right|^2 \tag{2.64}$$

$$\begin{aligned}\Rightarrow 4|\mathcal{A}_f(t)|^2 = {} & |e_1(t)|^2\left(A + \frac{q}{p}B\right)\left(A^* + \left[\frac{q}{p}B\right]^*\right)\\ & + |e_2(t)|^2\left(A - \frac{q}{p}B\right)\left(A^* - \left[\frac{q}{p}B\right]^*\right)\\ & + e_1(t)e_2^*(t)\left(A + \frac{q}{p}B\right)\left(A^* - \left[\frac{q}{p}B\right]^*\right)\\ & + e_1^*(t)e_2(t)\left(A^* + \left[\frac{q}{p}B\right]^*\right)\left(A - \frac{q}{p}B\right). \qquad (2.65)\end{aligned}$$

Exploiting the relations $(AB^* - A^*B) = 2i\mathcal{I}m(AB^*) = -2i\mathcal{I}m(A^*B)$ and $(AB^* + A^*B) = 2\mathcal{R}e(AB^*) = 2\mathcal{R}e(A^*B)$, Eqn. 2.64 is rewritten as

$$\begin{aligned}
\longleftrightarrow e^{\Gamma t}4|\mathcal{A}_f(t)|^2 = e^{-\Gamma y t}&\left(A + \frac{q}{p}B\right)\left(A^* + \left[\frac{q}{p}B\right]^*\right) \\
&+ e^{+\Gamma y t}\left(A - \frac{q}{p}B\right)\left(A^* - \left[\frac{q}{p}B\right]^*\right) \\
&+ e^{-ix\Gamma t}\left(A + \frac{q}{p}B\right)\left(A^* - \left[\frac{q}{p}B\right]^*\right) \\
&+ e^{+ix\Gamma t}\left(A^* + \left[\frac{q}{p}B\right]^*\right)\left(A - \frac{q}{p}B\right), \qquad (2.66) \\
\longleftrightarrow e^{\Gamma t}4|\mathcal{A}_f(t)|^2 = e^{-\Gamma y t}&\left\{|A|^2 + \left|\frac{q}{p}B\right|^2 + 2\mathcal{R}e\left(A\left[\frac{q}{p}B\right]^*\right)\right\} \\
&+ e^{+\Gamma y t}\left\{|A|^2 + \left|\frac{q}{p}B\right|^2 - 2\mathcal{R}e\left(A\left[\frac{q}{p}B\right]^*\right)\right\} \\
&+ e^{-ix\Gamma t}\left\{|A|^2 - \left|\frac{q}{p}B\right|^2 - 2i\mathcal{I}m\left(A\left[\frac{q}{p}B\right]^*\right)\right\} \\
&+ e^{+ix\Gamma t}\left\{|A|^2 - \left|\frac{q}{p}B\right|^2 + 2i\mathcal{I}m\left(A\left[\frac{q}{p}B\right]^*\right)\right\}. \qquad (2.67)
\end{aligned}$$

Therefore, the squared amplitude $|\mathcal{A}_f(t)|^2$ can be expressed as

$$\begin{aligned}
|\mathcal{A}_f(t)|^2 = \frac{1}{2}e^{-\Gamma t}&\left[\left(|A|^2 - \left|\frac{q}{p}B\right|^2\right)\cos(x\Gamma t) - 2\mathcal{I}m\left(AB^*\left[\frac{q}{p}\right]^*\right)\sin(x\Gamma t)\right. \\
&\left. + \left(|A|^2 + \left|\frac{q}{p}B\right|^2\right)\cosh(y\Gamma t) - 2\mathcal{R}e\left(AB^*\left[\frac{q}{p}\right]^*\right)\sinh(y\Gamma t)\right]. \qquad (2.68)
\end{aligned}$$

For a three-body decay, the amplitudes A and B depend on a point in phase-space, which is spanned by $m^2(K^0_S\pi^-)$ and $m^2(K^0_S\pi^+)$. The phase-space dependence and models used in this analysis are described in Chapt. 11.

2.3. CP violation

The symmetry under charge-parity transformation (*CP* symmetry [33]) holds if the Hamiltonian $\mathcal{H}$ is invariant under the CP transformation

$$\mathcal{H}_{CP} \equiv (CP)^\dagger \mathcal{H}(CP) = \mathcal{H}. \qquad (2.69)$$

In the case that the CP symmetry is broken, this phenomenon is called *CP* violation. *CP* violation has only been observed in weak processes. Under a *CP* transformation, a state $|\psi\rangle$ transforms via

$$CP|\psi\rangle = \eta_{CP}|\psi\rangle, \tag{2.70}$$

with the phase factor η_{CP} being normalised to $|\eta_{CP}|^2 = 1$. Phases in the transition amplitude originate from complex parameters in the Lagrangian density, where global phases can be redefined and thus have no impact on the discussion of *CP* violation. For a weak process, the phase factors for two *CP*-conjugate processes A_f and $\bar{A}_{\bar{f}}$ have opposite sign. In contrary to these weak phases, other processes can introduce phases, which have the same sign for *CP*-conjugate states. The most important same-sign phases arise from strong interactions, which are the so-called strong or scattering phases. To observe *CP*-violating phases, phase differences between amplitudes have to be measured requiring the interference of at least two amplitudes A_1 and A_2 with the weak phases $\phi_{1,2}$ and strong phases $\delta_{1,2}$. The amplitude and its *CP*-conjugate are then

$$A(i \to f) = |A_1|e^{i\phi_1}e^{i\delta_1} + |A_2|e^{i\phi_2}e^{i\delta_2}, \tag{2.71}$$
$$A(\bar{i} \to \bar{f}) = |A_1|e^{-i\phi_1}e^{i\delta_1} + |A_2|e^{-i\phi_2}e^{i\delta_2}, \tag{2.72}$$

leading to a difference in transition rates of

$$|A(\bar{i} \to \bar{f})|^2 - |A(i \to f)|^2 = 2|A_1||A_2|\sin(\phi_1 - \phi_2)\sin(\delta_1 - \delta_2). \tag{2.73}$$

Equation 2.73 applies to the measurement of rate asymmetries, which are defined as $|A(\bar{i} \to \bar{f})|^2 - |A(i \to f)|^2 / (|A(\bar{i} \to \bar{f})|^2 + |A(i \to f)|^2)$, which are even under *CP* transformations ($\eta_{CP} = 1$). Observables proportional to $\sin(\phi_1 - \phi_2)\cos(\delta_1 - \delta_2) + \cos(\phi_1 - \phi_2)\sin(\delta_1 - \delta_2)$, such as triple-product asymmetries [34, 35], are CP-odd ($\eta_{CP} = -1$).
CP violation is classified into three types: *CP* violation in decay (direct *CP* violation); *CP* violation in mixing; and *CP* violation in the interference of mixing and decay. The two latter types are denoted as indirect *CP* violation.

CP violation in decay

CP violation in decay or direct *CP* violation is present if the physical amplitude A_f for a process $i \to f$ differs from the CP-conjugate amplitude $\bar{A}_{\bar{f}}$

$$|\bar{A}_{\bar{f}}| \neq |A_f|. \tag{2.74}$$

Direct *CP* violation is the only type of *CP* violation, which is not restricted to neutral mesons undergoing mixing.

CP violation in mixing

The eigenstates of the *CP* operator do not coincide with the physical states if

$$|q| \neq |p|, \tag{2.75}$$

meaning that the two flavour components of the physical eigenstates have different weights. This phenomenon is known as *CP* violation in mixing.

CP violation in the interference of mixing and decay

As illustrated in Fig. 2.3, a D^0 meson can either decay directly in a final state $f = \bar{f}$ or via the oscillation into a $\overline{D}^0$ meson.

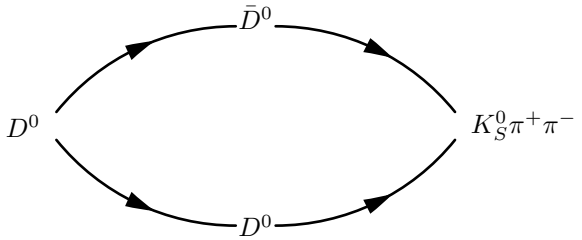

Figure 2.3.: *A D^0 meson either decays directly into $K^0_S\pi^+\pi^-$ or after oscillating into a $\overline{D}^0$ meson.*

For such a process, the total decay amplitude is

$$A(D^0 \to f) + A(D^0 \to \overline{D}^0)A(\overline{D}^0 \to f). \tag{2.76}$$

If the final state is reached via a $D^0 - \overline{D}^0$ oscillation, the relative phases between the two amplitudes $A(D^0 \to \overline{D}^0)$ and $A(\overline{D}^0 \to f)$ is relevant. The decay paths $D^0 \to f$ and $D^0 \to \overline{D}^0 \to f$ interfere with each other. In general, *CP* violation in the interference of mixing and decay is present for a non-vanishing phase

$$\phi_f = arg\left(\frac{q\bar{A}_f}{pA_f}\right) \neq 0, \tag{2.77}$$

which might depend on the final state f.

2.4. Existing measurements

Previous measurements using $D^0 \to K^0_S\pi^+\pi^-$ decays have been published by the CLEO, BaBar, Belle and CDF collaborations. A measurement of the time-integrated *CP* asymmetry was published by CDF, which is consistent with no direct *CP* violation [36]. The measurements of the $D^0 - \overline{D}^0$ mixing parameters and search for indirect *CP* violation have followed a model-dependent approach. A first model-independent measurement of the mixing parameters from $D^0 \to K^0_S\pi^+\pi^-$ decays has been published by LHCb [37]. These existing measurements reconstruct $D^0 \to K^0_S\pi^+\pi^-$ in the decay chain $D^{*+} \to D^0(\to K^0_S\pi^+\pi^-)\pi^+$, and use the charge of the soft pion from the D^* decay to determine the flavour of the D^0 at production.

In the following section, an overview of the existing measurements of the $D^0 - \overline{D}^0$ mixing parameters extracted from $D^0 \to K^0_S\pi^+\pi^-$ decays is presented.

2.4.1. Model-dependent CLEO measurement

The CLEO collaboration reported a measurement of x and y [38] on a dataset corresponding to a luminosity of $9\,\text{fb}^{-1}$ recorded with the CLEO II.V detector at the e^+e^- Cornell Electron Storage Ring (CESR).
The time-dependent amplitude given in Eqn. 2.68 also depends on a point in phase-space, which is spanned by $m^2(K^0_S\pi^+)$ and $m^2(K^0_S\pi^-)$. The phase-space dependence is contained in the amplitudes A and B, which are expressed as the sum of amplitudes of a quasi two-body decay through an intermediate resonance r. In the CLEO analysis, the resonances r contributing to the amplitude are $K^*(892)^-\pi^+$, $K^*_0(1430)^-\pi^+$, $K^*_2(1430)^-\pi^+$, $K^*(1680)^-\pi^+$, $K^0_S\rho(770)$, $K^0_S\omega(782)$, $K^0_S f_0(980)$, $K^0_S f_2(1270)$, $K^0_S f_0(1370)$, $K^*(892)^+\pi^-$ and a non-resonant component. Three different fit scenarios are reported: the first scenario allows for *CP* violation, the second assumes *CP* conservation and in the third scenario, a fit assuming CP conservation is performed separately to the D^0 and $\overline{D}^0$ samples. The CLEO analysis splits the amplitudes into components

$$\langle f|\mathcal{H}|D_{+,-}\rangle = A_{+,-}, \tag{2.78}$$
$$\langle \bar{f}|\mathcal{H}|D_{+,-}\rangle = \bar{A}_{+,-}, \tag{2.79}$$
$$\langle f|\mathcal{H}|{D^0}_F\rangle = A_F, \tag{2.80}$$
$$\langle \bar{f}|\mathcal{H}|{\overline{D}^0}_{\bar{F}}\rangle = \bar{A}_{\bar{F}}, \tag{2.81}$$

where the amplitudes A_+ and A_- denote CP-even and CP-odd modes, respectively. Decay amplitudes of a D^0 or $\overline{D}^0$ to a flavour eigenstate F are denoted by A_F and $\bar{A}_{\bar{F}}$, respectively. *CP* violation is included by the introduction of two parameters ϵ and ϕ in the fractions

$$\chi_F = \frac{q\bar{A}_F}{pA_F} = \left|\frac{\bar{A}_F}{A_F}\right| \frac{1-\epsilon}{1+\epsilon} e^{i(\delta+\phi)}, \tag{2.82}$$
$$\chi_{\bar{F}} = \frac{q\bar{A}_{\bar{F}}}{pA_{\bar{F}}} = \left|\frac{\bar{A}_{\bar{F}}}{A_{\bar{F}}}\right| \frac{1-\epsilon}{1+\epsilon} e^{-i(\delta-\phi)}, \tag{2.83}$$
$$\chi_\pm = \frac{q\bar{A}_\pm}{pA_\pm} = \pm\left|\frac{\bar{A}_\pm}{A_\pm}\right| \frac{1-\epsilon}{1+\epsilon} e^{i\phi}, \tag{2.84}$$

with the relative strong phase δ. The results from the *CP*-conserving fit are

$$x = (1.9^{+3.2}_{-3.3} \pm 0.4 \pm 0.4)\%, \tag{2.85}$$
$$y = (-1.4 \pm 2.4 \pm 0.8 \pm 0.4)\%, \tag{2.86}$$

with statistical, experimental systematic and modelling systematic uncertainty. At $95\%\,C.L.$ including systematic uncertainties, the limits on the mixing parameters are $-4.7\% < x < 8.6\%$ and $-6.1\% < y < 3.5\%$. From the *CP*-violating fit, the *CP* violation parameters are measured

to be $\epsilon = -0.3 \pm 0.5$ and $\phi = 42° \pm 78°$ and the mixing parameters are determined to be $x = (2.6^{+3.8}_{-9.0} \pm 0.4 \pm 0.4)\%$ and $y = (-0.3^{+4.0}_{-4.6} \pm 0.8 \pm 0.4)\%$. The results are consistent with the no-mixing hypothesis and with the conservation of *CP* symmetry.

2.4.2. Model-dependent BaBar measurement

At the asymmetric e^+e^- PEP-II collider, the BaBar experiment has collected a dataset corresponding to a luminosity of $468.5\,\text{fb}^{-1}$ at the $\Upsilon(4S)$ resonance [39]. The BaBar collaboration reported a measurement of $x = (0.16 \pm 0.23 \pm 0.12 \pm 0.08)\%$ and $y = (0.57 \pm 0.20 \pm 0.13 \pm 0.07)\%$ [39] where the uncertainties are statistical, systematic and model-induced. The model used in the BaBar analysis differs from the models used previously by CLEO [38] and Belle [40]. The resonances r contributing to the amplitude are $K^*(892)^-\pi^+$, $K_0^*(1430)^-\pi^+$, $K_2^*(1430)^-\pi^+$, $K^*(1680)^-\pi^+$, $K^0_S\rho(770)$, $K^0_S\omega(782)$, $K^0_S f_2(1270)$, $K^*(892)^+\pi^-$, $K_0^*(1430)^+\pi^-$, $K_2^*(1430)^+\pi^-$. The $\pi^+\pi^-$ S-wave is described by a K-matrix formalism with the P-vector approach and five poles and for the $K^0_S\pi^\pm$ S-wave, an amplitude similar to the amplitude measured by the LASS collaboration is used. A description of the K-matrix formalism with the P-vector approach and the LASS parameterisation is given in Chapt. 11.

As a cross check, the data are split into D^0 and $\overline{D}^0$ samples and the decay amplitudes for D^0 and $\overline{D}^0$ are forced to be the same whereas the mixing parameters are allowed to differ. This fit scenario allows to test for indirect *CP* violation. The mixing parameters obtained by the two independent fits are consistent and no evidence for *CP* violation in mixing is found.

2.4.3. Model-dependent Belle measurements

The Belle collaboration published the results of a mixing analysis and *CP* violation search on a subset of the final Belle dataset and in 2014, an updated analysis on the full dataset. The data were recorded with the Belle detector at the KEKB e^+e^- collider.

Measurement on $540\,\text{fb}^{-1}$

The mixing measurement is based on a dataset corresponding to a luminosity of $540\,\text{fb}^{-1}$ [40]. The amplitude model used in the mixing measurement has the following contributions: $K^*(892)^-\pi^+$, $K_0^*(1430)^-\pi^+$, $K_2^*(1430)^-\pi^+$, $K^*(1410)^-\pi^+$, $K^*(1680)^-\pi^+$, $K^0_S\rho(770)$, $K^0_S\omega(782)$, $K^0_S f_0(980)$, $K^0_S f_2(1270)$, $K^0_S f_0(1370)$, $K^0_S\rho(1450)$, $K^0_S\sigma_1$, $K^0_S\sigma_2$, $K^*(892)^+\pi^-$, $K_0^*(1430)^+\pi^-$, $K_2^*(1430)^+\pi^-$, $K^*(1410)^+\pi^-$, $K^*(1680)^+\pi^-$ and a non-resonant component. A fit assuming *CP* conservation yields $x = (0.80 \pm 0.29^{+0.09\,+0.10}_{-0.07\,-0.14})\%$ and $y = (0.33 \pm 0.24^{+0.08\,+0.06}_{-0.12\,-0.08})\%$ where the uncertainties are statistical, systematic and model systematic. The Dalitz plot distribution and the projections on $m^2(K^0_S\pi^-)$, $m^2(K^0_S\pi^+)$ and $m^2(\pi^+\pi^-) = m^2(\pi^+\pi^-)$ projections are illustrated in Fig. 2.4.

To allow for *CP* violation, the *CP* violation parameters $|q/p|$, ϕ and a non-resonant component for the $\overline{D}^0$ sample $\bar{a}_r(\text{NR})$, $\bar{\phi}_r(\text{NR})$ are included in the fit. From the fit to the independent D^0 and $\overline{D}^0$ samples, the amplitudes are found to be consistent and thus no evidence for direct *CP* violation is observed. The fit allowing for *CP* violation results in $x = (0.81 \pm 0.30^{+0.10\,+0.09}_{-0.07\,-0.16})\%$, $y = (0.37 \pm 0.25^{+0.07\,+0.07}_{-0.13\,-0.08})\%$, $|q/p| = 0.86^{+0.30\,+0.06}_{-0.29\,-0.03} \pm 0.08$ and $\phi(q/p) = (-14^{+16\,+5\,+2}_{-18\,-3\,-4})°$

where the uncertainties are statistical, systematic and model systematic. The results are found to be consistent with the hypothesis of *CP* conservation in mixing and the interference between mixing and decay.

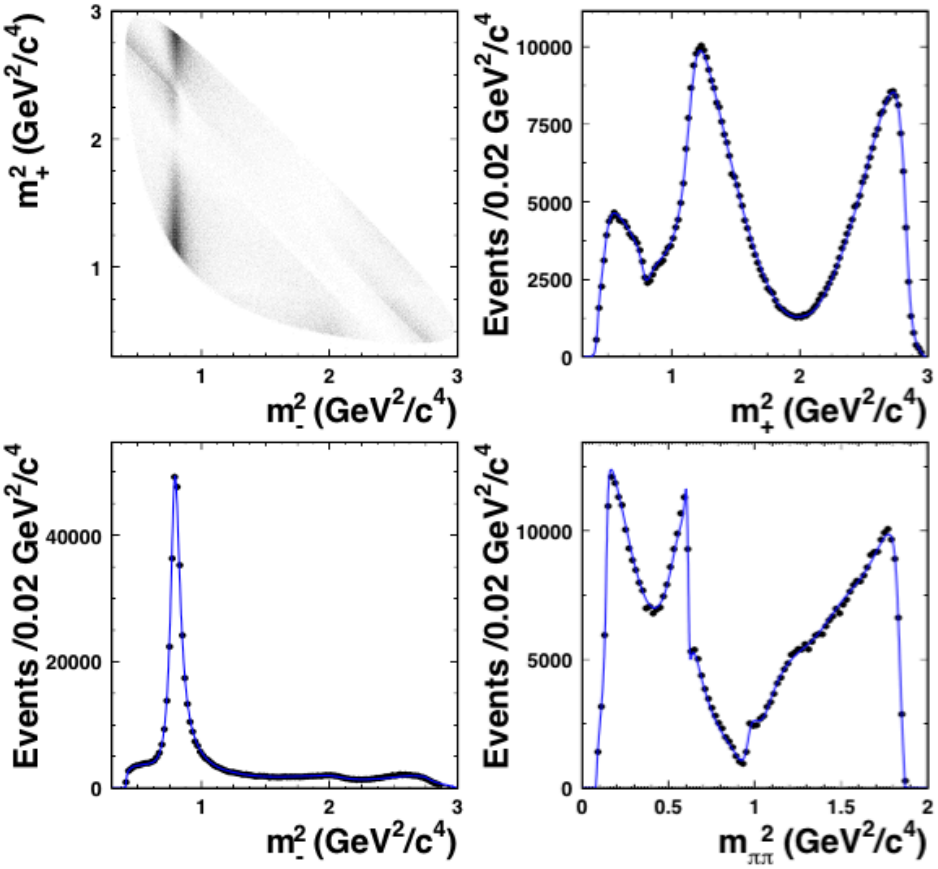

Figure 2.4.: *Dalitz plot distribution (upper left) and projections for data (points with error bars) on the $m^2(K^0_S\pi^+)$, $m^2(K^0_S\pi^-)$ and $m^2(\pi^+\pi^-)$ axes. The fit projections for the CP-conserving fit are drawn as blue curves. The figure is taken from [40]*

Measurement on $921\,\mathrm{fb}^{-1}$

The updated measurement [41] on a dataset corresponding to a luminosity of $921\,\mathrm{fb}^{-1}$ combines the previous Belle measurement [40] with the approach of the BaBar analysis [39]. The amplitude model uses the K-matrix formalism with the P-vector approximation for the $\pi^+\pi^-$ S-wave and a LASS parameterisation for the $K^0_S\pi^\pm$ S-wave (see Chapt. 11 for details). Contributions from P- and D-waves are $K^*(892)^-\pi^+$, $K^*_0(1430)^-\pi^+$, $K^*_2(1430)^-\pi^+$, $K^*(1410)^-\pi^+$, $K^*(1680)^-\pi^+$, $K^0_S\rho(770)$, $K^0_S\omega(782)$, $K^0_S f_2(1270)$, $K^0_S\rho(1450)$, $K^*(892)^+\pi^-$, $K^*_0(1430)^+\pi^-$, $K^*_2(1430)^+\pi^-$, $K^*(1410)^+\pi^-$, $K^*(1680)^+\pi^-$.

The no-*CP* violation fit results are $x = (0.56\pm0.19^{+0.03\,+0.06}_{-0.09\,-0.09})\%$ and $y = (0.30\pm0.15^{+0.04\,+0.03}_{-0.05\,-0.06})\%$ and allowing for indirect *CP* violation, the results of the mixing parameters are measured to be $x = (0.56 \pm 0.19^{+0.04\,+0.06}_{-0.08\,-0.08})\%$ and $y = (0.30 \pm 0.15^{+0.04\,+0.03}_{-0.05\,-0.07})\%$, which are consistent with the results from the *CP* conservation fit. The search for *CP* violation in mixing and in the interfer-

ence between mixing and decay yields $|q/p| = 0.90\,^{+0.16\,+0.05\,+0.06}_{-0.15\,-0.04\,-0.05}$ and $\phi = (-6 \pm 11 \pm 3\,^{+3}_{-4})^\circ$. The reported uncertainties are statistical, systematic and model systematic. The results of the search for *CP* violation are consistent with the conservation of *CP* symmetry in mixing and the interference of mixing and decay.

2.4.4. Model-independent LHCb measurement

The LHCb collaboration reported a measurement of x and y [37] on a dataset corresponding to a luminosity of $1\,\text{fb}^{-1}$ recorded with the LHCb detector in 2011 at the Large Hadron Collider (see Chapt. 3). In contrast to the model-dependent measurements performed by CLEO, BaBar and Belle, the analysis relies on a model-independent approach. The Dalitz plane is divided into 16 bins of constant strong phase $\Delta\delta_D$ difference as determined by the CLEO collaboration [42]. The strong phase difference is defined as the difference between the strong phases of $D^0 \to K^0_S\pi^+\pi^-$ and $\overline{D}^0 \to K^0_S\pi^+\pi^-$ decays. The binning scheme is illustrated in Fig. 2.5 in $m^2(K^0_S\pi^+) \equiv m^2_+$ and $m^2(K^0_S\pi^-) \equiv m^2_-$.

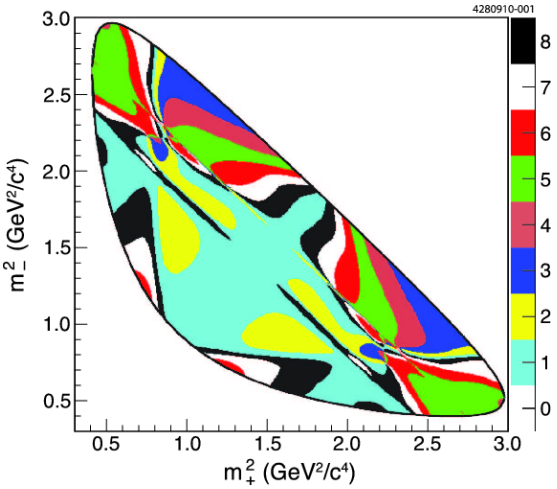

Figure 2.5.: *Binning of the $D^0 \to K^0_S\pi^+\pi^-$ Dalitz plot with 8 symmetric bins based on the model from Ref. [39]. The color scale represents the absolute value of the bin number. The bins are symmetric along the $m^2(\pi^+\pi^-)$ axis where bins -1 to -8 are above the diagonal and bins 1 to 8 below the diagonal. The figure is taken from [42]*

The mixing parameters are extracted from the time-dependent decay rates

$$\mathcal{P}(D^0) = e^{-\Gamma t}\left(T_i - \Gamma t\sqrt{T_i T_{-i}}\{yc_i + xs_i\}\right), \tag{2.87}$$

$$\mathcal{P}(\overline{D}^0) = e^{-\Gamma t}\left(T_i - \Gamma t\sqrt{T_i T_{-i}}\{yc_i + xs_i\}\right), \tag{2.88}$$

where the fractions of D^0 and $\overline{D}^0$ candidates per bin are denoted by T_i and T_{-i}, respectively. The interference between the D^0 and $\overline{D}^0$ amplitudes weighted by the strong phase difference $\Delta\delta_D$, as measured by CLEO, are given by

$$c_i \equiv \frac{1}{\sqrt{T_i T_{-i}}} \int_i |\mathcal{A}^*_{D^0}(m^2(K^0_S\pi^+), m^2(K^0_S\pi^-))| \times |\mathcal{A}_{\bar{D}^0}(m^2(K^0_S\pi^+), m^2(K^0_S\pi^-))| \cos(\Delta\delta_D) dm^2(K^0_S\pi^+) dm^2(K^0_S\pi^-), \quad (2.89)$$

$$s_i \equiv \frac{1}{\sqrt{T_i T_{-i}}} \int_i |\mathcal{A}^*_{D^0}(m^2(K^0_S\pi^+), m^2(K^0_S\pi^-))| \times |\mathcal{A}_{\bar{D}^0}(m^2(K^0_S\pi^+), m^2(K^0_S\pi^-))| \sin(\Delta\delta_D) dm^2(K^0_S\pi^+) dm^2(K^0_S\pi^-). \quad (2.90)$$

The mixing parameters are extracted from a simultaneous maximum likelihood to the D^0 decay time and $\ln\chi^2_{\mathrm{IP}}$ distributions to the data in each of the 16 bins split further according to the charge of the D^*. The impact parameter χ^2, χ^2_{IP}, is defined as the difference in the primary vertex χ^2 with and without the D^0 candidate. The χ^2_{IP} allows to separate D^* decays produced directly in the pp collision from decays involving a long-lived particle like a B meson. The mixing parameters are measured to be $x = (+0.86 \pm 0.53 \pm 0.17) \times 10^{-2}$ and $y = (+0.03 \pm 0.46 \pm 0.13) \times 10^{-2}$.

2.4.5. Current world average

The measurements mentioned above are combined with measurements of other observables, that are sensitive to mixing and indirect *CP* violation. This world average is provided by the Heavy Flavor Averaging Group (HFAG). A list of measurements entering the current world average of the mixing and indirect *CP* violation parameters is given in Ref. [43]. Furthermore, the model-independent measurement of x and y recently published by LHCb [37] (see Chapt. 2.4.4) enters the computation of the world average. The world averages of x, y, $|q/p|$ and ϕ are determined from a global fit to these measurements with ten free parameters: the mixing and indirect *CP* violation parameters, the strong phase differerences $\delta_{K\pi}$ and $\delta_{K\pi\pi}$, the ratio $R_D \equiv \Gamma(\overline{D}^0 \to K^-\pi^+)/\Gamma(D^0 \to K^-\pi^+)$ and the time-integrated *CP* asymmetries, $\mathcal{A}_{K\pi}$, $\mathcal{A}_{\pi\pi}$ and $\mathcal{A}_{KK}$, which are sensitive to direct *CP* violation.

The direct measurement of the mixing and *CP* violation parameters is possible in $D^0 \to K^0_S\pi^+\pi^-$ and $D^0 \to K^0_S K^+K^-$ decays as reported above. From semileptonic $D^0 \to K^+\ell^-\nu$, the observable $R_M \equiv \frac{1}{2}(x^2 + y^2)$ is measured. In addition, the quantities

$$y_{CP} \equiv \frac{1}{2}\left[(|q/p| + |p/q|)\, y\cos\phi - (|q/p| - |p/q|)\, x\sin\phi\right], \quad (2.91)$$

$$A_\Gamma \equiv \frac{1}{2}\left[(|q/p| - |p/q|)\, y\cos\phi - (|q/p| + |p/q|)\, x\sin\phi\right], \quad (2.92)$$

are sensitive to both mixing and indirect *CP* violation parameters. From $D^0 \to K^+\pi^-\pi^0$ decays, the mixing parameters rotated by the strong phase difference $\delta_{K\pi\pi}$ is measured. At CLEO-c, quantum-correlated pairs of D^0 and $\overline{D}^0$ mesons are produced, which allows a direct measurement of y, x^2, R_D as well of the strong phase difference $\cos\delta_{K\pi}$ and $\sin\delta_{K\pi}$. The analysis of $D \to K\pi$ decays grants access to R_D and the mixing parameters rotated by the strong phase difference $\delta_{K\pi}$, where some analyses allow for *CP* violation.

The current world averages on x and y and $|q/p|$ and ϕ are illustrated in Fig. 2.6. The mixing and *CP* violation parameters are [44]

$$\begin{aligned} x &= (0.49 \pm 0.15)\%, \\ y &= (0.62 \pm 0.09)\%, \\ |q/p| &= \quad 0.98 \pm 0.09, \\ \phi &= -0.02 \pm 0.13. \end{aligned}$$

The strongest constraints on the mixing parameters come from $D \to K\pi$ decays and from y_C, which imposes a restriction on y. The *CP* violation parameters are constrained mainly by measurements from $D \to K\pi$ decays and on the diagonal by A_Γ. Direct measurements of the mixing and *CP* violation parameters in $D^0 \to K^0_S\pi^+\pi^-$ decays lead to an elliptical constraint in both parameter spaces.

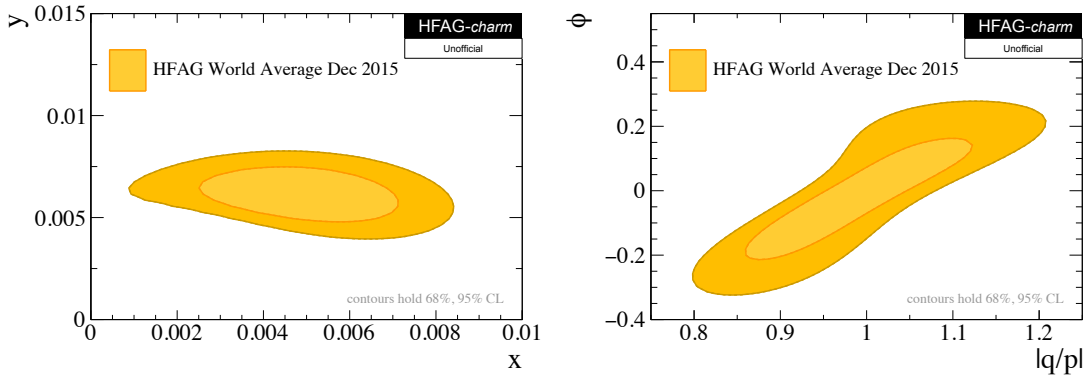

(a) *The world averages on the mixing parameters are* $x = (0.49 \pm 0.15)\%$ *and* $y = (0.62 \pm 0.09)\%$.

(b) *The world averages on the CP violation parameters are* $|q/p| = 0.98 \pm 0.09$ *and* -0.02 ± 0.13.

Figure 2.6.: *Current world averages on the mixing (left) and CP violation parameters (right) [44].*

3. The LHCb experiment

The data analysed in this thesis have been recorded with the LHCb experiment at the Large Hadron Collider (LHC) [45–48]. The LHC is a proton-proton (pp) collider, which was designed to run at a luminosity of $10^{34}\,\mathrm{cm}^{-2}\,\mathrm{s}^{-1}$ and achieve centre-of-mass energies of 14 TeV for pp collisions. For heavy ion collisions with lead (Pb), the design luminosity is $10^{27}\,\mathrm{cm}^{-2}\,\mathrm{s}^{-1}$ for nucleon beams with an energy of 2.8 TeV each. At the LHC, the ATLAS and CMS experiments are general-purpose detectors focusing particularly on precision tests of the Standard Model, Higgs physics and new physics searches whereas ALICE aims at the investigation of the quark-gluon plasma. Forward scattering is measured by TOTEM [49] and LHCf [50]. The LHCb experiment is a single-arm forward spectrometer primarily designed to measure mixing and CP violation as well as rare decays in the beauty and charm sectors. In the LHCb cavern, the MoEDAL [51] experiment is installed, which searches for magnetic monopoles. In the following section, an overview of the LHC is given and the layout of the LHCb detector is described.

3.1. The Large Hadron Collider

The proton beams circulating in the LHC [45–48] are preaccelerated by an injector chain consisting of a linear accelerator, the LINAC 2, the Proton Synchrotron Booster, Proton Synchrotron (PS) and the Super Proton Synchrotron (SPS) as illustrated in Fig. 3.1.

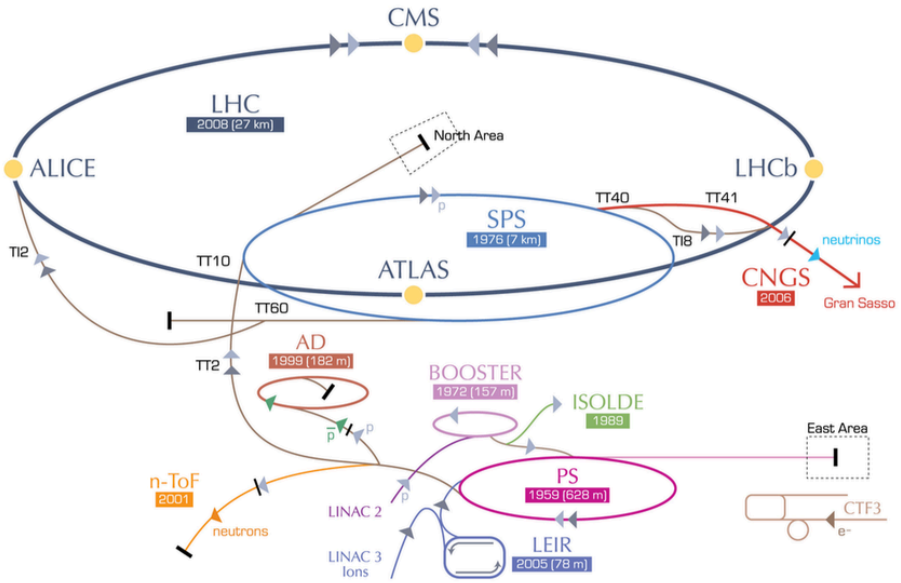

Figure 3.1.: *The CERN collider complex: Protons are accelerated successively with the linear accelerator (LINAC 2), the Proton Synchrotron Booster, the Proton Synchrotron (PS) and Super Proton Synchrotron (SPS) before being injected into the Large Hadron Collider (LHC) where the protons reach their final collision energy. The figure is adapted from Ref. [52].*

Proton beams are produced from hydrogen by stripping off the electron and by directing hydrogen atoms through an electric field. In the linear accelerator, the LINAC 2, protons are accelerated to an energy of 50 MeV before being injected into the Booster. In the Booster, six proton bunches in two batches of either $3+3$ or $4+2$ bunches with each bunch filled with up to $\sim 1.63 \times 10^{12}$ protons are accelerated up to 1.4 GeV, which is the required injection energy of the Proton Synchrotron. In the PS, the bunches are then split into three at an energy of 1.4 GeV and accelerated up to 25 GeV. Then, the bunches are further split into two. Thus, the number of bunches in each of the two Booster batches has been multiplied by a factor of six. The resulting 72 proton bunches are transferred to the SPS with a bunch spacing of 25 ns and then accelerated to the injection energy 450 GeV required by the LHC. The filling of the LHC requires 12 SPS cycles preceded by 3 to 4 PS cycles. The proton beams with a maximum of 2808 filled bunches are injected clockwise and counter clockwise into the two beam pipes of the LHC at 450 GeV and reach their collision energy after a circulation of ~ 20 min. In 2011, the proton beams were brought to collision at a centre-of-mass energy of 7 TeV and in 2012 at 8 TeV. During Run 1 in 2011 and 2012, the spacing of the ~ 1380 bunches in the LHC was 50 ns whereas in Run 2, which has started in 2015, the bunch spacing is reduced to 25 ns.

The LHC is built of eight arcs and eight straight sections, so-called insertions, with a circumference of 26.7 km as illustrated in Fig. 3.2. Each arc is made of 23 arc cells with a so-called FODO structure consisting of focusing quadrupole magnets, bending dipole magnets and higher order magnets for corrections to the beam. To reach the design centre-of-mass energy of 14 TeV, a dipole magnetic field of 8.33 T is required. The dipole magnet coils are made of superconducting niobium-titanium (NbTi) that becomes superconducting below a temperature of 10K and are operated at 1.9K to achieve the required magnetic field of 8.33 T. Since the LHC is a proton-proton collider, the magnetic fields are oriented oppositely for the two beam pipes.
An insertion consists of a transition region followed by a long straight section and a second transition region. The layout of the straight sections depends on whether it is used for physics or to inject, accelerate, dump or clean the beam. The interaction points (IP) are located at the centre of the insertion regions. The proton beams are accelerated at IP4 with 8 radio frequency (RF) cavities per beam. The cavities are operated at 400 MHz delivering an accelerating field of 5MV/m. At IP3 and IP7, the beams are cleaned by removing particles with large longitudinal or transversal amplitudes and the beam dump is located at IP6. At the other four interaction points, the four main LHC experiments are situated where the proton beams are brought to collision; ATLAS is situated at IP1, ALICE at IP2, CMS at IP5 and LHCb at IP8.

In contrast to the ATLAS and CMS experiments, the LHCb experiment aims at a design luminosity of $2 \times 10^{32}\,\mathrm{cm}^{-2}\,\mathrm{s}^{-1}$ to prevent ageing of the detectors and to keep the number of visible pp interactions per bunch crossing close to one. To keep the luminosity at LHCb constant during each fill, the beams are not focussed as strongly at IP8 as for ATLAS and CMS and the transverse beam overlap is modified by adjusting the relative offset between the proton beams. Through this levelling procedure, the luminosity seen by LHCb is kept stable within 5% during an LHC fill [54].

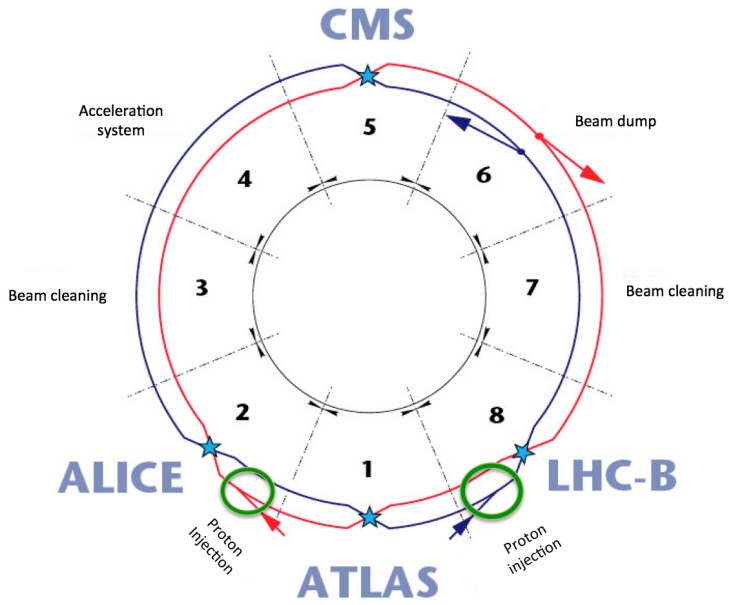

Figure 3.2.: *Schematic view of the LHC showing the eight arcs and straight intersections. The four main LHCb experiments ATLAS, CMS, ALICE and LHCb are located at four of the interaction points. The figure is taken from Ref. [53].*

3.2. The LHCb Detector

The LHCb detector [55] is a single-arm spectrometer illustrated in Fig. 3.3 with a forward angular coverage from 15 mrad to 300 mrad (250 mrad) in the horizontal (vertical) plane. The detector was designed as a forward spectrometer because beauty hadrons are produced primarily in a cone in either the forward or the backward direction. B-hadrons are produced in gg fusion and if the gluon energies are balanced, the B-hadrons are predominantly produced isotropically whereas for significantly different gluon energies, the beauty hadrons receive a high boost in the laboratory frame. The collision point is chosen as the origin of a right-handed coordinate system depicted in Fig. 3.3 and is inclined to align with the beam axis. The interaction point is located in the centre of the Vertex Locator (VELO) in the (x, y) plane. Built of silicon strip sensors, the VELO provides measurements of track and vertex coordinates with high precision. Apart from the VELO, the tracking system consists of the Tracker Turicensis (TT), and three tracking stations (T1- T3) subdivided into the Inner and Outer Trackers, (IT) and (OT). The TT as well as the IT are composed of silicon microstrip sensors whereas the OT is built of straw tubes measuring track coordinates and momenta. The magnetic field of LHCb is provided by a warm dipole magnet with an integrated field of 4 Tm. The VELO is located outside of the influence of the magnet, whereas the magnet's fringe field reaches the TT. Reliable and precise momentum measurements thus rely on information from the IT and OT and if applicable on the muon stations. A system of Ring Imaging Cherenkov Detectors (RICH) is used to obtain π, K and p identification. The calorimeter system composed of scintillating tiles and lead absorbers in the Electromagnetic Calorimeter (ECAL) and iron absorbers in the Hadronic Calorimeters (HCAL), respectively, provide identification and energy measurements of electrons, photons

and hadrons. To identify electrons in the trigger, a Scintillator Pad Detector (SPD) and a Preshower Detector (PS) are installed in front of the ECAL. The muon stations (M1-M5) use multi-wire proportional chambers with the exception of the inner region of M1 where triple-GEM detectors are installed. The subdetector systems are subdivided in two halves called the A- and C-sides where the A-side extends to positive x. Since the start of data taking in 2010, the LHCb detector recorded an integrated luminosity of $38\,\mathrm{pb}^{-1}$ in 2010, $1.1\,\mathrm{fb}^{-1}$ in 2011 and $2.1\,\mathrm{fb}^{-1}$ in 2012 [54].

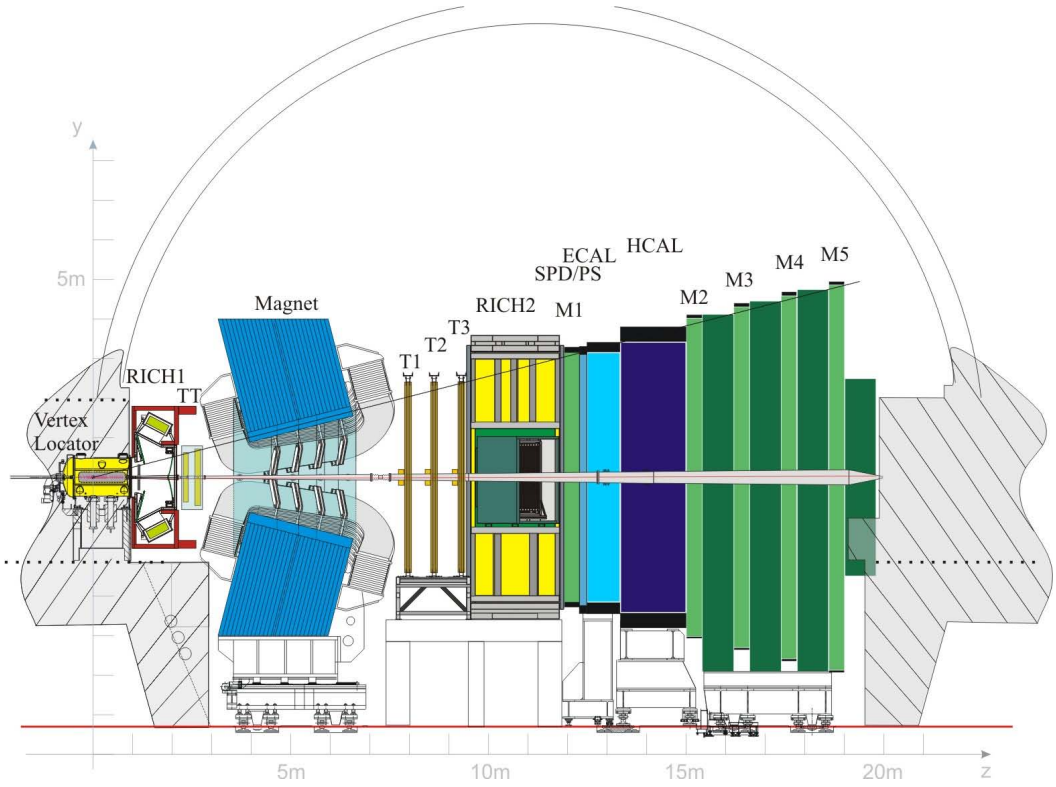

Figure 3.3.: *Schematic view of the LHCb detector. The figure is taken from Ref. [56].*

3.2.1. The Vertex Locator

The Vertex Locator [57] consists of silicon sensors arranged along the z-axis, which are operated inside a vacuum vessel. The sensors and the vacuum vessel are separated by a $300\,\mu\mathrm{m}$ thin corrugated aluminum foil, the RF-foil, from the LHC vacuum. The RF-foil not only protects the LHC vacuum from outgassing of the VELO modules but also provides shielding against radio-frequency pickup from the beams in the LHC. It was designed to minimise the amount of material a charged particle traverses before reaching the sensors. The beam pipe is coupled to the VELO exit window as can be seen from the schematic view of the VELO in Fig. 3.4. The VELO consists of 42 modules each with an R- and a Φ-sensor providing measurements of the track coordinates r and ϕ where r corresponds to the radial distance from the beam axis and ϕ is the azimuthal coordinate around the beam. The z coordinate is known from the position of each sensor within the detector. In addition to the 42 VELO modules, 4 R-sensors are placed upstream of the VELO modules, which serve as a veto system to distinguish between bunch crossings with a single or with multiple visible pp interactions.

The first active VELO modules are placed at a radial distance of 8 mm from the beam during physics operation. The VELO is built in two halves, which are retractable to 29 mm each in the horizontal plane to protect the detector during beam injection into the LHC. When the safety of the detector is ensured, the VELO halves are closed by a fully-automated procedure, which takes around 210 s to complete. A schematic cross section of the VELO in open and closed positions is shown in Fig. 3.5.

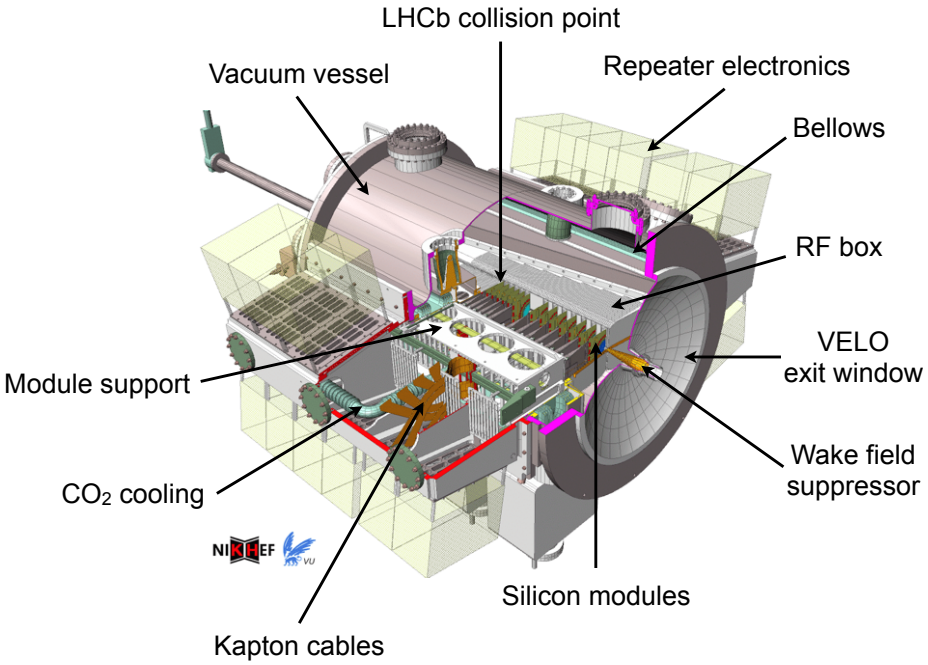

Figure 3.4.: *Schematic view of the VELO detector. The figure is adapted from Ref. [58].*

The semi-circular sensors are made of 300 µm thick n-doped silicon strips with n^+ implants that are mounted together with the readout on a module. A p-doped layer ensures the isolation of the strips. For the upgrade of the VELO, the usage of n^+-on-p silicon sensors is discussed, wherefore two sensors of one of the most upstream modules consist of n^+-on-p silicon strips. The 2048 strips on an R-sensor are subdivided into four 45° regions in ϕ to minimise the occupancy. To reduce the strip capacitance and occupancy, the Φ-sensors are split in an inner region and an outer region, which starts at a radius of 17.25 mm. In the inner region, the strip pitch increases linearly from 38 µm at the inner radius of 8.2 mm to 78 µm. The pitch in the outer region ranges from 39 µm to 102 µm. The pitch of the R-sensors increases linearly from 40 µm to 102 µm at a radius of 42 mm. Figure 3.6 illustrates the resolution as a function of the strip pitch and the resolution per pitch depending on the projected angle. The sensors are operated at 150 V and cooled to a temperature of $(-7 \pm 2)°C$.
At a radial distance of 8.2 mm and of 17.25 mm from the beam, respectively, the inner and outer strips are inclined to improve pattern recognition and allow track reconstruction in three dimensions. Adjacent Φ-sensors have opposite skew with respect to each other, which allows these sensors to resolve ambiguities in hit positions.

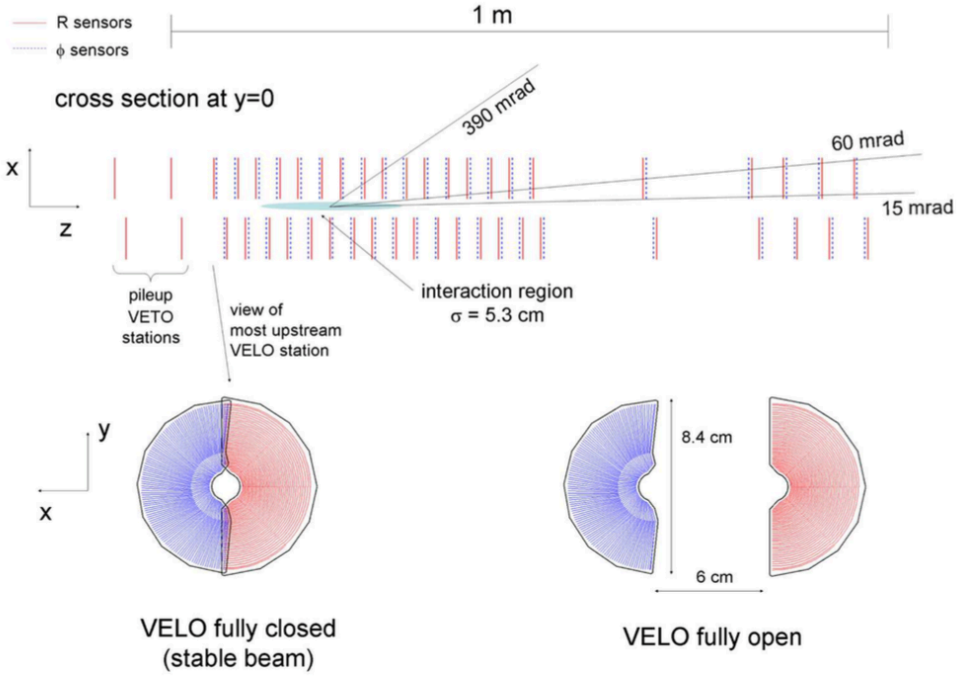

Figure 3.5.: *Cross section in the (x, z) plane of the pile-up system upstream of the sensors and the VELO sensors at $y = 0$. The most upstream station is shown in fully closed and fully opened positions. The figure is taken from Ref. [55].*

The performance of the VELO is reported in Ref. [57]. For a primary vertex (PV) with 25 tracks, the vertex position is measured with a precision of 13 µm in the transverse plane and with 71 µm along the z-axis. The distance between a track and the related PV at the track's point of closest approach to the PV is the impact parameter (IP) measurable with a resolution of < 35 µm for particles with $p_{\mathrm{T}} > 1$ GeV. The IP resolutions measured along the x- and y-axis behave linearly in $1/p_{\mathrm{T}}$ tending to a resolution of 12 µm. The excellent decay time resolution of ~ 50 fs allows *e.g.* the precision measurements of B_s^0-$\overline{B}_s^0$ oscillations.

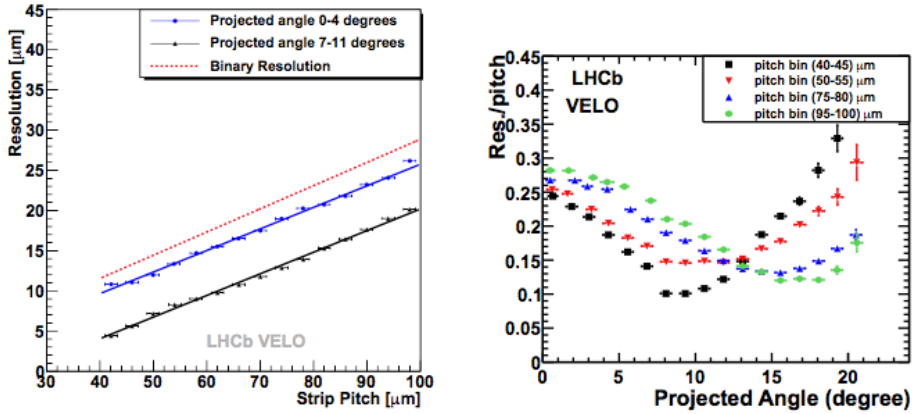

Figure 3.6.: *The VELO resolution is shown as a function of the pitch for projection angle regions of $0 - 4^\circ$ and $7 - 11^\circ$ and compared with a binary resolution (left). The resolution per pitch depending on the projected angle is given for four different pitch ranges (right). The figure is taken from Ref. [57].*

Due to the proximity of the sensor to the pp interaction vertex, the sensors are exposed to high radiation doses. For the most irradiated sensor regions, fluences up to 5×10^{13} 1 MeV neutron equivalents/ $\mathrm{cm}^2(\mathrm{n_{eq}})$ per fb^{-1} are measured. The fluence varies by approximately a factor of two with position along the z-axis. In the radial direction r, the fluence decreases as $r^{-1.9}$. Under irradiation, the n-doped sensors are expected to undergo space-charge sign inversion resulting in a reduction of their depletion voltage. The sensors are kept depleted over time by raising the depletion voltage accordingly. The radiation damages are expected not to affect the physics performance for depletion voltages below 500 V until the end of Run 2 after which the VELO upgrade will take place as detailed in Chapter 4.

3.2.2. The Silicon Tracker

The Silicon Tracker (ST) comprises the Tracker Turicensis and the Inner Tracker, which are built of 143, 360 and of 129, 024 p^+ on n doted silicion microstrips. The TT is a planar tracking detector located downstream of the LHCb magnet whereas the IT is placed upstream of the magnet. In between the VELO and TT, RICH1 is located downstream of the magnet. The IT is a cross-shaped region situated in the centre of the three tracking stations T1- T3 around the beam pipe. The four stations of the ST comprise four detection layers each. The silicon microstrips are arranged vertically in the first and last layers and rotated by a stereo angle of u and v in the second and third layer, respectively. The rotation of the layers by a stereo angle allows three-dimensional track reconstruction and improves the pattern recognition. The detection layers are housed in light tight, thermally and electrically insulated boxes in which the temperature is kept below $5°C$. To avoid condensation on the cold surfaces, the boxes are continuously flushed with nitrogen. The TT is subdivided into two half stations and the IT into four stations around the beam pipe, which are all retractable in the horizontal plane for detector maintenance. The ST operates in a lesser radiation environment and has not shown a sign of type-inversion during Run 1 [59].

3.2.2.1. The Tracker Turicensis

The TT covers the full LHCb acceptance and the layout of the third detection layer is illustrated in Fig. 3.7. The detection layers of the TT are subdivided into two halves covering half of the LHCb acceptance in height.

The half modules consist of seven 500 µm thick single-sided silicon sensors with a strip pitch of 183 µm, which are grouped either in two or in three different readout sectors. The readout sectors are classified as L, M and K sectors where the L sector is furthest away from the beam and the K sector is closest to the beam. Half modules are either classified as 4-2-1 types with 4 L, 2 M and 1 K sectors or as 4-3 types built of 4 L sectors and 3 M sectors. The readout hybrids for all sectors and the cooling are located at the end of one half module as illustrated in Fig. 3.8 for a 4-2-1 type half module.

Within a detection layer, adjacent half modules overlap in x and z (if applicable rotated by the corresponding stereo angle) to avoid acceptance gaps and improve the alignment of the half modules. The hit resolution of the TT was measured to be 52.6 µm in 2011 and 53.4 µm in 2012 [54].

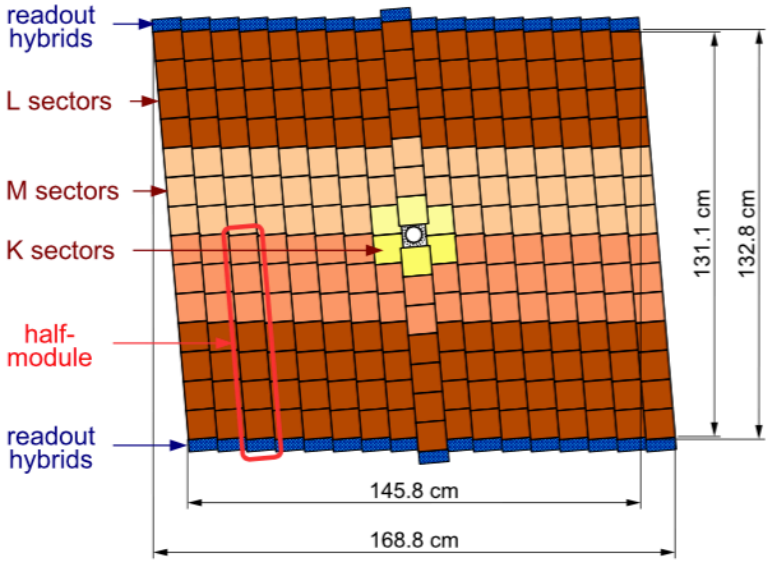

Figure 3.7.: *Layout of the third TT detection layer. The three readout sectors L, M and K sector are drawn in different colours. The figure is taken from Ref. [55].*

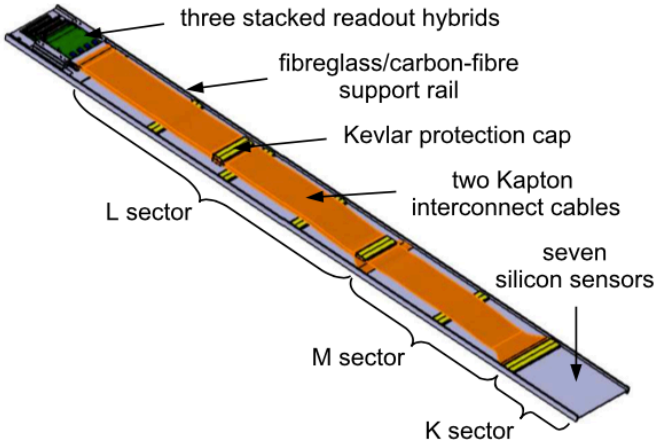

Figure 3.8.: *Layout of a 4-2-1 type TT half module. The figure is taken from Ref. [55].*

3.2.2.2. The Inner Tracker

The layout of the IT is illustrated in Fig. 3.9. Each of the four detection layers per box is made of seven modules, which overlap in x and z (if applicable rotated by the corresponding stereo angle) to minimise acceptance gaps and ensure a robust alignment. As indicated in Fig. 3.9, the bottom and top boxes contain single sensor modules whereas the A- and C-side boxes comprise two-sensor modules. The silicon sensors are single-sided sensors with 384 microstrips and a strip pitch of 198 µm. The sensor of a single-sensor module is 320 µm thick whereas the sensor thickness is increased to 410 µm for a two-sensor module. The hit resolution of the IT was measured to be 50.3 µm in 2011 and 54.9 µm in 2012 [54].

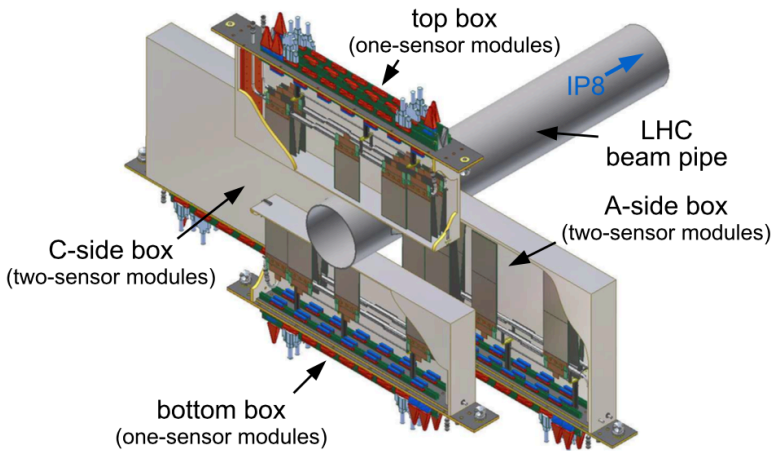

Figure 3.9.: *Layout of the four IT detector boxes for a single tracking station arranged around the beampipe. The figure is taken from Ref. [55].*

3.2.3. The Outer Tracker

The Outer Tracker is a straw-tube detector located in the outer regions of the tracking stations T1-T3. The straw-tubes have a diameter of 4.9 mm and are filled with a mixture of Argon (70%), CO_2 (28.5%) and O_2 (1.5%) to ensure a drift time of < 50 ns; a drift-coordinate resolution of 205 µm is achieved [60]. The gold plated tungsten anode wires with a diameter of 25 µm are set to +1550 V.

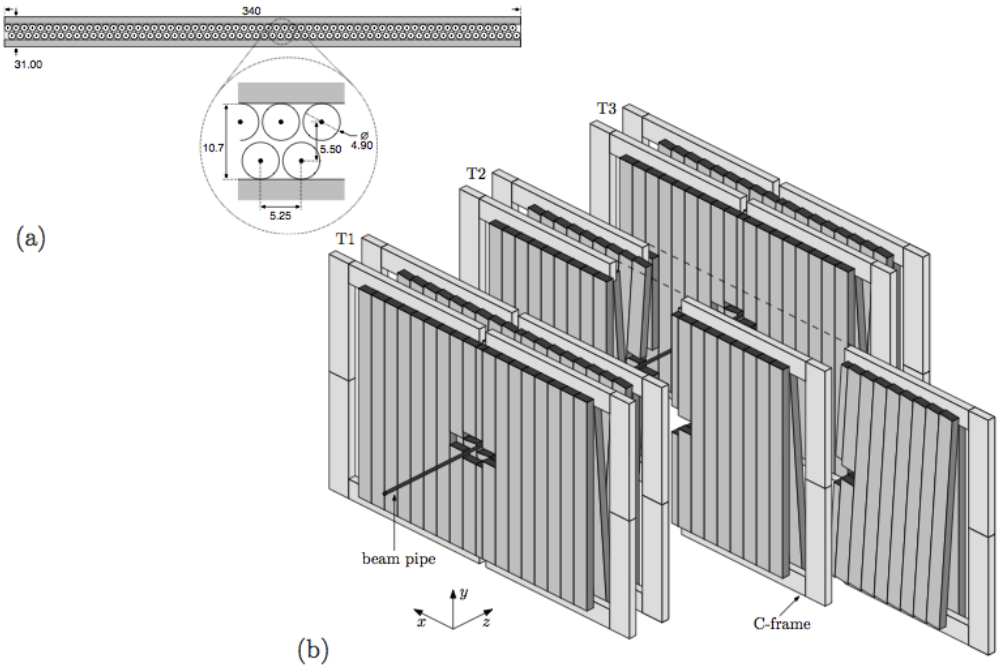

Figure 3.10.: *Layout of the OT detector boxes and the cross section of a single module. The figure is taken from Ref. [60].*

The OT extends to an upper acceptance of 300 mrad and 250 mrad in the bending and non-bending plane, respectively. The three OT stations are subdivided into two halves, which are retractable horizontally and the halves are further split into two independently movable half layers. A typical detector module consists of two panels with 64 straw tubes each sealed within a gas tight carbon-fiber box. The OT and the cross section of a single module are shown in Fig. 3.10. The radiation damage of the OT was studied during 2011 and 2012 and no degradation in performance was found [60].

3.2.4. The Ring Imaging Cherenkov Detectors

The particle identification of hadrons relies mainly on the two Ring Imaging Cherenkov detectors RICH1 and RICH2 located upstream and downstream of the magnet. Through the usage of different radiators, RICH detectors operate in different momentum ranges. In RICH1, fluorobutane (C_4F_{10}) radiators ensure a good performance in the low momentum range $\sim 1 - 60$ GeV. The performance of the aerogel radiators installed in RICH1 did not meet the design expectations and they have been removed before the start of Run 2. When charged particles pass through the radiators with a velocity that is larger than the speed of light in the radiator material with refractive index n, Cherenkov light is emitted in a cone along the direction of flight. The reconstruction of the opening angle θ_C

$$\cos(\theta_C) = \frac{m}{pn}, \tag{3.1}$$

in combination with the momentum p of the particle allows a measurement of the mass m of the incident particle. In the high momentum range from 15 GeV to more than 100 GeV, RICH2 is operating using a CF_4 radiator. Through a combination of spherical and flat mirrors, the Cherenkov light is focused and reflected out of the acceptance onto an array of Hybrid Photon Detectors (HPD). In this vacuum photon detector, the incident Cherenkov photon releases a photoelectron from the conversion in a photocathode. The photoelectron is then accelerated by a high voltage field onto a silicon detector. The Cherenkov angle is reconstructed from the impact points of the Cherenkov photons on the HPDs under the assumption that the photon was emitted halfway along the track trajectory through the radiator. The resolution of the Cherenkov angle is determined to be 1.6 mrad for C_4F_{10} and 0.7 mrad for CF_4 [61]. The momentum-dependence of the Cherenkov angle is shown in Fig. 3.11. The HPDs operate in a wavelength range of $200 - 600$ nm and are shielded from the magnetic field of the LHCb dipole by iron blocks. The optical system of RICH1, which covers the full LHCb acceptance, is located in the vertical plane as illustrated in Fig. 3.12.

In contrary to RICH1, the optical system of RICH2 is oriented in the horizontal plane. RICH2 covers only a limited angular acceptance of 15 mrad to 120 mrad (100 mrad) in the bending (non-bending) plane. The top view of RICH2 is shown in Fig. 3.13.

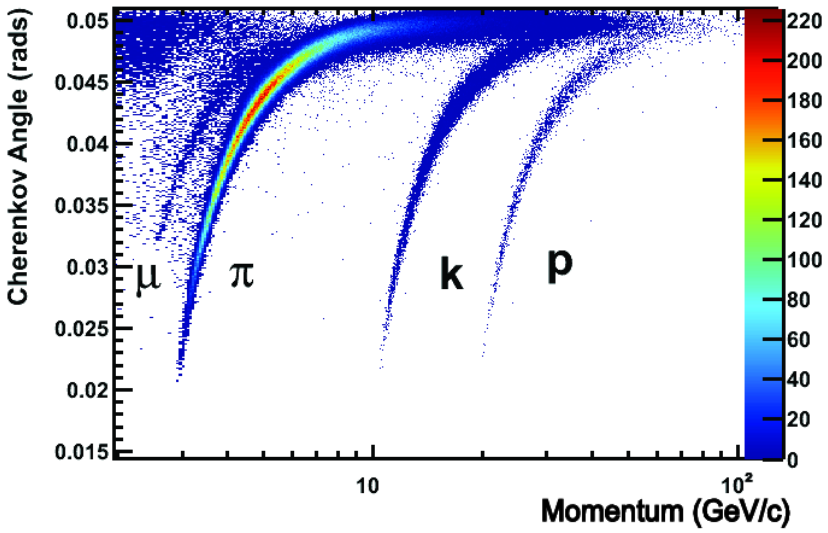

Figure 3.11.: *Reconstructed Cherenkov angle as a function of track momentum in RICH1* C_4F_{10} *radiator. The different particle mass hypotheses are indicated. The figure is taken from Ref. [61].*

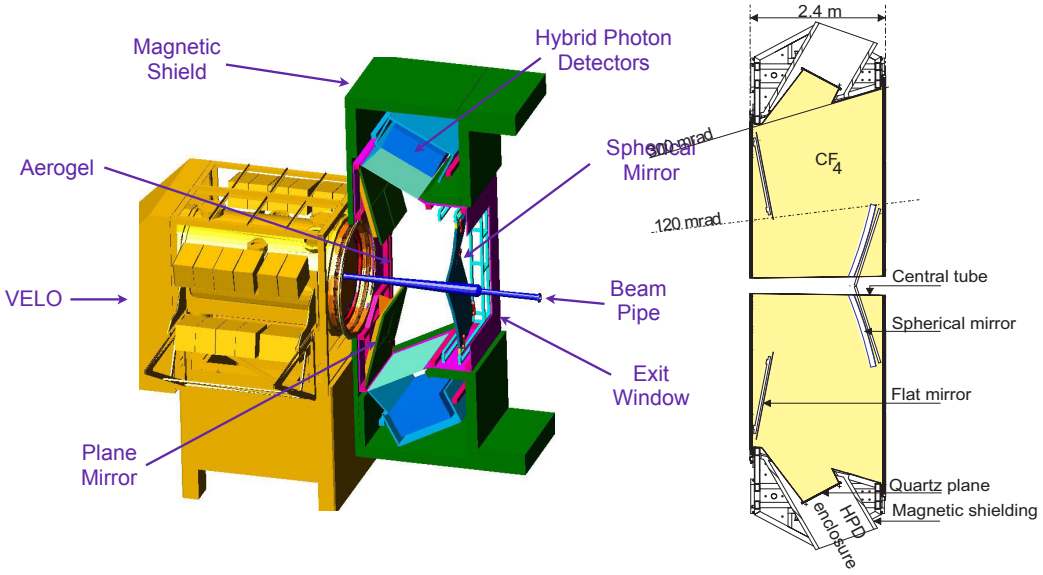

Figure 3.12.: *Cutaway model of RICH1 detector attached to the VELO. The figure is adapted from Ref. [62].*

Figure 3.13.: *Schematic top view of RICH2 detector. The figure is taken from Ref. [62].*

3.2.5. The Calorimeters

The calorimeter system of LHCb consists of an electromagnetic (ECAL) and a hadronic calorimeter (HCAL) providing electron, photon and hadron identification as well as a measurement of their energies and positions. Both calorimeters are shashlik calorimeters consisting of alternating scintillating tiles read out by wavelength shifting fibres and absorbers. The shashlik

layout provides a fast response, which is crucial for the performance of the hardware trigger (L0), which relies on the electron, hadron and photon clusters reconstructed in the calorimeters with high transverse energy E_{T}. To improve charged pion and electron separation, a Preshower Detector (PS) is placed in front of the ECAL. Electrons are separated from π^0 mesons with high transverse energy by a Scintillator Pad Detector (SPD) installed in front of the PS. Inbetween the SPD and the PS, a 15 mm thick lead tile serves as converter. Both SPD and PS use scintillator pads of high granularity, which are read out by wavelength shifting fibres coupled to Photomultiplier Tubes (PMTs). The detectors are divided into two halves, which are movable in the horizontal plane.
The ECAL covers the LHCb acceptance up to 300 mrad (250 mrad) in the bending (non-bending) plane whereas the inner acceptance is restricted to 25 mrad due to the high radiation dose. The ECAL is subdivided into an inner, middle and outer section with varying cell sizes to achieve a more uniformly distributed hit density over the full area of the ECAL. The ECAL modules illustrated in Fig. 3.14 for the inner section are made of a 2 mm thick lead absorber followed by a 120 µm thick reflecting TYVEK paper and 4 mm thick scintillator tiles. Each module consists in total of 66 lead-scintillator layers corresponding to a thickness of 25 radiation lengths (X_0) with a Molière radius of 3.5 cm. The energy resolution of the ECAL was determined to be $\sigma_E/E = (8.2 \pm 0.4)\%/\sqrt{E/\,\mathrm{GeV}} \oplus (0.87 \pm 0.07)\%$ for the inner modules and $\sigma_E/E = (9.4 \pm 0.2)\%/\sqrt{E/\,\mathrm{GeV}} \oplus (0.83 \pm 0.02)\%$ for the outer modules [63].

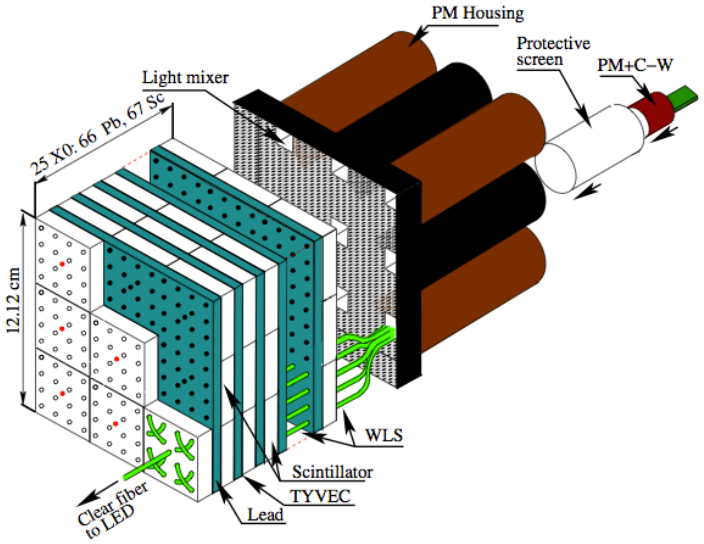

Figure 3.14.: *Schematic view of the ECAL inner module. The figure is taken from Ref. [63].*

The HCAL is segmented in the transverse plane into square cells of different sizes in an inner and outer region and additionally, divided vertically into two halves each consisting of 26 modules and is thus movable in the horizontal plane. A HCAL module shown in Fig. 3.15 consists of steel plates and scintillators, which are in total equivalent to 5.6 nuclear interaction lengths λ_I. The energy resolution of the HCAL is measured to be $\sigma_E/E = (69 \pm 50)\%/\sqrt{E/\,\mathrm{GeV}} \oplus (9 \pm 2)\%$ [64].

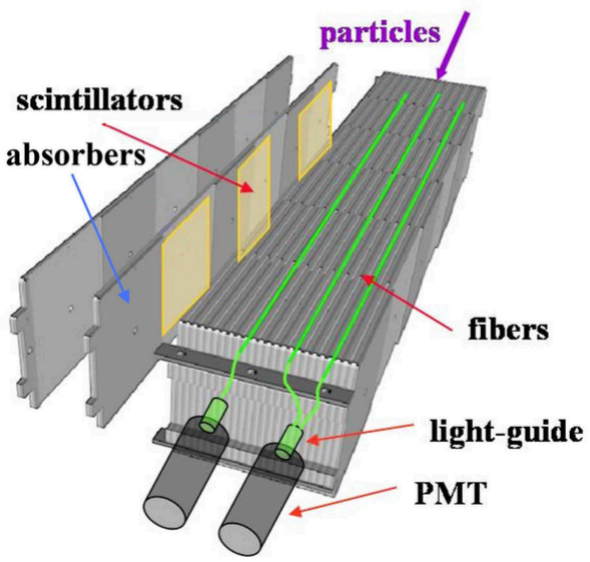

Figure 3.15.: *Schematic view of the HCAL module. The figure is taken from Ref. [55].*

3.2.6. The Muon System

The muon identification system comprises five muon stations. The first station M1 is situated upstream of the calorimeters whereas M2- M5 are located downstream and are followed by 80 cm thick iron tiles serving as a muon filter as illustrated in Fig. 3.16.

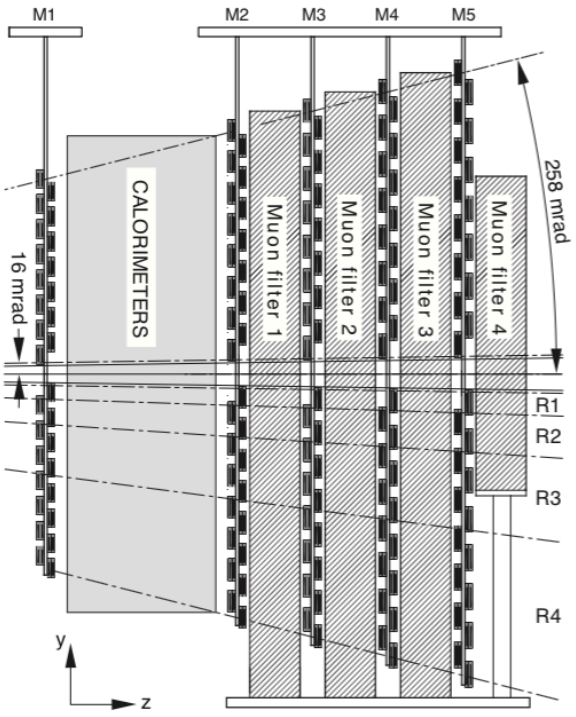

Figure 3.16.: *Schematic side view of the muon stations. The figure is taken from Ref. [55].*

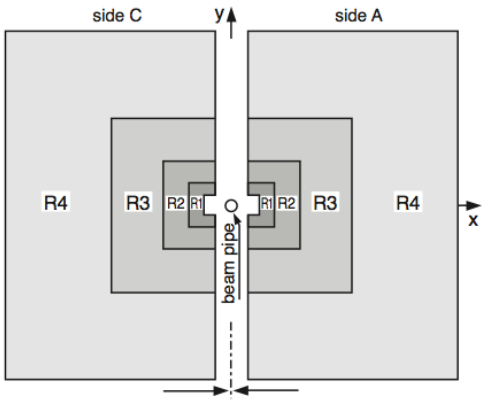

Figure 3.17.: *Schematic front view of the muon stations. The figure is taken from Ref. [65].*

With exception of the inner region of M1, where triple-GEM detectors are installed, the muon stations consist of 1380 multi-wire proportional chambers filled with a gas mixture of $Ar : CO_2 : CF_4$. The muon system provides track measurements and supplies information to the trigger. The first three muon stations have a high spatial resolution in the bending plane. From the measured trajectories the track direction is reconstruacted and the p_T of the muon candidates is calculated. The spatial resolution decreases significantly for M4 and M5 and thus these stations do not enter the trajectory or momentum measurements. To keep the particle flux and channel occupancy at a constant level, each muon station is divided into four regions $R1$ to $R4$ as illustrated in Fig. 3.17. The muon stations have an acceptance of 20 mrad (16 mrad) to 306 mrad (258 mrad) in the bending (non-bending) plane.

3.2.7. The LHCb Trigger

In Run 1, the LHCb trigger reduced the 30 MHz bunch crossing rate to 5 kHz [66], which is then stored and available for data analysis. This reduction is performed in two stages with the hardware Level-0 (L0) and the software-based High Level trigger (HLT). In the L0 trigger, the rate is reduced from $\sim$ 30 MHz to 1 MHz [66] by reconstructing electron, hadron and photon clusters in the calorimeters with high transverse energy and muon or di-muon candidates with high transverse momentum in the muon stations. From the number of hits in the SPD, the number of tracks in the calorimeters are estimated, which enters the L0 decision. The information required by the L0 trigger is collected by a L0 Decision Unit, which then either rejects an event or passes it on to the HLT. To reduce the rate down to 5 kHz [66], the HLT runs a C++ application on the Event Filter Farm with 29,000 logical CPU cores. The HLT exploits the full available data of the subdetector systems to reconstruct the events fully. The schematic flow of the LHCb trigger is given in Fig. 3.18.

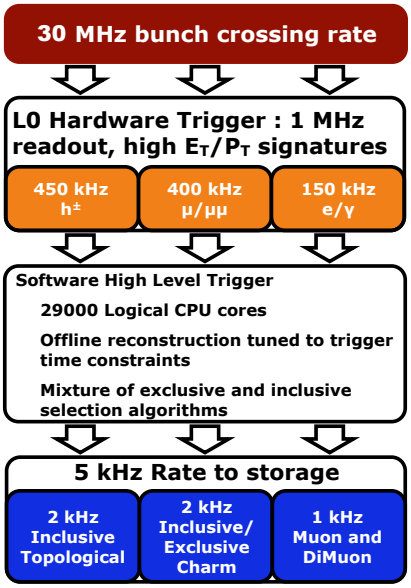

Figure 3.18.: *Schematic flow of the LHCb trigger in 2012. The figure is adapted from Ref. [66].*

4. The LHCb detector upgrade

The current LHCb detector introduced in Chapter 3.2 is expected to perform according to design specifications until the end of Run 2. A major upgrade to the experiment, with changes to most active elements, will be installed after Run 2. The upgraded LHCb detector is foreseen to operate for around 10 years and collect a dataset corresponding to an integrated luminosity of $50\,\text{fb}^{-1}$ [67] during Run 3 and 4. The LHCb upgrade detector will be able to run at higher instantaneous luminosities of up to $2 \times 10^{33}\,\text{cm}^{-2}\,\text{s}^{-1}$ [67] at a centre-of-mass energy of 14 TeV. The detector will be operated with a minimal bunch spacing of 25 ns in the LHC. Compared to the data-taking conditions in Run 1 and Run 2, the number of visible pp interactions per bunch crossing as well as the radiation dose will increase significantly in Run 3. The upgrade is based around reading out the full detector for every bunch crossing, which corresponds to a peak readout rate of 40 MHz. This allows vertexing and momentum information to be used in a trigger CPU farm at the first trigger level, overcoming the limitations of the L0 hardware trigger of the current experiment. To operate the readout at 40 MHz, most front-end electronics of the current detector have to be replaced during the Long Shutdown 2, which is foreseen to take place in 2019 and 2020. A schematic view of the upgrade LHCb detector is given in Fig. 4.1. During the upgrade of the LHCb detector, many of the subdetector systems will either undergo significant modifications or will be replaced.

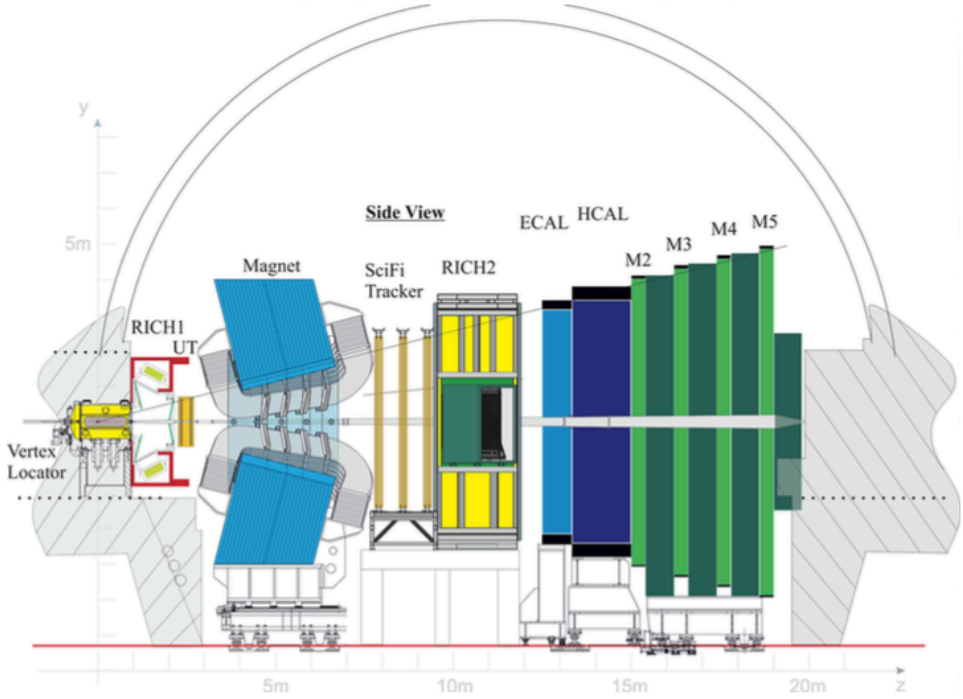

Figure 4.1.: *Schematic view of the LHCb upgrade detector. The figure is taken from Ref. [68].*

The current VELO (see Chapt. 3.2.1) with its silicon strip geometry will be replaced by the upgraded VELO with a silicon pixel layout [69]. In contrast to current operation, the first active VELO module will be placed $\sim 3\,\text{mm}$ closer in radial distance to the beam, namely at 5.1 mm, during data taking. The choice of a pixel layout leads to improved pattern recognition capabilities and track reconstruction speed. The small pixel dimensions of $55 \times 55\,\mu\text{m}$ and close distance to the beam ensures an excellent vertex reconstruction. The upgrade VELO modules will be cooled using a novel technique of evaporative CO_2 cooling inside micro-channels of a silicon substrate.
The current tracking system comprising the TT, the IT and OT will be replaced by the Upstream Tracker and the Scintillating Fibre Tracker [68]. The Upstream Tracker will consist of high granularity silicon micro-strip planes. These planes will extend over a larger fraction of the LHCb acceptance than the TT. Instead of employing two different technologies in the Inner and Outer Trackers, which consist of silicon micro-strips and straw tubes, respectively, the Silicon Fibre Tracker will be built of 2.5 m long scintillating fibres read out by silicon photo-multipliers.
The Cherenkov detector system, RICH1 and RICH2, will remain but requires significant modification. The RICH1 mechanics will be replaced and the optical system is being redesigned to improve the performance with higher occupancies. The photon sensors in both detectors require replacement as the current sensors have a 1 MHz readout chip encapsulated in the HPDs. Commercial multianode photomultipliers, which have externally accessible readout electronics, are chosen as replacement for the HPDs.
For the LHCb detector upgrade, the PS and SPD will be removed as no dedicated hardware trigger will be run. The electromagnetic and hadronic calorimeter system will remain unchanged apart from an upgrade of the front- and back-end electronics required by the operation of the upgrade detector at 40 MHz. The ECAL and HCAL modules are expected to cope with the increased radiation levels until the Long Shutdown 3 (currently scheduled for 2025), during which modifications might become necessary.
Because the upgraded LHCb detector will operate at luminosities of up to $2 \times 10^{33}\,\text{cm}^{-2}\,\text{s}^{-1}$ [67], the particle rates will increase accordingly. This increase in particle flux is not tolerable for muon station M1, which will be removed for the upgrade. To reduce the occupancy in the remaining muon stations, additional shielding will be installed around the beam pipe behind the hadronic calorimeter. The multi-wire proportional chambers of the muon stations are expected to meet design specifications until at least the Long Shutdown 3.

4.1. Clustering algorithm for VELO pixels

4.1.1. VELO upgrade design

The VELO upgrade will utilise 52 modules arranged perpendicular to the z-axis, of which 26 will be installed at each side of the beam. The schematic layout of half of the upgrade VELO detector with its 26 modules is shown in Fig. 4.2. The silicon sensors for the VELO upgrade will be bump-bonded to three application-specific integrated circuits (ASICs), called VELOPix. Each ASIC contains 256×256 silicon pixels with a dimension of $55 \times 55\,\mu\text{m}^2$.

The upgrade modules will comprise four sensors assembled on a $400\,\mu\text{m}$ thick silicon microchannel substrate and with a carbon fibre support. Two tiles consisting of one sensor and three

VELOPix chips each are glued on each side of the module substrate. The tiles overlap by 110 µm to avoid losing angled tracks.

The arrangement of the tiles in an L-shape rotated by 45° is illustrated in Fig. 4.3. The advantage of this configuration is a facilitated installation and if the occupancy during operation is too high, the active area can be moved and hence the occupancy can be reduced. A lower maximal column hit occupancy is achieved and thus the data rate in the columns is more uniform. The VELOPix chip is radiation hard and robust against Single Event Upsets, which are state changes of register bits or of memory caused by an ion interacting with the ASIC.

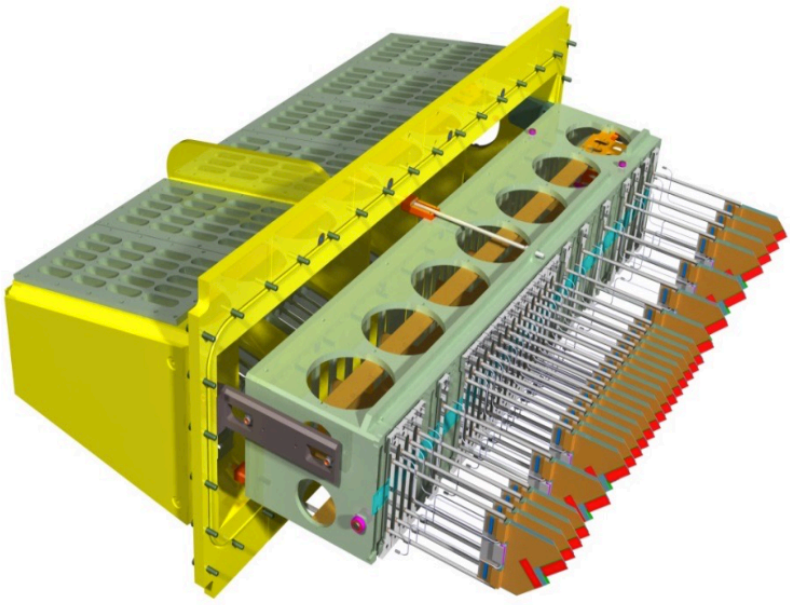

Figure 4.2.: *Schematic layout of half of the VELO pixel detector of the LHCb upgrade detector. The figure is taken from Ref. [70].*

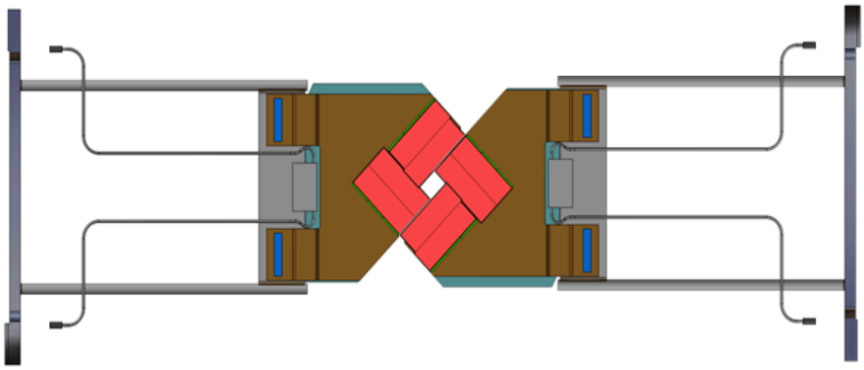

Figure 4.3.: *Schematic layout of two L-shaped VELO pixel modules of the LHCb upgrade detector: Each module contains two arrays of 3 sensors (red). Cooling of the sensors is provided by CO_2 microchannel cooling on a substrate (brown). The figure is taken from Ref. [70].*

4.1.2. VELOPix ASIC readout

The data collected by the VELO upgrade detector are transferred via kapton cables with two copper layers to opto and power boards located outside of the vacuum, which supply voltages and convert the serial data links from electrical to optical signals. The data sent out by the opto and power boards through optical fibres are received on the TELL40 data acquisition boards, which digitise the analogue signals and process data in field-programmable gate arrays (FPGAs). The processed data are then sent out to the CPU trigger farm. A schematic layout of the VELO pixel readout chain is shown in Fig. 4.4.

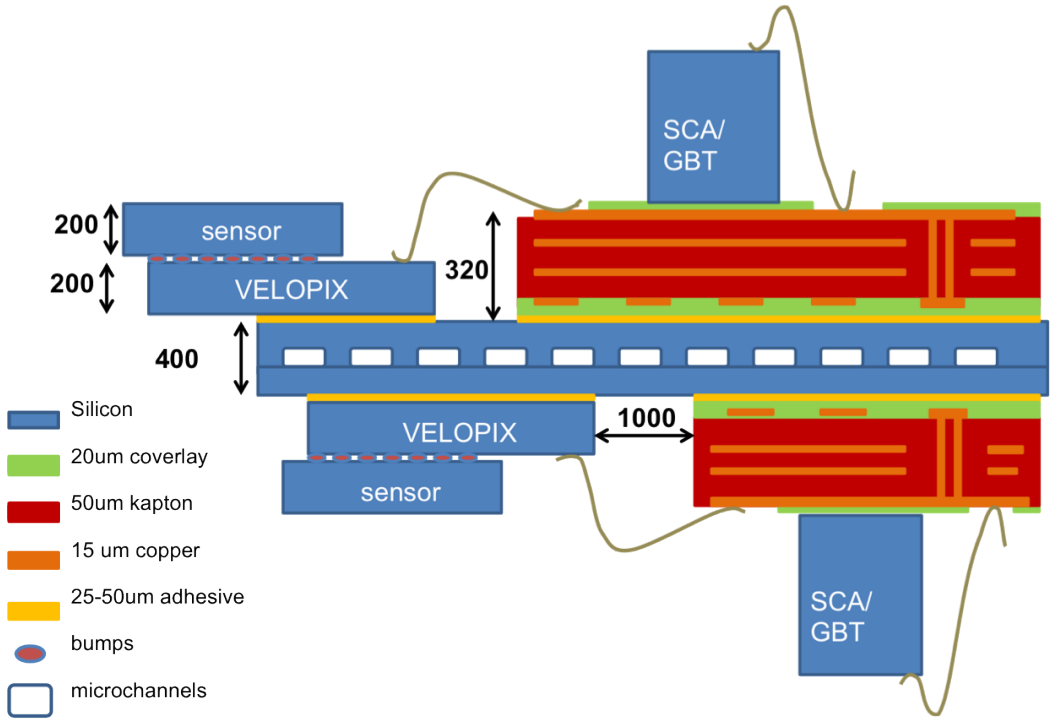

Figure 4.4.: *Schematic layout of the components of the VELO pixel readout chain. The measures are given in* µm. *The figure is taken from Ref. [69].*

The VELOPix is a binary data-driven readout ASIC, which can cope with data rates up to $4 \times 5.12\text{Gbit/s}$, where the factor of 4 represents the number of output serialisers per chip. A time-stamp and a label is added to the information of each hit. The hits from the 256×256 pixels are collected column-wise in so-called Super-Pixel Packets (SPPs), which describe an array of 2×4 pixels. Non-empty SPPs are sent out for each bunch crossing since the VELOPix does not possess a triggering scheme. The disadvantage of the VELOPix design is that the data are not sent ordered in time and thus the SPPs have to be reordered in time at a later stage of data processing. The data rate per VELOPix for the most active module is illustrated in Fig. 4.5. The ASICs are oriented such that the readout direction points away from the beam. The data are gathered in End-of-Column (EoC) logic blocks routed to four output serialisers as shown in Fig. 4.6. The output serialisers operate at a speed of about $5\text{Gbit}/s$ and are located at the same side of the ASIC as the digital-to-analogue converters (DACs), the phase-locked loop (PLL), the experimental control system (ECS) and the timing and fast control (TFC)

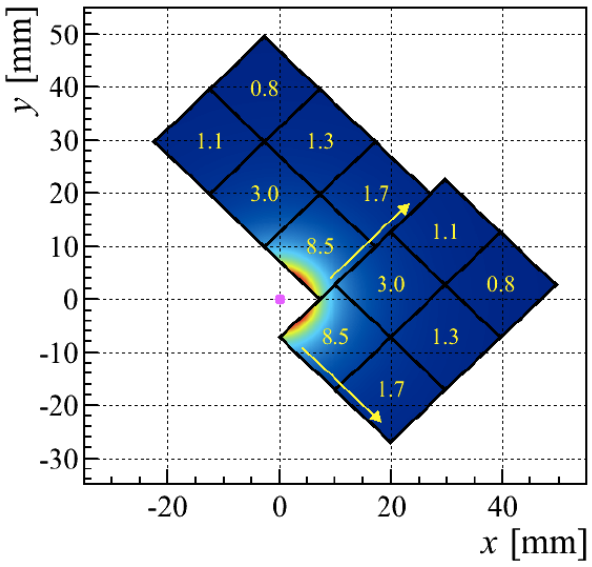

Figure 4.5.: *Data rate per VELOPix given in* Gbit/*s for the most active module. The readout direction is indicated by arrows. The figure is taken from Ref. [71].*

interfaces. The PLL provides the ASIC reference clock, which operates at a maximum of the LHC frequency of 40 MHz as does the VELOPix.

A frequency of 40 MHz corresponds to the frequency of subsequent collisions of bunch trains. Due to gaps in the LHC filling scheme, the average rate is 27 MHz. The PLL system clock determines the resolution of the time-stamp. The TFC and ECS control systems are responsible for the control of the entire readout of the LHCb detector and of the configuration, control and monitoring of the online system, respectively.

The basic readout unit of the VELOPix is the afore mentioned Super Pixel (SP), which is an array of 2×4 pixels. The advantage of using SPPs rather than single pixel packets is a reduction in bandwidth as 55% of the tracks will yield a cluster with a size of more than one pixel due to the small pixel size and the non-zero track angle. Instead of adding a time-stamp to each single pixel packet, which also shares a large fraction of the pixel position or address with the neighbouring pixels, this information is added for SPs and, as a consequence, the bandwidth is reduced by 30%. Each SPP contains the time-stamp corresponding to the LHCb bunch crossing ID, the address of the SPP and information on which pixels within the SP were hit (hit map). To minimise the loss of data due to the dead-time of the readout, each SP can store hits from two different bunch crossings temporarily. The readout of the VELOPix is done in columns by shifting the data from the top of the 64 SP wide column to the EoC resulting in a maximum latency of 64. When the SPPs have reached the EoC blocks located at the end of each column, the column number is added to the address of the SP resulting in 30-bit wide SPPs.

Four SPPs are grouped in 128-bit Gigabit Wireline Transmitter (GWT) frames with an 8-bit header as shown in Fig. 4.7. The header is used to synchronise the arriving GWT frames in the TELL40 boards.

The header of the GWT frames consists of a 4-bit wide constant pattern and 4 parity bits. The parity bits are calculated from the four SPPs in the GWT frame to ensure correct data transmission from the VELO pixel front-end to TELL40 boards. For an even number of bits

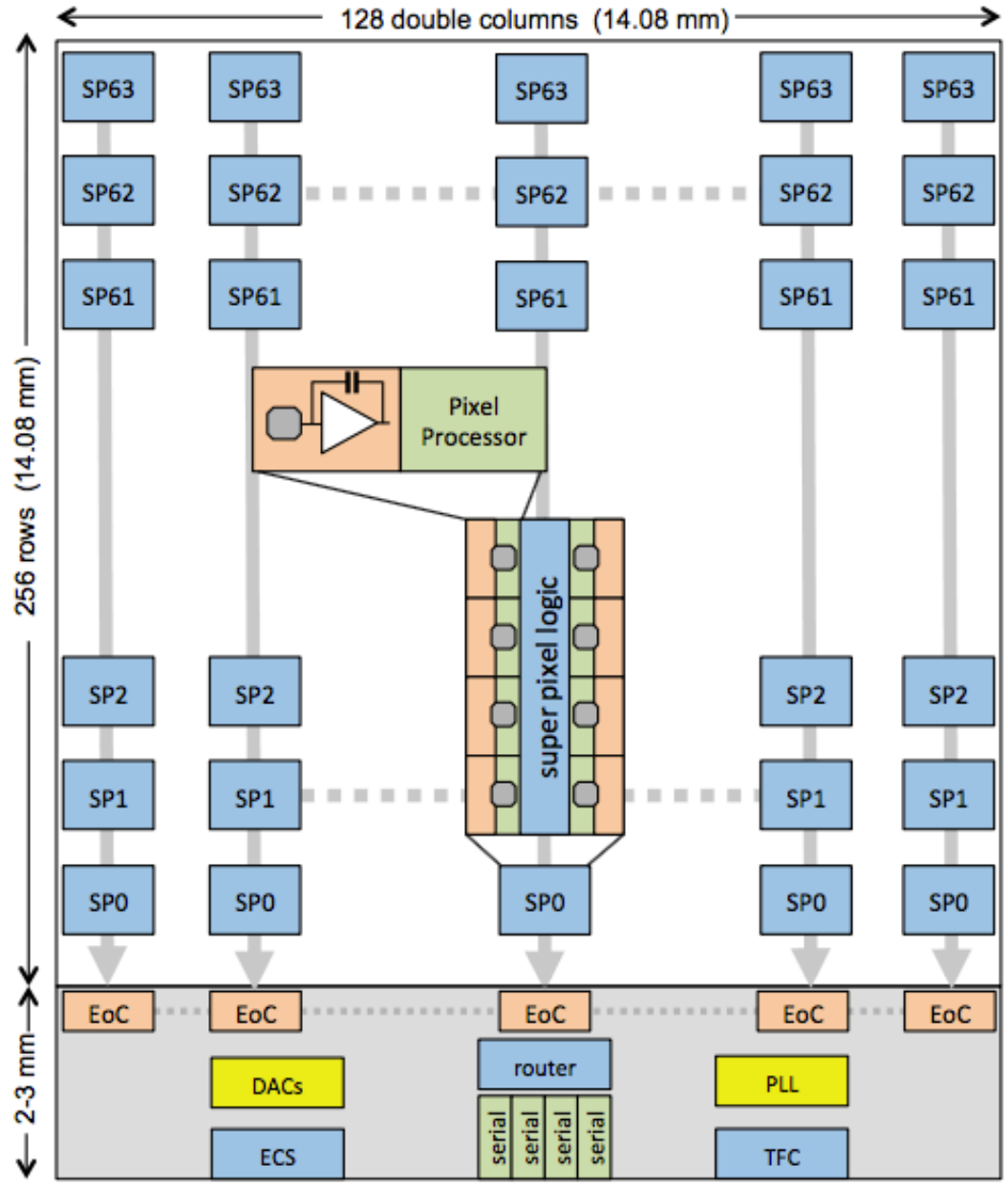

Figure 4.6.: *Block diagram of the VELOPix ASIC.* 2×4 *pixels are combined in Super Pixels (SPs). The figure is taken from Ref. [69].*

in the SPP with value one, the parity bit is set to zero and for an odd number, the parity bit equals one. The SPP address is composed of a 7-bit column and a 6-bit row ID. In addition to the address of the SP, the hitmap is stored. The 9-bit bunch crossing ID is encoded in Gray code, which is used to increase the robustness of data transmission.
The GWT frames arrive at a rate of 5.12 GHz on the TELL40 boards where they are split into single SPPs, the parity bit is checked and the bunch crossing ID is decoded to binary. In a second step, the split SPPs are processed by a router, which performs a time reordering of the SPPs and passes them on to a processor and finally to an event builder.

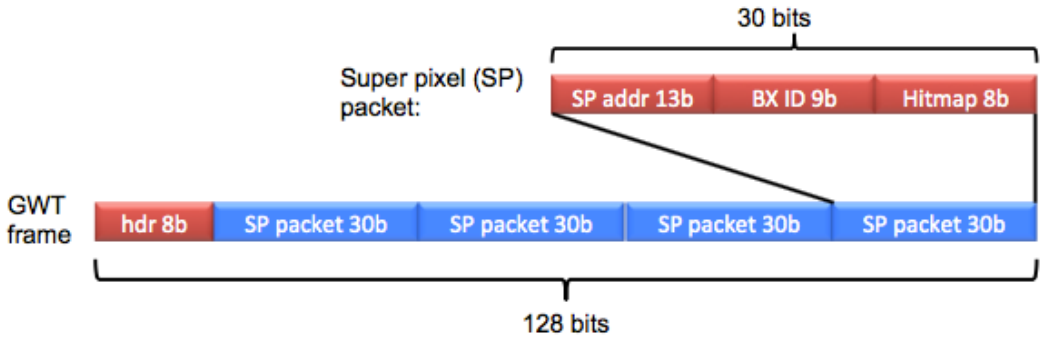

Figure 4.7.: *Four 30-bit SPPs are grouped with a 8-bit header in a GWT frame. Each SPP contains a 13-bit address, the 9-bit bunch crossing ID and the hitmap storing information on which pixel in the SP was hit. The figure is taken from Ref. [69].*

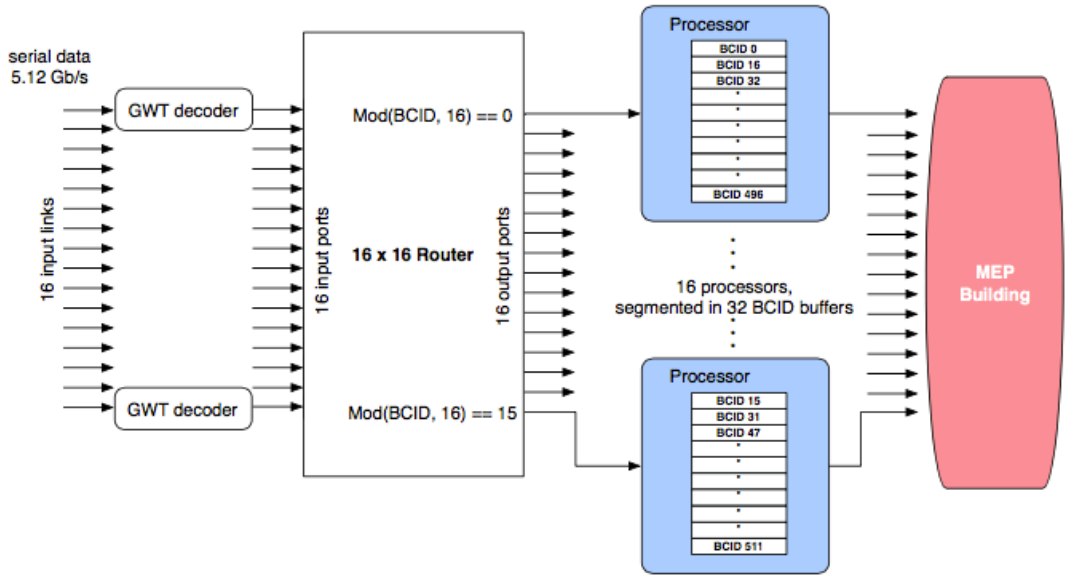

Figure 4.8.: *Block diagram of the VELO part of the TELL40 firmware. The SPPs arrive packed in GWT frames, are then decoded and passed to a router, which performs the time reordering of the SPPs. The time-ordered SPPs are passed to a processor, where the SPPs are sorted spatially and flagged if they are isolated before being sent to the event builder. The figure is taken from Ref. [69].*

4.1.3. Spatial sorting algorithm for FPGA board

The work carried out in the context of this thesis comprises feasibility studies of the implementation of a sorting algorithm in the processor. The motivation for studying the implementation of a sorting algorithm in the processor is to increase the CPU time available for evaluating the software trigger response, which is crucial for the performance of the upgrade of the LHCb detector. The algorithm under consideration performs first a spatial sorting of the readout columns. For each SPP, the column number of the neighbouring SPPs are checked and if they

are empty, then an isolation flag is set. In the trigger, the pattern of pixel hits in each isolated SP will then be considered within a look-up table. Due to the limited resources of the FPGA, only a part of the clustering, such as the spatial sorting and the determination of an isolation flag, can be performed.
The studies outlined in the following are performed on simulation reflecting data-taking conditions for Run 3. The simulated VELO pixel hits are converted to SPPs and a latency for each SPP is added. A study of this simulation found that on average, a cluster consists of ~ 1.3 SPs. Only 2% of clusters were found to extend over more than two SPs, whereas 23% of clusters have hits in two different SPs. Hence 75% of clusters are contained in a single SP, which means that the clustering in the trigger has to be run only in 25% of all clusters. The average number of pixels per cluster is ~ 1.9, where 46% contain hits of a single pixel; in 36% of cases, two pixels were hit; and for 10% of all clusters, the hits extend over three pixels. The distribution of fractions of all clusters with a certain number of pixels and SPs is illustrated in Fig. 4.9.

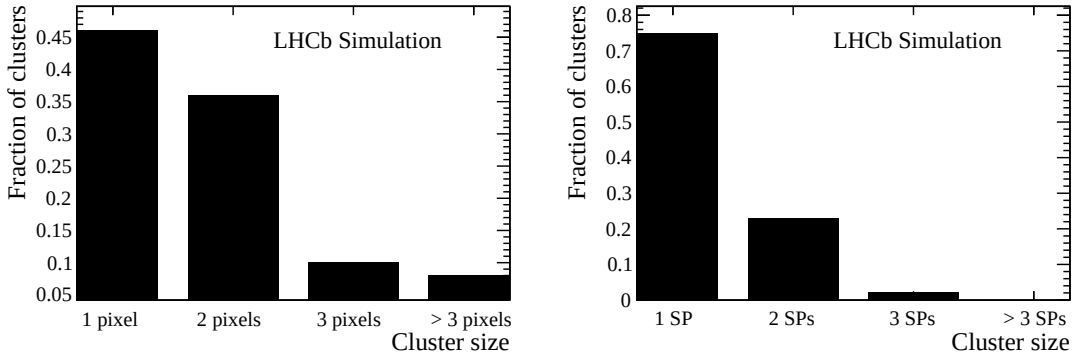

Figure 4.9.: *Distribution of the fraction of clusters with a certain size of pixels (left) and super pixels (right).*

Due to the CPU, memory and power consumption constraints of the FPGA in which the processor is implemented, a parallel bubblesort algorithm is chosen for the spatial sorting of the SPPs. The time-ordered SPPs are sorted according to their 11 most significant address bits (MSBs) corresponding to the 2-bit sensor, 2-bit ASIC and the 7-bit column information. The parallel bubblesort algorithm compares these 11 MSBs for each bunch crossing ID at a time and swaps the corresponding SPPs if their 11 MSBs are out of order. First, all SPs, which are on an even position are compared with their right neighbour; then the same is done for all SPs, which are on an odd position. For example, the first two SPs at positions zero and one, the SPs at positions two and three and so on are compared with each other. The comparison for the SPs at positions one and two, four and five and so on is done in parallel.
In the worst case scenario, the algorithm requires $\mathcal{O}(n^2)$ comparisons for n elements whereas the best case performance is $\mathcal{O}(n)$. The advantage of the parallel bubblesort over the bubblesort algorithm is that it requires less clock cycles. With n comparators, the spatial sorting takes between one and n clock cycles. Figure 4.10 illustrates the parallel bubblesort algorithm for the ordering of eight numbers.

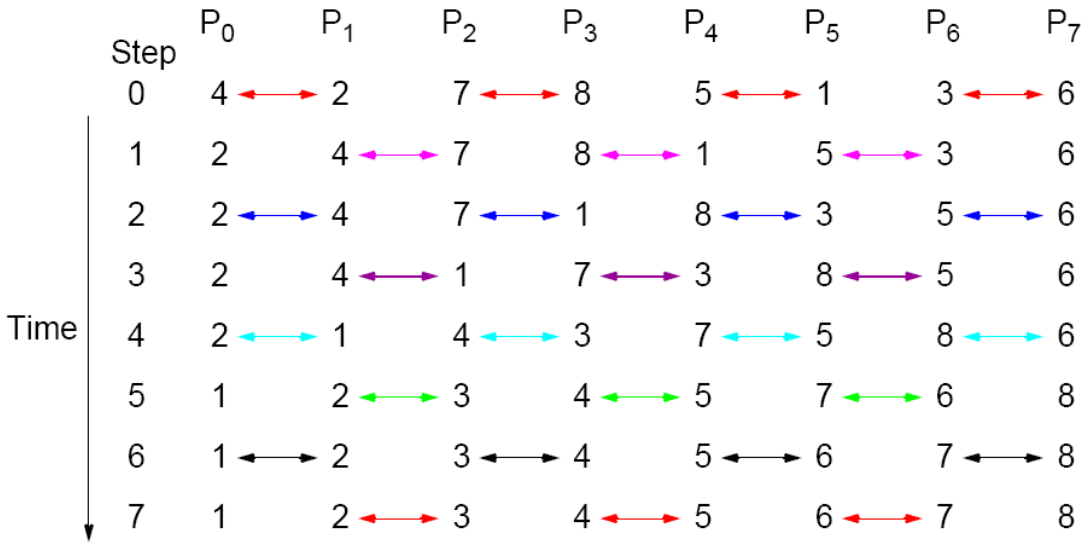

Figure 4.10.: *Illustration of the parallel bubblesort algorithm for the ordering of eight numbers. Pairs of Super Pixels are compared and swapped if out of order. The figure is taken from Ref. [72].*

After the spatial sorting, the adjacent SPs are checked for their column numbers. In the case that the adjacent SPs have a hit in the neighbouring columns of the SP, it is marked as not isolated and the modified SPP is shipped out that contains the sensor and ASIC ID, the SPP address, the hitmap and the isolation flag. As can be seen from Fig. 4.11, an SP will only be flagged as isolated in case the SP is truly isolated.

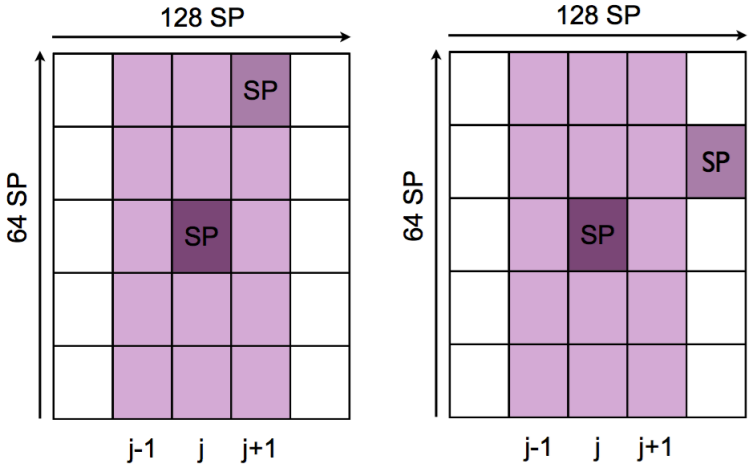

Figure 4.11.: *Illustration of non-isolated (left) and isolated (right) super pixels.*

The isolation flag does not allow to distinguish between SPPs with a direct neighbour, which is one of the eight adjacent SPs, or with an indirect neighbour, where an SP is in the adjacent column but not in the adjacent row. In an emulation of the clustering code, it is found that the fraction of SPP with indirect neighbours, which are incorrectly marked as non isolated is $< 1\%$. These incorrectly flagged SPPs will be reprocessed in the clustering as are all non isolated SPPs.

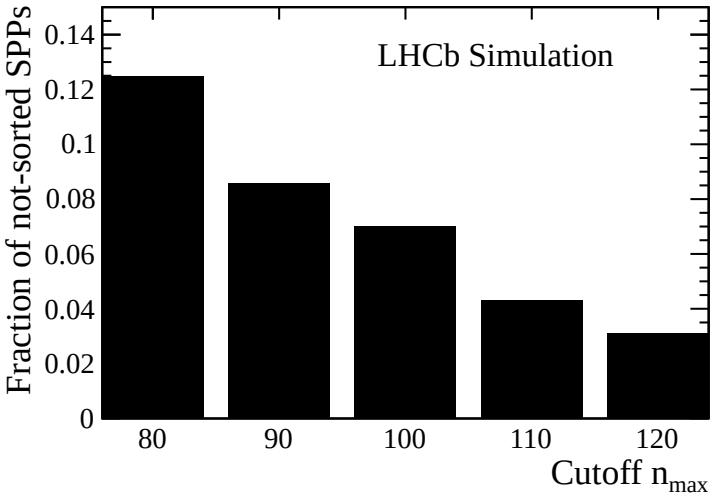

Figure 4.12.: *Fraction of unsorted SPPs depending on cutoff for a single module.*

The parallel bubblesort algorithm is only feasible timing-wise for a specific number of SPPs. This is implemented as a cutoff $n_{\max}$ and if the number of SPPs per bunch crossing is larger than this cutoff, no spatial sorting is performed. Instead, all SPPs are flagged as not isolated and are automatically reprocessed in the offline clustering. Figure 4.12 illustrates the fraction of unsorted SPPs for various values of $n_{\max}$ for a single module. As for a cutoff ≥ 110, the number of unsorted SPPs is sufficiently small, the sorting and flagging algorithm is expected to lead to a significant reduction of CPU time required in the trigger for the clustering.

5. Analysis method

In this thesis, the results of a time- and model-dependent amplitude analysis of $D^0 \to K^0_S\pi^+\pi^-$ decays are reported. The D^0 decays analysed originate from semileptonic B meson decays. The analysis extracts the mixing parameters x and y and prepares a search for indirect CP violation, which measures $|q/p|$ and $\phi = \arg(q,p)$.
As discussed for the D^0-$\overline{D}^0$ system in Chapt. 2.2, mixing of neutral mesons is a time-dependent phenomenon where the time evolution of the transition amplitude of a D^0 ($\overline{D}^0$) decay to a final state f has to be considered. The time-dependent amplitudes $\mathcal{A}_f(t)$ and $\bar{\mathcal{A}}_f(t)$ are given by

$$\mathcal{A}_f(t) \equiv \langle f|\mathcal{H}|D^0(t)\rangle = \frac{e_1(t)+e_2(t)}{2}\mathcal{A}_f + \frac{q}{p}\frac{e_1(t)-e_2(t)}{2}\bar{\mathcal{A}}_f, \tag{5.1}$$

$$\bar{\mathcal{A}}_f(t) \equiv \langle f|\mathcal{H}|\overline{D}^0(t)\rangle = \frac{e_1(t)+e_2(t)}{2}\bar{\mathcal{A}}_f + \frac{p}{q}\frac{e_1(t)-e_2(t)}{2}\mathcal{A}_f, \tag{5.2}$$

with the phase-space dependent amplitudes $\mathcal{A}_f$ and $\bar{\mathcal{A}}_f$ evolving in time with

$$e_{1,2}(t) = e^{-imt}e^{-\frac{\Gamma}{2}t}e^{\mp(y+ix)\frac{\Gamma}{2}t}. \tag{5.3}$$

The mixing parameters driving the time-dependent oscillation are $x \equiv (m_1 - m_2)/\Gamma$ and $y \equiv (\Gamma_1 - \Gamma_2)/(2\Gamma)$. The CP violation parameters $|q/p|$ and ϕ describe the superposition of the flavour eigenstates D^0 and $\overline{D}^0$ of the physical eigenstates D_1 and D_2, $|D_{1,2}\rangle = p|D^0\rangle \pm q|\overline{D}^0\rangle$. By measuring the time- and phase-space dependent distribution of $D^0 \to K^0_S\pi^+\pi^-$ decays, the mixing parameters can thus be extracted and a search for indirect CP violation can be performed.
The phase-space distribution of $D^0 \to K^0_S\pi^+\pi^-$ decays is modelled by expressing the three-body decay as a succession of two-body decays. First, the D^0 meson decays into an intermediate resonance r and one of its three daughters. In a second step, the resonance then decays into the two other D^0 daughters. The decay amplitude of a D^0 or $\overline{D}^0$ into $K^0_S\pi^\pm\pi^\mp$ is a superposition of all possible intermediate resonances and the single resonances interfere with each other across the phase-space spanned by $m^2(K^0_S\pi^-)$ and $m^2(K^0_S\pi^+)$. This phase-space for a three-body decay is the so-called Dalitz plane spanned by the Dalitz variables, $m^2(K^0_S\pi^-)$ and $m^2(K^0_S\pi^+)$. Due to the different masses and widths of the resonances, they manifest themselves in different phase-space regions. Scalar resonances appear as a band in the Dalitz plot whereas vector (tensor) resonances exhibit one (two) nodes as can be seen in Fig. 5.1. The amplitudes given at a certain point in phase-space are

$$\mathcal{A}(m^2(K^0_S\pi^-), m^2(K^0_S\pi^+)) = \sum_r c_r A_r(m^2(K^0_S\pi^-), m^2(K^0_S\pi^+)), \tag{5.4}$$

$$\bar{\mathcal{A}}(m^2(K^0_S\pi^-), m^2(K^0_S\pi^+)) = \sum_r \bar{c}_r A_r(m^2(K^0_S\pi^+), m^2(K^0_S\pi^-)), \tag{5.5}$$

where the sum is evaluated over all intermediate resonances r with complex amplitude A_r contributing to the $D^0 \to K^0_S\pi^+\pi^-$ decay with complex coefficients c_r. The modelling of the resonances contributing to the $D^0 \to K^0_S\pi^+\pi^-$ decay are subject to the analyst's choice depending not only on the size of the available dataset but also on the sensitivity to the regions of phase-space where the resonances are present. Therefore, this approach is model-dependent.

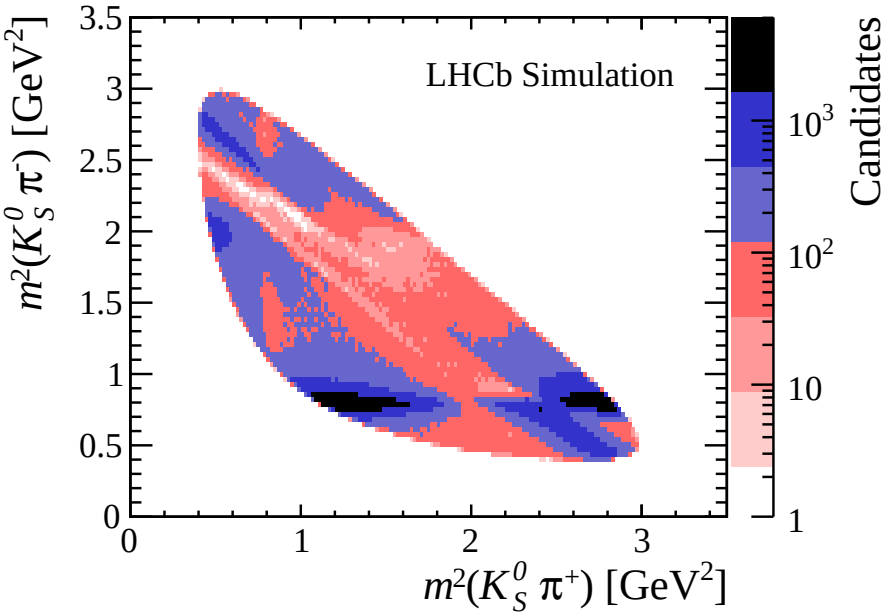

Figure 5.1.: *Simulated Dalitz plot of $D^0 \to K^0_S\pi^+\pi^-$ decays visualising the intermediate resonances and their interferences. At $m^2(K^0_S\pi^-) \approx 0.8\,\text{GeV}^2$, the $K^*(892)^-$ resonance decaying into $K^0_S\pi^-$ can be clearly identified. The $K^*(892)^-$ is a spin one particle and thus the band along the $m^2(K^0_S\pi^+)$ axis exhibits a single node.*

The parameters of interest x, y, $|q/p|$ and ϕ can be extracted from a fit in D^0 decay time and the Dalitz variables $m^2(K^0_S\pi^-)$, $m^2(K^0_S\pi^+)$ to data. The model (see Chapt. 11) used in this amplitude fit describes the amplitude of the $D^0 \to K^0_S\pi^+\pi^-$ decay as a superposition of various decays through intermediate resonances and their interferences as discussed above. The amplitudes of the $D^0 \to K^0_S\pi^+\pi^-$ decay via intermediate resonances depend not only on D^0 decay time but also on the Dalitz variables. The free parameters of the fit are the coefficients a_r and ϕ_r of the intermediate resonances as well as their masses and widths, the average D^0 lifetime τ and for the nominal result of this analysis, the mixing parameters x and y.

The data used in this analysis (see Chapt. 6) were recorded with the LHCb detector at the LHC (see Chapt. 3) in 2011 and 2012. The $D^0 \to K^0_S\pi^+\pi^-$ decays considered originate from semileptonic B meson decays. The analysis distinguishes between two different decay chains

$B^- \to D^0(\to K^0_S\pi^+\pi^-)\mu^-\overline{\nu}_\mu$ (single-tagged) and $\overline{B}^0 \to D^{*+}(\to D^0(\to K^0_S\pi^+\pi^-)\pi^+)\mu^-\overline{\nu}_\mu$ (double-tagged). The tags allow to identify the D^0 or $\overline{D}^0$ flavour at the time of production. In the single-tagged sample, the sign of the muon distinguishes the B^- decays to a D^0 from the B^+ decays to a $\overline{D}^0$ meson. The flavour of the D^0 ($\overline{D}^0$) meson in the double-tagged samples is indicated both by the charge of the muon and the π^+ (π^-) from the decay $D^{*+} \to D^0\pi^+$ ($D^{*-} \to \overline{D}^0\pi^-$). The single- and double-tagged decay chains are reconstructed inclusively and thus also comprise B decays to higher excited charm meson states such as $B^- \to D^{*0}\mu^-\overline{\nu}_\mu$ with *e.g.* $D^{*0} \to D^0\gamma$. The distinction between the single- and double-tagged decay chains is made since the additional information added by the pion from the D^* decay can be exploited to have a cleaner sample with less background. Since the double-tagged sample is a subset of the single-tagged sample, the candidates of the double-tagged sample are removed in a later stage of the analysis from the single-tagged sample to avoid double-counting of candidates.
Due to the long lifetime of the K^0_S meson of $(8.954 \pm 0.004) \times 10^{-11}$ s [11], about a third of all K^0_S mesons produced and decaying within the LHCb acceptance decay inside of the VELO acceptance. Depending on which tracking detectors contributed to the reconstruction of the K^0_S mesons, different track definitions are introduced. Figure 5.2 illustrates schematically the five different track types used in LHCb: VELO tracks and T tracks have only hits in the VELO or tracking stations T1-T3, respectively. An upstream track is built out of hits in the VELO and TT whereas hits in the TT and the tracking stations T1-T3 are used to reconstruct a downstream track. A track with hits in VELO and T1-T3 (and possibly with hits in the TT) is called a long track.

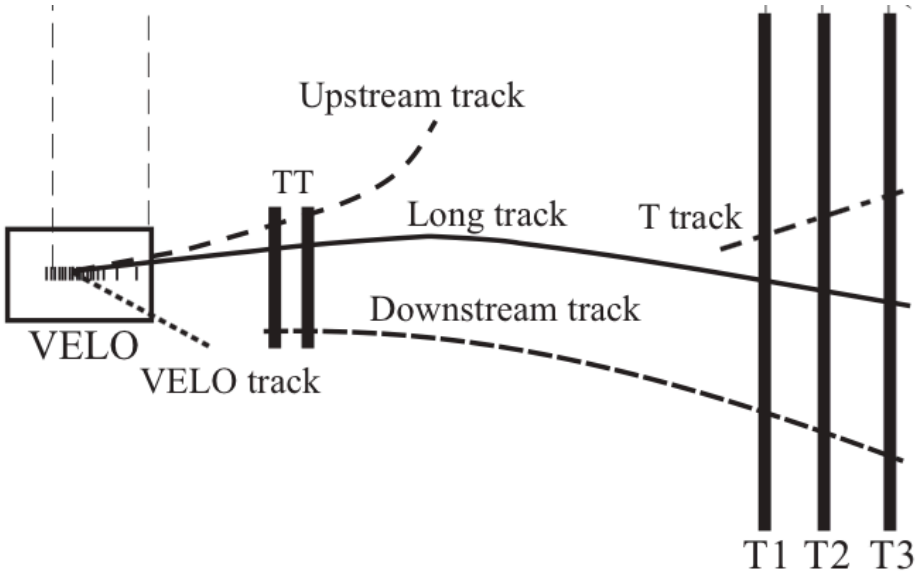

Figure 5.2.: *A schematic layout of the LHCb tracking systems is shown and the five different track types at LHCb, namely VELO, T, upstream, downstream and long tracks, are visualised. The LHCb magnet is located between the TT and the T1-T3 stations. The figure is taken from Ref. [54].*

In this analysis, K^0_S mesons are reconstructed in the decay $K^0_S \to \pi^+\pi^-$. Depending on whether the daughter pions are two downstream (D) or two long tracks (L), the K^0_S candidate is classified either as K^0_S(DD) or K^0_S(LL) candidate. K^0_S candidates formed from a combination of a long and a downstream track, which occurs rarely, are not used in the analysis. Due to the

better momentum resolution of long K^0_S candidates, the selection requirements differ for both types of K^0_S candidates.

After a trigger and a preselection, candidates passing a multivariate analysis are considered for the analysis (see Chapt. 7 and 8). The multivariate analysis relies solely on data. The distinction between signal and background in the training of the classifier is achieved through the use of so-called sWeights [73], which are calculated from a fit to the reconstructed D^0 mass, $m(D^0)$, as detailed in Chapt. 8. The remaining background consists mainly of random combinations of tracks rather than contributions from specific decay modes. No specific background decay mode with a mass peak in the $m(D^0)$ signal window was found, as is shown in Chapt. 9. In the amplitude fit, a description of the background in D^0 decay time and in the Dalitz plane is included. To obtain this distribution, sWeights are extracted from a fit to $m(D^0)$ for the single-tagged sample and from a fit to $\delta m = m(D^*) - m(D^0)$ for the double-tagged sample. The distributions of all candidates in D^0 decay time and in $(m^2(K^0_S\pi^-), m^2(K^0_S\pi^+))$ are split into signal and background categories by using these sWeights and are used as input for the amplitude fit. Depending on D^0 mass for the single-tagged sample and δm for the double-tagged sample, a signal probability is determined for each candidate to account for the remaining background in the selected data sample, as outlined in Chapt. 8.3. The decay time resolution of the LHCb detector and the variation of the efficiency of the reconstruction and selection across phase-space are measured as outlined in Chapt. 10 and corrected for in the amplitude fit.
To ensure the correctness of the results, the amplitude fit is validated on simulated samples reflecting different scenarios of *CP* violation and sets of mixing parameters. A summary of the validation studies is given in Chapt. 12 and the systematic uncertainties on the mixing parameters are evaluated in Chapt. 13.

6. Datasets and simulation

The time- and model-dependent amplitude analysis exploits data corresponding to a luminosity of $3\,\text{fb}^{-1}$ recorded with the LHCb detector (see Chapt. 3) in 2011 and 2012. Samples of $D^0 \to K^0_S\pi^+\pi^-$ decays originating from single- or double-tagged semileptonic B decays are selected. Since not all ingredients needed for the analysis can be determined on data, simulated samples are produced, which rely on a precise understanding of the underlying physics processes and, where needed, of the response of the LHCb detector. In Chapt. 6.1, the datasets and the simulated Monte Carlo (MC) data samples are listed. An overview of the simulation chain at LHCb relevant for the analysis presented in this thesis is given in Chapt. 6.2.

6.1. Datasets

In a preselection called Stripping, detailed in Chapt. 7.2, $D^0 \to K^0_S\pi^+\pi^-$ decays are reconstructed either as $B^- \to D^0(\to K^0_S\pi^+\pi^-)\mu^-\overline{\nu}_\mu$ (single-tagged) or
$\overline{B}^0 \to D^{*+}(\to D^0(\to K^0_S\pi^+\pi^-)\pi^+)\mu^-\overline{\nu}_\mu$ (double-tagged) candidates. The charge-violating decay $\overline{B}^0 \to D^{*+}(\to D^0(\to K^0_S\pi^+\pi^-)\pi^+)\mu^+\overline{\nu}_\mu$ allows to extract the fraction of candidates where the muon charge is misreconstructed and the D^0 flavour is assigned incorrectly. These decays are identified as wrong-sign decays, opposed to right-sign $\overline{B}^0 \to D^{*+}(\to D^0(\to K^0_S\pi^+\pi^-)\pi^+)\mu^-\overline{\nu}_\mu$ decays. While data-taking, the polarity of the LHCb magnet is changed frequently such that about half of the data are taken at a magnet polarity denoted by MagUp and the reverse polarity denoted by MagDown. The yields after the Stripping selection for both magnet polarities are listed in Tables 6.1 and 6.2 for the data recorded in 2011 and 2012.

The momentum calibration in LHCb is dependent on the detector alignment and thus changing over time. The latest calibration is used to adjust momenta [54]. This adjustment is only available for observables, which have been computed after a refit of the $D^0 \to K^0_S\pi^+\pi^-$ decay with DecayTreeFitter [74].

Table 6.1.: *Numbers of $D^0 \to K^0_S\pi^+\pi^-$ candidates from the 2011 dataset passing the Stripping selection and reconstructed as originating from single- or double-tagged semileptonic B decays. The yields are given for each magnet polarity and type of K^0_S candidate separately.*

Decay mode	K^0_S(LL)		K^0_S(DD)	
	MagUp	MagDown	MagUp	MagDown
Single-tagged	1,240,660	1,800,328	2,613,771	3,819,106
Double-tagged right-sign	508,591	741,995	806,876	1,192,745
Double-tagged wrong-sign	449,680	678,424	663,949	1,008,575

Table 6.2.: *Numbers of $D^0 \to K^0_S\pi^+\pi^-$ candidates from the 2012 dataset passing the Stripping selection and reconstructed as originating from single- or double-tagged semileptonic B decays. The yields are given for each magnet polarity and type of K^0_S candidate separately.*

Decay mode	K^0_S(LL)		K^0_S(DD)	
	MagUp	MagDown	MagUp	MagDown
Single-tagged	4,457,875	4,560,353	9,746,779	9,928,540
Double-tagged right-sign	1,891,942	1,942,791	3,102,248	3,170,429
Double-tagged wrong-sign	1,731,365	1,778,537	2,696,489	2,757,516

6.2. Simulation

The LHCb simulation framework [75] consists of a generation and a simulation phase. In the generation phase, the *pp* collision is generated by the Pythia package [76, 77] and the subsequent decays are modelled by EvtGen [78]. Radiative photons are simulated by the Photos package [79]. The tracking of particles through the detector is performed in the simulation phase. The interactions of particles with the detector material are simulated by the Geant4 toolkit [80, 81]. A detailed description of the detector material is stored in an XML geometry database and data taking conditions, notably alignment and calibration constants, are contained in an XML conditions database, which is frequently updated to reflect the current state of the detector. The analogue responses of the subdetector systems are simulated followed by a conversion to digital signals. After the simulation of the detector response and the digitisation, the simulated data are in the same format as the recorded data. Both simulated and collision data are then passed through the same trigger and reconstruction chain. The number of events that can be produced in full simulation is limited by CPU and storage requirements.

Faster MC generation is achieved through the usage of a 'particle gun': instead of generating the *pp* collisions, only the signal particles are generated, *e.g.* B mesons for single-tagged $B^- \to D^0(\to K^0_S\pi^+\pi^-)\mu^-\overline{\nu}_\mu$ decays. The signal particles are then decayed via EvtGen [78]. A realistic particle simulation is obtained by generating the momenta of the signal particle following a spectrum taken from a full simulation with Pythia [76, 77]. Furthermore, the collision vertex is smeared according to the beam spot parameters and it is possible to apply acceptance selection criteria during generation. Particle gun samples can be passed through Geant4; the response of the subdetector systems and the digitisation can be simulated. Although the particle gun simulation is much faster, Pythia samples possess an associated *pp* collision vertex, which allows the samples to be processed through the same trigger and reconstruction chain as data. For particle gun samples, the trigger and reconstruction chain has to be emulated carefully to remove selection criteria related to the *pp* collision vertex.

In the analysis reported in this thesis, particle gun samples are used in the measurement of the signal acceptance. For the acceptance measurement, the generated values of the observables have to be known before any reconstruction or selection was applied. Particle gun samples are the ideal production tool to obtain large samples containing truth information at generator-level in a sufficiently short time.

6.3. Monte Carlo simulation data samples

The full Monte Carlo simulation data samples used are listed in Tables 6.3 and 6.4 for beam energies of 3.5 TeV in 2011 and of 4.0 TeV in 2012, respectively. A realistic description of the recorded datasets is sought by generating an admixture of B decay channels leading to the same final state, *e.g.* through D_1', D_0^*, D_1 and D_2^* mesons. In the MC production, it is assumed that the decay widths of the D_1', D_0^*, D_1 and D_2^* mesons are saturated by two-body decays and the three-body decay $D_1 \to D^0\pi^+\pi^-$.

The simulated MC data samples are distinguished by a so-called event type, which uniquely identifies different decays and serves to distinguish between different selections applied to the samples during generation. Samples of event type *12875500* contain an admixture of various B decays in a $K_S^0\pi^+\pi^-$ final state where a loose selection during the generation is applied.

The selection criteria detailed in the following are applied at generator level to avoid simulating events that can be expected not to be retained by the selection at reconstruction level. The selection requirements are chosen to be almost 100% efficient with respect to the selection at reconstruction level detailed in Chapt. 7.2. The D^0 and μ candidates are required to be within the LHCb acceptance of $10 \leq \theta \leq 400$ mrad for charged and $5 \leq \theta \leq 400$ mrad for neutral particles. Samples with the same simulation conditions but with a tighter selection are identified by event type *12875520*. The muon and the daughter pions of the D^0 and the K_S^0 have to be within an acceptance of $5 \leq \theta \leq 400$ mrad. The muon momentum and transverse momentum are restricted to $p > 8$ GeV and $p_T > 1.3$ GeV. The z position of the K_S^0 decay vertex has to be less than $z < 2.5$ m, which ensures that the K_S^0 vertex can be reconstructed either in the VELO or in the TT. The K_S^0 daughter pions are required to have $p > 2.5$ GeV and the daughter pions of the D^0 have to satisfy $p > 2.1$ GeV. In addition, $p > 20$ GeV and $p_T > 1.9$ GeV thresholds are imposed on the D^0. Due to their relatively long lifetimes of $(1.638 \pm 0.004) \times 10^{-12}$ s for charged and $(1.519 \pm 0.005) \times 10^{-12}$ s [11] for neutral B mesons, the decay vertex of B mesons is displaced from the pp collision vertex (primary vertex or PV). Therefore, the flight distance of the B meson along the z-axis is required to be greater than 1.6 mm.

Table 6.3.: *Signal Monte Carlo simulation data samples generated with* Pythia8. *The event type and number of generated events for both magnet polarities for 2011 data-taking conditions are given.*

Decay mode		Event type	Generated events	
			MagUp	MagDown
$D^0 \to K_S^0\pi^+\pi^-$,	loose selection	12875500	2,502,492	2,504,992
$D^0 \to K_S^0\pi^+\pi^-$,	tight selection	12875520	2,505,193	2,505,694
$D^0 \to K_S^0\pi^+\pi^-$,	tight selection and Stripping	12875520	859,027	865,774

Table 6.4.: *Signal Monte Carlo simulation data samples generated with* PYTHIA8*. The event type and number of generated events for both magnet polarities for 2012 data-taking conditions are given.*

Decay mode		Event type	Generated events	
			MagUp	MagDown
$D^0 \to K^0_S \pi^+ \pi^-$,	loose selection	12875500	2,523,991	2,503,992
$D^0 \to K^0_S \pi^+ \pi^-$,	tight selection	12875520	2,502,795	2,503,093
$D^0 \to K^0_S \pi^+ \pi^-$,	tight selection and Stripping	12875520	1,668,069	1,669,432

To account for known differences in the resolution of the impact parameter between data and simulated MC data samples, a correction is applied to the simulated MC data samples. The differences arise primarily from the modelling of the complex geometry of the VELO RF foil. A better description of the IP resolutions is achieved by smearing the four-momenta of all particle candidates; this affects directly the IP resolution [57]. The effect is significant for 2011 but much less for 2012 where the agreement between simulated and recorded data is much better.

7. Trigger selection and preselection

This chapter summarises the trigger selection and cut-based preselection of $D^0 \to K^0_S\pi^+\pi^-$ candidates applied in this analysis.

7.1. Trigger selection

The LHCb trigger as described in Chapt. 3.2.7 consists of a L0 hardware trigger, which is subdivided into Muon, Dimuon, Electron, Hadron and Photon lines, and a software-based HLT trigger divided in HLT1 and HLT2. The HLT1 and HLT2 triggers consist of several so-called trigger lines comprising selections of decay channels or classes of decay channels such as three-body decays with a high energetic muon. Trigger decisions are classified depending on whether the candidate's signal final state tracks were involved in the decision that the event passed the trigger. Hence, the events may be classified as triggered on signal (TOS) or triggered independently of signal (TIS). The trigger requirements are identified by a prefix indicating which candidate has passed the selection criteria of the specific trigger line. In the analysis, trigger requirements are imposed on the B candidate, on the muon candidate and on the D^0 daughter pions. The events selected in the analysis are required to pass a specific set of trigger lines. Hence, full knowledge of the selection criteria that have been applied is retained. The trigger selection used in this analysis is

- `mu_L0MuonDecision_TOS` or `B_L0Global_TIS`
- `mu_Hlt1TrackAllL0Decision_TOS` or `piminus_Hlt1TrackAllL0Decision_TOS` or `piplus_Hlt1TrackAllL0Decision_TOS`
- `B_Hlt2SingleMuonDecision_TOS` or `B_Hlt2TopoMu2BodyBBDTDecision_TOS` or `B_Hlt2TopoMu3BodyBBDTDecision_TOS` or `B_Hlt2TopoMu4BodyBBDTDecision_TOS`

and is outlined in the following.

The general selection algorithm behind the above listed trigger requirements does not change over the data-taking periods in 2011 and 2012. Nevertheless, the thresholds of the selection variables were subject to change. These thresholds are stored in so-called Trigger Configuration Keys (TCKs), which have changed during data-taking. The most relevant used TCKs and corresponding requirements are listed in Tables 7.1 and 7.2 for 2011 and 2012, respectively.

The L0 trigger conditions `mu_L0MuonDecision_TOS` and `B_L0Global_TIS` indicate that either the Muon line or one out of the Muon, Dimuon, Photon, Electron or Hadron lines was activated by a particle in the event, which is part of the signal decay in the former and independent of the signal decay in the latter case. The lower threshold on the transverse momentum of the Muon line was 1.76 GeV in 2012 and 1.48 GeV in 2011 for the TCKs listed in Tables 7.1 and 7.2 with the exception of TCK 0x004a0033 where the Muon line threshold was at 0.8 GeV. The decision of the L0 trigger is further based on the number of hits in the SPD (see Chapt. 3.2.5 for details). The Dimuon lines require at least 900 hits in the SPD whereas the lower threshold of the other lines lies at 600 SPD hits. The number of hits in the SPD provides a measure of the multiplicity of the event and hence low-multiplicity events are rejected.

The decisions of the HLT1 trigger lines rely on the properties of individual tracks and not on information of the complete event. This includes pions, which are reconstructed as long tracks, and might originate from K_S^0 or Λ decays. The HLT1 line `Hlt1TrackAllL0Decision` requires at least 9 VELO hits, which are used in the track reconstruction, and less than 3 VELO hits, which were expected from the track extrapolation but not found. In addition to this requirement, which ensures that the track is built from a sufficient number of VELO hits, the number of OT and IT hits on the track is required to be OT hits + 2 × IT hits > 16. By selecting tracks, which fulfill these two requirements, a reliable track reconstruction is ensured. In addition, the IP with respect to the PV reconstructed in 3 dimensions has to be > 0.1 mm and $\chi^2_{\text{IP}} > 16$, which makes sure that the track is separated from the PV. The χ^2_{IP} is defined as the χ^2 difference of a PV reconstructed with and without the considered track. Thresholds placed on p_{T}, p and χ^2/ndf varied over time and are listed in Tables 7.1 and 7.2. The placement of the trigger requirements on daughter pions of the D^0 decay in addition to the muon relaxes the requirements and increases the signal yield.

The `Hlt2SingleMuon` line is suitable for the selection of semileptonic B meson candidates, which have a high-energetic muon. Therefore, the `Hlt2SingleMuon` line requires a single muon with a high transverse momentum $p_{\text{T}} > 1.3$ GeV, a track χ^2/ndf < 2 to ensure a good quality of the track fit and due to the long lifetime of the B meson candidate, the IP distance to the PV has to be > 0.5 mm, and $\chi^2_{\text{IP}} > 200$ with respect to the PV. For TCK 0x004a0033, which was run in 2011, the transverse momentum threshold was lowered to $p_{\text{T}} > 1.0$ GeV.

The `Hlt2TopoMu{2,3,4}BodyBBDTDecision` lines are inclusive trigger lines based on decisions from a Bonsai Boosted Decision Tree (BBDT) [82]. As input for the BBDT training, $\sum |p_{\text{T}}|$, ${p_{\text{T}}}^{\text{min}}$, χ^2_{IP}, the flight distance χ^2, DOCA as well as mass and corrected mass are used.
The trigger candidates for the two-body line are required to have a distance of closest approach between the two particles forming the candidate of less than 0.2 mm. The candidate is then used as input for the three-body line and combined with another particle in the event; the DOCA requirement is imposed on the combination of the two-particle object and the third particle. The same procedure is used to build candidates for the four-body lines. The corrected mass

$$m_{\text{corrected}} = \sqrt{m^2 + |\vec{p}'_{T,\text{miss}}|^2} + |\vec{p}'_{T,\text{miss}}|, \tag{7.1}$$

depends on the invariant mass m and the transverse missing momentum, $\vec{p}'_{T,\mathrm{miss}}$, relative to the flight direction of the candidate with respect to the best primary vertex. In the trigger system, the best primary vertex refers to the PV with the smallest IP. Only candidates with a BBDT output of greater than 0.1 are accepted. The corrected mass is used instead of the B meson mass to account for the non-reconstructed neutrino in the semileptonic B decay. The topological lines of the TCKs listed in Tables 7.1 and 7.2 require at least one track with $\chi^2_{\mathrm{IP}} > 16$ with respect to the PV, which ensures that the candidate is separated from the PV, and at least one candidate with transverse momentum of $p_{\mathrm{T}} > 1.5\,\mathrm{GeV}$. If this candidate is a muon, the transverse momentum cut is loosened to $p_{\mathrm{T}} > 1.0\,\mathrm{GeV}$. For TCKs 0x0094003d and 0x0097003d listed in Table 7.2, a cut of $p_{\mathrm{T}} > 1.7\,\mathrm{GeV}$ is applied independently of the particle type. In addition, the χ^2/ndf for K^0_{S}, $K^{\pm}$ and Λ tracks is restricted to $\chi^2/\mathrm{ndf} < 2$ to ensure that the track reconstruction has a good quality and to reduce the rate from fake tracks (ghost tracks). The sum of transverse momenta for all K^0_{S}, $K^{\pm}$ and Λ candidates has to be $p_{\mathrm{T}} > 3\,\mathrm{GeV}$ in the two-body and $p_{\mathrm{T}} > 4\,\mathrm{GeV}$ in the three- and four-body lines. The maximum number of K^0_{S} or Λ decay products in the direct decay (daughter) and in the subsequent decay of the direct decay products (granddaughter) is two, one and zero in the two-, three- and four-body lines, respectively. For TCKs 0x0094003d and 0x0097003d listed in Table 7.2, not more than two daughter or granddaughter K^0_{S} or Λ are allowed for the two- and three-body lines whereas the four-body line allows not more than one K^0_{S} or Λ daughter or granddaughter. No K^0_{S}(DD) were present in the 2011 TCKs. Apart from TCK 0x00790038 (see Table 7.1), no K^0_{S} and Λ mesons were used as input for the topological trigger lines. The χ^2/ndf is required to be $\chi^2/\mathrm{ndf} < 2.4$ and the sum of transverse momenta for all daughters has to be $p_{\mathrm{T}} > 3\,\mathrm{GeV}$ in the two-body and $p_{\mathrm{T}} > 4\,\mathrm{GeV}$ in the three- and four-body lines. A thorough discussion of the topological trigger is given in Ref. [83].

7.2. Preselection

The single- and double-tagged datasets are selected by reconstructing the decay chain step-by-step in reverse. From two pions, a K^0_{S} candidate is reconstructed, which is paired with two pions to form a D^0 candidate. The D^0 candidate is matched with a soft pion to build a D^*, which is then paired with a μ to reconstruct the double-tagged B candidate. Single-tagged B candidates are built by matching the D^0 with a muon. This reconstruction step where specific decay chains are reconstructed is called the Stripping in LHCb. The analysis of the single-tagged $D^0 \to K^0_{\mathrm{S}}\pi^+\pi^-$ mode uses the Stripping lines `Strippingb2D0MuXKsPiPiLLCharmFromBSemiLine` and `Strippingb2D0MuXKsPiPiDDCharmFromBSemiLine` for both K^0_{S}(LL) and K^0_{S}(DD) types reconstructed from two long or two downstream tracks, respectively. The Stripping lines for the double-tagged samples are `Strippingb2DstarMuXKsPiPiLLCharmFromBSemiLine` and `Strippingb2DstarMuXKsPiPiDDCharmFromBSemiLine`. The preselection criteria of the Stripping lines are chosen such that a possible bias of the Dalitz variables and D^0 decay time is minimised. The Stripping and cut-based selection are referred to as preselection. The offline selection criteria are summarised in Table 7.3 split by K^0_{S} type.

Table 7.1.: *The most relevant used Trigger Configuration Keys (TCKs) for this analysis in 2011 with their corresponding luminosity. The lower E_{T} thresholds for L0 Photon, Hadron and Electron lines are listed, as well as the lower p and p_{T} thresholds and the upper threshold for the track fit χ^2/ndf of the HLT1 lines. The luminosity is taken from [83].*

TCK	$\mathcal{L}$	L0			HLT1		
		Photon	Hadron	Electron			
	$[\,\mathrm{fb}^{-1}]$	$E_{\mathrm{T}}\,[\,\mathrm{GeV}]$	$E_{\mathrm{T}}\,[\,\mathrm{GeV}]$	$E_{\mathrm{T}}\,[\,\mathrm{GeV}]$	$p\,[\,\mathrm{GeV}]$	$p_{\mathrm{T}}\,[\,\mathrm{GeV}]$	χ^2/ndf
0x00790038	0.324	2.5	3.5	2.5	10.0	1.7	2.0
0x00760037	0.298	2.5	3.5	2.5	10.0	1.7	2.0
0x00730035	0.196	2.5	3.5	2.5	10.0	1.7	2.0
0x006d0032	0.062	2.5	3.5	2.5	10.0	1.7	2.0
0x005a0032	0.064	2.5	3.5	2.5	10.0	1.7	2.0
0x00360032	0.003	2.5	3.5	2.5	10.0	1.7	2.0
0x004a0033	0.002	2.5	2.4	2.5	10.0	1.7	2.0

Table 7.2.: *The most relevant used Trigger Configuration Keys (TCKs) for this analysis in 2012 with their corresponding luminosity. The lower E_{T} thresholds for L0 Photon, Hadron and Electron lines are listed, as well as the lower p and p_{T} thresholds and the upper threshold for the track fit χ^2/ndf of the HLT1 lines. The luminosity is taken from [83].*

TCK	$\mathcal{L}$	L0			HLT1		
		Photon	Hadron	Electron			
	$[\mathrm{fb}^{-1}]$	$E_{\mathrm{T}}\,[\mathrm{GeV}]$	$E_{\mathrm{T}}\,[\mathrm{GeV}]$	$E_{\mathrm{T}}\,[\mathrm{GeV}]$	$p\,[\mathrm{GeV}]$	$p_{\mathrm{T}}\,[\mathrm{GeV}]$	χ^2/ndf
0x00990042	0.555	2.72	3.62	2.72	3.0	1.6	2 .0
0x00a30044	0.288	2.96	3.68	2.96	3.0	1.6	2.0
0x0094003d	0.261	2.72	3.62	2.72	10.	1.7	1.5
0x0097003d	0.273	2.72	3.62	2.72	10.	1.7	1.5
0x00a10045	0.070	2.96	3.74	2.96	3.0	1.6	2.0
0x00990044	0.141	2.96	3.68	2.96	3.0	1.6	2.0
0x009f0045	0.028	2.96	3.74	2.96	3.0	1.6	2.0
0x00a10044	0.026	2.96	3.68	2.96	3.0	1.6	2.0
0x00a30046	0.030	2.86	3.74	2.86	3.0	1.7	1.5

7.2.1. K_S^0 reconstruction

K_S^0 candidates are reconstructed in the decay $K_S^0 \to \pi^+\pi^-$. The pions used in the reconstruction are required to have a momentum exceeding 2 GeV. Long pions have a $\chi^2_{\text{IP}} > 9$ whereas for pions reconstructed from downstream tracks, the criterion is loosed to $\chi^2_{\text{IP}} > 4$. In addition, the fit to the trajectory of the pion from a downstream track has to have a χ^2 between zero and ten. For pions reconstructed as long tracks, this criterion is tightened to a range between zero and five, since they have better track resolutions. Cloned trajectories are rejected for pion candidates formed from long tracks. To ensure that the two pions come from a common vertex, the χ^2 distance of closest approach (DOCA) between the pions as well as the vertex fit χ^2 have to be less than 25. The mass of such a K_S^0(LL) candidate is restricted to a window of ± 50 MeV around the reference value of (497.61 ± 0.02) MeV [11]. Due to a slightly degraded mass resolution of downstream tracks, the mass of K_S^0(DD) candidates prior to a vertex fit is restricted to a window of ± 80 MeV.

In addition, the K_S^0 daughter pions are required to have a good track fit [84] quality with $\chi^2/\text{ndf} < 4$ and for K_S^0(LL) candidates, the ghost probability of the daughter tracks has to be less than 0.5. The K_S^0 transverse momentum has to be $p_T > 250$ MeV and its momentum is required to be $p > 2$ GeV for K_S^0(LL) and $p > 3$ GeV for K_S^0(DD) candidates. The mass of the K_S^0 candidate has to lie within a window of ± 30 MeV with respect to the reference value of (497.61 ± 0.02) MeV [11]. The χ^2 distance between the K_S^0 candidate's best primary vertex (BPV) and its decay vertex has to be at least 100 due to the long lifetime of the K_S^0 meson. The best primary vertex is chosen as the primary vertex with the smallest χ^2_{IP}, which corresponds to the closest PV. To ensure a good quality of the vertex fit, the χ^2/ndf of the K_S^0 decay vertex fit is required to be less than 6. In addition, the cosine of the angle between the direction of flight of the K_S^0 from the BPV to the decay vertex and the K_S^0 momentum, the so-called direction angle (DIRA), is restricted to $\cos\theta_{\text{DIRA}} > 0.99$ requiring that the momentum and flight direction of the K_S^0 agree.

7.2.2. Bachelor pion reconstruction

The D^0 daughter or bachelor pions have a $\chi^2_{\text{IP}} > 4$. Pion candidates are reconstructed as long tracks with a track fit $\chi^2 < 5$. In addition, cloned trajectories, which share a large fraction of hits used in the track reconstruction [84], are rejected. The pions are required to have a momentum exceeding 2 GeV and a transverse momentum of at least 250 MeV, which is slightly above the threshold for which momenta can be well measured. To ensure a good quality of the pion track fit, the χ^2/ndf is restricted to $\chi^2/\text{ndf} < 4$ and the ghost-probability has to be not greater than 50%.

7.2.3. D^0 reconstruction

A K_S^0 is combined with two oppositely-charged pions to form a D^0 candidate. Prior to the vertex fit, the absolute difference between the measured mass of the combined D^0 daughters and the reference value of (1864.84 ± 0.07) MeV [11] has to be less than 100 MeV. The scalar sum over all daughter transverse momenta is required to be greater than 1.4 GeV and the transverse momentum of the combination has to exceed 2 GeV. To ensure that the D^0 daughters have a

common vertex, the maximum χ^2 DOCA evaluated between all possible combinations of two daughter particles is 20.

After the vertex fit [84], the mass window of the D^0 candidate is tightened to $\pm 80\,\text{MeV}$ around the reference value of $(1864.84 \pm 0.07)\,\text{MeV}$ [11]. The scalar sum of the transverse momenta of the four pions from the D^0 and K^0_S decays has to be greater than 1.4 MeV and for the D^0, a transverse momentum of $p_T > 2\,\text{GeV}$ is required. The χ^2/ndf of the D^0 decay vertex fit has to be less than 6 and the position along the z-axis of the D^0 candidate's decay vertex is restricted to $v_Z(K^0_S) - v_Z(D^0) > 10\,\text{mm}$ meaning that the K^0_S decay vertex has to lie ahead of the D^0 decay vertex along the z-axis. The latter requirement ensures that the K^0_S daughters are reconstructible in the tracking stations.

7.2.4. D^* reconstruction

A D^* candidate is reconstructed in the decay $D^{*+} \to D^0\pi^+$. The soft pion is reconstructed as a long track with a track fit χ^2 between zero and five and a transverse momentum of $p_T > 180\,\text{MeV}$. The low momentum threshold on the soft pions is a result from the small difference in mass between the D^* and D^0 candidates. For the soft pion, cloned trajectories are rejected. The delta mass of the combination, $\delta m \equiv m(D^*) - m(D^0)$, is required to be within $-5 < \delta m < 175\,\text{MeV}$. This criterion reduces backgrounds from combinations of D^0 candidates with soft pions, which are not associated with the signal tracks, because real D^* candidates exhibit a peak in δm around 145 MeV. The χ^2/ndf of the D^* meson decay vertex fit has to be $\chi^2/\text{ndf} < 8$ and the delta mass of the D^* meson is restricted to $0 < \delta m < 170\,\text{MeV}$.

7.2.5. Muon reconstruction

Muon candidates are reconstructed from long tracks, which also have hits in the muon stations and the flag ISMUON is true. The ISMUON flag [65] is based on the number of muon stations where a hit is found within a restricted area around the track extrapolation. Depending on the muon candidate momentum, the muon candidate is expected to reach a certain number of muon stations. The ISMUON flag is true if a candidate with $3 < p < 6\,\text{GeV}$ has hits in muon stations M2 and M3, and with $6 < p < 10\,\text{GeV}$, hits in M2, M3 and either M4 or M5 are required. Candidates with $p > 10\,\text{GeV}$ have to have hits in the four stations M2, M3, M4 and M5.

The χ^2 of the track fit is restricted to the range between zero and five and clone candidates are rejected. The momentum of the muon has to exceed 3 GeV, since the B meson is heavy and will have high-momentum daughters, and its transverse momentum $p_T > 800\,\text{MeV}$. The ghost probability of the track has to be less than 0.5 and the mass hypothesis has to be consistent with a muon. The track fit is required to be of good quality, $\chi^2/\text{ndf} < 4$ and χ^2_{IP} is required to be $\chi^2_{IP} \geq 4$.

7.2.6. B reconstruction

A D^0 or a D^* meson is combined with a muon candidate to form a B candidate. The mass of the combined B daughters has to be less than 6.2 GeV. After the vertex fit, the mass of the B candidate is restricted to $2.5 < m_B < 6.0\,\text{GeV}$, which encloses the reference value of the B

mass [11]. To ensure that flight direction and reconstructed momentum of the B candidate are in excellent agreement, $\cos\theta_{\mathrm{DIRA}} > 0.999$ is required. In addition, the fit of the B candidate's decay vertex has to have $\chi^2/\mathrm{ndf} < 6$.

7.2.7. Additional selection requirements

The $D^0 \to K^0_S\pi^+\pi^-$ decay is refitted with DecayTreeFitter (DTF) [74] where the masses of candidates are constrained to the world average in Ref. [11]. Through the refit with a mass constraint, the momentum resolution is improved. This analysis uses two instances of DTF with different mass constraints. In the first instance, the $D^0 \to K^0_S\pi^+\pi^-$ decay is refitted constraining the mass of the K^0_S candidate to 497.614 MeV [11] whereas in the second instance, the mass of the K^0_S candidate is constrained as well as the mass of the D^0 candidate. The latter is constrained to 1864.86 MeV [11]. The momenta entering the calculation of the Dalitz variables are calculated using the D^0 daughter momenta after a refit with DTF where both K^0_S and D^0 mass were constrained. This restricts the Dalitz variables of all candidates to the phase space consistent with energy and momentum conservation. The D^0 mass is computed with the momenta where the refit was undertaken with a K^0_S mass constraint, since this improves the D^0 mass resolution. Decay times are calculated without the application of the DTF because the DTF forces decay times to be greater than zero. For the double-tagged sample, the D^0 decay time is evaluated with respect to the B vertex instead of the D^* vertex.

After the $D^0 \to K^0_S\pi^+\pi^-$ decay was refitted with DTF, the fit has to have converged for both instances, which is equivalent to ensure that the number of degrees of freedom is greater than zero. To ensure a good quality of the DTF fit, the decay tree refit with a K^0_S mass constraint has to have $\chi^2 < 25$.

A signal mass window of $1805 \leq m(D^0) \leq 1925$ MeV is chosen. The broad range allows the study of background contributions in the lowest and highest mass regions where no signal is expected. To suppress $D^{*+} \to D^0(\to K^0_S\pi^+\pi^-)\pi^+$ candidates, which have been produced directly in the pp collision (prompt candidates), the vertex of the B candidate has to be at least 10σ away from the PV. This is achieved by requiring the flight distance χ^2 of the B candidate with respect to the PV to be $\chi^2_{\mathrm{FD}} > 100$. For $D^0 \to K^0_S(\mathrm{LL})\pi^+\pi^-$ decays, the flight distance χ^2 between the K^0_S candidate vertex and the PV is restricted to $\chi^2_{\mathrm{FD}} > 1000$. Background from muons not associated with the signal but coming from another decay in the event and particles misidentified as muons is reduced by a particle identification requirement, which ensures that the muon candidate is most likely a real muon, ProbNNmu ≥ 0.6. The probability of a muon to be reconstructed as a K^0_S or bachelor pion is reduced by requiring that the pions have a false ISMUON flag. The decay time resolution at LHCb causes the D^0 decay time to extend into a negative decay time range. Nevertheless, the D^0 decay time range below -0.001 ns is populated soley by background candidates. Thus, requiring $t(D^0) > -0.001$ ns leads to a significant background reduction.

Table 7.3.: *Overview of the preselection requirements split by K^0_S type.*

Variable	K^0_S(LL) line cut	K^0_S(DD) line cut
K^0_S daughter $\pi^\pm$ track χ^2	$[0, 5]$	$[0, 10]$
K^0_S daughter $\pi^\pm$ χ^2_{IP}	> 9	> 4
K^0_S daughter $\pi^\pm$ p	$> 2\,\text{GeV}$	
K^0_S daughter $\pi^\pm$ track χ^2/ndf	< 4	
K^0_S daughter $\pi^\pm$ track ghost probability	< 0.5	$\times$
K^0_S daughter $\pi^\pm$ ISMUON	false	
K^0_S daughter $\pi^\pm$ χ^2 DOCA	< 25	
K^0_S p	$> 2\,\text{GeV}$	$> 3\,\text{GeV}$
K^0_S p_T	$> 250\,\text{MeV}$	
K^0_S m before vertex fit	$< 50\,\text{MeV}$	$< 80\,\text{MeV}$
K^0_S m after vertex fit	$< 30\,\text{MeV}$	
K^0_S χ^2 distance between BPV and decay vertex	> 100	
K^0_S vertex χ^2/ndf	< 6	
K^0_S vertex χ^2	< 25	
K^0_S $\cos\theta_\text{DIRA}$	> 0.99	
K^0_S χ^2_{FD}	> 1000	$\times$
D^0 charged daughter track χ^2	$[0, 5]$	
D^0 charged daughter track χ^2/ndf	< 4	
D^0 charged daughter p	$> 2\,\text{GeV}$	
D^0 charged daughter p_T	$> 250\,\text{MeV}$	
D^0 charged daughter track ghost probability	< 0.5	
D^0 charged daughter χ^2_{IP}	> 4	
D^0 charged daughter ISMUON	false	
D^0 mass before vertex fit	$< 100\,\text{MeV}$	
D^0 p_T before vertex fit	$> 2\,\text{GeV}$	
D^0 scalar sum of daughter p_T	$> 1.4\,\text{GeV}$	
D^0 χ^2 DOCA before vertex fit	< 20	
D^0 m after vertex fit	$< 80\,\text{MeV}$	
D^0 vertex χ^2/ndf	< 6	
D^0 p_T	$> 2\,\text{GeV}$	
D^0 scalar sum of all four daughter $\pi^\pm$ p_T	$> 1.4\,\text{GeV}$	
D^0 $v_Z(K^0_S) - v_Z(D^0)$	$> 10\,\text{mm}$	
D^0 t	$> -0.001\,\text{ns}$	
D^0 m	$[1805\,\text{MeV}, 1925\,\text{MeV}]$	
D^* charged daughter p_T	$> 180\,\text{MeV}$	
D^* charged daughter track χ^2	$[0, 5]$	
D^* δm before vertex fit	$(-5\,\text{MeV}, 175\,\text{MeV})$	
D^0 vertex χ^2/ndf	< 8	
D^* δm	$(0\,\text{MeV}, 170\,\text{MeV})$	
$\mu^\pm$ p_T	$> 800\,\text{MeV}$	
$\mu^\pm$ p	$> 3\,\text{GeV}$	

$\mu^\pm$ track ghost probability	< 0.5
$\mu^\pm$ track χ^2/ndf	< 4
$\mu^\pm$ track χ^2	$[0, 5]$
$\mu^\pm$ χ^2_{IP}	> 4
$\mu^\pm$ PIDmu	> -0
$\mu^\pm$ ProbNNmu	≥ 0.6
$\mu^\pm$ ISMUON	true
B mass before vertex fit	$< 6.2\,\text{GeV}$
B mass	$(2.5\,\text{GeV}, 6.0\,\text{GeV})$
B vertex χ^2/ndf	< 6
B $\cos\theta_{\text{DIRA}}$	> 0.999
B χ^2_{FD}	> 100
DTF χ^2 ($m(K^0_{\text{S}})$ constraint)	< 25
DTF ndf ($m(K^0_{\text{S}})$ constraint)	> 0
DTF ndf ($m(D^0)$ and $m(K^0_{\text{S}})$ constraints)	> 0

8. Boosted Decision Tree selection

After the candidates have passed the trigger selection and preselection requirements detailed in Chapt. 7, the remaining background component in the dataset is further reduced by training a Boosted Decision Tree (BDT) whose output allows the distinction of signal- and background-like candidates. The BDT relies on distributions of observables, and their correlations, that differ significantly for signal $D^0 \to K^0_S \pi^+ \pi^-$ candidates and background processes. The BDT response is a single observable in the range $[-1, 1]$ and indicates the probability of a candidate to belong to either class. The input distributions used for the training of the BDT need to be separated into signal and background components. This can be achieved by using Monte Carlo simulations of signal and background processes. A common approach in data is to estimate the background distributions from regions in data where no signal contribution is present (sidebands) and to estimate the signal distributions by subtracting the background contributions. Instead of using sidebands, it is possible to exploit the whole range of the separation variable by using the sPlot formalism [73] that is taken in this analysis. The sPlot formalism relies on the knowledge of the signal and background shapes in a discriminating variable to compute so-called sWeights. The analysis makes use of the multivariate analysis software package Toolkit for Multivariate Analysis (TMVA) [85], which allows the training of a BDT with sWeights.

8.1. sPlot formalism

Background subtraction relying on data can be either achieved by estimating the background contribution in sidebands where the signal does not contribute or by using the sPlot formalism [73]. The latter is a more sophisticated sideband subtraction, which relies on the maximisation of the extended log-likelihood

$$L = \sum_{e=1}^{N} \ln \left\{ \sum_{i=1}^{N_s} N_i f_i(y_e) \right\} - \sum_{i=1}^{N_s} N_i, \tag{8.1}$$

with the total number of events in the dataset N, the number of species of events in the given dataset N_s, the average number of events expected for the i^{th} species N_i, and $f_i(y_e)$ the value of the probability density function (PDF) for the i^{th} species f_i at a set of discriminating variables y_e for event e. For most use cases including this analysis, the species are signal and background categories. For $D^0 \to K^0_S \pi^+ \pi^-$ decays, the mass of the D^0 candidate, $m(D^0)$, is chosen as a discriminating variable. A fit to $m(D^0)$ is performed with a certain signal and background PDF depending on the shape of the distribution. After maximisation of the extended log-likelihood L, an sWeight is computed for each event and both signal and background categories as

$$ {}_s\mathcal{P}_n(y_e) = \frac{\sum_{j=1}^{N_s} V_{nj} f_j(y_e)}{\sum_{k=1}^{N_s} N_k f_k(y_e)} \quad \text{with} \quad V_{nj}^{-1} = \frac{-\partial^2 L}{\partial N_n \partial N_j}, \tag{8.2} $$

where the weight can take both positive and negative values. By applying the signal and background sWeights to a distribution containing signal as well as background candidates, the resulting distributions are split into the two categories. This background subtraction technique is only valid if the discriminating variable, here $m(D^0)$, and the variable on which the sWeights are applied, are uncorrelated.

The input distributions are obtained on different subsamples, split by data-taking period (2011, 2012) and K^0_S reconstruction type (LL, DD). These splits are performed as the event distributions may be expected to vary between these samples, which are then further split by events in samples with even and odd event numbers. This split is performed to ensure a robust BDT selection. For each of these eight subsamples, sWeights are extracted and then used to train the BDT as explained in Chapt. 8.2.
The sWeights are extracted from the $m(D^0)$ distribution by performing an extended maximum likelihood fit. For the $D^0 \to K^0_S(\mathrm{LL})\pi^+\pi^-$ sample, the signal is modelled as a single Gaussian function, $G(m(D^0); \mu, \sigma)$, and a Crystal Ball function, $f_{CB}(m(D^0); \mu, \sigma, \alpha, n)$. The background is described by a Chebychev polynomial of first kind and first order,
$P_1(m(D^0); a) = am(D^0)/[\,\mathrm{MeV}] + 1$.

The PDF for the mass fit to $D^0 \to K^0_S(\mathrm{LL})\pi^+\pi^-$ candidates $F_{\mathrm{LL}}(m(D^0); \mu, \sigma, c, f, a, \alpha, n)$ is given by

$$ \begin{aligned} F_{\mathrm{LL}}(m_{D^0}; \mu, \sigma, c, f, a, \alpha, n) = & N \times \big\{ n_{sig} \left[c f_{CB}(m(D^0); \mu, f, \sigma, \alpha, n) \right. \\ & \left. + (1-c) G(m(D^0); \mu, \sigma) \right] \\ & + n_{bkg} P_1(m(D^0); a) \big\}, \end{aligned} \tag{8.3} $$

where the scaling factor f is required to be $f \geq 1$ and N denotes a normalisation factor. The number of signal and background candidates are denoted by n_{sig} and n_{bkg}, respectively. The single Gaussian function is

$$ G(m(D^0); \mu, \sigma) = \frac{1}{\sqrt{2\pi} f \sigma} e^{-\left(\frac{m(D^0)-\mu}{\sqrt{2} f \sigma}\right)^2}, \tag{8.4} $$

and the Crystal Ball function $f_{CB}(m(D^0); \mu, \sigma, \alpha, n)$ is defined as [86]

$$f_{CB}(m(D^0);\mu,f,\sigma,\alpha,n) = N_{CB}\times\begin{cases} e^{-\left(\frac{\mu-m(D^0)}{\sqrt{2}f\sigma}\right)^2} & \text{if } m(D^0)>\mu-\alpha f\sigma \\ \left(\frac{n}{\alpha}\right)^n e^{-\frac{\alpha^2}{2}} & \\ \times\left(\frac{n}{\alpha}-\alpha-\frac{(\mu-m(D^0))}{f\sigma}\right)^{-n} & \text{if } m(D^0)<\mu-\alpha f\sigma. \end{cases}$$

The normalisation factor N_{CB} of the Crystal Ball function is given by

$$N_{CB}^{-1} = \sigma\left(\frac{n}{\alpha}\frac{1}{n-1}e^{-\frac{1}{2}\alpha^2}+\sqrt{\frac{\pi}{2}}\left\{1+\mathrm{erf}\left(\frac{\alpha}{\sqrt{2}}\right)\right\}\right). \tag{8.5}$$

The parameters α and n of the Crystal Ball function are fixed to facilitate the convergence of the mass fit and have been determined from studies of the fit parameters. For $D^0\to K^0_S(\mathrm{LL})\pi^+\pi^-$, the parameters are set to $\alpha=2$ and $n=3$ and to $\alpha=3$ and $n=3$ for $D^0\to K^0_S(\mathrm{DD})\pi^+\pi^-$ samples. The background description differs for the $D^0\to K^0_S(\mathrm{DD})\pi^+\pi^-$ sample. Instead of a Chebychev polynomial of first kind and first order, a Chebychev polynomial of first kind and second order, $P_2(m(D^0);a_1,a_2)$

$$P_2(m(D^0);a_1,a_2) = a_2\left(2m(D^0)^2/[\,\mathrm{MeV}^2]-1\right)a_1 m(D^0)/[\,\mathrm{MeV}]+1, \tag{8.6}$$

is used. The fit function $F_{\mathrm{DD}}(m(D^0);\mu,\sigma,c,f,a,\alpha,n)$ is chosen as

$$\begin{aligned} F_{\mathrm{DD}}(m_{D^0};\mu,\sigma,c,f,a,\alpha,n) =& N\times\left\{n_{sig}\left[cf_{CB}(m(D^0);\mu,\sigma,\alpha,n)\right.\right. \\ &+(1-c)G(m(D^0);\mu,\sigma)\left.\right] \\ &\left.+n_{bkg}P_2(m(D^0);a_1,a_2)\right\}. \end{aligned} \tag{8.7}$$

The quality of the fits is assessed by calculating the reduced χ^2 value $\chi^2/ndof$ and the pull P_i between each data point d_i and the value of the fit model m_i at this point as $P_i=(d_i-m_i)/\sigma_i^{\mathrm{data}}$, with the data uncertainty on each point σ_i^{data}.

8.1.1. sWeight extraction for single-tagged decays

The results of the mass fits are summarised in Tables 8.1, 8.2, 8.3 and 8.4. The corresponding fits are illustrated in Figs. 8.1 and 8.2. The overall fit quality is good and apart from the width σ and the fraction of the Crystal Ball contribution to the signal, c, of the fits to the $K^0_S(\mathrm{LL})$ samples, the fit parameters are in agreement. To test if the signal and background distributions between even and odd samples agree, the parameters of the PDF apart from the number of signal and background candidates are fixed to the ones obtained from the odd sample and then applied to the even sample and vice versa. The χ^2 values of this and the nominal fit are given in Table 8.5 for comparison. These crosscheck fits show a similar description of the $m(D^0)$ distribution, and hence the observed differences in the fit parameters c and σ are irrelevant.

Table 8.1.: *Results of the $m(D^0)$ fit for the 2011 $B^- \to D^0(\to K^0_S(\mathrm{LL})\pi^+\pi^-)\mu^-\overline{\nu}_\mu$ datasets split by even and odd event numbers.*

Fit parameter	K^0_S (LL)	
	even	odd
$\mu\,[\mathrm{MeV}]$	1864.30 ± 0.05	1864.33 ± 0.05
$\sigma\,[\mathrm{MeV}]$	6.1 ± 0.2	6.7 ± 0.3
c	0.54 ± 0.07	0.72 ± 0.09
f	1.65 ± 0.04	1.67 ± 0.12
a	-0.021 ± 0.009	-0.037 ± 0.010
n_{sig}	44084 ± 250	44425 ± 252
n_{bkg}	38978 ± 240	38761 ± 240
$\chi^2/ndof$, $ndof = 93$	0.977	1.312

Table 8.2.: *Results of the $m(D^0)$ fit for the 2012 $B^- \to D^0(\to K^0_S(\mathrm{LL})\pi^+\pi^-)\mu^-\overline{\nu}_\mu$ datasets split by even and odd event numbers.*

Fit parameter	K^0_S (LL)	
	even	odd
$\mu\,[\mathrm{MeV}]$	1864.28 ± 0.03	1864.35 ± 0.03
$\sigma\,[\mathrm{MeV}]$	6.0 ± 0.2	6.5 ± 0.2
c	0.49 ± 0.07	0.67 ± 0.06
f	1.60 ± 0.03	1.71 ± 0.06
a	-0.026 ± 0.006	-0.018 ± 0.006
n_{sig}	95805 ± 377	96214 ± 381
n_{bkg}	103486 ± 387	103074 ± 390
$\chi^2/ndof$, $ndof = 93$	1.100	0.958

Table 8.3.: *Results of the $m(D^0)$ fit for the 2011 $B^- \to D^0(\to K^0_S(\mathrm{DD})\pi^+\pi^-)\mu^-\overline{\nu}_\mu$ datasets split by even and odd event numbers.*

Fit parameter	K^0_S (DD)	
	even	odd
$\mu\,[\,\mathrm{MeV}]$	1864.41 ± 0.04	1864.33 ± 0.04
$\sigma\,[\,\mathrm{MeV}]$	6.1 ± 0.3	6.3 ± 0.1
c	0.55 ± 0.10	0.59 ± 0.02
f	1.65 ± 0.07	1.52 ± 0.05
a_1	-0.005 ± 0.004	-0.002 ± 0.007
a_2	-0.022 ± 0.008	-0.038 ± 0.007
n_{sig}	88359 ± 407	87521 ± 403
n_{bkg}	196025 ± 523	196543 ± 521
$\chi^2/ndof$, $ndof = 92$	1.063	1.171

Table 8.4.: *Results of the $m(D^0)$ fit for the 2012 $B^- \to D^0(\to K^0_S(\mathrm{DD})\pi^+\pi^-)\mu^-\overline{\nu}_\mu$ datasets split by even and odd event numbers.*

Fit parameter	K^0_S (DD)	
	even	odd
$\mu\,[\,\mathrm{MeV}]$	1864.29 ± 0.03	1864.33 ± 0.03
$\sigma\,[\,\mathrm{MeV}]$	6.00 ± 0.2	6.2 ± 0.1
c	0.51 ± 0.07	0.58 ± 0.05
f	1.63 ± 0.04	1.64 ± 0.05
a_1	0.006 ± 0.003	0.010 ± 0.002
a_2	-0.031 ± 0.005	-0.029 ± 0.005
n_{sig}	212405 ± 648	213016 ± 649
n_{bkg}	543695 ± 867	542398 ± 866
$\chi^2/ndof$, $ndof = 92$	0.989	1.133

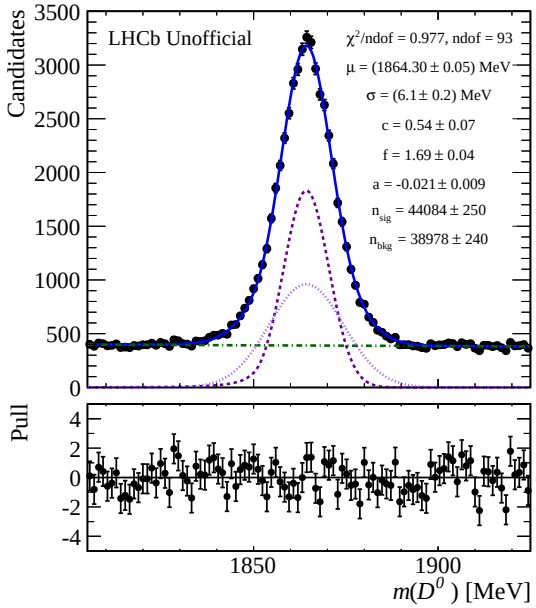

(a) *Even event numbers of the* $D^0 \to K^0_S(\mathrm{LL})\pi^+\pi^-$ *dataset*

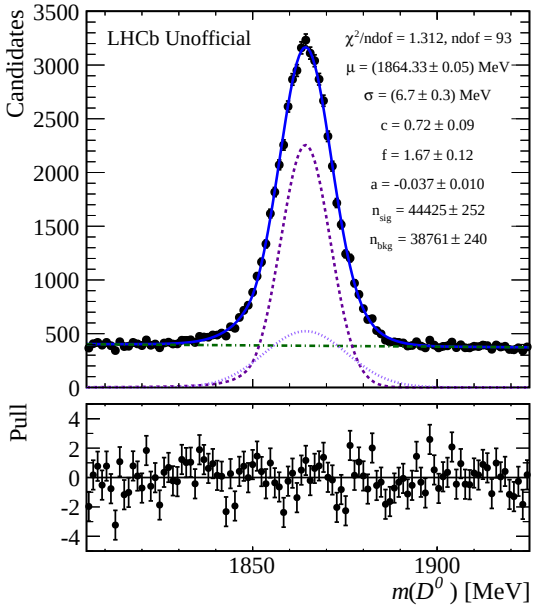

(b) *Odd event numbers of the* $D^0 \to K^0_S(\mathrm{LL})\pi^+\pi^-$ *dataset*

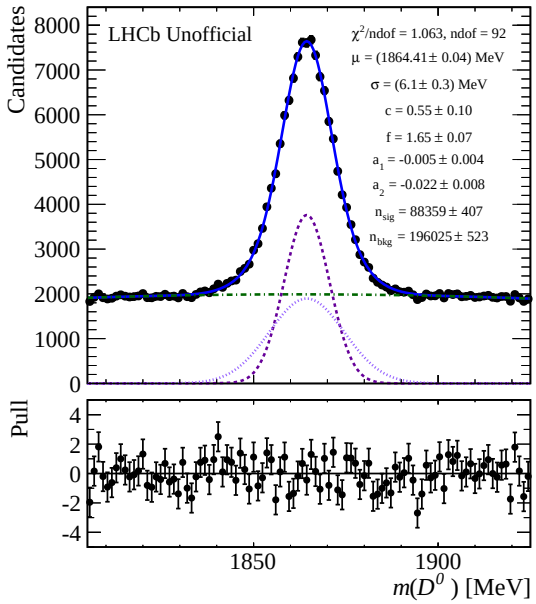

(c) *Even event numbers of the* $D^0 \to K^0_S(\mathrm{DD})\pi^+\pi^-$ *dataset*

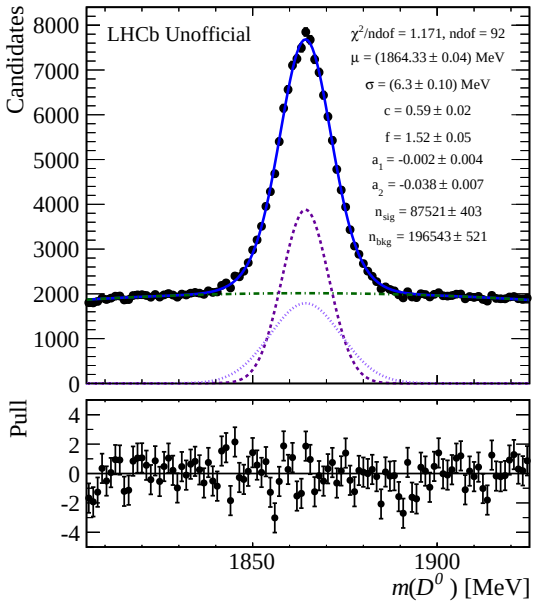

(d) *Odd event numbers of the* $D^0 \to K^0_S(\mathrm{DD})\pi^+\pi^-$ *dataset*

Figure 8.1.: *$m(D^0)$ distribution of the 2011 $B^- \to D^0(\to K^0_S\pi^+\pi^-)\mu^-\overline{\nu}_\mu$ datasets after the trigger selection and preselection (see Chapt. 7) split by K^0_S type and even and odd event numbers. The figure depicts the fit (solid blue line) to the data (black points) and the fit components. The signal consists of a Crystal Ball (dotted lavender line) and a Gaussian function (dashed magenta line). The background is modelled by a Chebychev polynomial (green dotted-dashed line).*

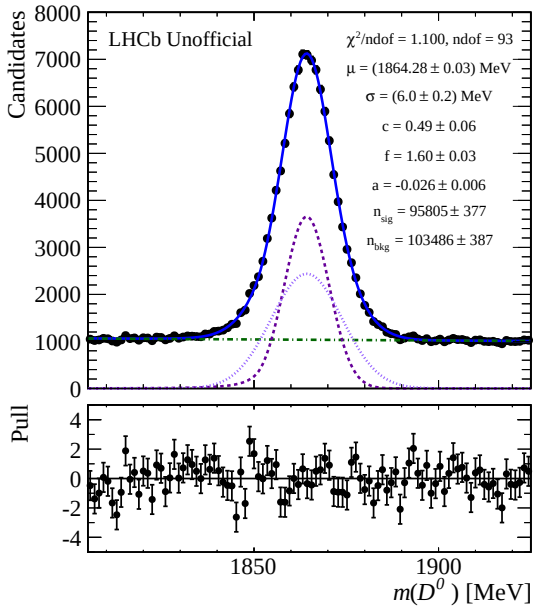

(a) *Even event numbers of the* $D^0 \to K^0_S(\mathrm{LL})\pi^+\pi^-$ *dataset*

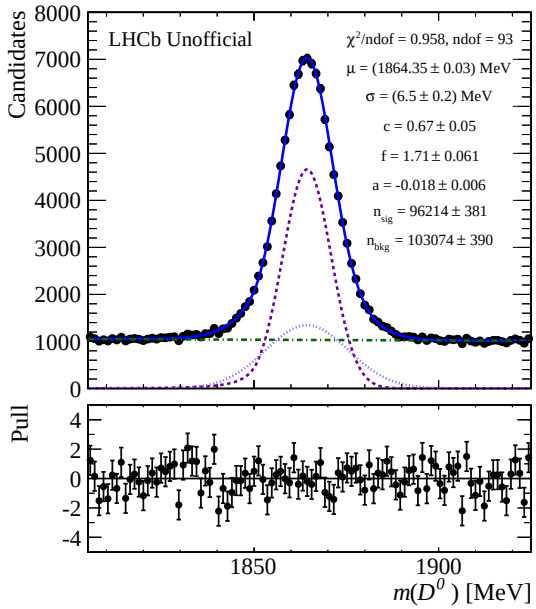

(b) *Odd event numbers of the* $D^0 \to K^0_S(\mathrm{LL})\pi^+\pi^-$ *dataset*

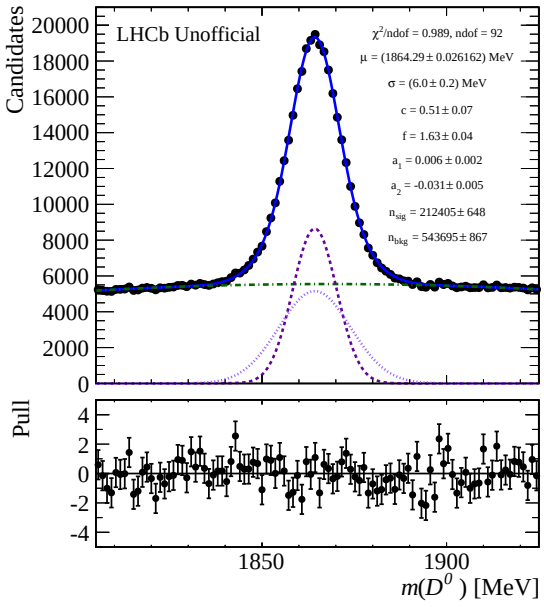

(c) *Even event numbers of the* $D^0 \to K^0_S(\mathrm{DD})\pi^+\pi^-$ *dataset*

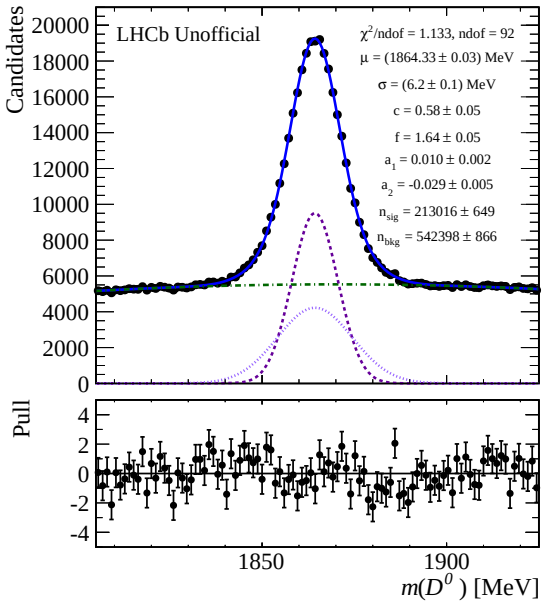

(d) *Odd event numbers of the* $D^0 \to K^0_S(\mathrm{DD})\pi^+\pi^-$ *dataset*

Figure 8.2.: *$m(D^0)$ distribution of the 2012 $B^- \to D^0(\to K^0_S\pi^+\pi^-)\mu^-\overline{\nu}_\mu$ datasets after the trigger selection and preselection (see Chapt. 7) split by K^0_S type and even and odd event numbers. The figure depicts the fit (solid blue line) to the data (black points) and the fit components. The signal consists of a Crystal Ball (dotted lavender line) and a Gaussian function (dashed magenta line). The background is modelled by a Chebychev polynomial (green dotted-dashed line).*

Table 8.5.: *Comparison of the χ^2 values of the nominal and crosscheck sWeight fit to $m(D^0)$ for the $B^- \to D^0(\to K^0_S\pi^+\pi^-)\mu^-\overline{\nu}_\mu$ datasets. In the crosscheck fit, the parameters of the even (odd) sample, apart from the number of signal and background candidates, are fixed to the ones obtained from the odd (even) sample*

Dataset	$\chi^2/ndof$	
	Nominal	Crosscheck
2011 K^0_S(LL) even	0.977 ($ndof = 93$)	1.060 ($ndof = 98$)
2011 K^0_S(LL) odd	1.312 ($ndof = 93$)	1.354 ($ndof = 98$)
2011 K^0_S(DD) even	1.063 ($ndof = 92$)	1.200 ($ndof = 98$)
2011 K^0_S(DD) odd	1.171 ($ndof = 92$)	1.237 ($ndof = 98$)
2012 K^0_S(LL) even	1.100 ($ndof = 93$)	1.225 ($ndof = 98$)
2012 K^0_S(LL) odd	0.958 ($ndof = 93$)	1.127 ($ndof = 98$)
2012 K^0_S(DD) even	0.989 ($ndof = 92$)	1.010 ($ndof = 98$)
2012 K^0_S(DD) odd	1.133 ($ndof = 92$)	1.137 ($ndof = 98$)

8.1.2. sWeight extraction for double-tagged decays

The results of the mass fits are summarised in Tables 8.6, 8.7, 8.8, and 8.9. The corresponding fits are illustrated in Figs. 8.3 and 8.4. The quality of the fits is good but discrepancies between the fit parameters between even and odd samples is larger than for the single-tagged sample. The same crosscheck as for the single-tagged datasets is performed. The comparison of the χ^2 values is given in Table 8.10 and as the crosscheck fits provide a similarly good description of the D^0 mass, the observed differences between the fit parameters are considered to be irrelevant.

Table 8.6.: *Results of the $m(D^0)$ fit for the 2011 $\overline{B}^0 \to D^{*+}(\to D^0(\to K^0_S(\mathrm{LL})\pi^+\pi^-)\pi^+)\mu^-\overline{\nu}_\mu$ datasets split by even and odd event numbers.*

Fit parameter	K^0_S (LL)	
	even	odd
μ [MeV]	1864.22 ± 0.11	1864.40 ± 0.10
σ [MeV]	6.0 ± 0.5	5.4 ± 0.6
c	0.50 ± 0.14	0.38 ± 0.14
f	1.70 ± 0.09	1.72 ± 0.12
a	-0.058 ± 0.023	-0.035 ± 0.022
n_{sig}	8875 ± 110	8755 ± 109
n_{bkg}	6377 ± 98	6598 ± 99
$\chi^2/ndof$, $ndof = 93$	1.095	1.014

Table 8.7.: *Results of the $m(D^0)$ fit for the 2012 $\overline{B}^0 \to D^{*+}(\to D^0(\to K^0_S(\mathrm{LL})\pi^+\pi^-)\pi^+)\mu^-\overline{\nu}_\mu$ datasets split by even and odd event numbers.*

Fit parameter	K^0_S (LL)	
	even	odd
$\mu\,[\mathrm{MeV}]$	1864.28 ± 0.07	1864.46 ± 0.08
$\sigma\,[\mathrm{MeV}]$	6.2 ± 0.6	7.4 ± 0.2
c	0.50 ± 0.19	0.89 ± 0.04
f	1.57 ± 0.07	2.09 ± 0.42
a	-0.019 ± 0.014	-0.019 ± 0.014
n_{sig}	19333 ± 167	19271 ± 168
n_{bkg}	17879 ± 162	17371 ± 162
$\chi^2/ndof$, $ndof = 93$	1.171	0.900

Table 8.8.: *Results of the $m(D^0)$ fit for the 2011 $\overline{B}^0 \to D^{*+}(\to D^0(\to K^0_S(\mathrm{DD})\pi^+\pi^-)\pi^+)\mu^-\overline{\nu}_\mu$ datasets split by even and odd event numbers.*

Fit parameter	K^0_S (DD)	
	even	odd
$\mu\,[\mathrm{MeV}]$	1864.40 ± 0.08	1864.38 ± 0.08
$\sigma\,[\mathrm{MeV}]$	6.3 ± 0.4	6.5 ± 0.7
c	0.59 ± 0.13	0.58 ± 0.27
f	1.72 ± 0.14	1.58 ± 0.19
a_1	-0.021 ± 0.012	-0.015 ± 0.011
a_2	-0.019 ± 0.024	-0.029 ± 0.026
n_{sig}	18108 ± 169	17720 ± 168
n_{bkg}	23514 ± 184	23961 ± 186
$\chi^2/ndof$, $ndof = 92$	0.913	1.251

Table 8.9.: *Results of the $m(D^0)$ fit for the 2012 $\overline{B}^0 \to D^{*+}(\to D^0(\to K^0_S(\mathrm{DD})\pi^+\pi^-)\pi^+)\mu^-\overline{\nu}_\mu$ datasets split by even and odd event numbers.*

Fit parameter	K^0_S (DD)	
	even	odd
$\mu\,[\mathrm{MeV}]$	1864.21 ± 0.05	1864.35 ± 0.05
$\sigma\,[\mathrm{MeV}]$	6.6 ± 0.3	6.3 ± 0.4
c	0.69 ± 0.11	0.57 ± 0.13
f	1.71 ± 0.19	1.63 ± 0.10
a_1	-0.017 ± 0.007	-0.022 ± 0.007
a_2	-0.037 ± 0.016	-0.029 ± 0.014
n_{sig}	42740 ± 267	43250 ± 267
n_{bkg}	66230 ± 308	66391 ± 308
$\chi^2/ndof$, $ndof = 92$	1.371	1.089

Table 8.10.: *Comparison of the χ^2 values of the nominal and crosscheck sWeight fit to $m(D^0)$ for the $\overline{B}^0 \to D^{*+}(\to D^0(\to K^0_S\pi^+\pi^-)\pi^+)\mu^-\overline{\nu}_\mu$ datasets. In the crosscheck fit, the parameters of the even (odd) sample, apart from the number of signal and background candidates, are fixed to the ones obtained from the odd (even) sample*

Dataset	$\chi^2/ndof$	
	Nominal	Crosscheck
2011 K^0_S(LL) even	$1.095\,(ndof = 93)$	$1.125\,(ndof = 98)$
2011 K^0_S(LL) odd	$1.014\,(ndof = 93)$	$1.076\,(ndof = 98)$
2011 K^0_S(DD) even	$0.913\,(ndof = 92)$	$0.918\,(ndof = 98)$
2011 K^0_S(DD) odd	$1.251\,(ndof = 92)$	$1.232\,(ndof = 98)$
2012 K^0_S(LL) even	$1.171\,(ndof = 93)$	$1.239\,(ndof = 98)$
2012 K^0_S(LL) odd	$0.900\,(ndof = 93)$	$1.094\,(ndof = 98)$
2012 K^0_S(DD) even	$1.371\,(ndof = 92)$	$1.390\,(ndof = 98)$
2012 K^0_S(DD) odd	$1.089\,(ndof = 92)$	$1.110\,(ndof = 98)$

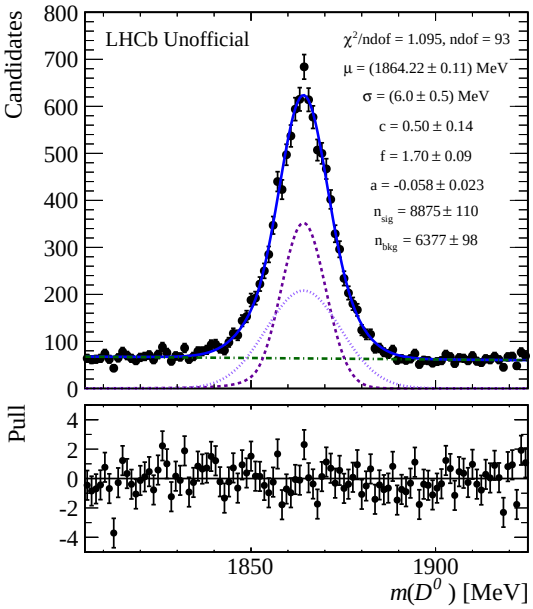

(a) *Even event numbers of the* $D^0 \to K^0_S(\mathrm{LL})\pi^+\pi^-$ *dataset*

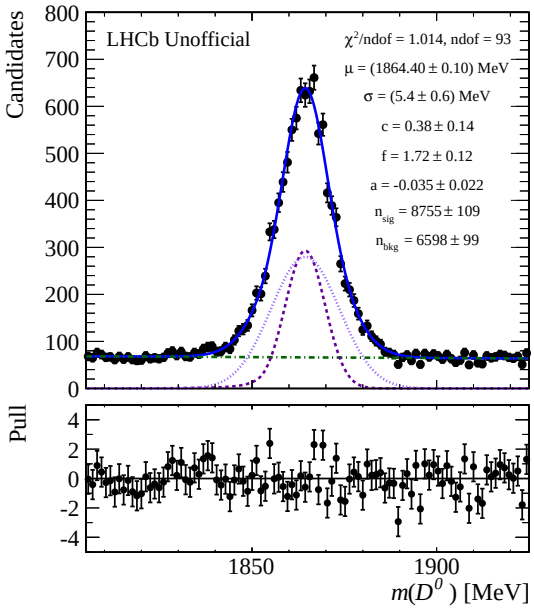

(b) *Odd event numbers of the* $D^0 \to K^0_S(\mathrm{LL})\pi^+\pi^-$ *dataset*

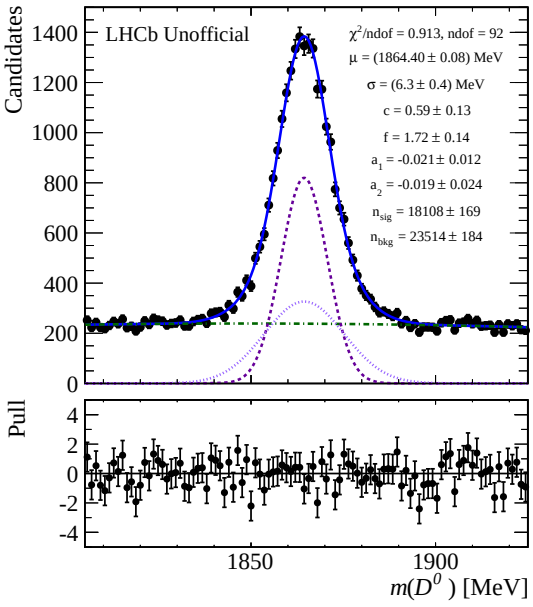

(c) *Even event numbers of the* $D^0 \to K^0_S(\mathrm{DD})\pi^+\pi^-$ *dataset*

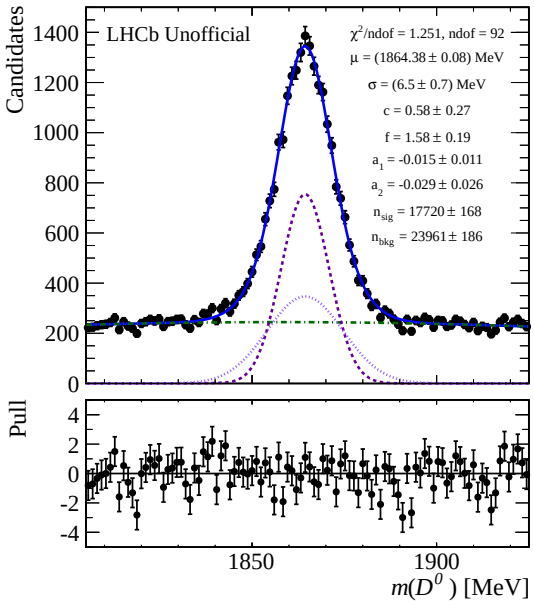

(d) *Odd event numbers of the* $D^0 \to K^0_S(\mathrm{DD})\pi^+\pi^-$ *dataset*

Figure 8.3.: *$m(D^0)$ distribution of the 2011 $\overline{B}^0 \to D^{*+}(\to D^0(\to K^0_S\pi^+\pi^-)\pi^+)\mu^-\overline{\nu}_\mu$ datasets after the trigger selection and preselection (see Chapt. 7) split by K^0_S type and even and odd event numbers. The figure depicts the fit (solid blue line) to the data (black points) and the fit components. The signal consists of a Crystal Ball (dotted lavender line) and a Gaussian function (dashed magenta line). The background is modelled by a Chebychev polynomial (green dotted-dashed line).*

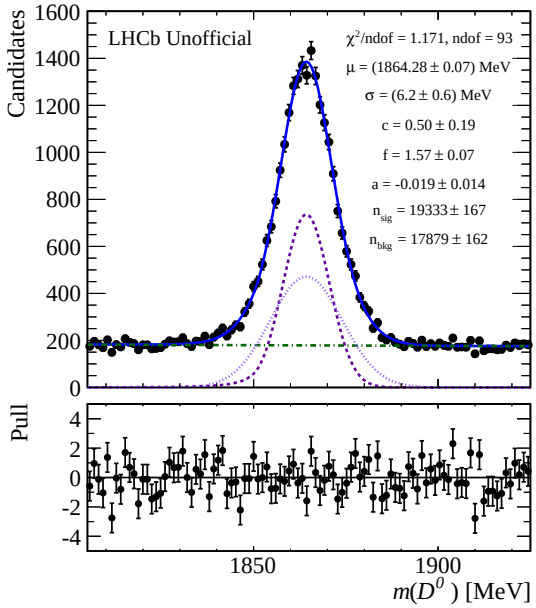

(a) *Even event numbers of the* $D^0 \to K^0_S(\mathrm{LL})\pi^+\pi^-$ *dataset*

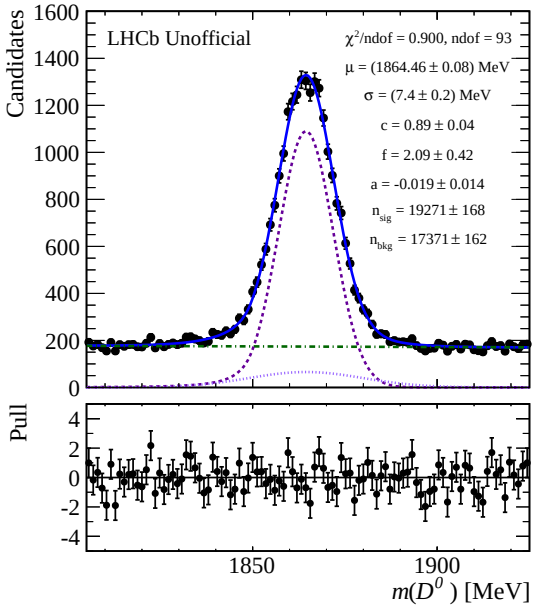

(b) *Odd event numbers of the* $D^0 \to K^0_S(\mathrm{LL})\pi^+\pi^-$ *dataset*

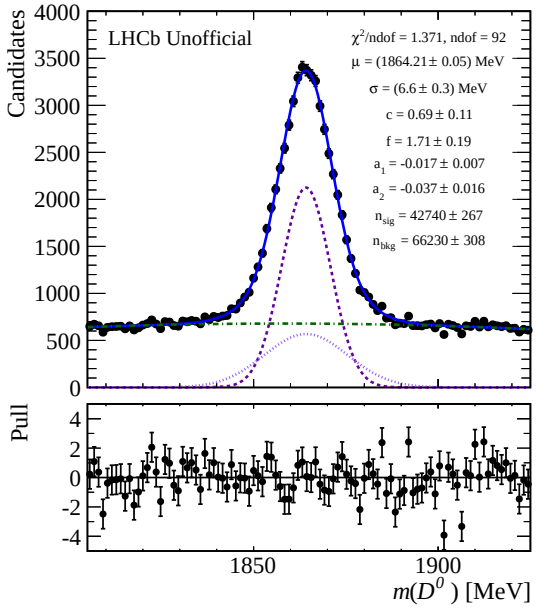

(c) *Even event numbers of the* $D^0 \to K^0_S(\mathrm{DD})\pi^+\pi^-$ *dataset*

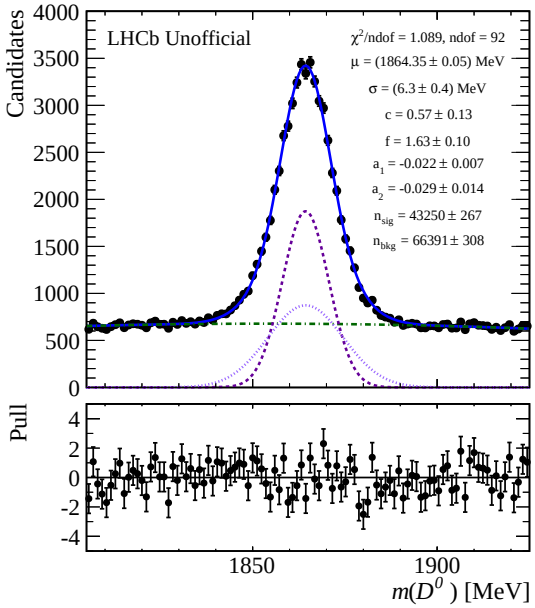

(d) *Odd event numbers of the* $D^0 \to K^0_S(\mathrm{DD})\pi^+\pi^-$ *dataset*

Figure 8.4.: *$m(D^0)$ distribution of the 2012 $\overline{B}^0 \to D^{*+}(\to D^0(\to K^0_S\pi^+\pi^-)\pi^+)\mu^-\overline{\nu}_\mu$ datasets after the trigger selection and preselection (see Chapt. 7) split by K^0_S type and even and odd event numbers. The figure depicts the fit (solid blue line) to the data (black points) and the fit components. The signal consists of a Crystal Ball (dotted lavender line) and a Gaussian function (dashed magenta line) and the background is described by a Chebychev polynomial (green dotted-dashed line).*

8.2. Boosted Decision Tree training and selection

The background rejection is further improved by training a Boosted Decision Tree (BDT) and using the response of the BDT as a discriminating variable between signal and background candidates. The BDT training is performed with the Toolkit for Multivariate Analysis (TMVA) [85]. The input distributions for the BDT training are obtained from the data after trigger selection and preselection as detailed in Chapt. 7. Each of the input distributions is weighted by signal and background sWeights (see Chapt. 8.1), to obtain separate signal and background distributions required by the BDT training. Comparisons of the BDT input distributions for even and odd datasets can be found in A

.

The input variables of the multivariate analysis are chosen from their discriminating power between signal and background. All variables are calculated without refitting the kinematics of the candidates with any mass constraints. Variables correlated with the D^0 mass, D^0 decay time or the Dalitz variables are omitted from the training to avoid biases.

A suitable variable for the training is the corrected mass of the B-meson candidate. The corrected mass m_{corr} accounts for the non-reconstructed neutrino in the semileptonic B decay, whereas the measured mass of the B is computed under the assumption that all daughters were reconstructed. Therefore, the corrected mass is a better approximation here than the invariant mass. The corrected mass depends on the invariant mass m of the B-meson candidate and the transverse missing momentum relative to the direction of flight with respect to the primary vertex, ${p_{\text{T}}}^{\text{miss}}$, and is defined as

$$m_{\text{corr}} = \sqrt{m^2 + |\vec{p_{\text{T}}}^{\text{miss}}|^2} + |\vec{p_{\text{T}}}^{\text{miss}}|. \tag{8.8}$$

As there can be more than one PV in an event, the PV with the smallest χ^2_{IP} is taken. Furthermore, the direction angle of the B-meson candidate, θ_{DIRA}, and its decay vertex $\chi^2/ndof$ have distinct shapes in signal and background components. The χ^2 of the B-meson candidate's PV has great discriminating power, since it is connected to the multiplicity of the event, as do the transverse momenta of the muon and D^0-meson candidate as well as the $\chi^2/ndof$ of the D^0-meson candidate's decay vertex. Figure 8.5 illustrates the distributions for signal and background used in the BDT training. The BDT is trained with these seven input distributions and learns to distinguish between signal- and background-like candidates. Furthermore, each of the eight samples is divided into a training and a testing sample of equal size. To ensure a robust selection, the BDT training of the even sample for a given year and K^0_{S} type and the corresponding optimal cut on the response are applied to the odd sample for the same year and K^0_{S} type and vice versa.

The comparison of test and training samples gives an indication if the BDT was overtrained meaning that specific features of the training sample, *e.g.* statistical fluctuations, were used in the BDT training. Overtraining can be quantified by a Kolmogorov-Smirnov test [87] where the result of this test can be interpreted as the likelihood that the training sample distribution could have been obtained on the test sample distribution and vice versa.

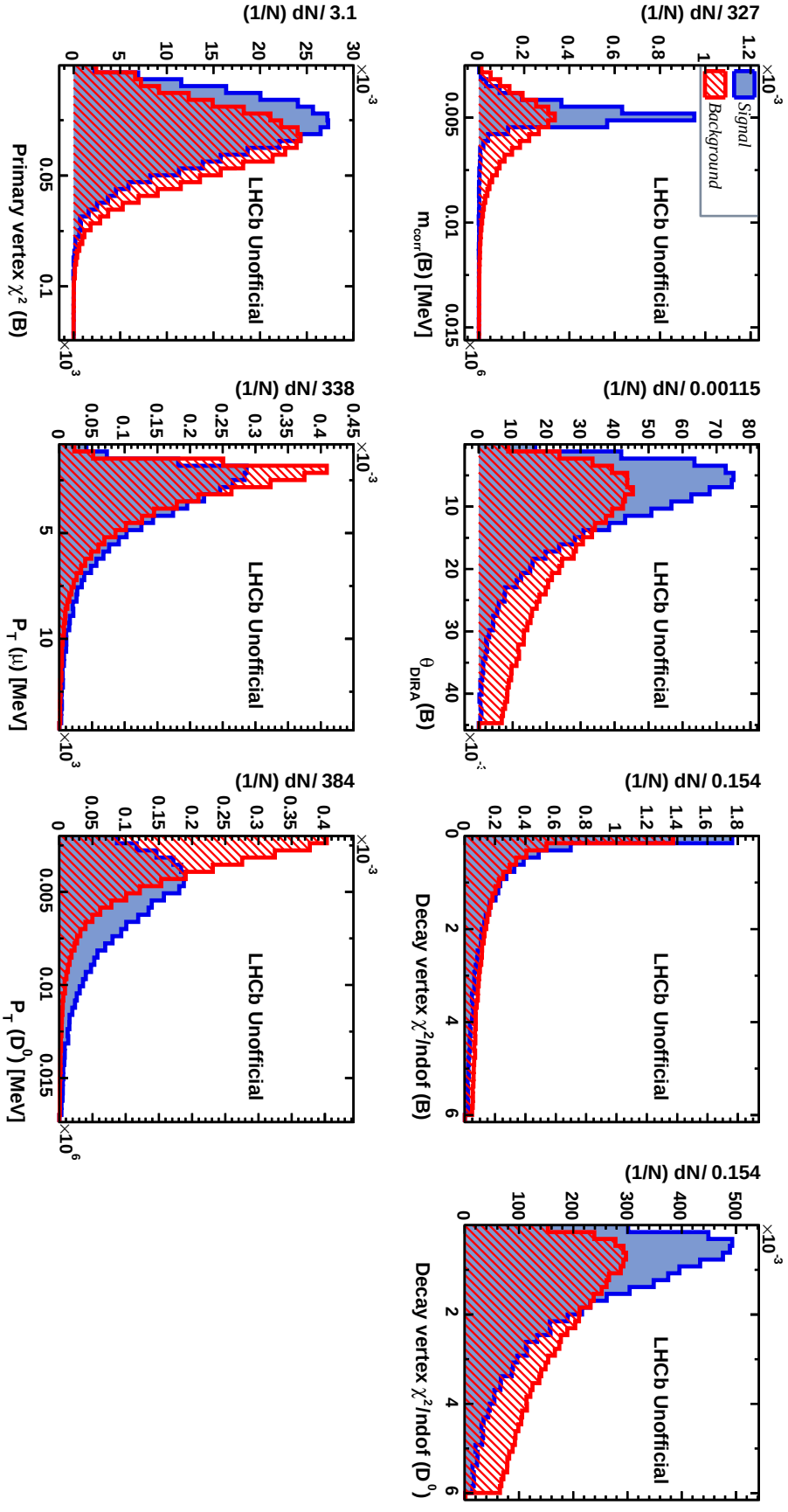

Figure 8.5.: *Distributions of the input variables used for training the BDT for the 2012 even $B^- \to D^0(\to K^0_S(\mathrm{DD})\pi^+\pi^-)\mu^-\bar{\nu}_\mu$ dataset.*

8.2.1. BDT training and selection for single-tagged decays

The signal efficiency versus background rejection rate, the so-called ROC or Receiver Operator Characteristics curve is determined by evaluating the signal efficiency and background rejection at various cuts on the BDT response. Hereby, the background rejection is defined as $1-\varepsilon(bkg)$ with $\varepsilon(bkg)$ being the background efficiency. An example ROC curve is shown in Fig. 8.6; the ROC curves for the other datasets can be found in Appendix B. Figures 8.7 and 8.8 show the response of the BDT for both signal and background categories evaluated on the test and training samples and thus provide a check if the BDT was overtrained, which is not the case.

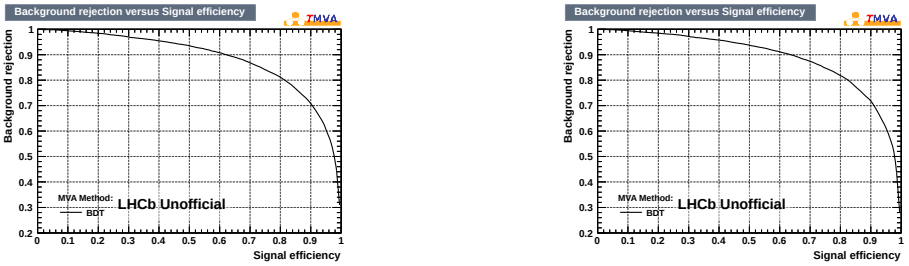

(a) *Even event numbers of the* $D^0 \to K^0_S(\mathrm{LL})\pi^+\pi^-$ *dataset*

(b) *Odd event numbers of the* $D^0 \to K^0_S(\mathrm{LL})\pi^+\pi^-$ *dataset*

Figure 8.6.: *Signal efficiency versus background rejection calculated for various cuts on the BDT response for the 2012* $B^- \to D^0(\to K^0_S(\mathrm{LL})\pi^+\pi^-)\mu^-\overline{\nu}_\mu$ *datasets split by and even and odd event numbers.*

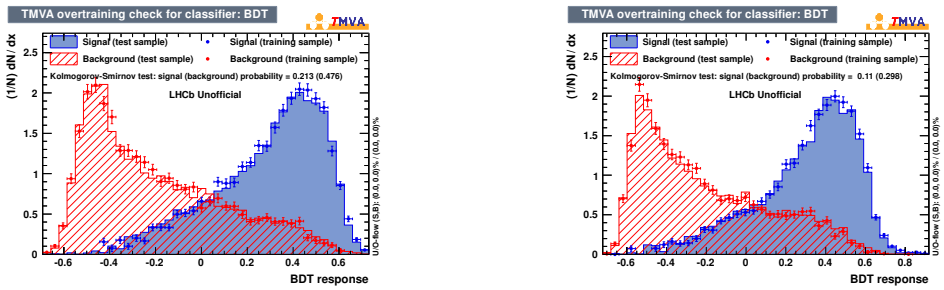

(a) *Even event numbers of the* $D^0 \to K^0_S(\mathrm{LL})\pi^+\pi^-$ *dataset*

(b) *Odd event numbers of the* $D^0 \to K^0_S(\mathrm{LL})\pi^+\pi^-$ *dataset*

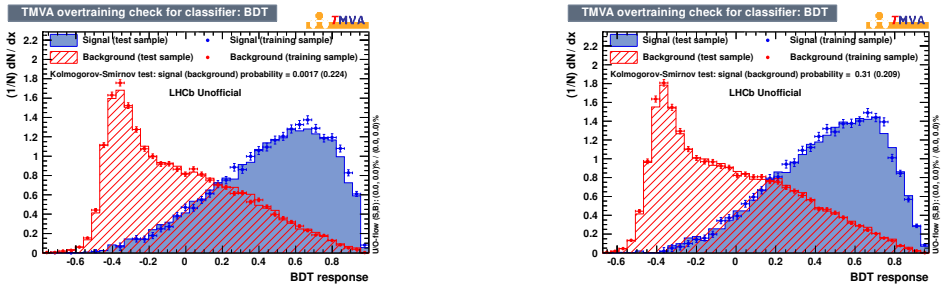

(c) *Even event numbers of the* $D^0 \to K^0_S(\mathrm{DD})\pi^+\pi^-$ *dataset*

(d) *Odd event numbers of the* $D^0 \to K^0_S(\mathrm{DD})\pi^+\pi^-$ *dataset*

Figure 8.7.: *Comparison of BDT response for both signal and background categories evaluated on the test and training samples for the 2011* $B^- \to D^0(\to K^0_S\pi^+\pi^-)\mu^-\overline{\nu}_\mu$ *datasets split by* K^0_S *type and even and odd event numbers.*

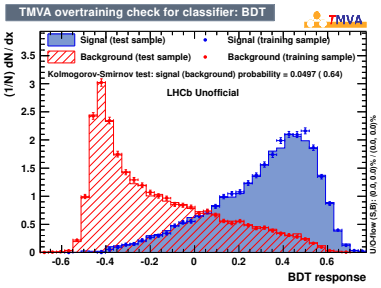

(a) *Even event numbers of the* $D^0 \to K^0_S(\mathrm{LL})\pi^+\pi^-$ *dataset*

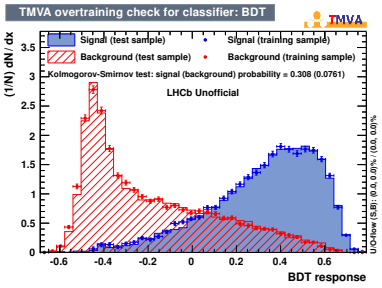

(b) *Odd event numbers of the* $D^0 \to K^0_S(\mathrm{LL})\pi^+\pi^-$ *dataset*

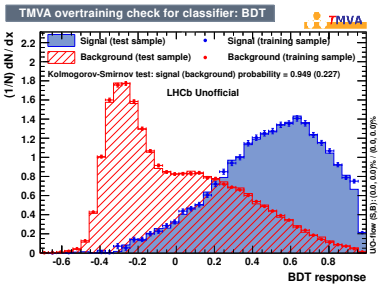

(c) *Even event numbers of the* $D^0 \to K^0_S(\mathrm{DD})\pi^+\pi^-$ *dataset*

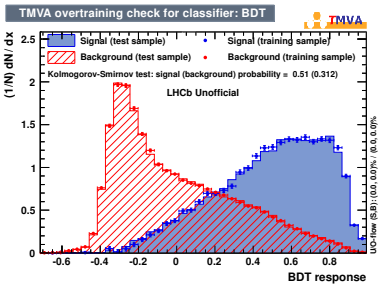

(d) *Odd event numbers of the* $D^0 \to K^0_S(\mathrm{DD})\pi^+\pi^-$ *dataset*

Figure 8.8.: *Comparison of BDT response for both signal and background categories evaluated on the test and training samples for the 2012* $B^- \to D^0(\to K^0_S\pi^+\pi^-)\mu^-\overline{\nu}_\mu$ *datasets split by* K^0_S *type and even and odd event numbers.*

The nominal cut on the BDT response is chosen as the point where the significance between signal S and background B in the training sample $S/\sqrt{S+B}$ reaches its maximum. The signal and background contributions are computed as the integral over the BDT response for a given cut value weighted by signal and background sWeights, respectively. The cut on the BDT response and the corresponding significance is listed in Table 8.11.

Table 8.11.: *Nominal cut value on the BDT response and corresponding significance for the 2011 and 2012* $B^- \to D^0(\to K^0_S\pi^+\pi^-)\mu^-\overline{\nu}_\mu$ *datasets split by even and odd event numbers and* K^0_S *type.*

	Cut on BDT response	Significance
2011 K^0_S(LL) even	−0.122	126.4
2011 K^0_S(LL) odd	−0.146	126.0
2011 K^0_S(DD) even	0.150	145.2
2011 K^0_S(DD) odd	0.153	145.8
2012 K^0_S(LL) even	−0.058	181.5
2012 K^0_S(LL) odd	−0.078	182.0
2012 K^0_S(DD) even	0.238	221.4
2012 K^0_S(DD) odd	0.166	221.3

To ensure that the significance is the best figure of merit for this analysis, meaning that the cut yields the best statistical precision or sensitivity on x and y, the nominal cut was tightened

by +0.05, +0.10 and +0.20. For each of the cut values, studies of pseudo-experiments were performed to evaluate the sensitivity on x and y. This showed that the nominal cut does yield the best statistical sensitivity on x and y and hence that the significance is a good figure of merit. The study is summarised in Appendix C.

The cut on the BDT response improves the purity of the dataset by reducing the background contribution significantly, as can be seen from the mass distributions in Figs. 8.9 and 8.10. The fit models are the same as reported earlier in Eq. 8.3 and 8.7. The signal yield, background rejection and purity of the 2011 and 2012 datasets after the complete selection chain are listed in Tables 8.12 and. 8.13, respectively. The uncertainties on the signal efficiency and background rejection are calculated by splitting the number of candidates before the BDT selection in the number of candidates after the BDT selection and all remaining candidates. The uncertainty on the latter is determined from Gaussian error propagation. In a second step, the uncertainties on the signal yield and background rejection are calculated by propagating the uncertainties of the number of candidates after the BDT selection and the remaining candidates assuming they are fully correlated. The uncertainty on the purity is calculated with Gaussian error propagation.

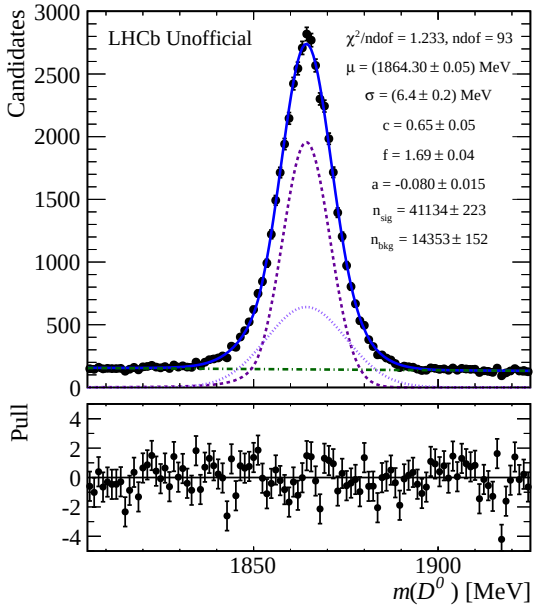

(a) *Even event numbers of the* $D^0 \to K^0_S(\mathrm{LL})\pi^+\pi^-$ *dataset*

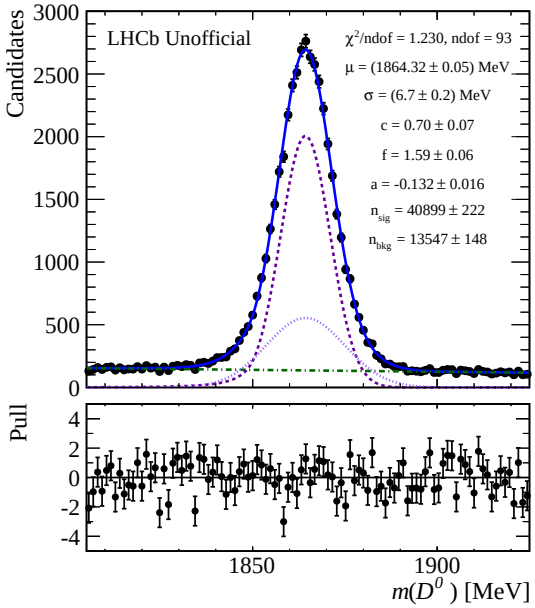

(b) *Odd event numbers of the* $D^0 \to K^0_S(\mathrm{LL})\pi^+\pi^-$ *dataset*

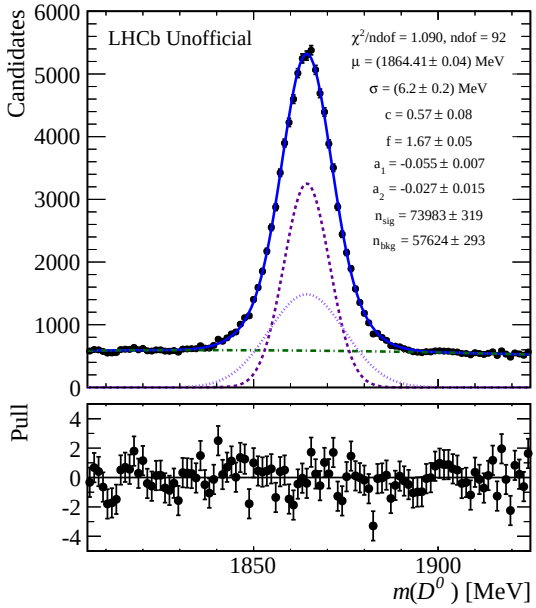

(c) *Even event numbers of the* $D^0 \to K^0_S(\mathrm{DD})\pi^+\pi^-$ *dataset*

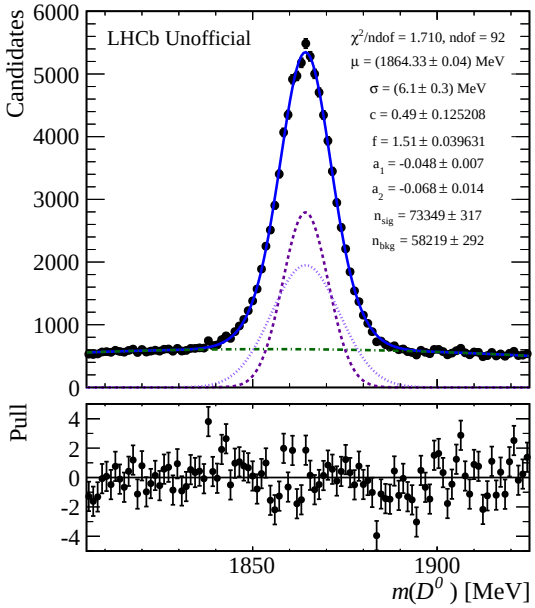

(d) *Odd event numbers of the* $D^0 \to K^0_S(\mathrm{DD})\pi^+\pi^-$ *dataset*

Figure 8.9.: *$m(D^0)$ distribution of the 2011 $B^- \to D^0(\to K^0_S\pi^+\pi^-)\mu^-\overline{\nu}_\mu$ datasets after the complete selection chain split by K^0_S type and even and odd event numbers. The figure depicts the fit (solid blue line) to the data (black points) and the fit components. The signal consists of a Crystal Ball (dotted lavender line) and a Gaussian function (dashed magenta line) and the background is described by a Chebychev polynomial (green dotted-dashed line).*

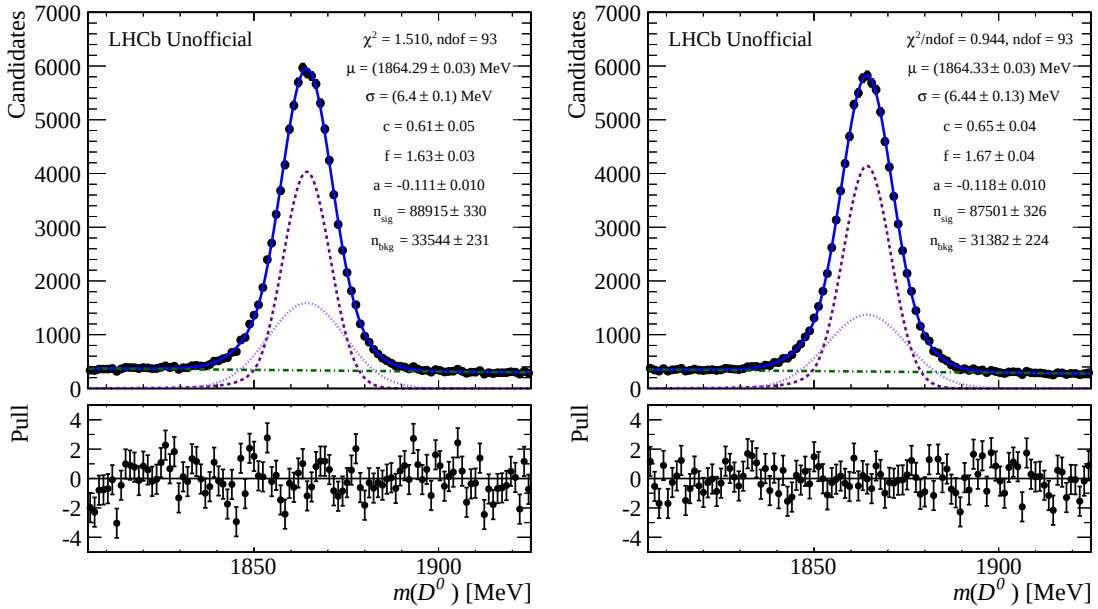

(a) *Even event numbers of the* $D^0 \to K^0_S(\mathrm{LL})\pi^+\pi^-$ *dataset* **(b)** *Odd event numbers of the* $D^0 \to K^0_S(\mathrm{LL})\pi^+\pi^-$ *dataset*

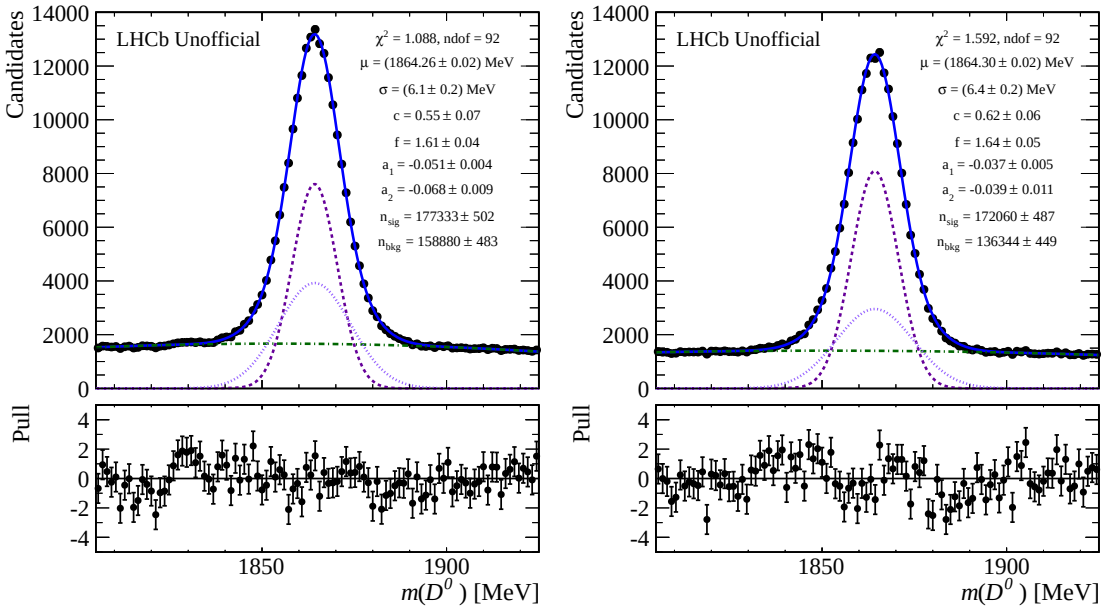

(c) *Even event numbers of the* $D^0 \to K^0_S(\mathrm{DD})\pi^+\pi^-$ *dataset* **(d)** *Odd event numbers of the* $D^0 \to K^0_S(\mathrm{DD})\pi^+\pi^-$ *dataset*

Figure 8.10.: *$m(D^0)$ distribution of the 2012 $B^- \to D^0(\to K^0_S\pi^+\pi^-)\mu^-\overline{\nu}_\mu$ datasets after the complete selection chain split by K^0_S type and even and odd event numbers. The figure depicts the fit (solid blue line) to the data (black points) and the fit components. The signal consists of a Crystal Ball (dotted lavender line) and a Gaussian function (dashed magenta line) and the background is described by a Chebychev polynomial (green dotted-dashed line).*

Table 8.12.: *Signal yield and efficiency, background rejection and purities of the 2011 $B^- \to D^0(\to K^0_S\pi^+\pi^-)\mu^-\overline{\nu}_\mu$ datasets after the complete selection chain split by even and odd event numbers and K^0_S type. The signal efficiency and background rejection are measured with respect to the data after trigger selection and preselection. The purities are given for the complete mass range and in a $\pm 30\,\mathrm{MeV}$ window around the D^0 mass peak position before and after cutting on the BDT response referred to as initial and final purity.*

	K^0_S (LL)		K^0_S (DD)	
	even	odd	even	odd
Signal yield	41134 ± 251	40899 ± 254	73983 ± 319	73349 ± 317
Signal efficiency	0.933 ± 0.007	0.921 ± 0.007	0.837 ± 0.005	0.838 ± 0.005
Background rejection	0.632 ± 0.007	0.650 ± 0.007	0.706 ± 0.003	0.704 ± 0.003
Purity	0.741 ± 0.002	0.751 ± 0.002	0.562 ± 0.002	0.557 ± 0.002
Initial purity in $(1865 \pm 30)\,\mathrm{MeV}$	$\approx 69\%$	$\approx 69\%$	$\approx 47\%$	$\approx 47\%$
Final purity in $(1865 \pm 30)\,\mathrm{MeV}$	$\approx 85\%$	$\approx 86\%$	$\approx 72\%$	$\approx 72\%$

Table 8.13.: *Signal yield and efficiency, background rejection and purities of the 2012 $B^- \to D^0(\to K^0_S\pi^+\pi^-)\mu^-\overline{\nu}_\mu$ datasets after the complete selection chain split by even and odd event numbers and K^0_S type. The signal efficiency and background rejection are measured with respect to the data after trigger selection and preselection. The purities are given for the complete mass range and in a $\pm 30\,\mathrm{MeV}$ window around the D^0 mass peak position before and after cutting on the BDT response referred to as initial and final purity.*

	K^0_S (LL)		K^0_S (DD)	
	even	odd	even	odd
Signal yield	88915 ± 386	87502 ± 382	177333 ± 502	172060 ± 487
Signal efficiency	0.928 ± 0.005	0.909 ± 0.005	835 ± 0.004	0.808 ± 0.004
Background rejection	0.676 ± 0.004	0.696 ± 0.005	0.708 ± 0.002	0.749 ± 0.002
Purity	0.726 ± 0.002	0.736 ± 0.002	0.527 ± 0.001	0.558 ± 0.002
Initial purity in $(1865 \pm 30)\,\mathrm{MeV}$	$\approx 65\%$	$\approx 65\%$	$\approx 44\%$	$\approx 44\%$
Final purity in $(1865 \pm 30)\,\mathrm{MeV}$	$\approx 84\%$	$\approx 85\%$	$\approx 69\%$	$\approx 72\%$

8.2.2. BDT training and selection for double-tagged decays

The signal efficiency versus background rejection rate is illustrated in Fig. 8.11 for 2012 K^0_S(LL) double-tagged data. The ROC curves for the other datasets can be found in Appendix B. Figures. 8.12 and 8.13 show the response of the BDT for both signal and background categories evaluated on the test and training samples. The BDTs are not overtrained.

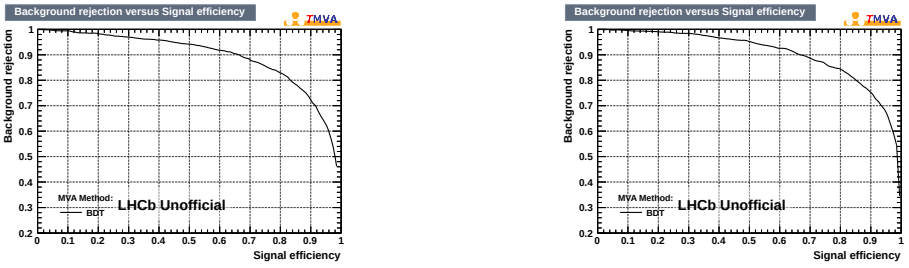

(a) *Even event numbers of the* $D^0 \to K^0_S(\mathrm{LL})\pi^+\pi^-$ *dataset*

(b) *Odd event numbers of the* $D^0 \to K^0_S(\mathrm{LL})\pi^+\pi^-$ *dataset*

Figure 8.11.: *Signal efficiency versus background rejection calculated for various cuts on the BDT response for the 2012* $\overline{B}^0 \to D^{*+}(\to D^0(\to K^0_S(\mathrm{LL})\pi^+\pi^-)\pi^+)\mu^-\overline{\nu}_\mu$ *dataset split by even and odd event numbers.*

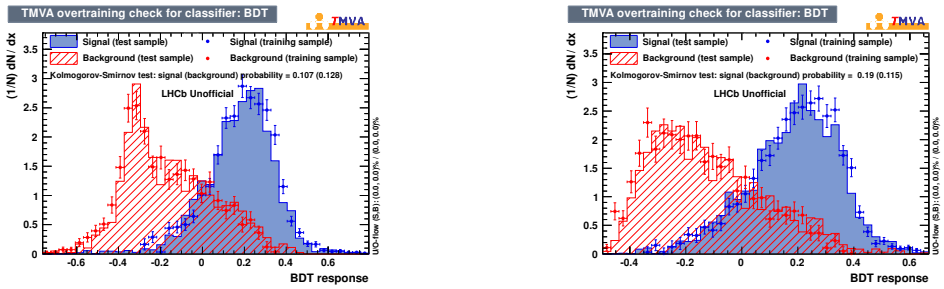

(a) *Even event numbers of the* $D^0 \to K^0_S(\mathrm{LL})\pi^+\pi^-$ *dataset*

(b) *Odd event numbers of the* $D^0 \to K^0_S(\mathrm{LL})\pi^+\pi^-$ *dataset*

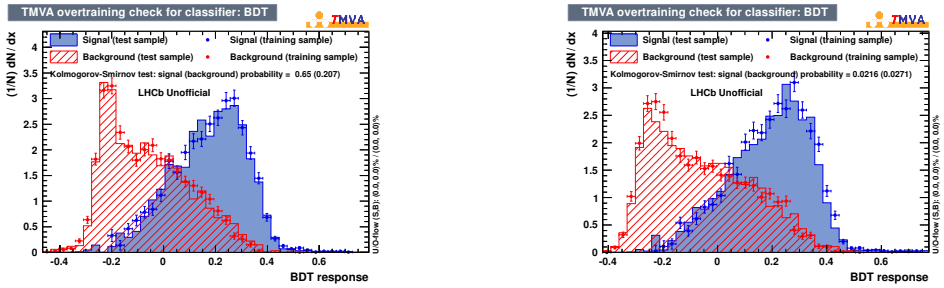

(c) *Even event numbers of the* $D^0 \to K^0_S(\mathrm{DD})\pi^+\pi^-$ *dataset*

(d) *Odd event numbers of the* $D^0 \to K^0_S(\mathrm{DD})\pi^+\pi^-$ *dataset*

Figure 8.12.: *Comparison of BDT response for both signal and background categories evaluated on the test and training datasets for the 2011* $\overline{B}^0 \to D^{*+}(\to D^0(\to K^0_S\pi^+\pi^-)\pi^+)\mu^-\overline{\nu}_\mu$ *dataset split by* K^0_S *type and even and odd event numbers.*

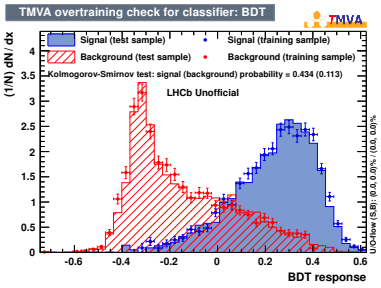

(a) *Even event numbers of the* $D^0 \to K^0_S(\mathrm{LL})\pi^+\pi^-$ *dataset*

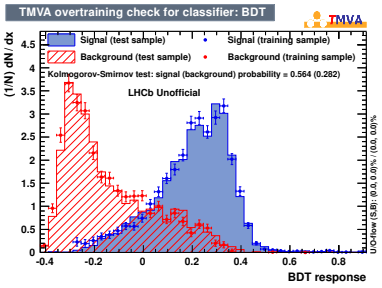

(b) *Odd event numbers of the* $D^0 \to K^0_S(\mathrm{LL})\pi^+\pi^-$ *dataset*

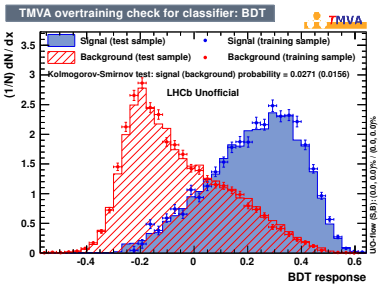

(c) *Even event numbers of the* $D^0 \to K^0_S(\mathrm{DD})\pi^+\pi^-$ *dataset*

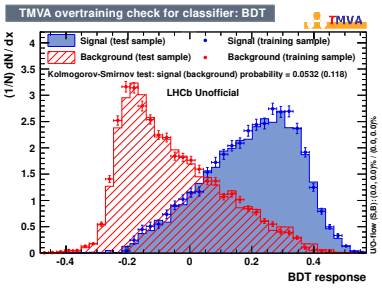

(d) *Odd event numbers of the* $D^0 \to K^0_S(\mathrm{DD})\pi^+\pi^-$ *dataset*

Figure 8.13.: *Comparison of BDT response for both signal and background categories evaluated on the test and training datasets for the 2012* $\overline{B}^0 \to D^{*+}(\to D^0(\to K^0_S\pi^+\pi^-)\pi^+)\mu^-\overline{\nu}_\mu$ *dataset split by* K^0_S *type and even and odd event numbers.*

The cut on the BDT response and the corresponding significance is listed in Table 8.14. After applying the cut on the BDT response to the datasets, the purity of the samples increases significantly. The mass distributions after cutting on the BDT response are shown in Figs. 8.14 and 8.15. The fit models are those given previously in Eq. 8.3 and 8.7. In Tables 8.15 and 8.16, the signal yield, background rejection and purity of the 2011 and 2012 datasets are given. The calculation of their corresponding uncertainty is the same as the one detailed for the single-tagged sample. After cutting on the BDT response, a cut of $1844.86 \leq m(D^0) \leq 1884.86\,\mathrm{MeV}$ is placed to further increase the purity of the double-tagged sample.

Table 8.14.: *Nominal cut value on the BDT response and corresponding significance for the 2011 and 2012* $B^- \to D^0(\to K^0_S\pi^+\pi^-)\mu^-\overline{\nu}_\mu$ *datasets split by even and odd event numbers and* K^0_S *type.*

	Cut on BDT response	Significance
2011 K^0_S(LL) even	−0.026	58.9
2011 K^0_S(LL) odd	−0.026	58.1
2011 K^0_S(DD) even	−0.002	73.4
2011 K^0_S(DD) odd	−0.010	73.0
2012 K^0_S(LL) even	−0.018	85.0
2012 K^0_S(LL) odd	−0.034	85.7
2012 K^0_S(DD) even	−0.030	110.6
2012 K^0_S(DD) odd	0.034	112.8

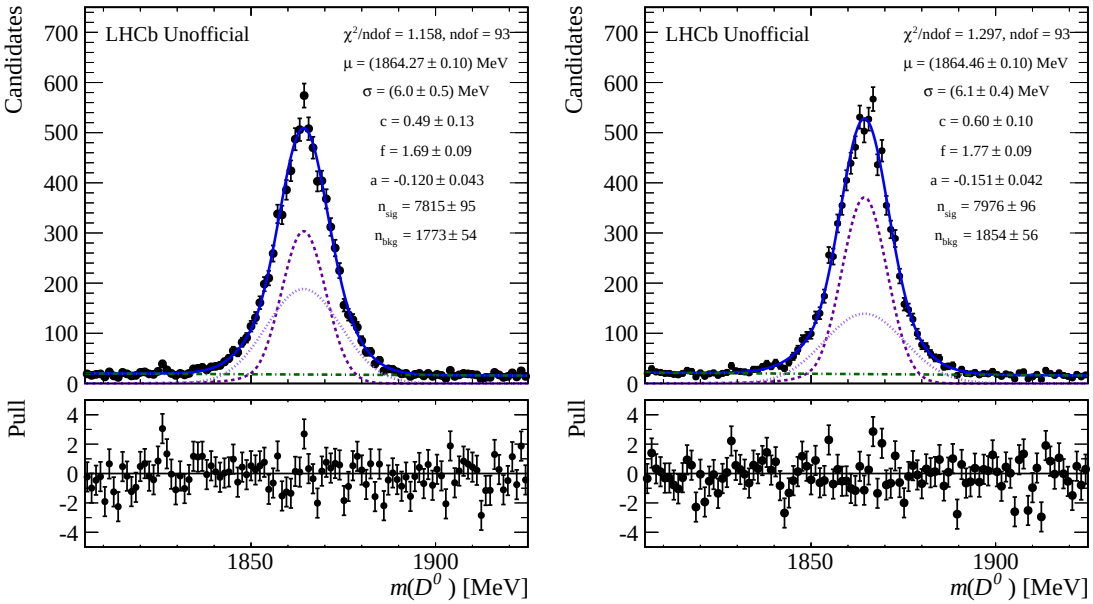

(a) *Even event numbers of the* $D^0 \to K^0_S(\mathrm{LL})\pi^+\pi^-$ *dataset*

(b) *Odd event numbers of the* $D^0 \to K^0_S(\mathrm{LL})\pi^+\pi^-$ *dataset*

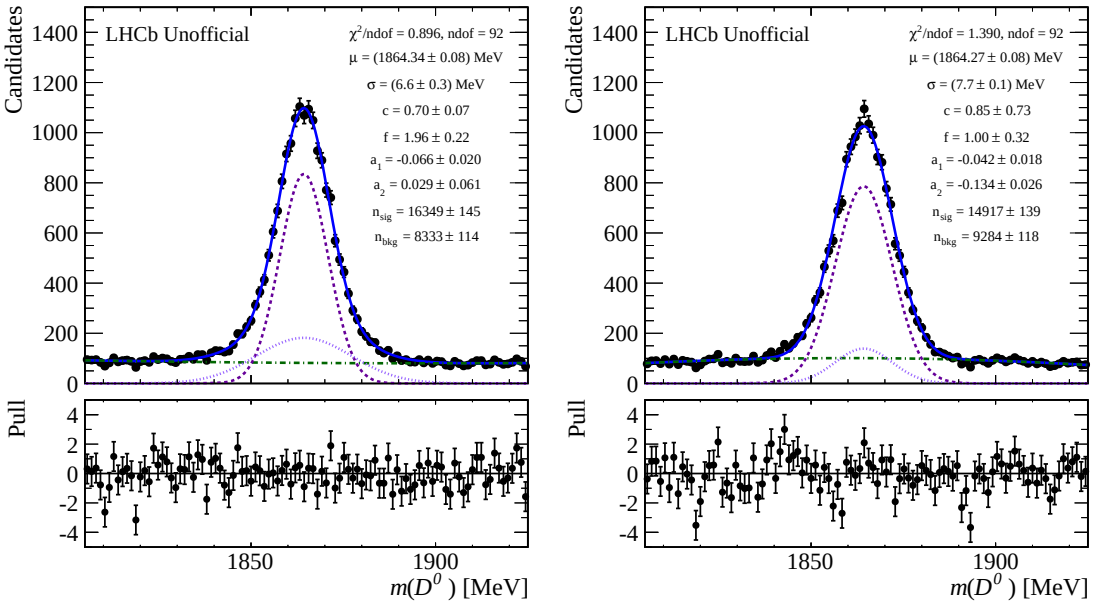

(c) *Even event numbers of the* $D^0 \to K^0_S(\mathrm{DD})\pi^+\pi^-$ *dataset*

(d) *Odd event numbers of the* $D^0 \to K^0_S(\mathrm{DD})\pi^+\pi^-$ *dataset*

Figure 8.14.: *$m(D^0)$ distribution of the 2011 $\overline{B}^0 \to D^{*+}(\to D^0(\to K^0_S\pi^+\pi^-)\pi^+)\mu^-\overline{\nu}_\mu$ datasets after the complete selection chain split by K^0_S type and even and odd event numbers. The figure depicts the fit (solid blue line) to the data (black points) and the fit components. The signal consists of a Crystal Ball (dotted lavender line) and a Gaussian function (dashed magenta line) and the background is described by a Chebychev polynomial (green dotted-dashed line).*

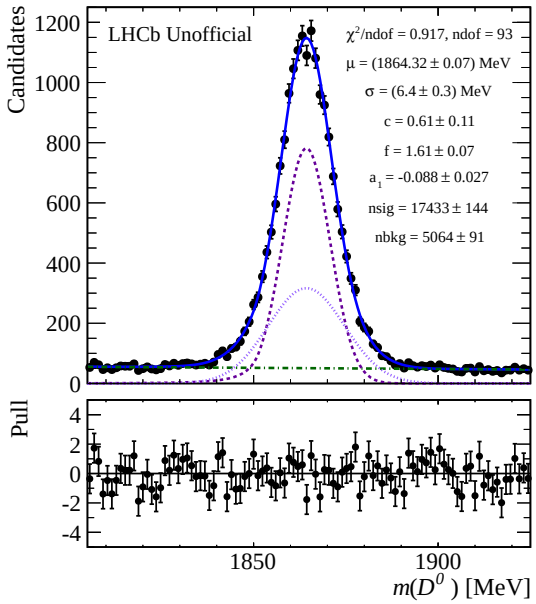

(a) *Even event numbers of the* $D^0 \to K^0_S(\mathrm{LL})\pi^+\pi^-$ *dataset*

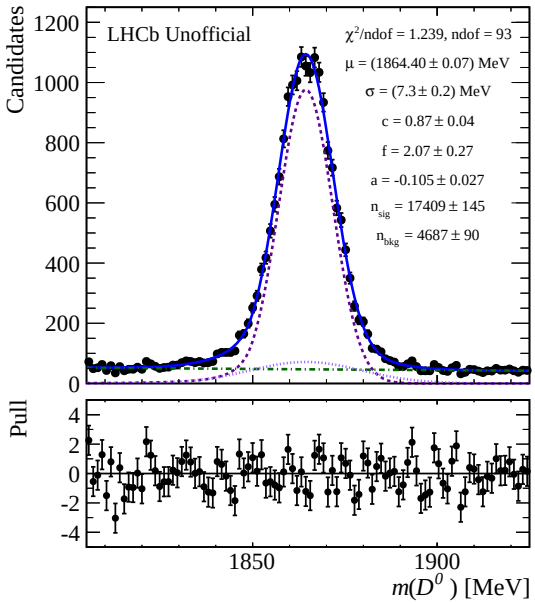

(b) *Odd event numbers of the* $D^0 \to K^0_S(\mathrm{LL})\pi^+\pi^-$ *dataset*

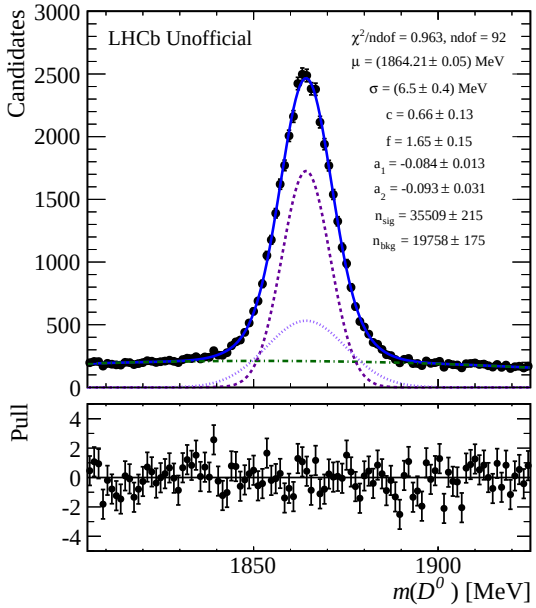

(c) *Even event numbers of the* $D^0 \to K^0_S(\mathrm{DD})\pi^+\pi^-$ *dataset*

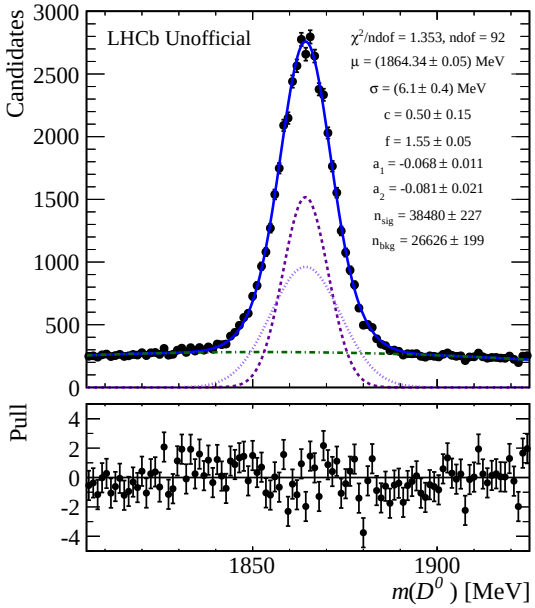

(d) *Odd event numbers of the* $D^0 \to K^0_S(\mathrm{DD})\pi^+\pi^-$ *dataset*

Figure 8.15.: *$m(D^0)$ distribution of the 2012 $\overline{B}^0 \to D^{*+}(\to D^0(\to K^0_S\pi^+\pi^-)\pi^+)\mu^-\overline{\nu}_\mu$ datasets after the complete selection chain split by K^0_S type and even and odd event numbers. The figure depicts the fit (solid blue line) to the data (black points) and the fit components. The signal consists of a Crystal Ball (dotted lavender line) and a Gaussian function (dashed magenta line) and the background is described by a Chebychev polynomial (green dotted-dashed line).*

Table 8.15.: *Signal yield and efficiency, background rejection and purities of the 2011 $\overline{B}^0 \to D^{*+}(\to D^0(\to K^0_S\pi^+\pi^-)\pi^+)\mu^-\overline{\nu}_\mu$ dataset after the complete selection chain split by even and odd event numbers and K^0_S type. The signal efficiency and background rejection are measured with respect to the data after trigger selection and preselection. The purities are given for the complete mass range and in a $\pm 30\,\mathrm{MeV}$ window around the D^0 mass peak position before and after cutting on the BDT response referred to as initial and final purity.*

	K^0_S (LL)		K^0_S (DD)	
	even	odd	even	odd
Signal yield	7815 ± 95	7976 ± 96	16349 ± 145	14918 ± 139
Signal efficiency	0.881 ± 0.016	0.911 ± 0.016	0.903 ± 0.012	0.842 ± 0.012
Background rejection	0.722 ± 0.019	0.719 ± 0.018	0.646 ± 0.009	0.613 ± 0.009
Purity	0.815 ± 0.005	0.811 ± 0.005	0.662 ± 0.004	0.616 ± 0.004
Initial purity in $(1865.0 \pm 30.0)\,\mathrm{MeV}$	$\approx 74\%$	$\approx 73\%$	$\approx 61\%$	$\approx 60\%$
Final purity in $(1865.0 \pm 30.0)\,\mathrm{MeV}$	$\approx 90\%$	$\approx 90\%$	$\approx 80\%$	$\approx 76\%$

Table 8.16.: *Signal yield and efficiency, background rejection and purities of the 2012 $\overline{B}^0 \to D^{*+}(\to D^0(\to K^0_S\pi^+\pi^-)\pi^+)\mu^-\overline{\nu}_\mu$ dataset after the complete selection chain split by even and odd event numbers and K^0_S type. The signal efficiency and background rejection are measured with respect to the data after trigger selection and preselection. The purities are given for the complete mass range and in a $\pm 30\,\mathrm{MeV}$ window around the D^0 mass peak position before and after cutting on the BDT response referred to as initial and final purity.*

	K^0_S (LL)		K^0_S (DD)	
	even	odd	even	odd
Signal yield	17433 ± 144	17409 ± 145	35509 ± 215	38480 ± 227
Signal efficiency	0.902 ± 0.011	0.903 ± 0.011	0.831 ± 0.008	0.890 ± 0.008
Background rejection	0.717 ± 0.011	0.731 ± 0.008	0.702 ± 0.006	0.599 ± 0.005
Purity	0.775 ± 0.003	0.788 ± 0.002	0.642 ± 0.002	0.591 ± 0.002
Initial purity in $(1865.0 \pm 30.0)\,\mathrm{MeV}$	$\approx 68\%$	$\approx 69\%$	$\approx 56\%$	$\approx 57\%$
Final purity in $(1865.0 \pm 30.0)\,\mathrm{MeV}$	$\approx 87\%$	$\approx 88\%$	$\approx 78\%$	$\approx 74\%$

8.3. Separation of single- and double-tagged datasets and extraction of signal probabilities

Due to the inclusive reconstruction in the preselection (see Chapt. 7.2), the double-tagged dataset is a subset of the single-tagged dataset. To avoid double-counting of candidates, double-tagged candidates have to be separated from the single-tagged sample. Double-tagged candidates are removed from the single-tagged dataset if the candidate's event number and the D^0 mass are the same. The datasets also contains genuine multiple $D^0 \to K^0_S\pi^+\pi^-$ candidates. These multiple candidates are removed by randomly rejecting all but one of these candidates. A signal probability is then determined for each candidate in the separated single- and double-tagged datasets.

The signal probabilities for single-tagged candidates rely on a fit to $m(D^0)$ with the fit models defined in Eqns. 8.7 and 8.7 and are computed as

$$P_{sig}(m(D^0)) = \frac{PDF_{sig}(m(D^0))n_{sig}}{PDF_{sig+bkg}(m(D^0))(n_{sig}+n_{bkg})}, \tag{8.9}$$

where n_{sig} and n_{bkg} refer to the number of signal and background candidates, respectively. The value of the total PDF for signal and background $PDF_{sig+bkg}(m(D^0))$ and of the signal component $PDF_{sig}(m(D^0))$ is evaluated at the D^0 mass of each candidate.

A tight cut of $1844.86 \leq m(D^0) \leq 1884.86\,\text{MeV}$ is placed on the mass distribution of the double-tagged sample and the signal probabilities are extracted from a fit to δm. The mass of the D^0-meson candidate is computed from the D^0 momenta without a fit to the kinematics of the event with any mass constraints. From the momenta of the D^0 and the soft pion, computed without any mass constraints, the D^* mass is reconstructed. The difference in D^* and D^0 mass is fitted with a triple Gaussian function as the signal component and a polynomial in $|\delta m - a_1|$ for the background component

$$\begin{aligned} F(\delta m;\mu,\sigma,f_1,f_2,c_1,c_2,a_1,g) = N \times \Big\{ & n_{sig} \times [c_1 G(\delta m;\mu,\sigma) + c_2 G(\delta m;\mu,f_1\sigma) \\ & + (1-c_1-c_2)G(\delta m;\mu,f_2\sigma)] + n_{bkg} \times \Big[g|\delta m - a_1|^{3/2} \\ & + (1-g)|\delta m - a_1|^{1/2} \Big] \Big\}, \end{aligned} \tag{8.10}$$

as illustrated in Fig. 8.16, where N is a normalisation factor. The signal probability is given by

$$P_{sig}(\delta m) = \frac{PDF_{sig}(\delta m) \times n_{sig}}{PDF_{sig+bkg}(\delta m) \times (n_{sig}+n_{bkg})}, \tag{8.11}$$

where n_{sig} and n_{bkg} refer to the number of signal and background candidates, respectively. The value of the total PDF for signal and background $PDF_{sig+bkg}(\delta m)$ and of the signal component $PDF_{sig}(\delta m)$ is evaluated at the δm value of each candidate.

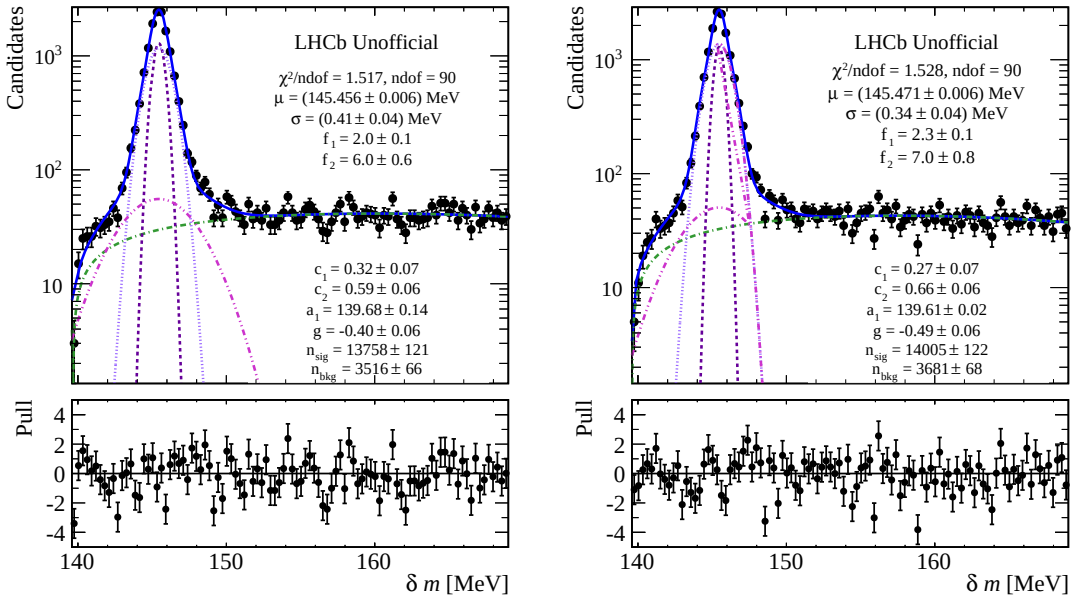

(a) D^0 *candidates* **(b)** $\overline{D}^0$ *candidates*

Figure 8.16.: *δm distribution of the 2012 $\overline{B}^0 \to D^{*+}(\to D^0(\to K^0_S(\mathrm{LL})\pi^+\pi^-)\pi^+)\mu^-\overline{\nu}_\mu$ dataset after the complete selection split by D^0 and $\overline{D}^0$. The figure depicts the fit (solid blue line) to the data (black points) and the fit components. The signal consists of a triple Gaussian function (dotted lavender line, dashed magenta line and dotted-dashed pink line) and the background is described by a polynomial (green dotted-dashed line).*

9. Backgrounds

After the selection detailed in Chapt. 7 and 8, a fraction of background events remains in the dataset. These contributions need to be taken into account when extracting the mixing and *CP* violation parameters by including a description of the remaining background in the fit. In this chapter, possible sources of backgrounds are discussed, concentrating on those arising from specific decay channels rather than from random combination of tracks.

The branching fraction of the signal decay $B^- \to D^0(\to K^0_S\pi^+\pi^-)\mu^-\overline{\nu}_\mu$ is assumed to be $\mathcal{B}(B^- \to D^0\ell^-\overline{\nu}_\ell) \times \mathcal{B}(D^0 \to K^0_S\pi^+\pi^-) = (2.27 \pm 0.11) \times (2.83 \pm 0.20) \times 10^{-4}$ [11], with $\ell = e, \mu, \tau$. The contribution from τ decays is measured to be $(7.7 \pm 2.5) \times 10^{-3}$ [11]. Apart from the direct decay of a B meson to a final state containing a D^0 meson, decays through higher excited states such as $B^- \to D^{*0}(2007)\ell^-\overline{\nu}_\ell$ are possible. The branching fraction of the decay $B^- \to D^{*0}(2007)\ell^-\overline{\nu}_\ell$ is $(5.69 \pm 0.19) \times 10^{-2}$ [11]. By assuming a lower signal decay branching fraction, conservative estimates of the contribution of possible background channels to the signal decay are given. For each possible background channel, the ratio of background to signal branching fraction is calculated. For decays where a particle needs to be misidentified such that it contributes to the background, a misidentification probability of ε_{misID} is taken into account. If the branching fraction ratio is small, this background source is considered negligible since the different kinematics would further reduce the background contribution.

In a second step, the fraction of background events inside the mass window used in the analysis of $1805 < m(D^0) < 1925\,\text{MeV}$, $\varepsilon_{m(D^0)}$, is calculated. Background samples are fully simulated and reconstructed. The reconstructed decays are truth-matched to the generated particles without the application of any other selection criteria if not mentioned otherwise. Truth-matching is the comparison of the generated hits of a track with the reconstructed tracks and if the overlap is sufficiently large, the track is reconstructed correctly. No trigger selection, preselection or BDT selection requirements are used and therefore those estimates can be considered upper limits. The fraction of candidates falling into the signal mass window

$$\varepsilon_{m(D^0)} = \frac{\#\text{Truth-matched events within } 1805 < m(D^0) < 1925\,\text{MeV}}{\#\text{Truth-matched events}} \tag{9.1}$$

is estimated as a measure of the background contribution and multiplied with the branching fraction ratio. This fraction is only determined where the background is not considered negligible.

In the following, apart from prompt $D^0 \to K^0_S\pi^+\pi^-$ decays, only semileptonic decay backgrounds are considered. The backgrounds are classified as negligible, suppressible or significant. Suppressible means that if this background is seen in data, it can be easily removed, *e.g.* by

the introduction of a cut.

9.1. Prompt $D^0 \to K^0_S \pi^+ \pi^-$

Background from $D^0 \to K^0_S \pi^+ \pi^-$ events produced at the primary vertex is significantly enhanced compared to the signal decay and is thus the main background source. The production cross-section at LHCb for charm is approximately twenty times that for beauty [88, 89]. Consequently, there is a potentially significant background in the selected dataset from $D^0 \to K^0_S \pi^+ \pi^-$ decays produced at the primary vertex. The measured D and D^* cross-sections at LHCb are $(1661 \pm 16_{\text{stat.}} \pm 128_{\text{syst.}} \pm 2_{\text{frag.}})\,\mu\text{b}$ and $(677 \pm 26_{\text{stat.}} \pm 77_{\text{syst.}} \pm 19_{\text{frag.}})\,\mu\text{b}$, respectively, for a centre-of-mass energy of $\sqrt{s} = 7\,\text{TeV}$ [88]. The branching fraction of $D^{*+} \to D^0 \pi^+$ decays is $(67.7 \pm 0.5)\%$ [11]. For $B^\pm$ mesons, the production cross-section at $\sqrt{s} = 7\,\text{TeV}$ is $(38.9 \pm 0.3_{\text{stat.}} \pm 2.5_{\text{syst.}} \pm 1.3_{\text{norm.}})\,\mu\text{b}$ [89]. Following Ref. [90], the cross-sections are scaled by the ratio of centre-of-mass energies of 8/7 to obtain those for 2012.
D^0 decays produced at the primary vertex are referred to as prompt decays. Considering the different production cross-sections at LHCb at 7 TeV and 8 TeV, the prompt $D^0 \to K^0_S \pi^+ \pi^-$ decay becomes an even larger background. Background from prompt D^0 decays peaks in D^0 mass identically to the signal decay. However, the D^0 will have decayed closer to the primary vertex. A lower cut on the flight distance χ^2 of the reconstructed B meson candidate $\chi^2_{\text{FD}} > 100$ is used to reduce background from prompt decays. For a MC sample reflecting 2012 data-taking conditions and with only LHCb geometrical acceptance cuts applied, 53 K^0_S(DD) and 17 K^0_S(LL) prompt candidates out of 503,2989 generated candidates remain after the complete selection. This is an inclusive simulation sample, and using truth-matching candidates originating from a long-lived secondary such as a $B^\pm$, B^0_s decay can also be removed. Indeed, once this is done, no candidates remain. To estimate an upper limit on the possible selection efficiency, in the absence of any surviving candidates, we assume that a single candidate passes, giving an efficiency for this prompt background of $2 \cdot 10^{-7}$. The signal efficiency is measured to be $3.4 \cdot 10^{-3}$. Taking into account the branching fraction, production cross section and selection efficiency ratios, the prompt component is estimated to be $< 3\%$ of the signal.

9.2. Hadronic D^0 decays

The possible background channels from hadronic D^0 decays, where the D^0 decays arise from semileptonic B decays as do the signal decays, are considered in detail in the following sections, and a summary is provided in Table 9.1.

9.2.1. $D^0 \to K^0_S \pi^+ \pi^- \pi^0$

Background from $D^0 \to K^0_S \pi^+ \pi^- \pi^0$ decays, where the π^0 is not reconstructed, is considered. This channel has a branching fraction of $\mathcal{B}(D^0 \to K^0_S \pi^+ \pi^- \pi^0) = (5.2 \pm 0.6) \times 10^{-2}$ [11]. The daughter momenta of a four-body decay are in general softer than for a three-body decay and due to the π^0 meson not being reconstructed, the reconstructed mass of the D^0 is shifted to lower values by around $m_{\pi^0} = 135\,\text{MeV}$ [11]. The ratio of background to signal branching fraction is 1.84 ± 0.25. For the K^0_S(LL) sample, a fraction of $(0.75 \pm 0.53) \times 10^{-2}$ candidates is within the signal mass window whereas for K^0_S(DD), the fraction is $(0.39 \pm 0.22) \times 10^{-2}$.

The contributions relative to the signal events are estimated to be $(1.38 \pm 0.99) \times 10^{-2}$ and $(0.72 \pm 0.42) \times 10^{-2}$ for K^0_S(LL) and K^0_S(DD) candidates, respectively.

9.2.2. $D^0 \to K^0_S K^\pm h^\mp$

Due to misidentification of kaons as pions with a mistag probability of $\varepsilon_{misID} \approx 10\%$ [54], the decays $D^0 \to K^0_S h^+ h^-$ with $h = \pi, K$ are a possible source of background. The daughter momenta are softer than for a real $D^0 \to K^0_S \pi^+ \pi^-$ decay, leading to a shift to lower masses with the shift for a $D^0 \to K^0_S K^+ K^-$ decay being larger than for a $D^0 \to K^0_S K^\pm \pi^\mp$ decay.

The branching fraction for the $K^0_S K^+ K^-$ final state is $(0.447 \pm 0.034) \times 10^{-2}$ [11]. To estimate the contribution of $D^0 \to K^0_S K^+ K^-$ decays, the ratio of the branching fractions is calculated and then corrected for misidentification resulting in

$$\frac{\mathcal{B}(D^0 \to K^0_S K^+ K^-)}{\mathcal{B}(D^0 \to K^0_S \pi^+ \pi^-)} \times \varepsilon^2_{misID} = (1.6 \pm 0.2) \times 10^{-3}. \tag{9.2}$$

The branching fractions of the $K^0_S \pi^\mp K^\pm$ modes are $\mathcal{B}(D^0 \to K^0_S K^+ \pi^-) = (0.21 \pm 0.04) \times 10^{-2}$ [11] and $\mathcal{B}(D^0 \to K^0_S \pi^+ K^-) = (0.35 \pm 0.05) \times 10^{-2}$ [11], respectively. In these channels, one daughter is being misidentified and the contributions are estimated to be

$$\frac{\mathcal{B}(D^0 \to K^0_S K^+ \pi^-)}{\mathcal{B}(D^0 \to K^0_S \pi^+ \pi^-)} \times \varepsilon_{misID} = (0.74 \pm 0.15) \times 10^{-2}, \tag{9.3}$$

$$\frac{\mathcal{B}(D^0 \to K^0_S \pi^+ K^-)}{\mathcal{B}(D^0 \to K^0_S \pi^+ \pi^-)} \times \varepsilon_{misID} = (1.24 \pm 0.20) \times 10^{-2}. \tag{9.4}$$

The decays $D^0 \to K^0_S K^+ \pi^-$ and $D^0 \to K^0_S K^+ K^-$ have relative contributions of order 10^{-3} and are negligible. The decay $D^0 \to K^0_S \pi^+ K^-$ has a slightly larger contribution but due to the large shift to low reconstructed D^0 masses around 1770 MeV, this decay is also neglected.

9.2.3. $D^0 \to K^0_S \pi^+ \pi^- \pi^+ \pi^-$

Background from $D^0 \to K^0_S \pi^+ \pi^- \pi^+ \pi^-$ decays, where two pions are not reconstructed, is considered. This channel has a branching fraction of $\mathcal{B}(D^0 \to K^0_S \pi^+ \pi^- \pi^+ \pi^-) = (2.69 \pm 0.31) \times 10^{-3}$ [11]. The daughter momenta of a five-body decay are much softer than for a three-body decay and due to the pions that are not reconstructed, the reconstructed mass of the D^0 are shifted to lower values than the nominal D^0 mass. The ratio of background to signal branching fraction is $(9.5 \pm 1.3) \times 10^{-2}$. No candidates with long K^0_S tracks are within the signal mass window but a fraction of $(0.21 \pm 0.21) \times 10^{-2}$ background candidates with downstream K^0_S tracks are in the signal mass window. This leads to a contribution relative to the signal of $(2.0 \pm 2.0) \times 10^{-4}$, which is considered negligible.

9.2.4. $D^0 \to K^0_S K^0_S$

In the case of one K^0_S not being reconstructed as K^0_S but as two separate pions, the decay mode $D^0 \to K^0_S K^0_S$ with a branching fraction of $\mathcal{B}(D^0 \to K^0_S K^0_S) = (1.7 \pm 0.4) \times 10^{-4}$ [11] produces the same final state particles as the signal. The ratio of background to signal branching fractions

is $(6.0 \pm 1.5) \times 10^{-3}$. This background could be removed by requiring the invariant mass of the two bachelor pions to be outside a narrow K^0_S mass window. Since no background from $D^0 \to K^0_S K^0_S$ decays has been seen in data, no cut on the invariant mass of the two bachelor pions is required. In addition, in this background the vertex quality of the D^0 decay vertex is worse than for $D^0 \to K^0_S \pi^+\pi^-$ decays. Through imposing a requirement on the D^0 vertex quality, backgrounds from $D^0 \to K^0_S K^0_S$ are further suppressed.

9.2.5. $D^0 \to K^0_S K^0_S \pi^+\pi^-$

Another potential background comes from $D^0 \to K^0_S K^0_S \pi^+\pi^-$ decays, where this channel has a branching fraction of $\mathcal{B}(D^0 \to K^0_S K^0_S \pi^+\pi^-) = (1.23 \pm 0.24) \times 10^{-3}$ [11]. The branching fraction ratio is estimated to be $(4.35 \pm 0.90) \times 10^{-2}$. In the case of one of the K^0_S mesons not being reconstructed in this channel, and a candidate with a K^0_S(DD) meson being found, $(1.8 \pm 1.7) \times 10^{-2}$ of the candidates lie within the signal mass window. No candidates with a K^0_S(LL) meson are in the signal mass window. Due to the low reconstructed mass efficiency, this background results in a contribution of $(7.6 \pm 7.7) \times 10^{-4}$ and thus can be neglected in the fit.

In the case of both bachelor pions not being reconstructed, the channel could still be a background due to the presence of two K^0_S mesons. However, a requirement on the invariant mass of the two bachelor pions could remove events where the daughter pions of one K^0_S are misreconstructed as bachelor pions of the signal $D^0 \to K^0_S \pi^+\pi^-$ decay. In data, no such background contribution is seen and hence, no requirement is placed on the invariant mass of the two bachelor pions.

9.2.6. $D^0 \to \pi^+\pi^-\pi^+\pi^-$

Since the K^0_S decays predominantly in two charged pions, the decay $D^0 \to \pi^+\pi^-\pi^+\pi^-$ has the same final state particles as a $D^0 \to K^0_S \pi^+\pi^-$ decay. The branching fraction for this background mode is $\mathcal{B}(D^0 \to \pi^+\pi^-\pi^+\pi^-) = (0.742 \pm 0.021) \times 10^{-2}$ [11]. The ratio of background to signal branching fraction is 0.26 ± 0.02.

The decay $D^0 \to \pi^+\pi^-\pi^+\pi^-$ peaks in the mass window with an efficiency of $(83.3 \pm 2.5) \times 10^{-2}$ and $(25.0 \pm 12.5) \times 10^{-2}$ for long and downstream pions. This leads to an overall contribution of $(2.17 \pm 0.18) \times 10^{-1}$ and of $(6.5 \pm 3.3) \times 10^{-2}$ for long and downstream decays, respectively. However, by using vertex displacement requirements on the K^0_S candidate in the preselection (see Table 7.3 for details), this background channel is highly suppressed.

9.2.7. $D^0 \to \pi^+\pi^-\pi^+\pi^-\pi^0$

The decay $D^0 \to \pi^+\pi^-\pi^+\pi^-\pi^0$ with a branching fraction of $(0.41 \pm 0.05) \times 10^{-2}$ [11] has to be considered as a possible background channel in case of the π^0 not being reconstructed. The ratio of background to signal branching fraction is 0.15 ± 0.02. The fraction of background candidates within the signal mass window is $(3.0 \pm 2.9) \times 10^{-2}$ for K^0_S mesons with long tracks leading to a contribution of $(0.45 \pm 0.45) \times 10^{-2}$. By using vertex displacement requirements on the K^0_S candidate in the preselection (see Table 7.3 for details), these background channels are highly suppressed.

Table 9.1.: *Ratio of background to signal branching fractions for D^0 decays. The fraction of candidates falling in the signal mass window, $\varepsilon_{m(D^0)}$, is only evaluated for channels with a significant branching fraction ratio.*

Mode	$\mathcal{B}(\text{bkg})/\mathcal{B}(\text{sig}) \times \varepsilon_{\text{misID}}$	$\varepsilon_{m(D^0)}$	$\mathcal{B}(\text{bkg})/\mathcal{B}(\text{sig}) \times \varepsilon_{\text{misID}} \times \varepsilon_{\text{m(D}^0\text{)}}$	Category
$D^0 \to K^0_S \pi^+ \pi^- \pi^0$	1.84 ± 0.25	K^0_S(LL): 2/267 K^0_S(DD): 3/773	K^0_S(LL): $(1.38 \pm 0.99) \times 10^{-2}$ K^0_S(DD): $(7.1 \pm 4.2) \times 10^{-3}$	significant
$D^0 \to K^0_S K^+ K^-$	$(1.58 \pm 0.16) \times 10^{-3}$	K^0_S(LL): – K^0_S(DD): –	K^0_S(LL): – K^0_S(DD): –	negligible
$D^0 \to K^0_S K^+ \pi^-$	$(0.74 \pm 0.15) \times 10^{-2}$	K^0_S(LL): – K^0_S(DD): –	K^0_S(LL): – K^0_S(DD): –	negligible
$D^0 \to K^0_S K^- \pi^+$	$(1.24 \pm 0.20) \times 10^{-2}$	K^0_S(LL): – K^0_S(DD): –	K^0_S(LL): – K^0_S(DD): –	negligible
$D^0 \to K^0_S \pi^+ \pi^- \pi^+ \pi^-$	$(9.5 \pm 1.3) \times 10^{-2}$	K^0_S(LL): 0 K^0_S(DD): 1/47	K^0_S(LL): – K^0_S(DD): $(2.0 \pm 2.0) \times 10^{-3}$	negligible
$D^0 \to K^0_S K^0_S$	$(6.0 \pm 1.5) \times 10^{-3}$	K^0_S(LL): – K^0_S(DD): –	K^0_S(LL): – K^0_S(DD): –	suppressible
$D^0 \to K^0_S K^0_S \pi^+ \pi^-$	$(4.35 \pm 0.90) \times 10^{-2}$	K^0_S(LL): 0 K^0_S(DD): 1/57	K^0_S(LL): – K^0_S(DD): $(7.6 \pm 7.7) \times 10^{-4}$	negligible
$D^0 \to \pi^+ \pi^- \pi^+ \pi^-$	0.26 ± 0.02	long: 185/222 downstream: 3/12	long: $(2.17 \pm 0.18) \times 10^{-1}$ downstream: $(6.5 \pm 3.3) \times 10^{-2}$	suppressible
$D^0 \to \pi^+ \pi^- \pi^+ \pi^- \pi^0$	0.15 ± 0.02	long: 1/33 downstream: 0	long: $(0.45 \pm 0.45) \times 10^{-2}$ downstream: –	suppressible

9.3. Semileptonic decays

Another class of backgrounds are semileptonic decays like $D^0 \to K^*(892)^- e^+ \nu_e$ where the electron or muon is misidentified as a pion. The electron channel has a branching fraction of $\mathcal{B}(D^0 \to K^*(892)^- e^+ \nu_e) = (2.16 \pm 0.16) \times 10^{-2}$, whereas the branching fraction of the muonic mode $D^0 \to K^*(892)^- \mu^+ \nu_\mu$ is $\mathcal{B}(D^0 \to K^*(892)^- \mu^+ \nu_\mu) = (1.91 \pm 0.24) \times 10^{-2}$. The probability of misidentifying an electron as pion is $\approx 8\%$ whereas for muons, it is $\approx 3\%$ [54]. Considering these mistag probabilities, the contributions of the decays $D^0 \to K^*(892)^- e^+ \nu_e$ and $D^0 \to K^*(892)^- \mu^+ \nu_\mu$ are estimated to be $(6.11 \pm 0.63) \times 10^{-2}$ and $(2.02 \pm 0.29) \times 10^{-2}$, respectively. In addition, background from the muon channel is further suppressed by applying particle identification criteria using the muon chambers for the bachelor and K^0_S daughter pions.

A MC sample of $D^0 \to K^*(892)^- e^+ \nu_e$ with 85,000 candidates was generated and passed through the dedicated `Strippingb2D0MuXKsPiPiLL(DD)CharmFromBSemiLine` Stripping lines. Out of this sample, a single candidate passed each of the lines where the candidate of the K^0_S(LL) line is outside and the K^0_S(DD) candidate inside the signal mass window. The muon channel is analysed with a sample of 90,000 candidates where 2 candidates passed the K^0_S(DD) and 1 candidate passed the K^0_S(LL) Stripping line. In this case, all candidates passing the Stripping lines are in the signal D^0 mass range. Due to the low fraction of candidates passing the Stripping selection, this background will not contribute significantly.

9.4. D_s^+ decays

Further potential backgrounds also include decays of D_s^+ mesons and require the consideration of the production branching fractions when estimating the background contribution. Due to the higher D_s^+ mass, the momenta of three reconstructed daughters from multi-body decays can add up to the D^0 mass leading to a possible source of peaking background, which is broadly.

The D_s^+ is either produced through the decay $B^- \to D_s^{*+} K^- \ell^- \overline{\nu}_\ell$ where the kaon is not reconstructed, through the decay $B_s^0 \to D_s^- \ell^+ \overline{\nu}_\ell$ or through a Λ_b^0 meson, $\Lambda_b^0 \to D_s^- \Lambda_c^+$ followed by the decay $\Lambda_c^+ \to \Lambda \mu^+ \overline{\nu}_\mu$ [11]. The Λ_b^0 decay leads to a state with a D_s^+, Λ and a muon. If the decay is reconstructed as semileptonic B decay without the Λ, the reconstructed B mass is shifted to lower masses by around 1116 MeV [11]. In addition to this large shift, the D_s^+ has to be misreconstructed as $D^0 \to K^0_S \pi^+ \pi^-$ decay. Hence, production of D_s^+ mesons through Λ_b^0 decays is expected to contribute insignificantly. The production of D_s^+ mesons through a semileptonic B^0 decay is not known. The contributions of the afore mentioned decay chains are discussed in the following. Possible backgrounds arise from the following D_s^+ decays: The decay $D_s^+ \to K^0_S K^+ \pi^+ \pi^-$ has a branching fraction of $\mathcal{B}(D_s^+ \to K^0_S K^+ \pi^+ \pi^-) = (1.03 \pm 0.10) \times 10^{-2}$ [11] and could contribute where either the kaon is not reconstructed or the positively charged pion is lost, followed by a misidentification of the kaon as pion. The pions cover a momentum range up to 35 GeV and this leads to a misidentification probability of $\approx 10\%$ [54]. In addition, the decay channel $D_s^+ \to K^0_S \pi^+ \pi^+ \pi^-$ with a π^+ not being reconstructed has the same final state particles as a $D^0 \to K^0_S \pi^+ \pi^-$ decay. This decay has a branching fraction of $\mathcal{B}(D_s^+ \to K^0_S \pi^+ \pi^+ \pi^-) = (0.30 \pm 0.11) \times 10^{-2}$ [11]. Another possible contribution arises from $D_s^+ \to K^0_S \pi^+ \pi^+ K^-$ decays with a branching fraction of

$\mathcal{B}(D_s^+ \to K_S^0\pi^+\pi^+K^-) = (1.66 \pm 0.11) \times 10^{-2}$ [11] where the kaon is misidentified as a pion. Further possible partially reconstructed background sources are $D_s^+ \to 3\pi^+2\pi^-$ decays with a branching fraction of $\mathcal{B}(D_s^+ \to 3\pi^+2\pi^-) = (7.9 \pm 0.8) \times 10^{-3}$, $D_s^+ \to 3\pi^+2\pi^-\pi^0$ decays with $\mathcal{B}(D_s^+ \to 3\pi^+2\pi^-\pi^0)$ of $(4.9 \pm 3.2) \times 10^{-2}$ and $D_s^+ \to K_S^0K_S^0\pi^+$ decays with a branching fraction of $\mathcal{B}(D_s^+ \to K_S^0K_S^0\pi^+) = (7.7 \pm 0.6) \times 10^{-3}$.

9.4.1. D_s^+ decays through B production

The decay $B^- \to D_s^{*+}K^-\ell^-\overline{\nu}_\ell$ has a branching fraction of $(3.0 \pm 1.4) \times 10^{-4}$ [11] (conservative uncertainty) and can contribute as a background if the kaon is not reconstructed. The branching fraction ratio is

$$\frac{\mathcal{B}(B^- \to D_s^{*+}K^-\ell^-\overline{\nu}_\ell)}{\mathcal{B}(B^- \to D^0\ell^-\overline{\nu}_\ell)} = (0.013 \pm 0.006). \tag{9.5}$$

Table 9.2 lists the branching fraction ratios for all considered D_s^+ decay channels including misidentification probabilities. The only relevant channel, which is further studied, is the decay $D_s^+ \to 3\pi^+2\pi^-\pi^0$. The fraction of candidates falling inside the D^0 signal mass window with long pion tracks is found to be 1/67 whereas no candidates with downstream pion tracks are found. This renders the contribution to be of order 10^{-4}, and this background is considered negligible.

For the analysis of semileptonically-tagged $D^0 \to K_S^0\pi^+\pi^-$ decays, partially reconstructed D_s^+ backgrounds from a semileptonic B decay are not taken into account due to their low expected contributions to the signal mass window.

9.4.2. D_s^+ decays through B_s^0 production

Compared to production of D_s^+ mesons through a semileptonic B^- decay, the branching fraction of the decay $B_s^0 \to D_s^-\ell^+\overline{\nu}_\ell$ is much larger with $\mathcal{B}(B_s^0 \to D_s^-\ell^+\overline{\nu}_\ell) = (7.9 \pm 2.4) \times 10^{-2}$ [11]. The ratio of the background to signal production branching fraction is

$$\frac{\mathcal{B}(B_s^0 \to D_s^-\ell^+\overline{\nu}_\ell)}{\mathcal{B}(B^- \to D^0\ell^-\overline{\nu}_\ell)} = (3.5 \pm 1.1), \tag{9.6}$$

In addition, the production ratio of 4:1 between B^- and B_s^0 mesons has to be taken into account [89]. The branching fraction ratios and contributions for all considered D_s^+ decay including misidentification probabilities are given in Table 9.3.

The decay $D_s^+ \to K_S^0K^+\pi^+\pi^-$ with the kaon not reconstructed contributes to the signal mass window with $\varepsilon_{m(D^0)} = (5.0 \pm 4.9) \times 10^{-2}$ for K_S^0(LL) candidates. This leads to a contribution of $(1.6 \pm 1.6) \times 10^{-2}$ for the K_S^0(LL) sample, whereas no K_S^0(DD) candidates are found in this channel.

For the decay $D_s^+ \to K_S^0\pi^+\pi^+\pi^-$, the fraction of K_S^0(LL) candidates in the signal mass range is $(2.9 \pm 2.9) \times 10^{-2}$, which renders the overall contribution to be $(4.6 \pm 5.0) \times 10^{-4}$. In the

K^0_S(DD) sample, a larger candidate fraction of $(5.8 \pm 2.5) \times 10^{-2}$ populates the signal mass window resulting in a contribution of $(5.4 \pm 3.5) \times 10^{-3}$.

Two possible background contributions arise from the decay $D_s^+ \to K^0_S K^0_S \pi^+$. In the first case, the pion is not reconstructed and a fraction of $(7.1 \pm 4.9) \times 10^{-2}$ K^0_S(DD) candidates populate the signal mass window leading to a contribution of $(1.7 \pm 1.3) \times 10^{-2}$. This background can be further suppressed by introducing a cut on the invariant mass of the two pions that are reconstructed as bachelor pions of the signal decay; which was not needed in data. It could also happen that the π^+ of one K^0_S candidate is lost and the π^- of the K^0_S meson is reconstructed as bachelor pion of the signal decay. By comparison, a similar fraction of candidates in the signal mass window as for $D_s^+ \to 3\pi^+ 2\pi^-$ is expected. In addition, the bachelor pions are required to form a common vertex with the K^0_S candidate. If the π^- of the K^0_S candidate is reconstructed as bachelor pion, this pion does not point to the same vertex as the K^0_S and the π^+ candidates.

The decay $D_s^+ \to 3\pi^+ 2\pi^-$ contributes with a candidate fraction of $(3.3 \pm 2.3) \times 10^{-2}$ to the signal mass window where the pions are long tracks. No candidates from downstream pion tracks are found. For long pion tracks, this background is expected to have a contribution of $(0.81 \pm 0.62) \times 10^{-2}$. A similar decay is $D_s^+ \to 3\pi^+ 2\pi^- \pi^0$ with a non-reconstructed π^0. In this case, $(1.5 \pm 1.5) \times 10^{-2}$ of candidates built from long tracks lie within the signal mass window. This leads to a contribution of $(2.3 \pm 2.8) \times 10^{-2}$. By imposing vertex requirements on the K^0_S candidate of the signal decay (see Table 7.3 for details), backgrounds from $D_s^+ \to 3\pi^+ 2\pi^- (\pi^0)$ decays are suppressed.

9.5. Treatment of background contributions in the amplitude fit

The background channels discussed in Chapt. 9.1- 9.4 are mostly found to be either negligible or easily suppressible by applying vertex requirements or by introducing cuts on the invariant mass of the bachelor pions. Studies with MC samples of the significant channels $D^0 \to K^0_S K^\pm \pi^\mp$ and $D_s^+ \to K^0_S K^+ \pi^+ \pi^-$, where the latter originates from B_s^0 decays, containing 3 million events, showed that these backgrounds are flat in $m(D^0)$ and have small relative contributions to the $m(D^0)$ sidebands. Therefore, the background shapes included in the amplitude fit are extracted from sWeighted data after final selection and the removal of multiple candidates (see Chapt. 8.3). The sWeights are extracted from a fit to either $m(D^0)$ for the single-tagged datasets or from a fit to δm for the double-tagged datasets. Figure 9.1 shows the fits used to extract the background shapes for the 2011 K^0_S(LL) datasets with a D^0 tag.

Table 9.2.: *Ratio of background to signal branching fractions for D_s^+ decays originating from $B^- \to D_s^+ K^- \ell^- \overline{\nu}_\ell$ decays. The fraction of candidates falling in the signal mass window, $\varepsilon_{m(D^0)}$, is only evaluated for channels with a significant branching fraction ratio.*

Mode	$\mathcal{B}(\text{bkg})/\mathcal{B}(\text{sig}) \times \varepsilon_{\text{misID}}$	$\varepsilon_{m(D^0)}$	$\mathcal{B}(\text{bkg})/\mathcal{B}(\text{sig}) \times \varepsilon_{\text{misID}} \times \varepsilon_{\text{m(D}^0\text{)}}$	Category
$D_s^+ \to K_S^0 K^+ \pi^+ \pi^-$	$(4.8 \pm 2.3) \times 10^{-3}$	K_S^0(LL): – K_S^0(DD): –	K_S^0(LL): – K_S^0(DD): –	negligible
$D_s^+ \to K_S^0 K^+ \pi^+ \pi^-$, Kaon misid	$(4.8 \pm 2.3) \times 10^{-4}$	K_S^0(LL): – K_S^0(DD): –	K_S^0(LL): – K_S^0(DD): –	negligible
$D_s^+ \to K_S^0 \pi^+ \pi^+ \pi^-$	$(1.40 \pm 0.84) \times 10^{-3}$	K_S^0(LL): – K_S^0(DD): –	K_S^0(LL): – K_S^0(DD): –	negligible
$D_s^+ \to K_S^0 \pi^+ \pi^+ K^-$	$(7.8 \pm 3.7) \times 10^{-4}$	K_S^0(LL): – K_S^0(DD): –	K_S^0(LL): – K_S^0(DD): –	negligible
$D_s^+ \to K_S^0 K_S^0 \pi^+$	$(3.6 \pm 1.7) \times 10^{-3}$	K_S^0(LL): – K_S^0(DD): –	K_S^0(LL): – K_S^0(DD): –	negligible
$D_s^+ \to 3\pi^+ 2\pi^-$	$(3.7 \pm 1.8) \times 10^{-3}$	long: – downstream: –	long: – downstream: –	negligible
$D_s^+ \to 3\pi^+ 2\pi^- \pi^0$	$(2.3 \pm 1.9) \times 10^{-2}$	long: 1/67 downstream: –	long: $(3.4 \pm 4.4) \times 10^{-4}$ downstream: –	negligible

Table 9.3.: *Ratio of background to signal branching fractions for D_s^+ decays originating from ($\overline{B}_s^0 \to D_s^+ \ell^- \overline{\nu}_\ell$) decays. The fraction of candidates falling in the signal mass window, $\varepsilon_{m(D^0)}$, is only evaluated for channels with a significant branching fraction ratio.*

Mode	$\mathcal{B}$(bkg)/$\mathcal{B}$(sig) $\times$ $\varepsilon_{\text{misID}}$	$\varepsilon_{m(D^0)}$	$\mathcal{B}$(bkg)/$\mathcal{B}$(sig) $\times$ $\varepsilon_{\text{misID}}$ $\times$ $\varepsilon_{\text{m(D}^0\text{)}}$	Category
$D_s^+ \to K_S^0 K^+ \pi^+ \pi^-$	$(3.2 \pm 1.1) \times 10^{-1}$	K_S^0(LL): 1/20 K_S^0(DD): 0	K_S^0(LL): $(1.6 \pm 1.6) \times 10^{-2}$ K_S^0(DD): –	significant
$D_s^+ \to K_S^0 K^+ \pi^+ \pi^-$, Kaon misid	$(3.2 \pm 1.1) \times 10^{-2}$	K_S^0(LL): – K_S^0(DD): –	K_S^0(LL): – K_S^0(DD): –	negligible
$D_s^+ \to K_S^0 \pi^+ \pi^+ \pi^-$	$(9.2 \pm 4.5) \times 10^{-2}$	K_S^0(LL): 1/35 K_S^0(DD): 5/86	K_S^0(LL): $(2.6 \pm 2.9) \times 10^{-3}$ K_S^0(DD): $(5.4 \pm 3.5) \times 10^{-3}$	negligible
$D_s^+ \to K_S^0 \pi^+ \pi^+ K^-$	$(5.1 \pm 1.7) \times 10^{-2}$	K_S^0(LL): – K_S^0(DD): –	K_S^0(LL): – K_S^0(DD): –	negligible
$D_s^+ \to K_S^0 K_S^0 \pi^+$	$(0.24 \pm 0.08) \times 10^{-1}$	K_S^0(LL): 0 K_S^0(DD): 2/28	K_S^0(LL): – K_S^0(DD): $(1.7 \pm 1.3) \times 10^{-2}$	suppressible
$D_s^+ \to 3\pi^+ 2\pi^-$	$(2.43 \pm 0.81) \times 10^{-1}$	long: 2/60 downstream: 0	long: $(0.81 \pm 0.62) \times 10^{-2}$ downstream: –	suppressible
$D_s^+ \to 3\pi^+ 2\pi^- \pi^0$	1.5 ± 1.1	long: 1/67 downstream: 0	long: $(2.3 \pm 2.8) \times 10^{-2}$ downstream: –	suppressible

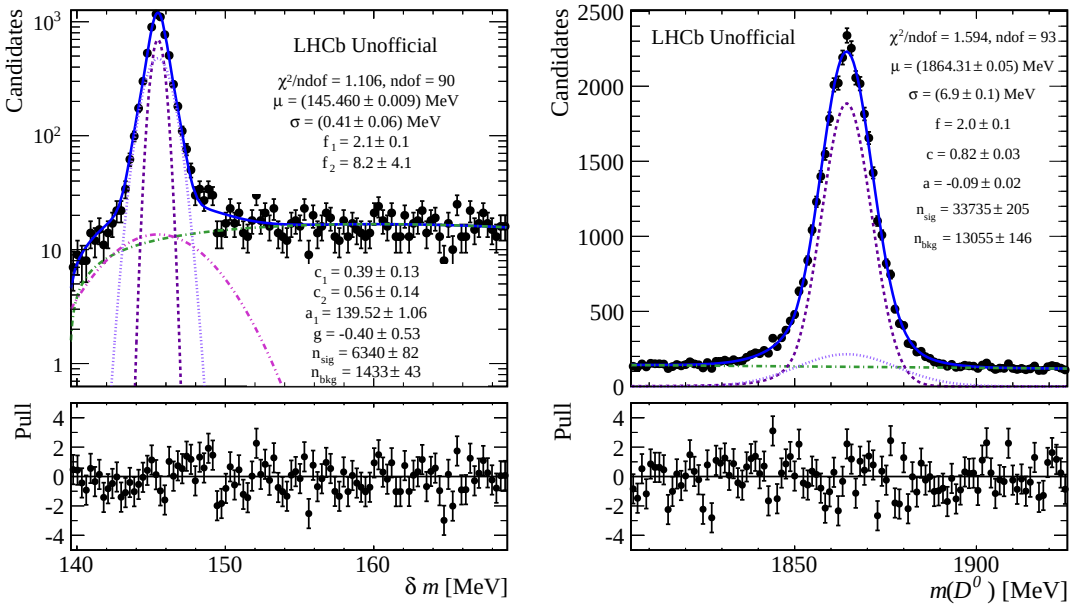

Figure 9.1.: *δm (left) and $m(D^0)$ (right) distribution of the 2011 $D^0 \to K^0_S(\mathrm{LL})\pi^+\pi^-$ datasets after the complete selection with a D^0 tag. The figure depicts the fits (solid blue line) to the data (black points) and the fit components described in Chapt. 8.3.*

The Dalitz variables are computed with the momenta refitted with a K^0_S and D^0 mass constraint. This ensures all events lie within the physical Dalitz plane boundaries given by energy and momentum conservation. The D^0 decay time and Dalitz variable distributions are weighted by the background sWeights and filled in two histograms. From each histogram, a text file is created, which contains the bin centre and content of each bin. These text files containing information on the background distributions in D^0 decay time and phase space are then read in by the fitting code. In addition, a smearing is used to smooth the distributions before they are used in the fit. Thus, in the amplitude fit itself, no sWeights are used directly.

The smearing of the background distributions in phase-space is done with the MEERKAT package [91]. The input distribution is replaced by a sum of Gaussian kernels of a given width. The kernel width has to be small enough to model the details of the distribution but large enough to actually have a smoothing effect. For each candidate with a given $m^2(K^0_S\pi^+)$ and $m^2(K^0_S\pi^-)$, a kernel is drawn centred on this point. The MEERKAT [91] ensures the correct behaviour at the phase-space boundaries.

The background decay time distribution is fitted with a single exponential and the sum of two negative exponentials for the positive and negative tails, respectively. Example fits for the negative and positive tails of the decay time distribution are illustrated in Fig. 9.2. The bin-by-bin value from the sWeighted distribution is then replaced by the integral of this smooth function over the bin width.

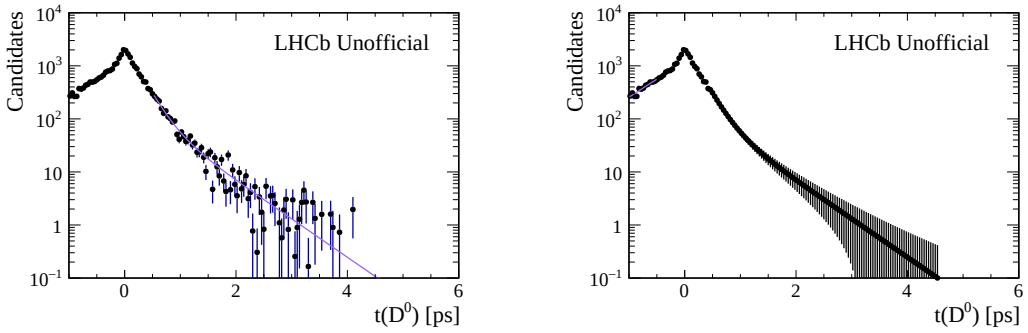

(a) *Positive tail* **(b)** *Negative tail*

Figure 9.2.: *Fits to the background D^0 decay time distribution in the positive tail (left) and the negative tail (right). The figures depicts the fit (solid violet line) to the data (black points). In Fig. 9.2b, the data in the bins of the positive tail have been replaced by the integral of the smooth function over the bin width.*

9.6. Background from wrongly tagged muons

Background from wrongly tagged muons is especially important in searches for *CP* violation since the flavour of the D^0 is determined by the muon charge. The Stripping lines `Strippingb2DstarMuXKsPiPiLLCharmFromBSemiLine` and `Strippingb2DstarMuXKsPiPiDDCharmFromBSemiLine` (see Chapt. 7), used for the double-tagged analysis, allow to use the physical opposite-sign $B^0 \to D^{*-}\mu^+$ decays, and the mistagged same-sign $B^0 \to D^{*-}\mu^-$ reconstructed decays. The same- and opposite sign samples are processed through the complete selection chain (see. Chapt. 7 and 8). A fit to δm is performed for the remaining candidates in the range $139.6 \leq \delta m \leq 169\,\text{MeV}$, where the momenta of the soft pion and the D^0 decay candidates are not refitted with mass constraints. The fit function consists of a triple Gaussian signal component $G(\delta m; \mu, \sigma)$ introduced in Chapt. 8.1 and a polynomial background in $|\delta m - a_1|$ and is defined as

$$\begin{aligned} &F_{\text{muontag}}(\delta m; \mu, \sigma, f_1, f_2, c_1, c_2, a_1, g) \\ &\quad = N \times \Bigg\{ n_{sig} \Big[c_1 G(\delta m; \mu, \sigma) + c_2 G(\delta m; \mu, f_1\sigma) + (1 - c_1 - c_2) G(\delta m; \mu, f_2\sigma) \Big] \\ &\qquad + n_{bkg} \Big[g|\delta m - a_1|^{3/2} + (1-g)\sqrt{|\delta m - a_1|} \Big] \Bigg\}. \end{aligned} \tag{9.7}$$

For the opposite-sign decays, the shape of the signal is fixed due to the low available statistics, whereas the background shape is allowed to float. The fits are illustrated in Fig. 9.3 for the opposite-sign and in Fig. 9.4 for the same-sign sample. The probability of having a muon with an incorrect tag is estimated as

$$\omega_{\text{muontag}} = \frac{n_{sig}(\text{SS})}{n_{sig}(\text{SS}) + n_{sig}(\text{OS})}, \tag{9.8}$$

since the probability to reconstruct the pion charge incorrectly is negligible. The values and

mistag probabilities are listed in Table 9.4. As can be seen from Table 9.4, the mistag probabilities are small.

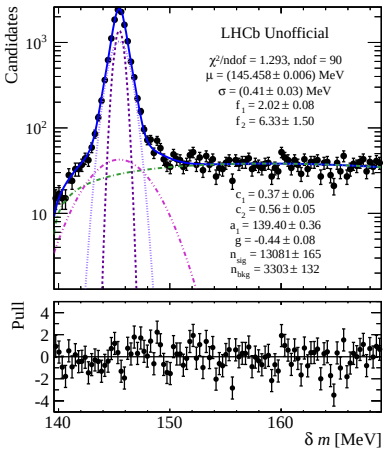

(a) *2011* K^0_S(LL)

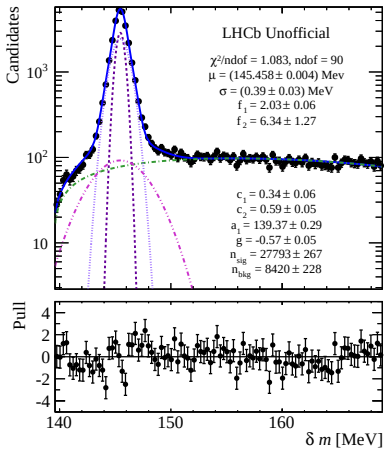

(b) *2011* K^0_S(DD)

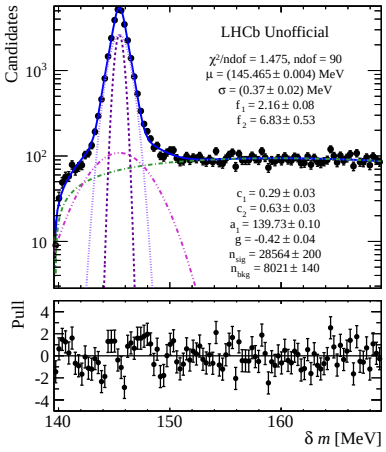

(c) *2012* K^0_S(LL)

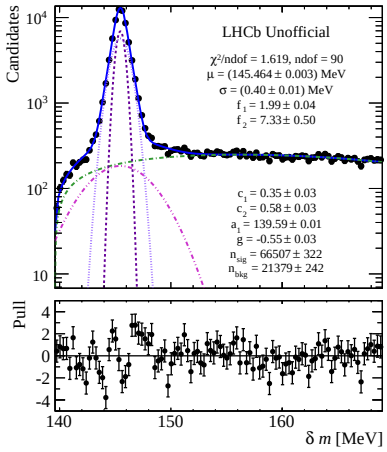

(d) *2012* K^0_S(DD)

Figure 9.3.: *δm distribution for opposite sign $B^0 \to D^{*-}\mu^+$ decays after the complete selection chain split by K^0_S type and data-taking period. The figure depicts the fit (solid blue line) to the data (black points) and the fit components. The signal is modelled by a triple Gaussian (dotted lavender line, dashed magenta line and dotted-dashed pink line) and the background is described by a polynomial (green dotted-dashed line).*

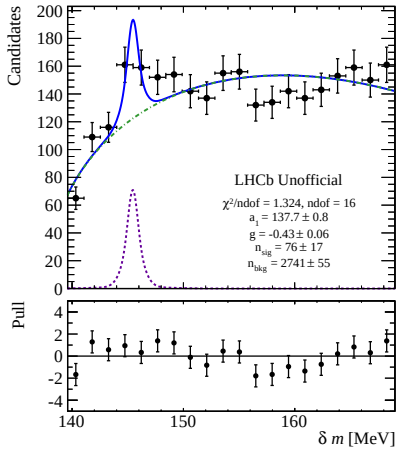

(a) *2011* K^0_S(LL)

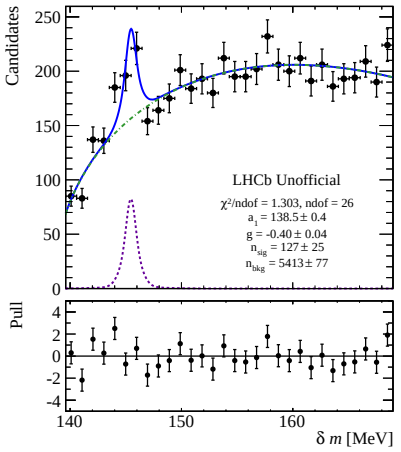

(b) *2011* K^0_S(DD)

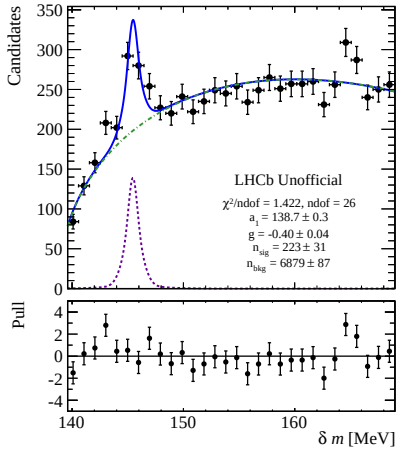

(c) *2012* K^0_S(LL)

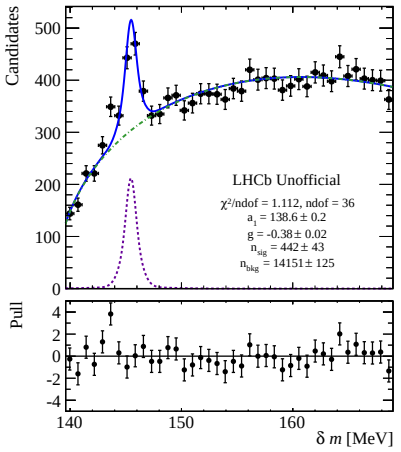

(d) *2012* K^0_S(DD)

Figure 9.4.: *δm distribution for same-sign $B^0 \to D^{*-}\mu^-$ decays after the complete selection chain split by K^0_S type and data-taking period. The figure depicts the fit (solid blue line) to the data (black points) and the fit components. The signal is modelled by a single Gaussian (dashed magenta line) and the background is described by a polynomial (green dotted-dashed line).*

Table 9.4.: *Signal yields in the same-sign $B^0 \to D^{*-}\mu^-$ and opposite-sign $B^0 \to D^{*-}\mu^+$ decays of the $\overline{B}^0 \to D^{*+}(\to D^0(\to K^0_S\pi^+\pi^-)\pi^+)\mu^-\overline{\nu}_\mu$ datasets and the corresponding mistag probability split by year and K^0_S type.*

	n_{sig}(SS)	n_{sig}(OS)	ω_{muontag} [%]
2011 K^0_S(LL)	76±17	13081 ± 165	0.58 ± 0.13
2011 K^0_S(DD)	127 ± 25	27793 ± 267	0.45 ± 0.09
2012 K^0_S(LL)	223 ± 31	28564 ± 200	0.77 ± 0.11
2012 K^0_S(DD)	442 ± 43	66507 ± 321	0.66 ± 0.06

10. Acceptance and resolution effects

Having been built as a single-arm forward spectrometer, the LHCb detector covers a limited range in solid angle. This leads to a limited geometrical acceptance, and the design of the detector and the applied selection criteria lead to a limited acceptance for characteristics such as particle momenta or decay times. A correction is required for these acceptance effects as well as for detector resolution effects. The acceptance and resolution are determined from MC simulation samples, which also model the detector response.

10.1. Phase-space acceptance

For the amplitude analysis it is crucial to model acceptance variations in D^0 decay time $t(D^0)$ and across the Dalitz plane. The aim of the acceptance study is not only to measure the acceptance but to find a mathematical parameterisation describing the variations as a function of position in the Dalitz plane, which will enter the amplitude fit. The acceptance is measured on simulated MC data with tight generator-level cuts applied, listed in Tables 6.3 and 6.4. The most straightforward parameterisation of the acceptance variations is found to be in terms of $m^2(\pi^+\pi^-)$ and $\cos(\theta)$ where θ is the decay angle between the π^- (π^+) and D^0 ($\overline{D}^0$) in the $\pi^+\pi^-$ rest frame, *i.e.* it has the form of an helicity angle. These variables are a good choice as they are correlated with the momenta of the daughter particles: $m^2(\pi^+\pi^-)$ depends on the K^0_S momentum and $\cos(\theta)$ on the bachelor pion momenta. The cosine of the decay angle is given by

$$\begin{aligned}\cos(\theta) = &\frac{1}{\sqrt{(m^2(\pi^+\pi^-) - (m^2(\pi^+) - m^2(\pi^-)))^2 - 4m^2(\pi^+\pi^-)m^2(\pi^-)}} \\ &\times \left\{ \frac{m^2(\pi^+\pi^-)(m^2(K^0_S\pi^+) - m^2(K^0_S\pi^-))}{\sqrt{(-m^2(\pi^+\pi^-) + (m^2(D^0) - m^2(K^0_S)))^2 - 4m^2(\pi^+\pi^-)m^2(K^0_S)}} \right. \\ &\left. + \frac{(m^2(\pi^-) - m^2(\pi^+))(m^2(D^0) - m^2(K^0_S))}{\sqrt{(-m^2(\pi^+\pi^-) + (m^2(D^0) - m^2(K^0_S)))^2 - 4m^2(\pi^+\pi^-)m^2(K^0_S)}} \right\}. \end{aligned} \tag{10.1}$$

To determine if the acceptance is time-dependent, the acceptance is measured in bins in $t(D^0)$, which are then subdivided into two-dimensional bins in $m^2(\pi^+\pi^-)$ and $\cos(\theta)$. This study in ranges of $t(D^0)$ showed no dependency of the acceptance on D^0 decay time. Therefore, the acceptance is solely measured in two-dimensional bins in the Dalitz plane. The boundaries of the two-dimensional bins are chosen such that each bin contains approximately the same amount of data. In each bin, the mass of the D^0 candidate, after a refit of the decay with a K^0_S mass constraint and having passed the complete selection chain (see Chapt. 7 and 8), is fitted with a single Gaussian function as signal and a constant function as background component. An example fit is shown in Fig 10.1 for the lowest $(\cos(\theta), m^2(\pi^+\pi^-))$ bin of the 2012 K^0_S(LL)

sample. The number of signal events n_{sig} is extracted from the extended maximum likelihood fit and serves as numerator of the acceptance. For the K^0_S(LL) samples, 18×18 bins are used whereas the number of bins in the K^0_S(DD) samples is increased to 31×31 due to the larger available statistics.

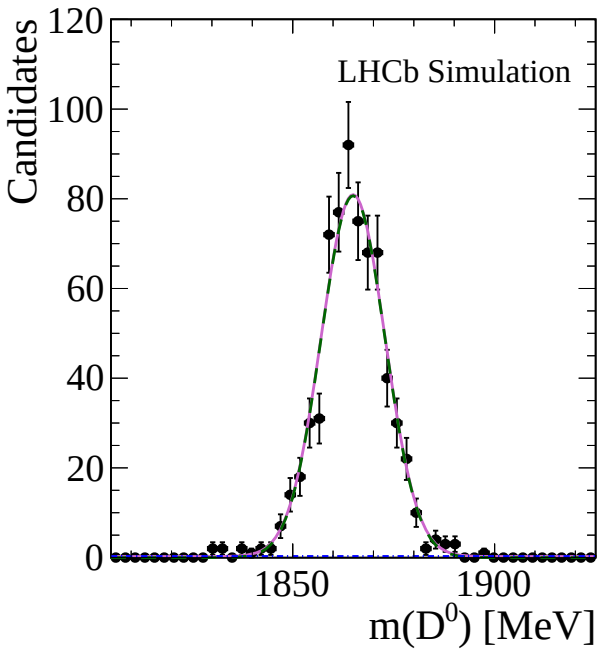

Figure 10.1.: *$m(D^0)$ distribution in the lowest $m^2(\pi^+\pi^-)$ and $\cos(\theta)$ bin of the 2012 K^0_S(LL) single-tagged MC sample with tight generator-level cuts after the complete selection chain. The figure depicts the fit (dashed magenta line) to the data (black points) and the fit components. The signal consists of a Gaussian function (dashed green line). The background is modelled by a constant function (solid blue line).*

The acceptance in each two-dimensional $(\cos(\theta), m^2(\pi^+\pi^-))$ bin is calculated as

$$\varepsilon = \frac{n_{sig}}{n_{gen}}, \tag{10.2}$$

where the denominator is evaluated by counting the total number of generated candidates, n_{gen}, prior to the application of any selection criteria. The denominator uses a particle gun sample (see Chapt. 6.2) on generator-level as input, which uses the full PYTHIA 8 momentum distributions of the B candiadate without the application of acceptance cuts.

The measured acceptances and the barycentre of the $\cos(\theta)$ and $m^2(\pi^+\pi^-)$ distributions in each two-dimensional bin in $(\cos(\theta), m^2(\pi^+\pi^-))$ are taken as input for a two-dimensional fit to extract an analytic parameterisation, which describes the acceptance variations as a function of $\cos(\theta)$ and $m^2(\pi^+\pi^-)$.
As can be seen from the example distributions in Figs. 10.2 and 10.3 for the 2012 K^0_S(LL) sample, the acceptance variation can be fitted with the form

$$\begin{aligned}\varepsilon(m^2(\pi^+\pi^-),\cos(\theta)) = q_0 \times m^4(\pi^+\pi^-) + q_1 \times m^2(\pi^+\pi^-) \\ + q_2 \times m^2(\pi^+\pi^-)\cos^2(\theta) + q_3 \times \cos^2(\theta) \\ + q_4 \times \cos(\theta) + q_5.\end{aligned} \tag{10.3}$$

The uncertainties on the measured acceptance are calculated as binomial errors whereas the uncertainty on the parameterised acceptance results from a Gaussian error propagation of the fit uncertainties. Correlations between the fit parameters were taken into account. In Appendix D, the projections of the phase-space acceptance on the $m^2(\pi^+\pi^-)$ and $\cos(\theta)$ axes are shown in bins of $\cos(\theta)$ and $m^2(\pi^+\pi^-)$, respectively.

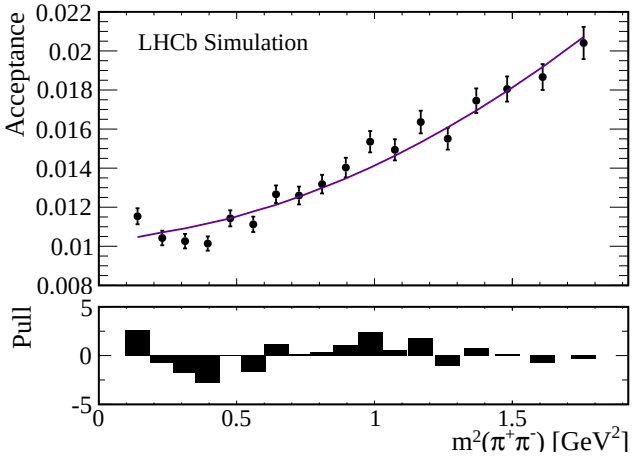

Figure 10.2.: *Single-tagged phase-space acceptance as a function of $m^2(\pi^+\pi^-)$ in the lowest $\cos(\theta)$ bin for the 2012 K^0_S(LL) MC sample with tight generator-level cuts after the complete selection chain. The black points correspond to the measured acceptance whereas the parameterisation is depicted in purple.*

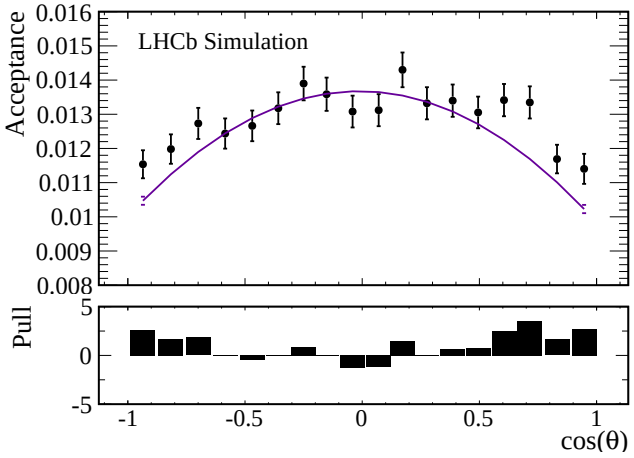

Figure 10.3.: *Single-tagged phase-space acceptance as a function of $\cos(\theta)$ in the lowest $m^2(\pi^+\pi^-)$ bin for the 2012 K^0_S(LL) MC sample with tight generator-level cuts after the complete selection chain. The black points correspond to the measured acceptance whereas the parameterisation is depicted in purple.*

Figures 10.4 and 10.5 show the measured and parameterised acceptance as function of $(\cos(\theta), m^2(\pi^+\pi^-))$ for the K^0_S(LL) 2012 sample. The difference between the two acceptances is depicted in Fig. 10.5.

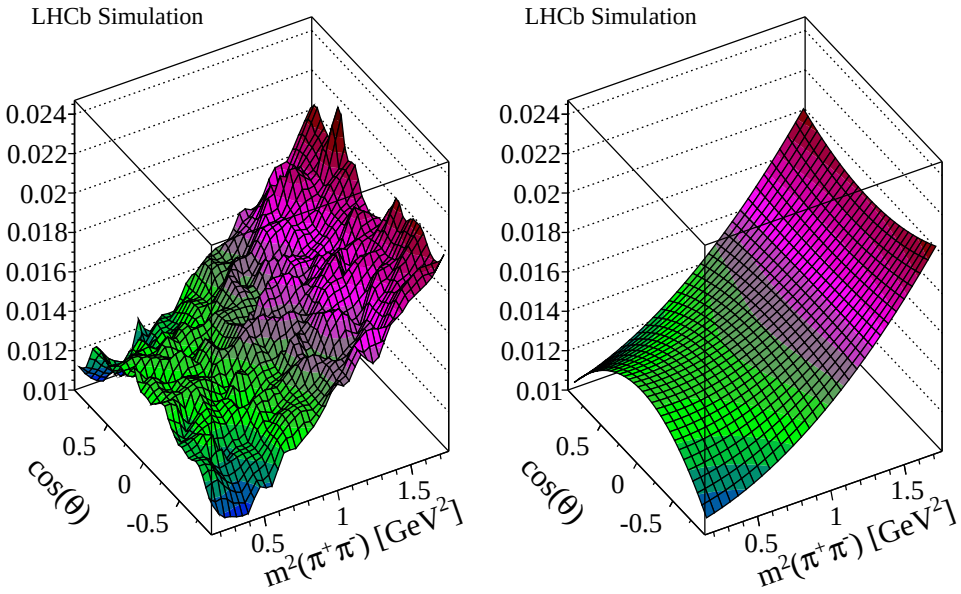

Figure 10.4.: *Measured (left) and parameterised (right) single-tagged phase-space acceptance as a function of* $(\cos(\theta), m^2(\pi^+\pi^-))$ *for the 2012* K^0_S(LL) *MC sample with tight generator-level cuts after the complete selection chain.*

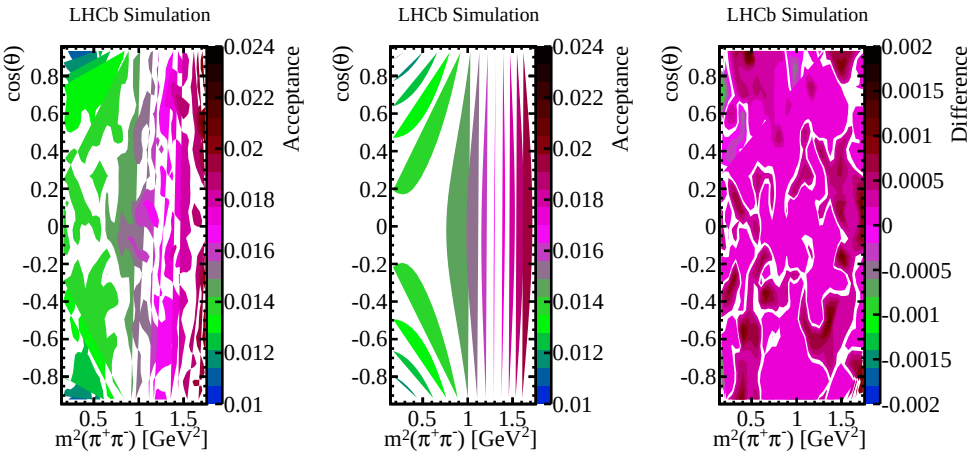

Figure 10.5.: *Measured (left) and parameterised (centre) single-tagged phase-space acceptance as a function of* $(\cos(\theta), m^2(\pi^+\pi^-))$ *for the 2012* K^0_S(LL) *MC sample with tight generator-level cuts after the complete selection chain. The difference of the measured and parameterised acceptance is shown on the right.*

The acceptance parameterisation for $\overline{B}^0 \to D^{*+}(\to D^0(\to K^0_S\pi^+\pi^-)\pi^+)\mu^-\overline{\nu}_\mu$ decays is extracted following the same procedure as for the $B^- \to D^0(\to K^0_S\pi^+\pi^-)\mu^-\overline{\nu}_\mu$ decays. The kinematic distributions used to evaluate the acceptance agree well for the single- and double-tagged

samples, as shown in Appendix E, consequently the same MC samples with tight generator-level cuts applied are used to determine the acceptance for double-tagged decays.

The comparison between the measured acceptance and the parameterisation is illustrated in Figs. 10.6 and 10.7 for the 2012 K^0_S(LL) subsample of the single- and double-tagged samples. The parameters of the final acceptance parameterisation are listed in Tables 10.1 and 10.2 for single- and double-tagged decays.

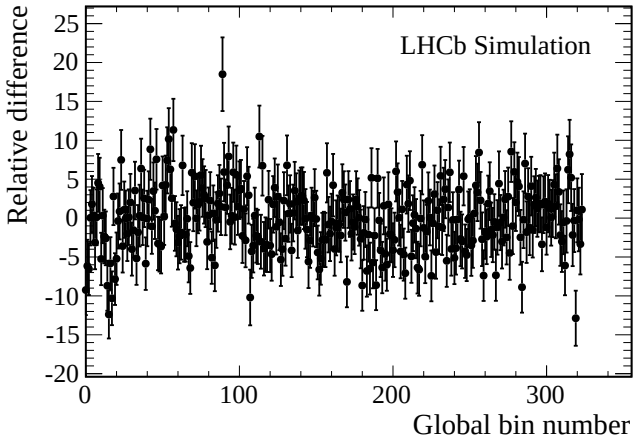

Figure 10.6.: *Relative difference of the parameterised to measured single-tagged phase-space acceptance for the 2012 K^0_S(LL) MC sample with tight generator-level cuts after the complete selection chain. The global bin number is defined as follows: 0-17 corresponds to the first $m^2(\pi^+\pi^-)$ bin with consecutive bins in $\cos(\theta)$, 18-35 corresponds to the second bin in $m^2(\pi^+\pi^-)$ bin with consecutive bins in $\cos(\theta)$ etc.*

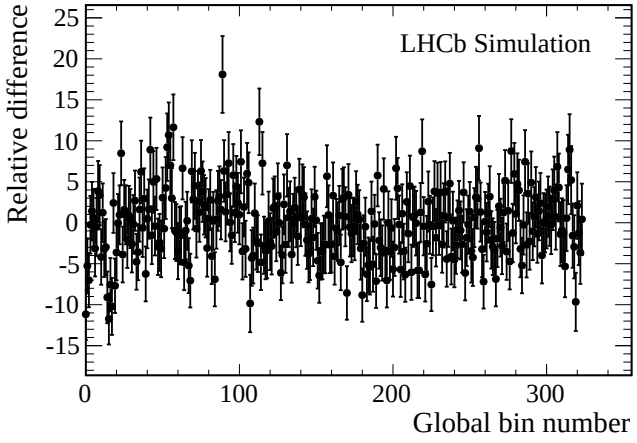

Figure 10.7.: *Relative difference of the parameterised to measured double-tagged phase-space acceptance for the 2012 K^0_S(LL) MC sample with tight generator-level cuts after the complete selection chain. The global bin number is defined as follows: 0-17 corresponds to the first $m^2(\pi^+\pi^-)$ bin with consecutive bins in $\cos(\theta)$, 18-35 corresponds to the second bin in $m^2(\pi^+\pi^-)$ bin with consecutive bins in $\cos(\theta)$ etc.*

Table 10.1.: *Parameters of the single-tagged phase-space acceptance $\varepsilon(m^2(\pi^+\pi^-), \cos(\theta))$ split by year and K^0_S type for a MC sample with tight generator-level cuts after the complete selection chain.*

	2011		2012	
	K^0_S(LL)	K^0_S(DD)	K^0_S(LL)	K^0_S(DD)
$q_0\,[10^{-3}\,\text{GeV}^4]$	3.14 ± 0.21	4.70 ± 0.34	2.70 ± 0.15	3.28 ± 0.25
$q_1\,[10^{-3}\,\text{GeV}^2]$	-2.16 ± 0.40	1.31 ± 0.62	-1.59 ± 0.27	1.99 ± 0.47
$q_2\,[10^{-3}\,\text{GeV}^2]$	2.97 ± 0.32	7.51 ± 0.50	3.18 ± 0.22	8.98 ± 0.37
$q_3\,[10^{-3}]$	-4.11 ± 0.28	-8.98 ± 0.43	-4.20 ± 0.20	-9.58 ± 0.33
$q_4\,[10^{-5}]$	-11.21 ± 7.11	-7.15 ± 11.11	-8.60 ± 4.88	-9.45 ± 8.46
$q_5\,[10^{-2}]$	1.56 ± 0.02	3.58 ± 0.03	1.38 ± 0.02	3.97 ± 0.02

Table 10.2.: *Parameters of the double-tagged phase-space acceptance $\varepsilon(m^2(\pi^+\pi^-), \cos(\theta))$ split by year and K^0_S type for MC sample with tight generator-level cuts after the complete selection chain.*

	2011		2012	
	K^0_S(LL)	K^0_S(DD)	K^0_S(LL)	K^0_S(DD)
$q_0\,[10^{-3}[\,\text{GeV}^4]$	3.11 ± 0.21	5.24 ± 0.35	2.74 ± 0.15	3.76 ± 0.26
$q_1\,[10^{-3}[\,\text{GeV}^2]$	-2.16 ± 0.39	0.77 ± 0.64	-1.58 ± 0.27	1.57 ± 0.48
$q_2\,[10^{-3}[\,\text{GeV}^2]$	2.96 ± 0.32	7.97 ± 0.51	3.12 ± 0.22	9.57 ± 0.38
$q_3\,[10^{-3}]$	-4.11 ± 0.28	-9.43 ± 0.44	-4.16 ± 0.19	-10.18 ± 0.33
$q_4\,[10^{-5}]$	-8.93 ± 7.05	-4.86 ± 11.35	-8.40 ± 4.91	-7.33 ± 8.68
$q_5\,[10^{-2}]$	1.54 ± 0.02	3.76 ± 0.03	1.39 ± 0.01	4.21 ± 0.02

The parameter q_4 has large uncertainties and assuming Gaussian uncertainties, the one-tailed p-values are calculated as an estimate of how consistent this parameter is with being zero. All p-values are found to be below 50% and hence, parameter q_4 cannot be set to zero.

10.2. Decay-time acceptance

The `Hlt2TopoMu{2,3,4}BodyBBDTDecision` trigger lines, described in Chapt. 7.1, utilise a distance of closest approach requirement when forming the trigger candidates. This causes a decay-time acceptance, which has to be corrected for in the amplitude fit. The decay-time acceptance $\varepsilon(t)$ is determined from MC samples with tight generator-level cuts applied, listed in Tables 6.3 and 6.4, which are passed through the complete selection chain. The selection decision is evaluated on reconstructed variables. The decay-time acceptance is evaluated as the ratio of the generated D^0 decay time distribution after the complete selection and after the Stripping, since this part of the preselection does not introduce decay-time dependent acceptance effects. The decay-time acceptance is obtained by fitting the ratio distribution with an exponential function of the form $b \times \exp(-a \times t(D^0))$, where b is a normalisation factor. The implementation of the decay-time acceptance in the amplitude fit is outlined in detail in

Chapt. 11.3.

The decay-time acceptance is illustrated in Figs. 10.8 and 10.9 for the single- and double-tagged samples. The slope of the exponential function is given in Tables 10.3 and 10.4 for single- and double-tagged samples. The D^0 lifetimes with and without correction of the decay-time acceptance are given in Table 10.3 for the single-tagged sample. They are obtained by a fit to data that is blinded in x and y and with an isobar model including the resonances listed in Table 11.4 under the assumption of no *CP* violation. The blinding procedure is outlined in Chapt. 11.4 and details on the isobar model are given in Chapt. 11.1.6.

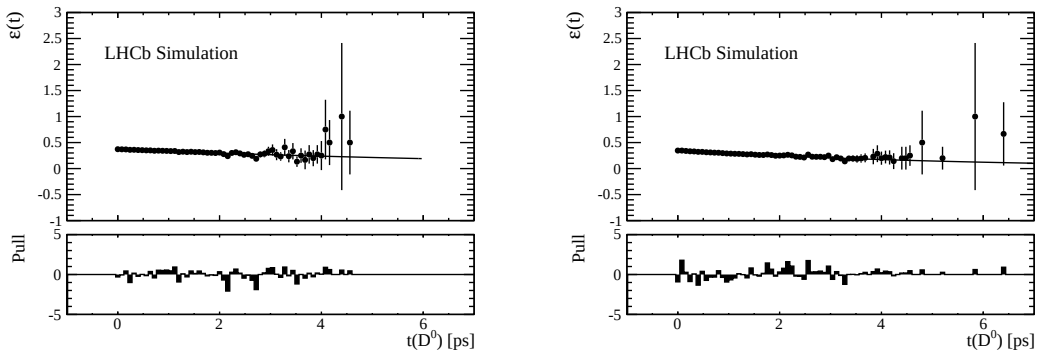

(a) *2011* K^0_S(LL) **(b)** *2011* K^0_S(DD)

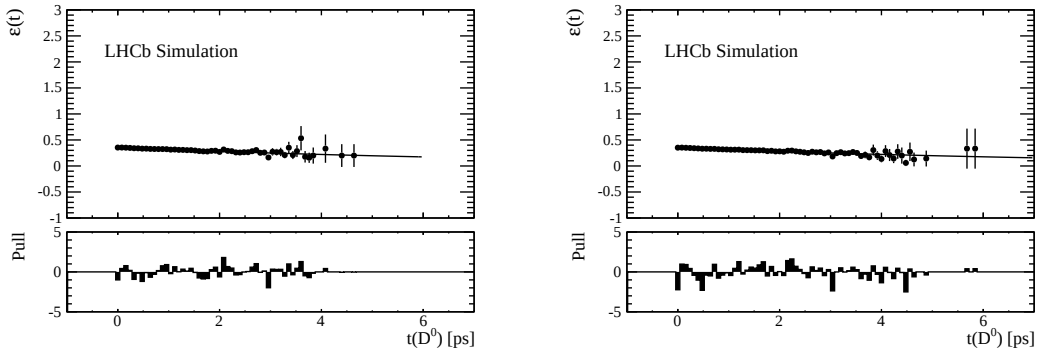

(c) *2012* K^0_S(LL) **(d)** *2012* K^0_S(DD)

Figure 10.8.: *Decay-time acceptance bias for the* $B^- \to D^0(\to K^0_S\pi^+\pi^-)\mu^-\overline{\nu}_\mu$ *sample split by year and* K^0_S *type.*

Table 10.3.: *Slope of the exponential fit to the decay-time acceptance as well as the uncorrected and corrected* D^0 *lifetimes split by year and* K^0_S *type for* $B^- \to D^0(\to K^0_S\pi^+\pi^-)\mu^-\overline{\nu}_\mu$ *decays. The world average of the* D^0 *lifetime is* (410.10 ± 1.5) fs *[11].*

Mode	$a\,[\mathrm{ps}^{-1}]$	$\tau(D^0)\,[\mathrm{fs}]$	$\tau(D^0)_{\mathrm{corr}}\,[\mathrm{fs}]$
2011 K^0_S(LL)	0.112 ± 0.008	387.9 ± 1.6	405.5 ± 1.7
2011 K^0_S(DD)	0.174 ± 0.005	382.0 ± 1.2	409.2 ± 1.4
2012 K^0_S(LL)	0.119 ± 0.006	393.1 ± 1.0	412.4 ± 1.2
2012 K^0_S(DD)	0.117 ± 0.003	393.8 ± 0.8	412.8 ± 0.9

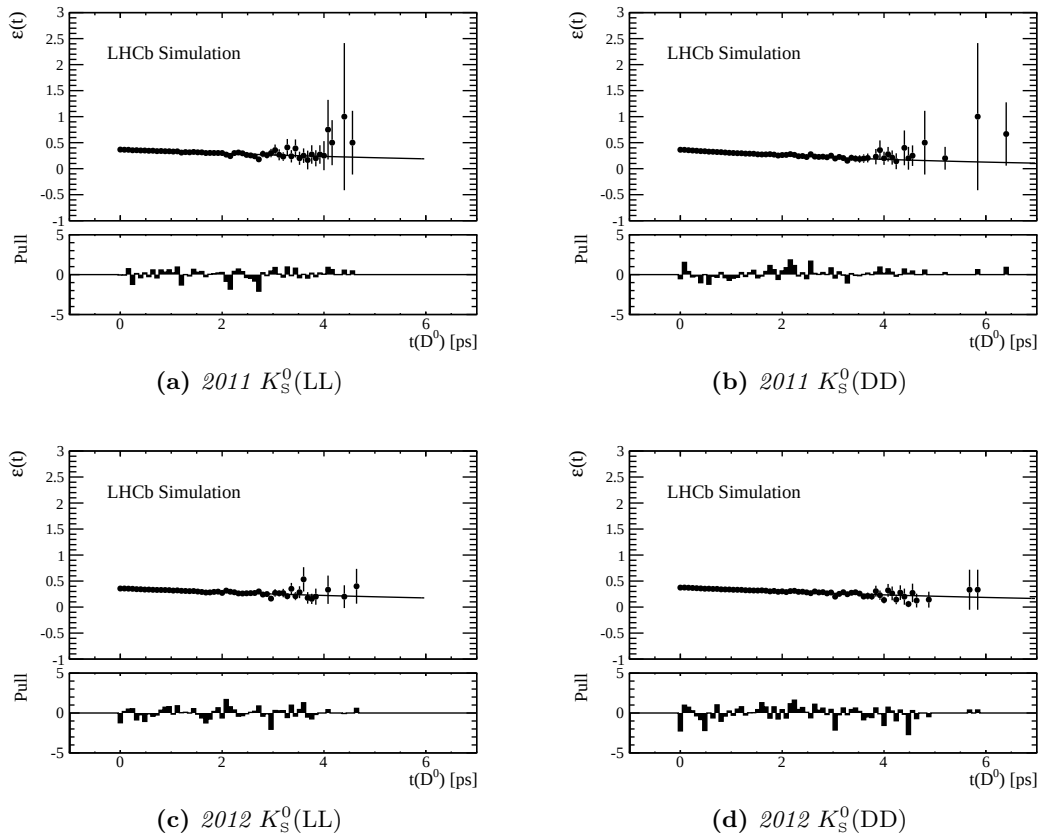

(a) *2011* K^0_S(LL) **(b)** *2011* K^0_S(DD)

(c) *2012* K^0_S(LL) **(d)** *2012* K^0_S(DD)

Figure 10.9.: *Decay-time acceptance for the* $\overline{B}^0 \to D^{*+}(\to D^0(\to K^0_S\pi^+\pi^-)\pi^+)\mu^-\overline{\nu}_\mu$ *sample split by year and* K^0_S *type.*

Table 10.4.: *Slope of the exponential fit to the decay-time acceptance split by year and* K^0_S *type for* $\overline{B}^0 \to D^{*+}(\to D^0(\to K^0_S\pi^+\pi^-)\pi^+)\mu^-\overline{\nu}_\mu$ *decays.*

Mode	$a\,[\,\mathrm{ps}^{-1}]$
2011 K^0_S(LL)	0.111 ± 0.008
2011 K^0_S(DD)	0.177 ± 0.005
2012 K^0_S(LL)	0.119 ± 0.006
2012 K^0_S(DD)	0.119 ± 0.003

10.3. Upper decay-time acceptance

In addition to the decay-time acceptance in D^0 decay time caused by the `Hlt2TopoMu{2,3,4}BodyBBDTDecision` trigger lines (see 10.2), a decay-time dependent acceptance is introduced by the track-finding algorithm. When matching VELO R and ϕ sensor hits to form VELO tracks, the track-finding algorithm applies a clone-killing that removes tracks sharing a large fraction of VELO segments. The clone-killing algorithm favours tracks originating from the beam line (on-axis tracks). For $D^0 \to K^0_S\pi^+\pi^-$, most tracks have a large flight distance and are consequently mostly off-axis tracks. For this reason, the clone-killing algorithm causes tracks from long-lived particles to be reconstructed with a lower acceptance

compared to tracks from short-lived particles. This upper decay-time acceptance is evaluated in two steps: First, the acceptance is computed as a function of the z-component of the shortest displacement vector between the particle's decay vertex and the nominal beam, d_z. In a second step, the D^0 and K^0_S end vertices are moved in steps along the beam line to determine the dependence of d_z^2 on $t(D^0)$. The beam position in x and y is calculated as the average of the (x, y) positions of all PVs

$$x_{beam} = \frac{\sum x_{PV}}{n_{PV}}, \tag{10.4}$$

$$y_{beam} = \frac{\sum yPV}{n_{PV}}, \tag{10.5}$$

where n_{PV} is the number of PVs. The z-component of the beam position $b = (x_{beam}, y_{beam}, z_{beam})$ is assumed to be zero. The displacement of the particle's decay vertex with respect to the beam position $\vec{b}$ is given by

$$\vec{s} = \vec{v} - \vec{b}, \tag{10.6}$$

with the decay vertex $\vec{v}$. The z-component of the shortest displacement vector between the particle trajectory and the nominal beam, d_z, then is calculated as

$$d_z = \left[\frac{\vec{k}}{|\vec{k}|} \times (0, 0, 1) \right] \cdot \vec{s}, \tag{10.7}$$

where the particle's momentum is denoted by $\vec{k}$ and $(0, 0, 1)$ points along the beam line.

The acceptance as a function of d_z^2 is evaluated with MC truth information on generator-level only samples with acceptance cuts applied, listed in Tables 6.3 and 6.4. For each of the bachelor pion and the K^0_S daughter pion tracks the acceptance is computed. This is obtained from the ratio of reconstructed tracks and those at generator-level, which are assessed as reconstructible long tracks. In the determination of the upper decay-time acceptance tracks are considered reconstructed if they share at least 70% of the clusters in the VELO and 70% in the seeding stations with the reconstructible track [92]. The seedings stations are the stations of the TT used to reconstruct track segments, which are then extrapolated to the VELO. As can be seen from Fig. 10.10, the efficiencies can be parameterised as follows

$$\varepsilon(d_z^2) = \alpha + \beta \times d_z^2, \quad \text{for bachelor pions,} \tag{10.8}$$

$$\varepsilon(d_z^2) = \alpha + \beta \times d_z^2 + e^{\gamma + \delta \times d_z^2}, \quad \text{for } K^0_S \text{ daughter pions.} \tag{10.9}$$

The parameters defined in Eqns. 10.8 and 10.9 are listed in Table 10.5 and are used to evaluate the upper decay-time acceptance for single- and double-tagged decays. It should be noted that the D^0 upper decay time acceptance is indeed the D^0 upper decay time acceptance convoluted with the detector resolution. Additional material can be found in Appendix F.

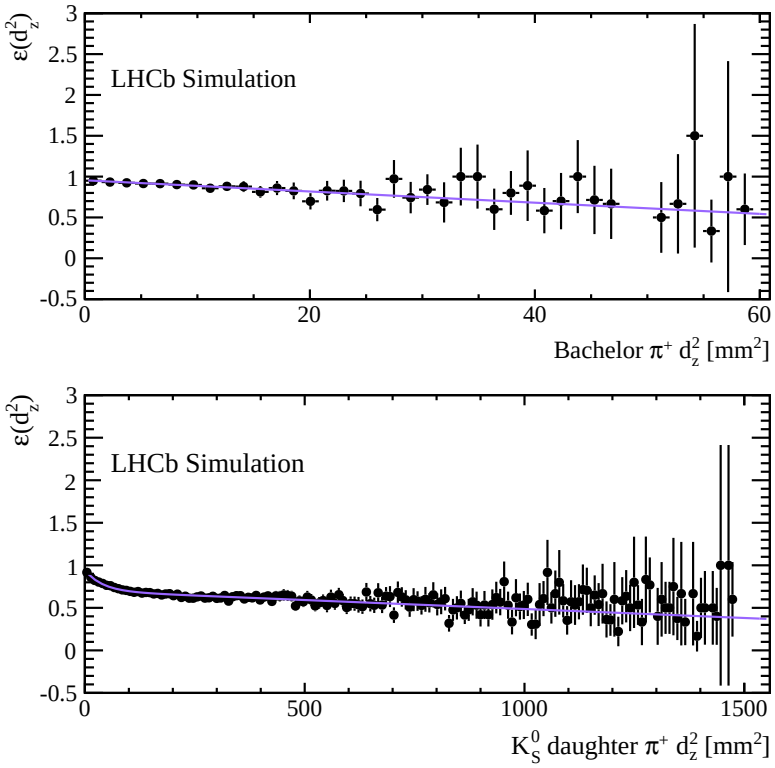

Figure 10.10.: *Tracking acceptance as a function of d_z^2 for the positively charged bachelor and K_S^0 daughter pions for 2012. The measured efficiencies (black) are overlaid with a fit according to Eqns. 10.8 and 10.9 (purple).*

Table 10.5.: *Parameters of the tracking acceptance as function of d_z split by year and listed for the bachelor and K_S^0 daughter pions.*

	2011	2012
	Bachelor π^+	
α	0.969 ± 0.001	0.955 ± 0.001
$\beta\,[\mathrm{mm}^{-2}]$	-0.005 ± 0.001	-0.007 ± 0.001
	Bachelor π^-	
α	0.968 ± 0.001	0.955 ± 0.001
$\beta\,[\mathrm{mm}^{-2}]$	-0.004 ± 0.001	-0.007 ± 0.001
	K_S^0 daughter π^+	
α	0.74 ± 0.01	0.697 ± 0.009
$\beta\,[\mathrm{mm}^{-2}]$	-0.00017 ± 0.00003	-0.00021 ± 0.00002
γ	-1.52 ± 0.05	-1.41 ± 0.03
$\delta\,[\mathrm{mm}^{-2}]$	-0.019 ± 0.002	-0.025 ± 0.002
	K_S^0 daughter π^-	
α	0.74 ± 0.01	0.709 ± 0.008
$\beta\,[\mathrm{mm}^{-2}]$	-0.00019 ± 0.00002	-0.00026 ± 0.00002
γ	-1.56 ± 0.05	-1.46 ± 0.03
$\delta\,[\mathrm{mm}^{-2}]$	-0.019 ± 0.002	-0.027 ± 0.002

The decay-time dependence is evaluated by moving the D^0 and K^0_S decay vertices in steps along the D^0 direction of flight $\vec{f}$, where $\vec{f}$ is a unit vector with space dimension. This second step is performed on data after the complete selection. In this study, the single- and double-tagged samples have not been split and the double-tagged sample does not have the cut $1844.86 \leq m(D^0) \leq 1884.86\,\text{MeV}$ applied. This will not change the outcome of the study, as the upper decay-time acceptance is caused by the tracking algorithm. For step i, the displacement vector of a particle is given by

$$\vec{s}(i) = \vec{v} - \vec{b} + i \times \vec{f}, \tag{10.10}$$

with the direction of flight $\vec{f}$ and decay vertex $\vec{v}$. The D^0 and K^0_S vertices are moved until the z-component of the vertex lies behind the z-component of the primary vertex p. The D^0 decay time at each step i is computed as

$$\begin{aligned} t(i) = \frac{1}{c}\frac{m(D^0)}{f(D^0)} \big\{ &(v_x(D^0) + i \times f_x(D^0) - p_x(D^0))^2 \\ &+(v_y(D^0) + i \times f_y(D^0) - p_y(D^0))^2 \\ &+(v_z(D^0) + i \times f_z(D^0) - p_z(D^0))^2 \big\}^{1/2}, \end{aligned} \tag{10.11}$$

where c is the speed of light. In Eqn. 10.11, $m(D^0)$ refers to the mass of the D^0 and p to the corresponding PV.
This yields a distribution of d_z versus D^0 decay time, which is fitted with a first order polynomial

$$d_z(t(D^0)) = p_0[\,\text{mm}^2] + \text{p}_1 \times \text{t(D}^0)[\,\text{mm}^2]/[\,\text{ps}] \tag{10.12}$$

for each event. An example distribution is shown in Fig. 10.11.

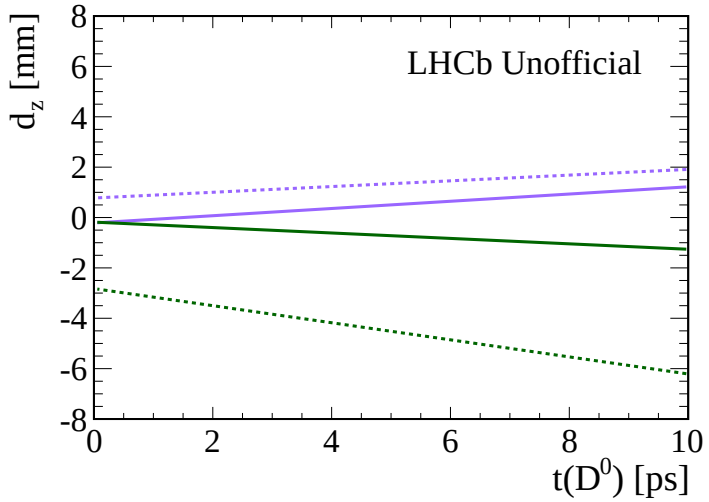

Figure 10.11.: *Example d_z distribution depending on D^0 decay time. The distributions for the bachelor π^+ (lavender, solid), bachelor π^- (green, solid), K^0_S daughter π^+ (lavender, dashed) and K^0_S daughter π^- (green, dashed).*

For each event, the decay time-dependent acceptance is calculated by replacing d_z in Eqns. 10.8 and 10.9 and by the linear dependence of d_z on decay time (see Eqn. 10.12). To retrieve the overall acceptance for K^0_S(LL) samples, the efficiencies for both bachelor pions and both K^0_S daughter pions are multiplied, whereas for K^0_S(DD) samples the efficiencies of the K^0_S daughter pions are omitted as they do not decay inside the VELO. The upper decay-time acceptance is obtained by dividing the D^0 decay time distribution, weighted by the per-event efficiency, by the unweighted distribution.

The upper decay-time acceptance $\varepsilon_{\mathrm{UDT}}(t)$ for single-tagged decays is shown in Fig. 10.12, and the double-tagged upper decay-time acceptance is illustrated in Fig. 10.13.

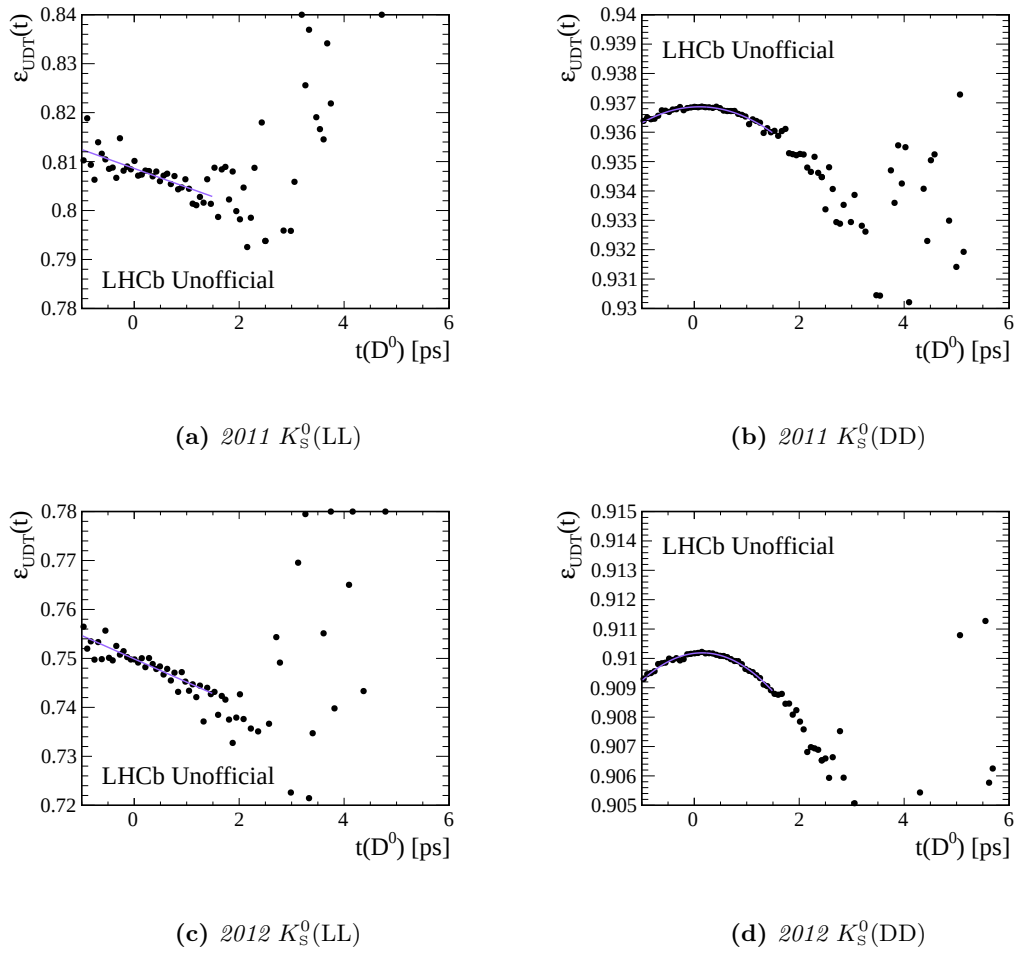

(a) *2011* K^0_S(LL) **(b)** *2011* K^0_S(DD)

(c) *2012* K^0_S(LL) **(d)** *2012* K^0_S(DD)

Figure 10.12.: *Upper decay-time acceptance for* $B^- \to D^0(\to K^0_S\pi^+\pi^-)\mu^-\overline{\nu}_\mu$ *decays split by year and* K^0_S *type.*

The overall variations of the single-tagged upper decay-time acceptance in the range $[-1.0, 1.5]$ ps are 0.009 and 0.011 for 2011 K^0_S(LL) and 2012 K^0_S(LL). For the K^0_S(DD) sample, the variations are almost an order of magnitude smaller and lie at 0.001 and 0.002 for 2011 and 2012, respectively. To estimate if the inclusion of this effect is significant, the upper decay-time acceptance for the K^0_S(LL) samples is fitted within $[-1.0, 1.5]$ ps, where the spread of points is relatively small with an exponential function $\exp(-a \times t(D^0))$. The upper decay-time acceptance was then included in the correction of the selection bias as detailed in Chapt. 11.3. In doing so, the

lifetime changes from (405.5 ± 1.7) fs to (406.3 ± 1.7) fs for 2011, and from (412.4 ± 1.2) fs to (413.5 ± 1.2) fs for 2012. This is a very small relative effect of 0.20% and 0.27%. The correction of the K^0_S(DD) sample is expected to lie a factor 7 to 9 below this and is thus considered negligible. By including the upper decay-time acceptance in the amplitude fit, the absolute shifts in the mixing parameters are $\sim \mathcal{O}(10^{-5})$ and thus the D^0 upper decay-time acceptance has a negligible effect on the mixing result.

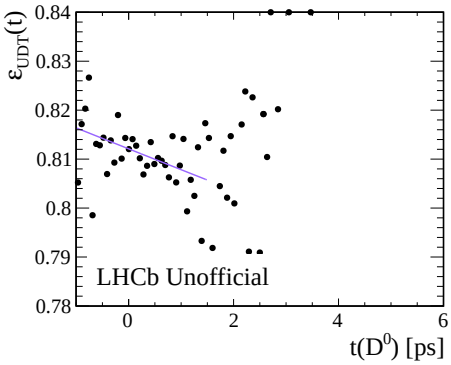

(a) *2011* K^0_S(LL)

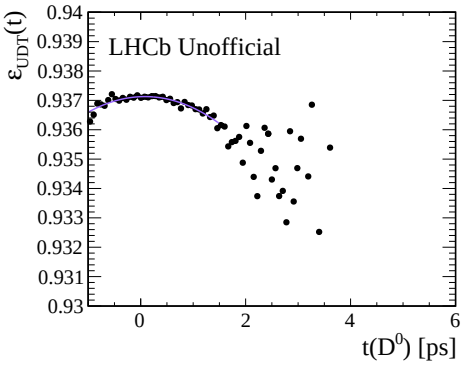

(b) *2011* K^0_S(DD)

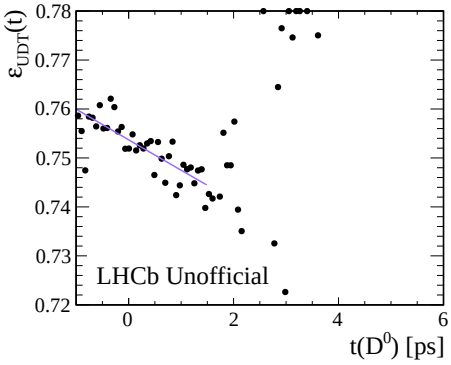

(c) *2012* K^0_S(LL)

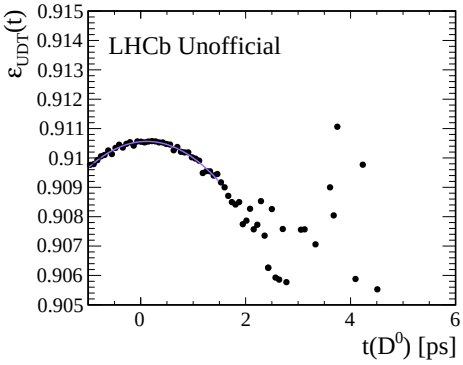

(d) *2012* K^0_S(DD)

Figure 10.13.: *Upper decay-time acceptance for* $\overline{B}^0 \to D^{*+}(\to D^0(\to K^0_S\pi^+\pi^-)\pi^+)\mu^-\overline{\nu}_\mu$ *decays split by year and* K^0_S *type.*

The variations of the double-tagged upper decay-time acceptance are similar to the ones obtained from the single-tagged sample and will change the D^0 lifetime at the order of per mille or less and have a negligible effect on the mixing parameters. Due to the negligible changes, no upper decay-time acceptance is included in the amplitude fit.

10.4. Decay time and phase-space resolutions

The decay time resolution is defined as the distribution of the difference between reconstructed and generated decay time $t' - t$ and is fitted from simulation with a triple Gaussian function

$$R(t,t';\mu,\sigma_1,\sigma_2,\sigma_3,f,g) = N\left(\frac{f}{\sqrt{2\pi}\sigma_1}\times e^{-\left(\frac{t'-t-\mu}{\sqrt{2}\sigma_1}\right)^2} + \frac{g}{\sqrt{2\pi}\sigma_2}\times e^{-\left(\frac{t'-t-\mu}{\sqrt{2}\sigma_2}\right)^2} + \frac{(1-f-g)}{\sqrt{2\pi}\sigma_3}\times e^{-\left(\frac{t'-t-\mu}{\sqrt{2}\sigma_3}\right)^2}\right), \tag{10.13}$$

where N is a normalisation factor. The decay time resolution parameters are listed in Tables 10.6 and 10.7 for single- and double-tagged decays, respectively. An average effective resolution of 95 fs (96 fs) is measured for single-tagged (double-tagged) decays where the effective resolutions for each subsample σ^i_{eff} are weighted by their corresponding fraction of events f_i as

$$\sigma^2_{\text{eff}} = \sum_i f_i \left(\sigma^i_{\text{eff}}\right)^2, \quad \text{with} \tag{10.14}$$

$$\sigma^i_{\text{eff}} = \sqrt{f\sigma_1^2 + g\sigma_2^2 + (1-f-g)\sigma_3^2}. \tag{10.15}$$

The decay time resolutions are illustrated in Figs. 10.14 and 10.15.

Table 10.6.: *Parameters of the D^0 decay time resolution for $B^- \to D^0(\to K^0_S\pi^+\pi^-)\mu^-\overline{\nu}_\mu$ decays split by year and K^0_S type.*

	2011		2012	
	K^0_S(LL)	K^0_S(DD)	K^0_S(LL)	K^0_S(DD)
$\mu/\,[10^{-7}\,\text{ns}]$	-7.82 ± 1.77	-9.13 ± 1.17	-9.73 ± 1.41	-10.13 ± 0.86
$\sigma_1\,[10^{-5}\,\text{ns}]$	8.07 ± 0.17	8.32 ± 0.11	8.21 ± 0.14	8.49 ± 0.08
$\sigma_2\,[10^{-5}\,\text{ns}]$	4.09 ± 0.09	3.86 ± 0.05	4.19 ± 0.06	3.99 ± 0.04
$\sigma_3\,[10^{-4}\,\text{ns}]$	1.73 ± 0.04	1.95 ± 0.02	1.74 ± 0.03	1.97 ± 0.02
f	0.52 ± 0.02	0.50 ± 0.01	0.52 ± 0.01	0.50 ± 0.01
g	0.39 ± 0.02	0.36 ± 0.01	0.38 ± 0.02	0.34 ± 0.01

Table 10.7.: *Parameters of the D^0 decay time resolution for $\overline{B}^0 \to D^{*+}(\to D^0(\to K^0_S\pi^+\pi^-)\pi^+)\mu^-\overline{\nu}_\mu$ decays split by year and K^0_S type.*

	2011		2012	
	K^0_S(LL)	K^0_S(DD)	K^0_S(LL)	K^0_S(DD)
$\mu\,[10^{-7}\,\text{ns}]$	-6.75 ± 1.77	-7.60 ± 1.16	-8.50 ± 1.41	-7.26 ± 0.85
$\sigma_1\,[10^{-4}\,\text{ns}]$	1.74 ± 0.03	1.98 ± 0.02	1.73 ± 0.03	2.00 ± 0.02
$\sigma_2\,[10^{-5}\,\text{ns}]$	4.10 ± 0.07	3.88 ± 0.05	4.15 ± 0.06	4.00 ± 0.04
$\sigma_3\,[10^{-5}\,\text{ns}]$	8.12 ± 0.12	8.39 ± 0.09	8.16 ± 0.10	8.59 ± 0.08
f	0.09 ± 0.00	0.15 ± 0.00	0.11 ± 0.01	0.16 ± 0.00
g	0.39 ± 0.02	0.35 ± 0.01	0.37 ± 0.01	0.34 ± 0.01

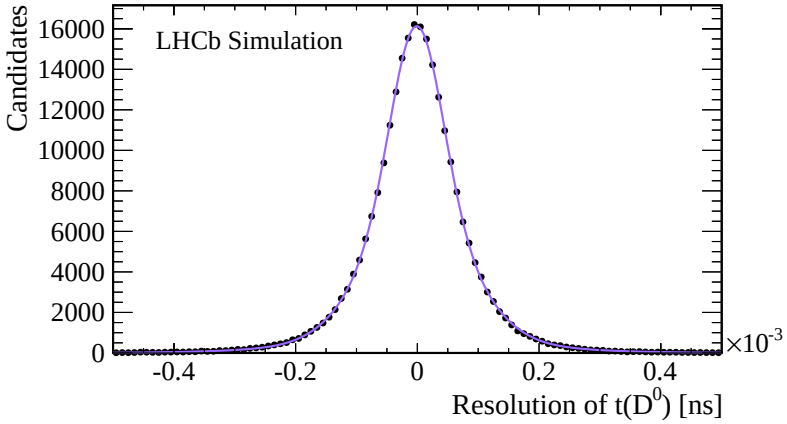

Figure 10.14.: *Single-tagged decay time resolution for the 2012 K^0_S(LL) MC sample with tight generator-level cuts after the complete selection chain. The figure depicts the fit (blue line) to the data (black points).*

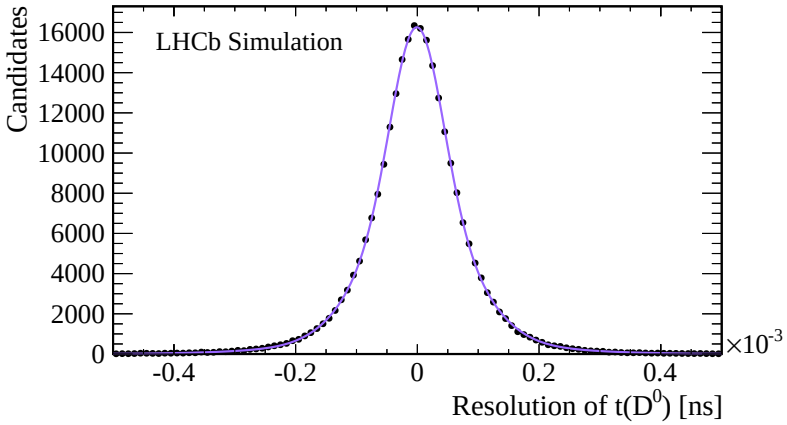

Figure 10.15.: *Double-tagged decay time resolution for the 2012 K^0_S(LL) MC sample with tight generator-level cuts after the complete selection chain. The figure depicts the fit (blue line) to the data (black points).*

The resolutions of $m^2(K^0_S\pi^+)$ and $m^2(K^0_S\pi^-)$ are correlated through energy and momentum conservation, and hence the phase-space resolution is measured in a set of uncorrelated variables. These uncorrelated variables are the sum and difference of $m^2(K^0_S\pi^+)$ and $m^2(K^0_S\pi^-)$, denoted by $u \equiv m^2(K^0_S\pi^+) + m^2(K^0_S\pi^-)$ and $v \equiv m^2(K^0_S\pi^+) - m^2(K^0_S\pi^-)$, respectively. The resolutions in u and v are computed as the difference between reconstructed and generated values, $u' - u$ and $v' - v$, and are fitted with a double Gaussian function

$$T_{\mathrm{PS}}(u, u'; \mu, \sigma, f, c) = N \left(\frac{c}{\sqrt{2\pi}\sigma} \times e^{-\left(\frac{u'-u-\mu}{\sqrt{2}\sigma}\right)^2} + \frac{(1-c)}{\sqrt{2\pi}f\sigma} \times e^{-\left(\frac{u'-u-\mu}{\sqrt{2}f\sigma}\right)^2} \right), \tag{10.16}$$

$$T_{\mathrm{PS}}(v, v'; \mu, \sigma, f, c) = N \left(\frac{c}{\sqrt{2\pi}\sigma} \times e^{-\left(\frac{v'-v-\mu}{\sqrt{2}\sigma}\right)^2} + \frac{(1-c)}{\sqrt{2\pi}f\sigma} \times e^{-\left(\frac{v'-v-\mu}{\sqrt{2}f\sigma}\right)^2} \right), \tag{10.17}$$

where N is a normalisation factor. The resolutions are expected to vary across phase-space and are thus measured in bins of u and v defined in Figure 10.16. The effective resolutions are given in Table 10.8 for single-tagged decays as the soft pion of the double-tagged decay will

not influence the phase-space resolution. The effect of the phase-space resolution on the mixing parameters is studied with pseudo-experiments as discussed in Chapt. 12.1.

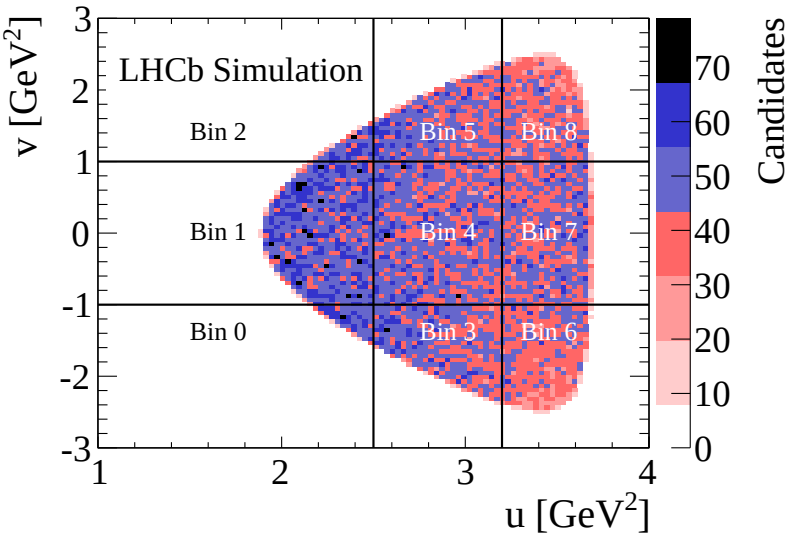

Figure 10.16.: *Phase-space binning for resolution study in u and v.*

Table 10.8.: *Effective width of the phase-space resolution in u and v split by year and K^0_S type for single-tagged decays.*

	Effective width [MeV^2]			
	2011		2012	
	K^0_S(LL)	K^0_S(DD)	K^0_S(LL)	K^0_S(DD)
u bin 0	5371	6986	5626	6989
u bin 1	4172	5672	4330	5773
u bin 2	5618	6845	5681	7050
u bin 3	5219	7070	5373	7207
u bin 4	4698	6733	4847	6818
u bin 5	5292	7362	5377	7193
u bin 6	3204	4943	3334	4950
u bin 7	3039	4525	3188	4591
u bin 8	3215	4951	3404	4954
v bin 0	9874	11314	8342	11205
v bin 1	9239	11756	9237	11894
v bin 2	18264	11000	8974	11119
v bin 3	8323	10377	8763	11021
v bin 4	10613	13174	10890	13665
v bin 5	8426	10719	8584	10767
v bin 6	8272	10207	8709	10367
v bin 7	12843	13666	12434	13585
v bin 8	8540	10296	8672	10168

11. Fit model

The mixing and possibly the *CP* violation parameters are extracted from an unbinned three-dimensional maximum likelihood fit in D^0 decay time $t(D^0) \equiv t'$, $m^2(K^0_S\pi^+)$ and $m^2(K^0_S\pi^-)$. The fit is performed simultaneously over eight sub-samples of the recorded data, which are obtained by splitting the total dataset by data-taking period (2011 and 2012), by K^0_S type (K^0_S(LL) and K^0_S(DD)), and by type of flavour tag (single- or double-tagged). In this chapter, the PDF of the amplitude fit is derived, which is given as

$$\begin{aligned}
&\mathcal{P}(t',m^2(K^0_S\pi^+), m^2(K^0_S\pi^-), p_{\rm sig}, tag, \vec{\alpha}) \\
&\quad = p_{sig}\left[(1-\omega_{\rm muontag})\mathcal{P}_{sig}(t', m^2(K^0_S\pi^+), m^2(K^0_S\pi^-), tag, \vec{\alpha})\right. \\
&\qquad \left. + \omega_{\rm muontag}\mathcal{P}_{sig}(t', m^2(K^0_S\pi^+), m^2(K^0_S\pi^-), -tag, \vec{\alpha})\right] \\
&\qquad + (1-p_{sig})\mathcal{P}_{\rm bkg}(t', m^2(K^0_S\pi^+), m^2(K^0_S\pi^-), tag), \qquad (11.1)
\end{aligned}$$

where p_{sig} is the per-event signal probability, extracted with a $m(D^0)$ or δm fit as given in Eqns. 8.9 and 8.11, *tag* is the flavour tag and takes values of $+1\,(-1)$ for D^0 ($\overline{D}^0$) decays, and $\vec{\alpha}$ is the vector of fit parameters, including the mistag fraction, $\omega_{\rm muontag}$, given in Eqn. 9.8. The background PDF, $\mathcal{P}_{\rm bkg}(t', m^2(K^0_S\pi^+), m^2(K^0_S\pi^-), tag)$, is determined in a non-parametric way as described in Chapt. 9.5 and therefore does not depend on the fit parameters. The signal PDF for the correct and misreconstructed tag is given by

$$\begin{aligned}
&\mathcal{P}_{sig}(t',m^2(K^0_S\pi^+), m^2(K^0_S\pi^-), +1, \vec{\alpha}) \\
&\qquad = \left[\left(|\mathcal{A}_f(t, m^2(K^0_S\pi^+), m^2(K^0_S\pi^-))|^2\varepsilon(t)\right) \otimes R(t, t', \mu_t, \sigma_t)\right] \\
&\qquad\quad \times \varepsilon(\cos(\theta), m^2(\pi^+\pi^-)), \qquad (11.2) \\
&\mathcal{P}_{sig}(t',m^2(K^0_S\pi^+), m^2(K^0_S\pi^-), -1, \vec{\alpha}) \\
&\qquad = \left[\left(|\bar{\mathcal{A}}_f(t, m^2(K^0_S\pi^+), m^2(K^0_S\pi^-))|^2\varepsilon(t)\right) \otimes R(t, t', \mu_t, \sigma_t)\right] \\
&\qquad\quad \times \varepsilon(\cos(\theta), m^2(\pi^+\pi^-)), \qquad (11.3)
\end{aligned}$$

where $\mathcal{A}_f(t, m^2(K^0_S\pi^+), m^2(K^0_S\pi^-))$ and $\bar{\mathcal{A}}_f(t, m^2(K^0_S\pi^+), m^2(K^0_S\pi^-))$ are the time-dependent amplitude models described in Chapt. 11.1, $\varepsilon(t)$ and $\varepsilon(\cos(\theta), m^2(\pi^+\pi^-))$ are the time- and phase-space-dependent acceptances discussed in Chapt. 10. Chapter 11.2 describes the convolution of the time dependent PDF with the resolution function, $R(t, t', \mu_t, \sigma_t)$ (see Chapt. 10.4), and Chapt. 11.3 discusses how the decay-time acceptance $\varepsilon(t)$ is included. In the following, the notation for $\mathcal{A}(t) \equiv \mathcal{A}_f(t, m^2(K^0_S\pi^+), m^2(K^0_S\pi^-))$ and $\bar{\mathcal{A}}(t) \equiv \bar{\mathcal{A}}_f(t, m^2(K^0_S\pi^+), m^2(K^0_S\pi^-))$ is used.

11.1. Amplitude model

The general time-dependence of D^0 decays into a final state f is derived in Chapt. 2, leading to the relation (repeated for convenience from Eqn. 2.68)

$$|\mathcal{A}(t)|^2 = \frac{1}{2}e^{-\Gamma t}\left[\left(|A|^2 - \left|\frac{q}{p}B\right|^2\right)\cos(x\Gamma t) - 2\mathcal{I}m\left(AB^*\left[\frac{q}{p}\right]^*\right)\sin(x\Gamma t)\right.$$
$$\left. + \left(|A|^2 + \left|\frac{q}{p}B\right|^2\right)\cosh(y\Gamma t) - 2\mathcal{R}e\left(AB^*\left[\frac{q}{p}\right]^*\right)\sinh(y\Gamma t)\right]. \quad (2.68)$$

The corresponding anti-particle decay rate $|\bar{\mathcal{A}}(t)|^2$ follows from Eqn. 2.63. For a three-body decay, the amplitudes A and B depend on a point in phase-space, which is spanned by $m^2(K^0_S\pi^-)$ and $m^2(K^0_S\pi^+)$. These amplitudes for a three-body decay are expressed as the sum of amplitudes of a quasi two-body decay through an intermediate resonance r, each multiplied by a complex coefficient c_r, which encodes relative differences in amplitudes and phases, including also strong phase differences,

$$A(m^2(K^0_S\pi^-), m^2(K^0_S\pi^+)) = \sum_r c_r A_r(m^2(K^0_S\pi^-), m^2(K^0_S\pi^+)), \quad (11.4)$$
$$B(m^2(K^0_S\pi^-), m^2(K^0_S\pi^+)) = \sum_r \bar{c}_r A_r(m^2(K^0_S\pi^+), m^2(K^0_S\pi^-)). \quad (11.5)$$

In Eqns. 11.4 and 11.5, no direct *CP* violation is assumed and hence, the following relation holds

$$A_r(m^2(K^0_S\pi^-), m^2(K^0_S\pi^+)) = \bar{A}_r(m^2(K^0_S\pi^+), m^2(K^0_S\pi^-)). \quad (11.6)$$

The model-dependence of the analysis method enters through the choice of resonances contributing to the sum in Eqns. 11.4 and 11.5 and the chosen parameterisation of A_r. In this chapter, various possible parameterisations of the amplitude A_r will de detailed, following Refs. [93] and [94] closely.

The amplitude of the $D^0 \to K^0_S\pi^+\pi^-$ decay is expressed as the sum of quasi two-body decays through an intermediate resonance r as $D \to rc$ with $r \to ab$. The amplitude of this quasi two-body decay to a final state of three pseudo-scalar mesons with total angular momentum J and parity P of $J^P = 0^-$ such as K^0_S and $\pi^\pm$ is given by

$$A_r = \sum_\lambda \langle ab|r_\lambda\rangle \mathcal{T}_r \langle cr_\lambda|D\rangle \quad (11.7)$$
$$= Z_L(\vec{h},\vec{k})B_L^{r\to ab\,\prime}(|\vec{k}|,|\vec{k_r}|)\mathcal{T}_r(m_{ab})B_L^{D\to rc\,\prime}(|\vec{h}|,|\vec{h_r}|), \quad (11.8)$$

where the sum is evaluated over all helicity states λ of the intermediate resonance. The angular distribution of the final state particles is denoted by $Z_L(\vec{h},\vec{k})$ where L denotes the orbital angular momentum between r and c. For $D^0 \to K^0_S\pi^+\pi^-$ decays, the orbital angular momentum

number is the same for r and c as for a and b since the D^0 decays into three pseudo-scalar particles. The vectors $\vec{k}$ and $\vec{h}$ refer to the three-momenta of c and a in the rest frame of the resonant D^0 daughter pair and k and h are the corresponding four-momenta. The moduli of the three-momenta are given by

$$|\vec{h}\,| = \frac{\sqrt{[m_{ab}^2 - (m_D + m_c)^2][m_{ab}^2 - (m_D - m_c)^2]}}{2m_D}, \tag{11.9}$$

$$|\vec{k}\,| = \frac{\sqrt{[m_{ab}^2 - (m_a + m_b)^2][m_{ab}^2 - (m_a - m_b)^2]}}{2m_{ab}}. \tag{11.10}$$

The four-momenta evaluated at the pole mass m_r of the intermediate resonance are given by k_r and h_r, respectively. The form factors of the D^0 and the intermediate resonance are the Blatt-Weisskopf barrier factors $B_L^{r\to ab\,\prime}(|\vec{k}\,|, |\vec{k_r}|)$ and $B_L^{D\to rc\,\prime}(|\vec{h}\,|, |\vec{h_r}|)$ [95, 96] listed in Table 11.1. In a strong decay, the maximum angular momentum in a strong decay is limited by the four-momentum $k\,(h)$. If decay products with a meson radius of $\sim 1\,\mathrm{fm}$ have a small momentum, then they have difficulty to generate a sufficiently large angular momentum to conserve the spin of the resonance. In this analysis, the Blatt-Weisskopf effective radius d is fixed to $d = 1.5\,\mathrm{GeV}^{-1}$ for intermediate resonances and to $5.0\,\mathrm{GeV}^{-1}$ for the D^0 meson and is varied for systematic studies as detailed in Chapt. 13.2.1.

Table 11.1.: *Blatt-Weisskopf barrier factors depending on $z = (|\vec{k}|d)^2$ and $z_0 = (|\vec{k_0}|d)^2$ where $k_0 = k(m_{ab} = m_r)$ as defined in the text.*

L	$B'_L(\lvert\vec{k}\rvert, \lvert\vec{k_0}\rvert)$
0	1
1	$\sqrt{\frac{1+z_0}{1+z}}$
2	$\sqrt{\frac{(z_0-3)^2+9z_0}{(z-3)^2+9z}}$

The angular distributions $Z_L(\vec{h}, \vec{k}\,)$ are obtained by evaluating the spin sums in the matrix element given in Eqn. 11.8. The two vertices describing the $D \to rc$ and $r \to ab$ decays each obtain a spin factor. Scalar resonances are not polarised and therefore their angular distribution is uniform

$$Z_0(\vec{h}, \vec{k}\,) = 1. \tag{11.11}$$

For vector resonances, the polarisations of the decay vertices are ϵ_λ^μ and ϵ_λ^ν , respectively. Hence, the spin sum of the decay is evaluated to be

$$\sum_\lambda \varepsilon_\lambda^{\mu\,*} \varepsilon_\lambda^\nu = -g_{\mu\nu} + \frac{k^\mu k^\nu}{m^2}, \tag{11.12}$$

where the four-momentum of the resonant pair is k, whose three-momentum is given in Eqn. 11.10. If transversality is required by imposing $\epsilon_\lambda^\mu k_\mu = 0$, the denominator of the spin sum depends

on $m = m_{ab}$, which is the so-called Zemach formalism. Contracting the indices in the spin sum term with the indices in the matrix element leads to

$$Z_1(\vec{h},\vec{k}\,) = m_{ac}^2 - m_{bc}^2 - \frac{\left(m_D^2 - m_c^2\right)\left(m_a^2 - m_b^2\right)}{m_{ab}^2}. \tag{11.13}$$

For tensor resonances, the polarisation vectors are $\varepsilon_\lambda^{\mu\nu\,*}$ and $\varepsilon_\lambda^{\alpha\beta}$, and the spin sum was calculated in Ref. [97]

$$\sum_\lambda \varepsilon_\lambda^{\mu\nu\,*}\varepsilon_\lambda^{\alpha\beta} = \frac{1}{2}\left(T^{\mu\alpha}T^{\nu\beta} + T^{\mu\beta}T^{\nu\alpha}\right) - \frac{1}{3}T^{\mu\nu}T^{\alpha\beta}, \tag{11.14}$$

with

$$T^{\mu\nu} = -g_{\mu\nu} + \frac{k^\mu k^\nu}{m^2}, \tag{11.15}$$

resulting in an angular distribution of

$$\begin{aligned} Z_2(\vec{h},\vec{k}\,) = &\left[m_{ac}^2 - m_{bc}^2 - \frac{\left(m_D^2 - m_c^2\right)\left(m_a^2 - m_b^2\right)}{m_{ab}^2}\right]^2 \\ &- \frac{1}{3}\left[m_{ab}^2 - 2(m_D^2 + m_c^2) + \frac{\left(m_D^2 - m_c^2\right)^2}{m_{ab}^2}\right] \\ &\times \left[m_{ab}^2 - 2(m_a^2 + m_b^2) + \frac{\left(m_a^2 - m_b^2\right)^2}{m_{ab}^2}\right], \end{aligned} \tag{11.16}$$

in the Zemach formalism, which enforces $T^{\mu\nu} = -g_{\mu\nu}k^\mu k^\nu / m_{ab}^2$.
The phase-space dependence of the amplitude is contained in the dynamical function $\mathcal{T}_r$, which is discussed in Chapt. 11.1.1 to 11.1.4 for various parameterisations. The dynamical function $\mathcal{T}_r$ is derived starting from the S-matrix, which describes the amplitude of the transition of an initial state i to a final state f via the scattering operator $\mathcal{S}$

$$S_{fi} = \langle f|\mathcal{S}|i\rangle. \tag{11.17}$$

The scattering operator can be written in terms of the transition operator $\mathcal{T}$

$$\mathcal{S} = \mathbb{1} + 2i\mathcal{T}, \tag{11.18}$$

where $\mathcal{T}$ mediates the interaction between initial and final state. From the unitarity of the scattering operator $\mathcal{S}\mathcal{S}^\dagger = \mathcal{S}^\dagger\mathcal{S} = \mathbb{1}$, it follows

$$
\begin{aligned}
2\mathcal{T}^\dagger\mathcal{T} &= i(\mathcal{T}^\dagger - \mathcal{T}), && (11.19)\\
\longleftrightarrow 2i\mathcal{T}^\dagger\mathcal{T} &= \mathcal{T} - \mathcal{T}^\dagger, && (11.20)\\
\longleftrightarrow 2i\mathcal{T} &= \left(\mathcal{T}^{-1}\right)^\dagger \mathcal{T} - \mathbb{1}, && (11.21)\\
\longleftrightarrow 2i\mathbb{1} &= \left(\mathcal{T}^{-1}\right)^\dagger - \mathcal{T}^{-1}, && (11.22)\\
\longleftrightarrow \mathcal{T}^{-1} + i\mathbb{1} &= \left(\mathcal{T}^{-1}\right)^\dagger - i\mathbb{1}, && (11.23)\\
\longleftrightarrow \mathcal{T}^{-1} + i\mathbb{1} &= \left(\mathcal{T}^{-1} + i\mathbb{1}\right)^\dagger \equiv K^{-1}, && (11.24)
\end{aligned}
$$

where the hermitian K-matrix is introduced. The transition matrix can be expressed in terms of the K-matrix as

$$\mathcal{T} = (\mathbb{1} - iK)^{-1}K = K(\mathbb{1} - iK)^{-1}. \tag{11.25}$$

Both K-matrix and transition matrix are not invariant under Lorentz transformations. By introducing a diagonal phase-space matrix $\rho = 2k/m$ in Eqn. 11.18, Lorentz invariance is ensured, resulting in

$$\mathcal{S} = \mathbb{1} + 2i\rho^{\frac{1}{2}}\hat{\mathcal{T}}\rho^{\frac{1}{2}}, \tag{11.26}$$

where k is the momentum of a or b in the rest frame of the resonant pair with mass m. The Lorentz-invariant transition matrix, $\hat{\mathcal{T}}$, and the Lorentz-invariant K-matrix, $\hat{\mathcal{K}}$, are given by

$$
\begin{aligned}
\hat{\mathcal{T}} &= \hat{K}(\mathbb{1} - i\rho\hat{K})^{-1}, && (11.27)\\
\hat{K}^{-1} &= \hat{\mathcal{T}}^{-1} + i\rho. && (11.28)
\end{aligned}
$$

In case of a (1×1) transition matrix for the decay of a D^0 through an intermediate resonance r, the matrix element equals the Lorentz-invariant dynamical function $\hat{\mathcal{T}}_r$, which is discussed in Chapt. 11.1.1 to 11.1.4 for various resonance parameterisations.

Two different amplitude models are studied, which are summarised in Chapt. 11.1.6 and 11.1.7. The isobar model described in Chapt. 11.1.6 is chosen as the nominal model and the alternative model discussed in Chapt. 11.1.7 is then used to evaluate a systematic uncertainty as detailed in Chapt. 13.2.1.4.

11.1.1. Breit-Wigner

The relativistic Breit-Wigner propagator is given by

$$\hat{\mathcal{T}}_r = \frac{1}{(m_r^2 - m_{ab}^2) - im_r\Gamma(m_{ab})}, \tag{11.29}$$

with the running width $\Gamma(m_{ab})$ [93] defined as

$$\Gamma(m_{ab}) = \Gamma_r \times \left(\frac{m_r}{m_{ab}}\right)\left(\frac{q}{q_r}\right)^{(2L+1)} B'_L(k,k_0)^2. \tag{11.30}$$

The Blatt-Weisskopf barrier factors $B'_L(q,q_0)$ are listed in Table 11.1. Breit-Wigner amplitudes provide a decent description of isolated resonances but can break unitarity in regions where they overlap. Hence, Breit-Wigner propagators are only appropriate for the description of non-overlapping resonances, which are far from thresholds.

11.1.2. Gounaris-Sakurai

The decay $\rho(770) \to \pi^+\pi^-$ is described by a Gounaris-Sakurai propagator [98] including Blatt-Weisskopf factors given by

$$\hat{\mathcal{T}}_r = \frac{1 + d\frac{\Gamma_r}{m_r}}{(m_r^2 - m_{ab}^2 + f) - im_r\Gamma(m_{ab})}, \tag{11.31}$$

instead of a relativistic Breit-Wigner propagator (see Chapt. 11.1.1). The advantage of the Gounaris-Sakurai propagator over the Breit-Wigner propagator (see Chapt. 11.1.1) is that it corrects for the finite width of the $\rho(770)$. The Gounaris-Sakurai propagator is expressed in terms of

$$d = \frac{3}{\pi}\frac{m_\pi^2}{k_r^2}\log\left(\frac{m_r + 2k_r}{2m_\pi}\right) + \frac{m_r}{2\pi h_r} - \frac{m_\pi^2 m_r}{\pi h_r^3}, \tag{11.32}$$

and $f(m_{ab}^2)$, which is defined as

$$\begin{aligned} f(m_{ab}^2) = \frac{\Gamma_r m_r^2}{k_r} \times \Bigg\{ & \frac{k^2}{k_r^2}\left[H(m_{ab}^2) - H(m_r^2)\right] \\ & + (m_r^2 - m_{ab}^2) \times \left[H(m_r^2)\left(\frac{1}{8k_r^2} - \frac{1}{2m_r^2}\right) + \frac{1}{2\pi m_r^2}\right]\Bigg\}, \end{aligned} \tag{11.33}$$

where k is the magnitude of the four-momentum of a in the rest frame of the resonant pair as defined in Eqn. 11.10. The helper function $H(m^2)$ is given by

$$H(m^2) = \frac{2k}{\pi m}\ln\left(\frac{m + 2k}{2m_\pi}\right). \tag{11.34}$$

Neither the mass-dependent constant d nor the helper functions $f(m_{ab}^2)$ and $H(m^2)$ have any physical meaning.

11.1.3. LASS

The parametrisation of the S-wave amplitude in the $K_S^0\pi^\pm$ channel is based on the findings of the LASS collaboration [99] in an elastic scattering experiment of $K^-p \to K^-\pi^+\eta$. The

LASS collaboration reported the line shape of a spinless broad resonance with a mass around 1430 MeV decaying into $K^0_S\pi^-$ final states. The line shape of this resonance is described by the sum of an inelastic Breit-Wigner term and a non-resonant term

$$\mathcal{T}_{\text{LASS}} = \sin\delta_R e^{i\delta_R} e^{2i\delta_B} + \sin\delta_B e^{i\delta_B}. \tag{11.35}$$

The non-resonant term is given by an effective range parameterisation as

$$\cot\delta_B = \frac{1}{sk} + \frac{rk}{2}, \tag{11.36}$$

where s denotes the scattering length, r the effective range and k refers to the magnitude of the momentum of a in the rest frame of the resonant pair as defined in Eqn. 11.10. The Breit-Wigner term enters through the phase δ_R defined as

$$\tan\delta_R = \frac{m_r\Gamma(m^2)}{m_r^2 - m^2}, \tag{11.37}$$

where the invariant mass m^2 refers to the appropriate $K^0_S\pi^\pm$ pair. A more general amplitude, which is not only valid for elastic scattering but also for production experiments, is obtained by introducing magnitudes B, R and relative phases ϕ_B, ϕ_R, for the Breit-Wigner and background terms, respectively. This leads to

$$\hat{\mathcal{T}}_{K^0_S\pi,\,S} = R\sin\delta_R e^{i(\delta_R+\phi_R)} e^{2i(\delta_B+\phi_B)} + B\sin(\delta_B+\phi_B) e^{i(\delta_B+\phi_B)}. \tag{11.38}$$

The amplitude is rewritten by exploiting the following relations

$$e^{i\delta_B}\sin\delta_B = \frac{1}{\cot\delta_B - i}, \tag{11.39}$$

$$e^{2i\delta_B} = \frac{\cot\delta_B + i}{\cot\delta_B - i}, \tag{11.40}$$

$$\sin\delta_R e^{i\delta_R} = \frac{m_r\Gamma(m^2)}{m_R^2 - m^2 - i m_r\Gamma(m^2)}, \tag{11.41}$$

resulting in

$$\begin{aligned}\hat{\mathcal{T}}_{K^0_S\pi,\,S} = {} & R e^{i\phi_R}\frac{m_r\Gamma(m^2)}{m_R^2 - m^2 - i m_r\Gamma(m^2)} e^{2i\phi_B}\frac{\cot\delta_B + i}{\cot\delta_B - i} \\ & + B e^{i\phi_B}\frac{\cos\phi_B + \cot\delta_B\sin\phi_B}{\cot\delta_B - i}.\end{aligned} \tag{11.42}$$

11.1.4. K-matrix formalism in the production vector approach

The S-wave amplitude in the $\pi^+\pi^-$ channel can be expressed by the K-matrix formalism [100, 101]. The K-matrix formalism preserves unitarity by construction. However, the K-matrix

formalism in the production or P-vector approach used in this analysis does not necessarily preserve unitarity. For overlapping resonances, Breit-Wigner amplitudes fail to model the amplitude correctly, which can be achieved by using the K-matrix formalism instead. The K-matrix amplitude for the $\pi\pi$ S-wave in the production vector approach, which follows from Eqns. 11.25 and 11.27, is defined as

$$\hat{\mathcal{T}}_{\pi\pi,\,S} \equiv P_0 = (\mathbb{1} - i\hat{\rho}\hat{K})^{-1}\hat{P}, \tag{11.43}$$

where $\hat{P}$ is the production vector, $\hat{\rho}$ the phase-space matrix and $\hat{K}$ is the K-matrix. The K-matrix formalism describes two-body scattering processes whereas the K-matrix in the production vector approach is a generalised K-matrix formalism allowing the production of S-wave resonances decaying into a dipion final state in D^0 decays. The following considerations hold if the dipion system does not interact with the K^0_S of the $D^0 \to K^0_S\pi^+\pi^-$ decay.
The matrix element ij of the K-matrix is given by

$$\hat{K}_{ij} = \left(\sum_\alpha \frac{g_i^\alpha g_j^\alpha}{m_\alpha^2 - s} + f_{ab}^{scatt}\frac{1\,\mathrm{GeV}^2 - s_0^{scatt}}{s - s_0^{scatt}}\right)\frac{1\,\mathrm{GeV}^2 - s_{A_0}}{s - s_{A_0}}\left(s - s_A\frac{m_\pi^2}{2}\right), \tag{11.44}$$

where indices i, j denote the following final states: $\pi\pi$, $K\bar{K}$, $\eta\eta$, $\eta\eta'$, 4π. The sum over α runs over the poles of the K-matrix at mass m_α, which do not correspond to physical particles. The real couplings between pole α and channel i are denoted by g_i^α. The couplings and pole masses are extracted from a fit to data taken by scattering experiments [100, 101]. The relevant final state is a dipion state, which can be reached through a direct decay from poles m_α. However, these poles can also decay into other channels apart from $\pi\pi$ if the pole mass is greater than the production threshold of the decay channel. For example, the first pole with $m_1 = 0.651\,\mathrm{GeV}$ can decay into a $K\bar{K}$ pair. Through a rescattering process, the kaon pair can produce a dipion final state or any of the other accessible states.
The second term accounts for a slowly varying contribution to the scattering amplitude, which is described by parameters f_{ij}^{scatt}, s_0^{scatt}, where $f_{ij}^{scatt} = 0$ for $i \neq \pi\pi$. The correction term with Adler zeroes, chosen to be $s_A = 1$ and $s_{A_0} = -0.15\,\mathrm{GeV}^2$, suppresses an artificial singularity near the $\pi\pi$ threshold. As reported in Ref. [100], the K-matrix parameters do not depend on the exact value of $s_A = 1$ and s_{A_0} restricted to the ranges $s_A \sim (0.1 - 0.5)\,\mathrm{m}_\pi^2$ and $s_{A_0} \sim (0.1 - 0.5)\,\mathrm{GeV}^2$. The elements of the diagonal phase-space matrix $\hat{\rho}_{ij} = \delta_{ij}\rho_j$ for the two-body channels with masses $m_{i,1}$ and $m_{i,2}$ are

$$\rho_i = \sqrt{1 - \frac{(m_{i,1} + m_{i,2})^2}{s}}, \quad \text{where} \quad i = \pi\pi,\, K\bar{K},\, \eta\eta,\, \eta\eta', \tag{11.45}$$

where the indices 1 and 2 refer to the two particles in channel i, *e.g.* to η and η'. The phase-space factor for the 4π final state [100] is given by

$$\rho_{4\pi} = \begin{cases} \sqrt{1-\frac{16m_\pi^2}{s}} & \text{for} \quad s > 1\,\text{GeV}^2 \\ \sqrt{1-16m_\pi^2}\,\big[1.2274 + 0.00370909 \times s^{-2} & \\ -0.111203 \times s^{-1} - 6.39017 \times s & \\ +16.8358 \times s^2 \ - 21.8845 \times s^3 + 11.3153 \times s^4\big] & \text{for} \quad s \leq 1\,\text{GeV}^2. \end{cases}$$

The production vector P takes a similar form to the K-matrix

$$\hat{P}_j = \sum_\alpha \frac{\beta^\alpha g_j^\alpha}{m_\alpha^2 - s} + f_{1j}^{prod} \frac{1\,\text{GeV}^2 - s_0^{prod}}{s - s_0^{prod}}. \tag{11.46}$$

The complex production parameters β^α, the parameters f_{1j}^{prod} and s_0^{prod} are floated in the amplitude fit. Here, the parameters f_{1j}^{prod} with $j = K\bar{K}$, $\eta\eta$, $\eta\eta'$, 4π are measured with respect to $f_{\pi\pi}^{prod}$. The pole masses and the real couplings of the poles α are listed in Table 11.2. The values for f_{1b}^{scatt} and s_0^{scatt} are taken from Table 11.3 [100, 101].

Table 11.2.: *Pole masses m_α and their corresponding base residue functions to final states $\pi\pi$, $K\bar{K}$, $\eta\eta$, $\eta\eta'$, 4π. The values are taken from Ref. [100, 101].*

$m_\alpha\,[\,\text{GeV}]$	$g_{\pi\pi}\,[\,\text{GeV}]$	$g_{K\bar{K}}\,[\,\text{GeV}]$	$g_{\eta\eta}\,[\,\text{GeV}]$	$g_{\eta\eta'}\,[\,\text{GeV}]$	$g_{4\pi}\,[\,\text{GeV}]$
0.65100	0.22889	-0.55377	0.00000	-0.39899	-0.34639
1.20360	0.94128	0.55095	0.00000	0.39065	0.31503
1.55817	0.36856	0.23888	0.55639	0.18340	0.18681
1.21000	0.33650	0.40907	0.85679	0.19906	-0.00984
1.82206	0.18171	-0.17558	-0.79658	-0.00355	0.22358

Table 11.3.: *Parameters f_{1j}^{scatt} and s_0^{scatt} describing the slowly varying component of the scattering amplitude. The values are taken from Ref. [100, 101].*

$s_0^{scatt}\,[\,\text{GeV}^2]$	$f_{\pi\pi,\pi\pi}^{scatt}$	$f_{\pi\pi,K\bar{K}}^{scatt}$	$f_{\pi\pi,\eta\eta}^{scatt}$	$f_{\pi\pi,\eta\eta'}^{scatt}$	$f_{\pi\pi,4\pi}^{scatt}$
-3.92637	0.23399	0.15044	-0.20545	0.32825	0.35412

11.1.5. EvtGen and GooFit differences

The fitting framework used for the analysis, GooFit [102–104], has been written following closely the EvtGen [78] model `DOMIXDALITZ`. In this model, some inconsistencies were found that are detailed in this chapter.
As discussed in Chapt. 11.1.2, the Gounaris-Sakurai propagator [98] is given by

$$\hat{\mathcal{T}}_r = \frac{1 + d\frac{\Gamma_r}{m_r}}{(m_r^2 - m_{ab}^2 + f) - im_r\Gamma(m_{ab})}. \tag{11.47}$$

In the EvtGen model, `DOMIXDALITZ`, this propagator is implemented as

$$\mathcal{T}_r = \frac{1 + d\frac{\Gamma_r}{m_r}}{(m_r^2 - m_{ab}^2 + f) - i m_{ab}\Gamma(m_{ab})}. \tag{11.48}$$

In this analysis, the correct Gounaris-Sakurai propagator given in Eqn. 11.47 is used in the amplitude fit to data but for studies of pseudo-experiments, which rely on EvtGen, the EvtGen propagator in Eqn. 11.48 is used in GooFit.

In addition, in Eqn. 11.8, the Blatt-Weisskopf meson radius d in $B_L^{D\to rc\prime}(|\vec{h}\,|, |\vec{h_r}|)$ was fixed to zero in EvtGen, resulting in the Blatt-Weiskopf factor to be $B_L^{D\to rc\prime}(|\vec{h}\,|, |\vec{h_r}|) = 1$. For consistency, the Blatt-Weisskopf factor $B_L^{D\to rc\prime}(|\vec{h}\,|, |\vec{h_r}|) = 1$ is used for studies of pseudo-experiments and in the amplitude fit to data, the Blatt-Weisskopf meson radius is set to $d = 5.0\,\mathrm{GeV}^{-1}$.

11.1.6. Isobar model

The total amplitude of the decay $D^0 \to K^0_S\pi^+\pi^-$ is modelled as a linear superposition of quasi two-body amplitudes where the D^0 decays through intermediate resonances. In the isobar model, a non-resonant contribution $\hat{\mathcal{T}}_{\mathrm{nr}} = c_{\mathrm{nr}}$ is modelled as a uniform amplitude with constant magnitude and phase, which is added to the sum of the isobar resonances as

$$\mathcal{T}(D^0 \to K^0_S\pi^+\pi^-) = \hat{\mathcal{T}}_{\mathrm{nr}} + \sum_r c_r \hat{\mathcal{T}}_r. \tag{11.49}$$

The intermediate resonances are described by relativistic Breit-Wigner propagators as detailed in Chapt. 11.1.1, with exception of the $\rho(770)$ where a Gounaris-Sakurai propagator is used (see Chapt. 11.1.2). The free parameters of the amplitude fit in the isobar model are $\tau(D^0)$, x, y, the masses and widths of the resonances as well as the real and imaginary parts of the complex coefficients c_r. For studies of pseudo-experiments, $|q/p|$ and ϕ might be included in the fit.

Table 11.4 lists the contributions to the isobar model. Two artificial resonances $\sigma_{1,2}$ are added to the model to ensure robustness of the amplitude fit.

Table 11.4.: *Intermediate resonances contributing to the isobar model used for the amplitude fit to data with their masses, widths and spins. The masses and widths are taken from [11]. The values for $\sigma_{1,2}$ are taken from the* EvtGen *implementation.*

Resonance	Mass [GeV]	Width [GeV]	Spin
	$\pi^+\pi^-$		
σ_1	0.528	0.512	0
$\rho(770)$	0.775 ± 0.000	0.149 ± 0.001	1
$\omega(782)$	0.783 ± 0.000	0.009 ± 0.000	1
$f_0(980)$	0.99 ± 0.02	0.04 to 0.10	0
σ_2	1.033	0.099	0
$f_2(1270)$	1.275 ± 0.001	$0.185^{+0.003}_{-0.002}$	2
$f_0(1370)$	1.2 to 1.5	0.2 to 0.5	0
$\rho(1450)$	1.465 ± 0.025	0.40 ± 0.06	1
$f_0(1500)$	1.505 ± 0.006	0.109 ± 0.007	0
	$K^0_S\pi^+$		
$K^*(892)^+$	0.892 ± 0.000	0.051 ± 0.001	1
$K^*_0(1430)^+$	1.425 ± 0.050	0.270 ± 0.080	0
$K^*_2(1430)^+$	1.426 ± 0.002	0.099 ± 0.003	2
	$K^0_S\pi^-$		
$K^*(892)^-$	0.892 ± 0.000	0.051 ± 0.001	1
$K^*_0(1430)^-$	1.425 ± 0.050	0.270 ± 0.080	0
$K^*_2(1430)^-$	1.426 ± 0.002	0.099 ± 0.003	2
	non-resonant $K^0_S\pi^+\pi^-$		

Because only the differences in amplitude and phase contain physical information, the amplitudes and phases are measured with respect to the $\rho(770)$, whose real and imaginary parts of $c_{\rho(770)}$ are set to one and zero, respectively.

11.1.7. K -matrix and LASS model

In the K-matrix and LASS amplitude model, the $\pi\pi$ S-wave is described by the K-matrix formalism in the P-vector approach with the corresponding amplitude $\hat{\mathcal{T}}_{\pi\pi,\,S}$. The K-matrix term, $\hat{\mathcal{T}}_{\pi\pi,\,S}$, described in Chapt. 11.1.4 and the LASS amplitude, $\hat{\mathcal{T}}_{K^0_S\pi,\,S}$, detailed in Chapt. 11.1.3 for the $K^0_S\pi^\pm$ S-wave, are added to the remaining amplitudes, which are described by an isobar model, as

$$\begin{aligned}\mathcal{T}(D^0 \to K^0_S\pi^+\pi^-) = \hat{\mathcal{T}}_{\pi\pi,\,S} + c_{K^0_S\pi,\,S}\hat{\mathcal{T}}_{K^0_S\pi,\,S} \\ + \sum_r c_r \hat{\mathcal{T}}_r.\end{aligned} \tag{11.50}$$

The K-matrix amplitude $\hat{\mathcal{T}}_{\pi\pi,\,S}$ does not have an additional complex coefficient since this amplitude already contains complex coefficients, which are floated in the fit. Apart from the $\rho(770)$ described by a Gounaris-Sakurai propagator (see Chapt. 11.1.2), relativistic Breit-Wigner prop-

agators (see Chapt. 11.1.1) are used for the parametrisation of $\mathcal{T}_r$. The free parameters of the amplitude fit are $\tau(D^0)$, x, y, the masses and widths of the resonances as well as the real and imaginary parts of the complex coefficients c_r. In addition, the K-matrix parameters $\beta^\alpha g$, f_{1b}^{prod} and s_0^{prod} and the LASS parameters ϕ_R, B, ϕ_B, s and r are floated in the amplitude fit, with exception of f_{15}^{prod}, which is fixed to zero due to the lack of sensitivity. The parameter R is fixed to one and hence, R and B can be interpreted as fractions of the inelastic Breit-Wigner and non-resonant terms. For studies of pseudo-experiments, $|q/p|$ and ϕ might be included in the fit.

Table 11.5 lists the contributions to the K-matrix and LASS model used in this analysis.

Table 11.5.: *Intermediate resonances contributing to the K-matrix and LASS model used for the amplitude fit to data with their masses, widths and spins. The masses and widths are taken from Ref. [11].*

Resonance	Mass [GeV]	Width [GeV]	Spin
	$\pi^+\pi^-$		
$\rho(770)$	0.775 ± 0.000	0.149 ± 0.001	1
$\omega(782)$	0.783 ± 0.000	0.009 ± 0.000	1
$f_2(1270)$	1.275 ± 0.001	$0.185^{+0.003}_{-0.002}$	2
$\rho(1450)$	1.465 ± 0.025	0.40 ± 0.06	1
S-wave	$\times$	$\times$	0
	$K^0_S\pi^+$		
$K^*(892)^+$	0.892 ± 0.000	0.051 ± 0.001	1
$K^*_0(1430)^+$	1.425 ± 0.050	0.270 ± 0.080	0
$K^*_2(1430)^+$	1.426 ± 0.002	0.099 ± 0.003	2
	$K^0_S\pi^-$		
$K^*(892)^-$	0.892 ± 0.000	0.051 ± 0.001	1
$K^*_0(1430)^-$	1.425 ± 0.050	0.270 ± 0.080	0
$K^*_2(1430)^-$	1.426 ± 0.002	0.099 ± 0.003	2
$K^*(1680)^-$	1.717 ± 0.027	0.322 ± 0.110	1

The amplitudes and phases are measured with respect to the $\rho(770)$, whose real and imaginary parts of $c_{\rho(770)}$ are set to one and zero, respectively.

11.2. Convolution with decay-time resolution

The PDF of the time-dependent amplitude fit given in Eqn. 11.2 contains a convolution of the time-dependent amplitude with the decay-time resolution function $R(t, t', \mu_t, \sigma_t)$. In the fitting framework GooFit [102–104], an approximation is used for the convolution of the amplitudes with the decay-time resolution function. Through the convolution, Faddeeva functions arise, which are approximated by a Taylor expansion with cosine and sine functions. This approach is valid because the cosine and sine terms vary slowly compared to the decay-time resolution function. In the following, the convolution of the time-dependent amplitudes with a decay-time

resolution is detailed.

Starting from Eqn. 2.68, the decay-time and phase-space dependent terms factorise. Therefore, the decay-time integrals can be calculated separately as

$$\int_{-\infty}^{+\infty} T_0(t;\Gamma,y)\Theta(t)\,\mathrm{d}t \equiv \int_0^{+\infty} e^{-\Gamma t}\cosh(y\Gamma t)\,\mathrm{d}t = \frac{\tau}{1-y^2}, \tag{11.51}$$

$$\int_{-\infty}^{+\infty} T_1(t;\Gamma,x)\Theta(t)\,\mathrm{d}t \equiv \int_0^{+\infty} e^{-\Gamma t}\cos(x\Gamma t)\,\mathrm{d}t = \frac{\tau}{1+x^2}, \tag{11.52}$$

$$\int_{-\infty}^{+\infty} T_2(t;\Gamma,y)\Theta(t)\,\mathrm{d}t \equiv \int_0^{+\infty} e^{-\Gamma t}\sinh(y\Gamma t)\,\mathrm{d}t = \frac{\tau\, y}{1-y^2}, \tag{11.53}$$

$$\int_{-\infty}^{+\infty} T_3(t;\Gamma,x)\Theta(t)\,\mathrm{d}t \equiv \int_0^{+\infty} e^{-\Gamma t}\sin(x\Gamma t)\,\mathrm{d}t = \frac{\tau\, x}{1+x^2}, \tag{11.54}$$

where $\tau \equiv 1/\Gamma$. The Heaviside function $\Theta(t)$ is needed to ensure that the decay time distribution is a probability density distribution with unity integral in the physical decay time range $[0,\infty)$. In LHCb, the decay time is measured with a finite precision of ~ 95 fs for $D^0 \to K^0_S\pi^+\pi^-$ decays as shown in Chapt. 10.4. The decay-time resolution is measured as the difference between reconstructed t' and generated D^0 decay time t, and is modelled by a triple Gaussian function. Equation 2.68 is expressed in terms of generated decay time and to account for the decay-time resolution, the terms in Eqn 2.68 are convolved with the resolution function. For simplification, the convolution with a single Gaussian function is detailed because the convolution with a triple Gaussian function equals the sum of three convolutions with a single Gaussian function. The convolved terms then describe the connection between reconstructed and generated decay times. The single Gaussian function normalised in $(-\infty,\infty)$ is given by

$$G(t'-t;\mu,\sigma) = \frac{1}{\sqrt{2\pi}\sigma} \times e^{-\left(\frac{(t'-t)-\mu}{\sqrt{2}\sigma}\right)^2}. \tag{11.55}$$

The convolution integral between $T_n(t)$ and a single Gaussian function $G(t'-t;\mu,\sigma)$ is defined as

$$P_n(t';\Gamma,x(y),\mu,\sigma) = T_n(t;\Gamma,x(y)) \otimes G(t'-t;\mu,\sigma) \tag{11.56}$$

$$= \int_{-\infty}^{+\infty} T_n(t;\Gamma,x(y))\Theta(t)G(t'-t;\mu,\sigma)\,\mathrm{d}t \tag{11.57}$$

$$= \int_0^{+\infty} T_n(t;\Gamma,x(y))G(t'-t;\mu,\sigma)\,\mathrm{d}t. \tag{11.58}$$

The notation of the integrals and terms are the same as used in the fitter, where an approximation is used for the convolution with $T_1(t;\Gamma,x)\Theta(t)$ and $T_3(t;\Gamma,x)\Theta(t)$.
The convolution of the terms $T_0(t;\Gamma,y) = e^{-\Gamma t}\cosh(y\Gamma t)$ and $T_2(t;\Gamma,y) = e^{-\Gamma t}\sinh(y\Gamma t)$ with a Gaussian resolution function is straightforward.

$$P_{0,2}(t';\Gamma,y,\mu,\sigma) = \int_0^{+\infty} T_{0,2}(t;\Gamma,y)G(t'-t;\mu,\sigma)\,\mathrm{d}t \tag{11.59}$$

$$= \int_0^{+\infty} e^{-\Gamma t}\begin{pmatrix}\cosh(y\Gamma t)\\ \sinh(y\Gamma t)\end{pmatrix} G(t'-t;\mu,\sigma)\,\mathrm{d}t \tag{11.60}$$

$$= \frac{1}{2}\int_0^{+\infty} e^{-\Gamma t}e^{y\Gamma t}G(t'-t;\mu,\sigma)\,\mathrm{d}t$$

$$\pm \frac{1}{2}\int_0^{+\infty} e^{-\Gamma t}e^{-y\Gamma t}G(t'-t;\mu,\sigma)\,\mathrm{d}t \tag{11.61}$$

$$\equiv \frac{1}{\sqrt{2\pi}\sigma}\left(\frac{I_{+y}\pm I_{-y}}{2}\right). \tag{11.62}$$

The integrals $I_{\pm y}$ are given by

$$I_{\pm y} = \int_0^{+\infty} e^{-\Gamma t(1\mp y)}e^{-\left(\frac{(t'-t)-\mu}{\sqrt{2}\sigma}\right)^2}\,\mathrm{d}t, \tag{11.63}$$

$$= \int_0^{+\infty} \exp\left(-\frac{t^2}{2\sigma^2} - t\left[\Gamma(1\mp y) - \frac{(t'-\mu)}{\sigma^2}\right] - \frac{1}{2\sigma^2}(t'-\mu)^2\right)\mathrm{d}t. \tag{11.64}$$

The detailed derivation of the integrals $I_{\pm y}$ is given in Appendix G and leads to

$$I_{\pm y} = \sigma\sqrt{\frac{\pi}{2}}e^{-q+(u_0^{\pm y})^2}\mathrm{erfc}(u_0^{\pm y}), \tag{11.65}$$

with

$$q = \frac{1}{2\sigma^2}(t'-\mu)^2, \text{ and } u_0^{\pm y} = \frac{\sigma}{\sqrt{2}}\left(\Gamma(1\mp y) - \frac{(t'-\mu)}{\sigma^2}\right). \tag{11.66}$$

The convolution of terms $T_1(t;\Gamma,y) = e^{-\Gamma t}\cos(x\Gamma t)$ and $T_3(t;\Gamma,y) = e^{-\Gamma t}\sin(x\Gamma t)$ with a Gaussian resolution function uses the Taylor expansions

$$\cos(x\Gamma t) = 1 - \frac{(x\Gamma t)^2}{2!} + \mathcal{O}((x\Gamma t)^4), \tag{11.67}$$

$$\sin(x\Gamma t) = (x\Gamma t) - \frac{(x\Gamma t)^3}{3!} + \mathcal{O}((x\Gamma t)^5). \tag{11.68}$$

The convolution integrals are given by

$$P_{1,3}(t';\Gamma,x,\mu,\sigma) = \int_0^{+\infty} T_{1,3}(t;\Gamma,y)G(t'-t;\mu,\sigma)\,\mathrm{d}t \tag{11.69}$$

$$= \int_0^{+\infty} e^{-\Gamma t}\begin{pmatrix}\cos(x\Gamma t)\\ \sin(x\Gamma t)\end{pmatrix} G(t'-t;\mu,\sigma)\,\mathrm{d}t \tag{11.70}$$

$$\approx \frac{1}{\sqrt{2\pi}\sigma}\int_0^{+\infty} e^{-\Gamma t}\begin{pmatrix}1-(x\Gamma t)^2/2\\ x\Gamma t-(x\Gamma t)^3/6\end{pmatrix} e^{-\left(\frac{(t'-t)-\mu}{\sqrt{2}\sigma}\right)^2}\,\mathrm{d}t. \tag{11.71}$$

The integral $P_1(t';\Gamma,x,\mu,\sigma)$ is written as

$$P_1(t';\Gamma,x,\mu,\sigma) = \frac{1}{\sqrt{2\pi}\sigma}\int_0^{+\infty}\left(1-(x\Gamma t)^2/2\right)e^{-\Gamma t}e^{-\left(\frac{(t'-t)-\mu}{\sqrt{2}\sigma}\right)^2}\,\mathrm{d}t \tag{11.72}$$

$$= \frac{1}{\sqrt{2\pi}\sigma}\left(\int_0^{+\infty}e^{-\Gamma t}e^{-\left(\frac{(t'-t)-\mu}{\sqrt{2}\sigma}\right)^2}\,\mathrm{d}t - \frac{1}{2}\int_0^{+\infty}(x\Gamma t)^2 e^{-\Gamma t}e^{-\left(\frac{(t'-t)-\mu}{\sqrt{2}\sigma}\right)^2}\,\mathrm{d}t\right) \tag{11.73}$$

$$= \frac{1}{\sqrt{2\pi}\sigma}\left(I_{t0}-\frac{1}{2}I_{t2}\right), \tag{11.74}$$

and $P_3(t';\Gamma,x,\mu,\sigma)$ as

$$P_3(t';\Gamma,x,\mu,\sigma) = \frac{1}{\sqrt{2\pi}\sigma}\int_0^{+\infty}\left(x\Gamma t-(x\Gamma t)^3/6\right)e^{-\Gamma t}e^{-\left(\frac{(t'-t)-\mu}{\sqrt{2}\sigma}\right)^2}\,\mathrm{d}t \tag{11.75}$$

$$= \frac{1}{\sqrt{2\pi}\sigma}\left(\int_0^{+\infty}x\Gamma t e^{-\Gamma t}e^{-\left(\frac{(t'-t)-\mu}{\sqrt{2}\sigma}\right)^2}\,\mathrm{d}t - \frac{1}{6}\int_0^{+\infty}(x\Gamma t)^3 e^{-\Gamma t}e^{-\left(\frac{(t'-t)-\mu}{\sqrt{2}\sigma}\right)^2}\,\mathrm{d}t\right) \tag{11.76}$$

$$= \frac{1}{\sqrt{2\pi}\sigma}\left(I_{t1}-\frac{1}{6}I_{t3}\right), \tag{11.77}$$

where

$$I_{tn} = \int_0^{+\infty}(x\Gamma t)^n e^{-\Gamma t}e^{-\left(\frac{(t'-t)-\mu}{\sqrt{2}\sigma}\right)^2}\,\mathrm{d}t. \tag{11.78}$$

The detailed derivation of the integrals I_{tn} is given in Appendix G and results in

$$I_{t0} = \frac{1}{\sqrt{r}}e^{-q+u_0^2}I_{g0}(u_0), \tag{11.79}$$

$$I_{t1} = \left(\frac{x\Gamma}{\sqrt{r}}\right)\frac{1}{\sqrt{r}}e^{-q+u_0^2}\left[I_{g1}(u_0)-u_0 I_{g0}(u_0)\right], \tag{11.80}$$

$$I_{t2} = \left(\frac{x\Gamma}{\sqrt{r}}\right)^2\frac{1}{\sqrt{r}}e^{-q+u_0^2}\left[I_{g2}(u_0)-2u_0 I_{g1}(u_0)+u_0^2 I_{g0}(u_0)\right], \tag{11.81}$$

$$I_{t3} = \left(\frac{x\Gamma}{\sqrt{r}}\right)^3\frac{1}{\sqrt{r}}e^{-q+u_0^2}\left[I_{g3}(u_0)-3u_0 I_{g2}(u_0)+3u_0^2 I_{g1}(u_0)-u_0^3 I_{g0}(u_0)\right]. \tag{11.82}$$

The integrals I_{tn} depend on integrals of the Gaussian function given by

$$I_{g0}(u_0) = \int_{u_0}^{+\infty}e^{-u^2}\,\mathrm{d}u = \frac{\sqrt{\pi}}{2}\mathrm{erfc}(u_0), \tag{11.83}$$

$$I_{g1}(u_0) = \int_{u_0}^{+\infty}ue^{-u^2}\,\mathrm{d}u = \frac{1}{2}e^{-u_0^2}, \tag{11.84}$$

$$I_{g2}(u_0) = \int_{u_0}^{+\infty} u^2 e^{-u^2}\,\mathrm{d}u = \frac{1}{2}\left(u_0 e^{-u_0^2} + \frac{\sqrt{\pi}}{2}\mathrm{erfc}(u_0)\right), \tag{11.85}$$

$$I_{g3}(u_0) = \int_{u_0}^{+\infty} u^3 e^{-u^2}\,\mathrm{d}u = \frac{1}{2}e^{-u_0^2}(u_0^2+1), \tag{11.86}$$

with

$$u_0 = \frac{p}{2\sqrt{r}},\ r = \frac{1}{2\sigma^2},\ p = \Gamma - \frac{(t'-\mu)}{\sigma^2},\ q = \frac{1}{2\sigma^2}(t'-\mu)^2, \text{ and } u = \sqrt{r}t + u_0. \tag{11.87}$$

11.3. Correction of decay-time acceptance

In addition to the decay-time resolution function $R(t,t',\mu_t,\sigma_t)$, a decay-time acceptance $\varepsilon(t)$ is included in the PDF of the time-dependent amplitude fit given in Eqn. 11.2. The decay-time acceptance arises from a bias caused by the selection in D^0 decay time as discussed in Chapt. 10.2 and is a function of the generated D^0 decay time. Before convoluting with the decay-time resolution as explained in Chapt. 11.2, the decay-time acceptance is included in the amplitude fit by introducing an additional exponential function, e^{-at}. The normalisation integrals in Eqn. 11.51 change to

$$\begin{aligned}\int_{-\infty}^{+\infty} T_0(t;\Gamma,y)\Theta(t)e^{-at}\,\mathrm{d}t &= \int_0^{+\infty} e^{-(\Gamma+a)t}\cosh(y\Gamma t)\,\mathrm{d}t \\ &= \frac{a+\Gamma}{a^2+2a\Gamma+\Gamma^2(1-y^2)}, \end{aligned}\tag{11.88}$$

$$\begin{aligned}\int_{-\infty}^{+\infty} T_1(t;\Gamma,x)\Theta(t)e^{-at}\,\mathrm{d}t &= \int_0^{+\infty} e^{-(\Gamma+a)t}\cos(x\Gamma t)\,\mathrm{d}t \\ &= \frac{a+\Gamma}{a^2+2a\Gamma+\Gamma^2(1+x^2)}, \end{aligned}\tag{11.89}$$

$$\begin{aligned}\int_{-\infty}^{+\infty} T_2(t;\Gamma,y)\Theta(t)e^{-at}\,\mathrm{d}t &= \int_0^{+\infty} e^{-(\Gamma+a)t}\sinh(y\Gamma t)\,\mathrm{d}t \\ &= \frac{\Gamma y}{a^2+2a\Gamma+\Gamma^2(1-y^2)}, \end{aligned}\tag{11.90}$$

$$\begin{aligned}\int_{-\infty}^{+\infty} T_3(t;\Gamma,x)\Theta(t)e^{-at}\,\mathrm{d}t &= \int_0^{+\infty} e^{-(\Gamma+a)t}\sin(x\Gamma t)\,\mathrm{d}t \\ &= \frac{\Gamma x}{a^2+2a\Gamma+\Gamma^2(1+x^2)}. \end{aligned}\tag{11.91}$$

The inclusion of the decay-time acceptance follows the convolution of the time-dependent amplitude with the decay-time resolution function $R(t,t',\mu_t,\sigma_t)$ detailed in Chapt. 11.2 closely; only relevant changes in the convolution integrals are discussed in the following.

11.3.1. Convolution with decay-time resolution for $T_{0,2}(t;\Gamma,y)\Theta(t)$

The convolution of terms $T_0(t;\Gamma,y) = e^{-\Gamma t}\cosh(y\Gamma t)$ and $T_2(t;\Gamma,y) = e^{-\Gamma t}\sinh(y\Gamma t)$ with a Gaussian resolution function changes as follows:

$$P_{0,2}(t';\Gamma,y,\mu,\sigma) = \int_0^{+\infty} T_{0,2}(t;\Gamma,y)e^{-at}G(t'-t;\mu,\sigma)\,\mathrm{d}t \tag{11.92}$$

$$\pm\frac{1}{2}\int_0^{+\infty} e^{-(\Gamma+a)t}\begin{pmatrix}e^{-y\Gamma t}\\ e^{-y\Gamma t}\end{pmatrix}G(t'-t;\mu,\sigma)\,\mathrm{d}t \tag{11.93}$$

$$\equiv \frac{1}{\sqrt{2\pi}\sigma}\left(\frac{I_{+y}\pm I_{-y}}{2}\right). \tag{11.94}$$

The integrals $I_{\pm y}$ are then given by

$$I_{\pm y} = \int_0^{+\infty} e^{-\Gamma t(1\mp y+a/\Gamma)}e^{-\left(\frac{(t'-t)-\mu}{\sqrt{2}\sigma}\right)^2}\,\mathrm{d}t, \tag{11.95}$$

$$= \int_0^{+\infty}\exp\left(-\frac{t^2}{2\sigma^2}-t\left[\Gamma(1\mp y+a/\Gamma)-\frac{(t'-\mu)}{\sigma^2}\right]\right.$$
$$\left.-\frac{1}{2\sigma^2}(t'-\mu)^2\right)\,\mathrm{d}t. \tag{11.96}$$

Folding in the correction of the decay-time acceptance, $u_0^{\pm y}$ and u are expressed as

$$u_0^{\pm y} = \frac{\sigma}{\sqrt{2}}\left(\Gamma(1\mp y)+a-\frac{(t'-\mu)}{\sigma^2}\right), \text{ and } u = \frac{t}{\sqrt{2}\sigma}+u_0^{\pm y}. \tag{11.97}$$

The integrals $I_{\pm y}$ are then given by

$$I_{\pm y} = \sigma\sqrt{\frac{\pi}{2}}e^{-q+(u_0^{\pm y})^2}\mathrm{erfc}(u_0^{\pm y}) \tag{11.98}$$

and the only required changes is the addition of the decay-time acceptance slope a to $u_0^{\pm y}$.

11.3.2. Convolution with decay-time resolution for $T_{1,3}(t;\Gamma,x)\Theta(t)$

The convolution integrals for $T_{1,3}(t;\Gamma,y)$ including the correction of the decay-time acceptance e^{-at} are given by

$$P_{1,3}(t';\Gamma,x,\mu,\sigma) = \int_0^{+\infty} T_{1,3}(t;\Gamma,y)e^{-at}G(t'-t;\mu,\sigma)\,\mathrm{d}t \tag{11.99}$$

$$\approx \frac{1}{\sqrt{2\pi}\sigma}\int_0^{+\infty} e^{-(\Gamma+a)t}\begin{pmatrix}1-(x\Gamma t)^2/2\\ x\Gamma t-(x\Gamma t)^3/6\end{pmatrix}$$
$$\times\, e^{-\left(\frac{(t'-t)-\mu}{\sqrt{2}\sigma}\right)^2}\,\mathrm{d}t. \tag{11.100}$$

The integral $P_1(t';\Gamma,x,\mu,\sigma)$ is written as

$$P_1(t';\Gamma,x,\mu,\sigma) = \frac{1}{\sqrt{2\pi}\sigma}\left(\int_0^{+\infty} e^{-(\Gamma+a)t}e^{-\left(\frac{(t'-t)-\mu}{\sqrt{2}\sigma}\right)^2}\,\mathrm{d}t\right.$$
$$\left.-\frac{1}{2}\int_0^{+\infty}(x\Gamma t)^2e^{-\Gamma t}e^{-\left(\frac{(t'-t)-\mu}{\sqrt{2}\sigma}\right)^2}\,\mathrm{d}t\right) \tag{11.101}$$

$$= \frac{1}{\sqrt{2\pi}\sigma}\left(I_{t0} - \frac{1}{2}I_{t2}\right), \tag{11.102}$$

and $P_3(t';\Gamma,x,\mu,\sigma)$ as

$$\begin{aligned} P_3(t';\Gamma,x,\mu,\sigma) = \frac{1}{\sqrt{2\pi}\sigma}\Bigg(&\int_0^{+\infty} x\Gamma t e^{-(\Gamma+a)t} e^{-\left(\frac{(t'-t)-\mu}{\sqrt{2}\sigma}\right)^2}\,\mathrm{d}t \\ &-\frac{1}{6}\int_0^{+\infty}(x\Gamma t)^3 e^{-\Gamma t} e^{-\left(\frac{(t'-t)-\mu}{\sqrt{2}\sigma}\right)^2}\,\mathrm{d}t\Bigg) \qquad (11.103) \\ = \frac{1}{\sqrt{2\pi}\sigma}&\left(I_{t1} - \frac{1}{6}I_{t3}\right). \qquad (11.104) \end{aligned}$$

This changes the definition of

$$I_{tn} = \int_0^{+\infty}(x\Gamma t)^n e^{-(\Gamma+a)t} e^{-\left(\frac{(t'-t)-\mu}{\sqrt{2}\sigma}\right)^2}\,\mathrm{d}t. \tag{11.105}$$

Folding in the correction of the decay-time acceptance, leads to

$$u_0 = \frac{\sigma}{\sqrt{2}}\left(\Gamma + a - \frac{(t'-\mu)}{\sigma^2}\right). \tag{11.106}$$

The integrals I_{tn} remain unchanged and the only required changes is the addition of the decay-time acceptance slope a to u_0.

11.4. Blinding procedure

The amplitude fit to data is performed blind, which means that the parameters of interest, x, y, $|q/p|$, and ϕ, are smeared such that their central values remain unknown until the analysis procedure and especially the fit model are finalised. This is done to avoid that the analyst tweaks the analysis procedure to obtain a desirable result. In this analysis, different blinding strategies are used for x, y, ϕ and $|q/p|$. The central values of x, y and ϕ are blinded by adding a random offset to the central value, which does not blind the uncertainty. The phase ϕ is blinded by adding a random number drawn from a uniform distribution in the range $[-1,1]$ to the parameter. The mixing parameters are blinded by adding a random offset to the parameter, which is drawn randomly from a uniform distribution in the range [-0.05, 0.05]. However, for $|q/p|$, studies of pseudo-experiments (see Chapt. 12.3) showed that the uncertainty of $|q/p|$ depends on its central value. Hence applying the blinding by adding an offset to the central value of $|q/p|$ would allow the analyst to deduce the central value of $|q/p|$. The magnitude of q/p is thus scaled by a factor of $(1+s)$ where s is a random number drawn from a uniform distribution in the range $[-1,1]$, and which leads to a blinding of the uncertainty on $|q/p|$.

12. Fit validation

The fitting framework is validated with detailed studies of pseudo-experiments. The simulated data used in these pseudo-experiments are generated with a 'particle gun', which produces only the signal B mesons instead of the full pp collision, as discussed in Chapt. 6.2. The momentum spectrum of the B mesons is generated according to the momentum spectrum taken from a full simulation that includes the pp interaction simulated with PYTHIA [76, 77]. The $D^0 \to K^0_S\pi^+\pi^-$ decay is generated using the model `DOMIXDALITZ` as implemented in EVTGEN [78]. The $D^0 \to K^0_S\pi^+\pi^-$ decay can be either modelled as an isobar model (see Chapt. 11.1.6) or as a model, which is detailed in Chapt. 11.1.7, including the K-matrix formalism in the production vector approach and LASS parameterisations. The model `DOMIXDALITZ` allows to set the real and imaginary parts of q/p and the mixing parameters x and y.

Realistic simulated data samples are generated with the PHOTOS package [79] for the generation of radiative photons, accounting for acceptance and resolution effects, and including a background component. The phase-space acceptance determined in Chapt. 10.1 is applied by rejecting candidates for which a uniform random number in the interval $(0, 1)$ is greater than the acceptance corresponding to the candidate's position in phase space. The efficiency of applying the acceptance correction is improved by rescaling the phase space acceptance to have a maximum of one. The generated decay-time distribution is smeared by the measured decay-time resolution (see Chapt. 10.4). Background distributions in D^0 decay time and phase-space are extracted from data as explained in Chapt. 9.5 and complete the simulated data samples used for the pseudo-experiment studies.

Sensitivities to the parameters of interest and possible biases of the fitting framework are studied with these pseudo-experiments. The studies are performed for both available models in the EVTGEN [78] implementation under the assumption of no *CP* violation and are detailed in Chapt. 12.1 and 12.2 together with the validation of the fit including *CP* violation in Chapt. 12.3.

Unless indicated otherwise, the simulated data used for the pseudo-experiments consist of subsamples reflecting data-taking conditions in 2011 and 2012 as well as differences between K^0_S(LL) and K^0_S(DD) types, such as signal to background ratio, phase-space efficiency and decay-time resolution parameterisations. In the amplitude fit, which is used to validate the fit, the masses and widths of the resonances are fixed, whereas the parameters of interest (x and y and where appropriate $|q/p|$ and ϕ), the D^0 decay time $\tau(D^0)$ and the complex coefficients of the amplitudes are floating.

12.1. Isobar model

The simulated data samples are generated according to an isobar model (see Chapt. 11.1.6) including the resonances listed in Table 12.1. In the validation fit, the masses and widths are fixed to the values reported in Table 12.1.

Table 12.1.: *Intermediate resonances contributing to the isobar model used in simulated pseudo-experiment studies with their masses, widths and spins. The numbers and the model are taken from the* D0mixDalitz *model implemented in* EvtGen *[78].*

Resonance	Mass [GeV]	Width [GeV]	Spin
	$\pi^+\pi^-$		
$\rho(770)$	0.776	0.146	1
ω	0.783	0.008	1
$f_0(980)$	0.975	0.044	0
$f_0(1370)$	1.434	0.173	0
$f_2(1270)$	1.275	0.185	2
σ_1	0.528	0.512	0
σ_2	1.033	0.099	0
	$K^0_S\pi^+$		
$K^*(892)^+$	0.894	0.046	1
$K^*_0(1430)^+$	1.459	0.175	0
$K^*_2(1430)^+$	1.426	0.099	2
	$K^0_S\pi^-$		
$K^*(892)^-$	0.894	0.046	1
$K^*_0(1430)^-$	1.459	0.175	0
$K^*_2(1430)^-$	1.426	0.099	2
$K^*(1680)^-$	1.677	0.205	1
	non-resonant $K^0_S\pi^+\pi^-$		

12.1.1. Sensitivity and fit validation

The sensitivity is extracted and a validation of the fitting framework is performed by fitting an ensemble of 300 pseudo-experiments generated with $x = y = 0.5\%$ and $\tau(D^0) = 410.1\,\text{ps}$. The sensitivity is estimated from the distributions of the statistical uncertainties on x and y, which results in a sensitivity on x of 0.21×10^{-2} and on y of 0.18×10^{-2}. The uncertainties returned by the amplitude fit are compatible with the spread of x and y as shown in Fig. 12.1.
As a cross check, the sensitivity is estimated from an amplitude fit to data, where the central values of x and y are blinded as explained in Chapt. 11.4. For the data fit, the masses and widths of the resonances have been floated around the reference values given in Ref. [11] with exception of the mass of the $\rho(770)$, $\omega(782)$, $f_0(980)$ and $f_2(1270)$. In addition the width of the $f_2(1270)$ is fixed. Since the σ_1 and σ_2 resonances do not correspond to real particles, their masses and widths refer to the EvtGen [78] implementation. The resonances contributing to the isobar model in data are listed in Table 11.4. This amplitude fit to data yields similar sensitivities to the ones obtained from pseudo-experiment studies, namely sensitivities of 0.22×10^{-2} on

x and of 0.19×10^{-2} on y. In Fig. 12.2, the results of an example amplitude fit to a single pseudo-experiment are shown in the Dalitz plane and the corresponding projections on D^0 decay time and on the Dalitz variables are illustrated in Figs. 12.3 and 12.4. Figure 12.2a shows the simulated data, the fitted PDF including signal and background components is illustrated in Fig. 12.2b and the background only distribution is given in Fig. 12.2c. The quality of the fit is assessed in the pull, which is the difference between data and value of the PDF in each bin divided by the uncertainty on the data shown in Fig. 12.2d. As can be seen from Fig. 12.2d, the pull exhibits a structure in $m^2(\pi^+\pi^-)$, which is caused by the real part of the $\omega(782)$ amplitude; the fit is not sensitive to this parameter. In the projections illustrated in Fig. 12.4, high pulls in the boundary regions and in regions of phase-space, where the projections are steeply changing, are observed. This is caused by the plotting of the fit model as the PDF of the amplitude fit is evaluated at the centre of each bin. An improvement is achieved by dividing each bin into finer bins but for steeply changing regions, the number of finer bins is insufficient to achieve a reliable pull distribution. The fine binning is limited by the memory of the GPU.

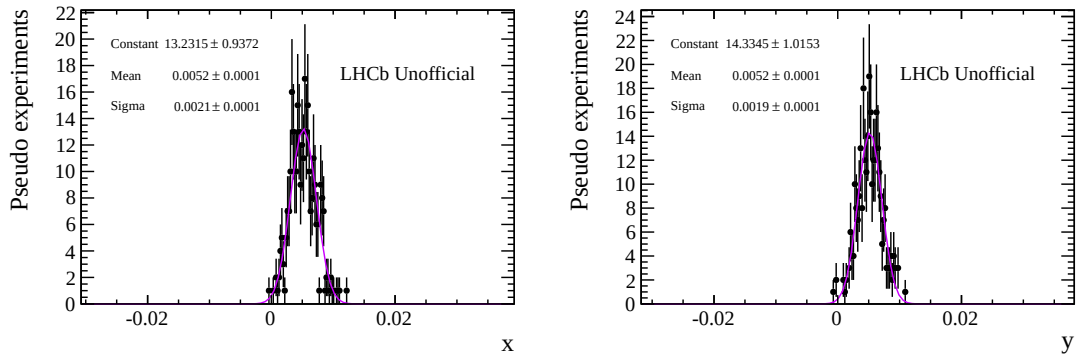

(a) *Distribution of x* **(b)** *Distribution of y*

Figure 12.1.: *Distribution of x and y in simulated pseudo-experiments fitted with a single Gaussian function. The Gaussian widths $\sigma(x) = (0.2104 \pm 0.0086) \times 10^{-2}$ and $\sigma(y) = (0.1934 \pm 0.0079) \times 10^{-2}$ are compatible with the averages of the fitted uncertainties on x and y, $\sigma(x)_{\text{fit}} = (0.2052 \pm 0.0003) \times 10^{-2}$ and $\sigma(y)_{\text{fit}} = (0.1837 \pm 0.0003) \times 10^{-2}$.*

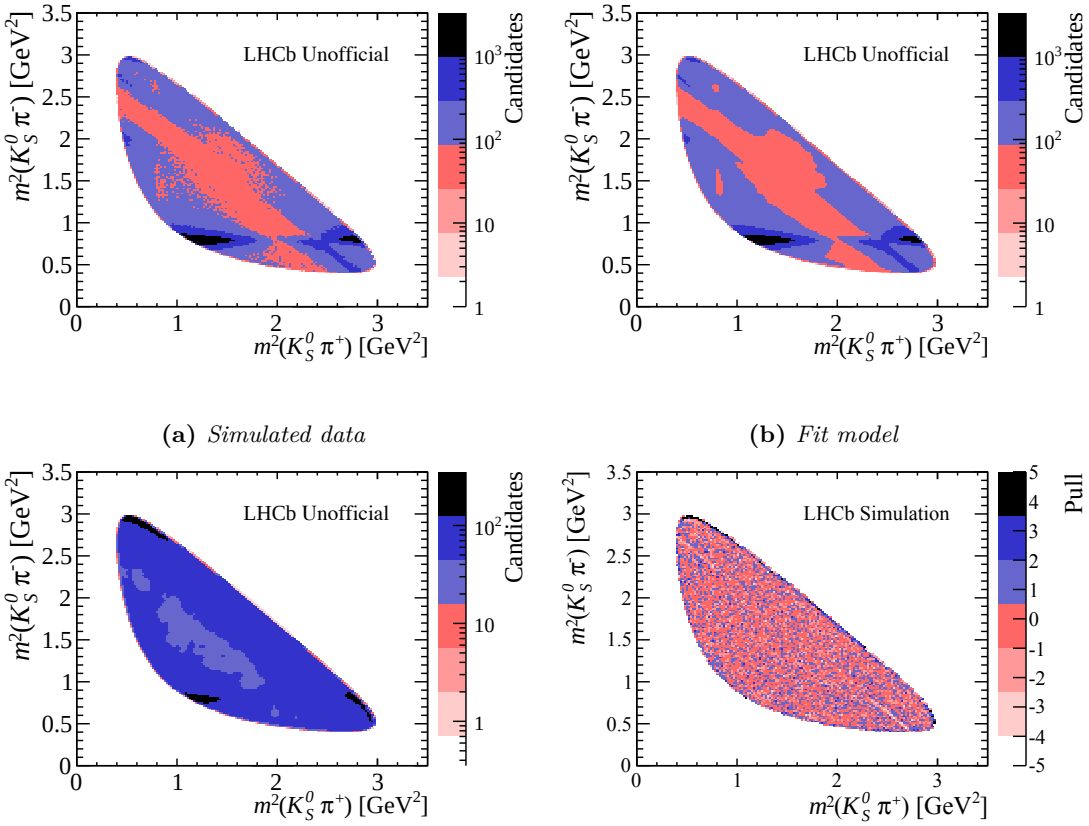

(a) *Simulated data* **(b)** *Fit model*

(c) *Background* **(d)** *Pull*

Figure 12.2.: *Results of an example amplitude fit to a single simulated pseudo-experiment with the isobar model.*

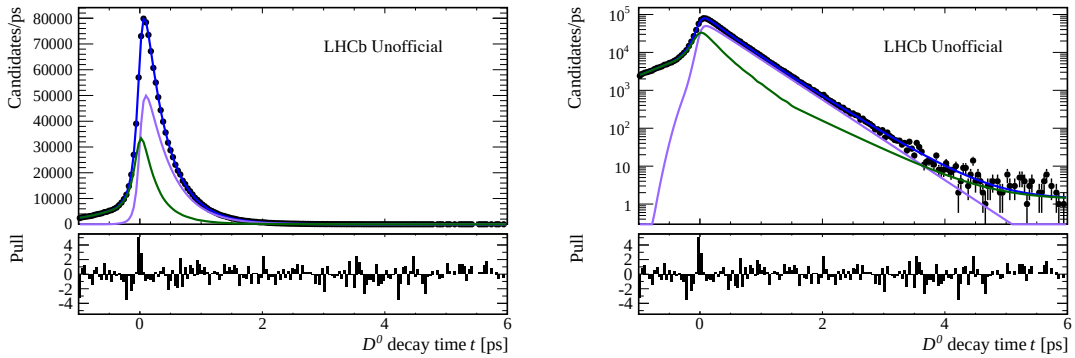

Figure 12.3.: *Projection on D^0 decay time of an example amplitude fit to a single simulated pseudo-experiment with the isobar model. The data points are shown in black, the total PDF in blue, the signal PDF in violet and the background PDF in green. The distributions are shown on a linear (left) and on a log scale (right).*

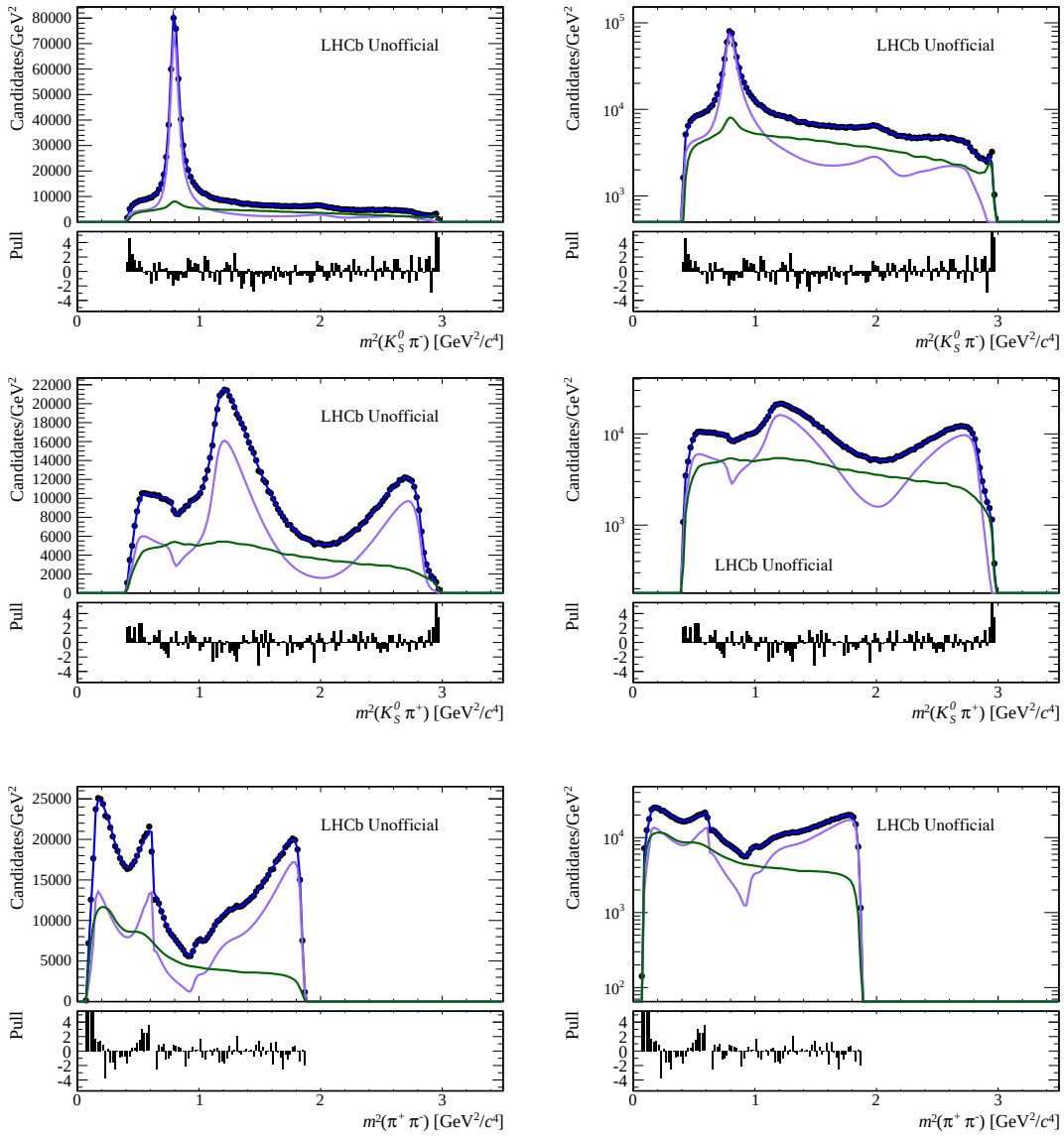

Figure 12.4.: *Phase-space projections of an example amplitude fit to a single simulated pseudo-experiment with the isobar model. The data points are shown in black, the total PDF in blue, the signal PDF in violet and the background PDF in green. The distributions are shown on a linear (left) and on a log scale (right).*

A validation of the fitting framework is performed by fitting the afore mentioned ensemble of 300 pseudo-experiments. The pull distributions of the parameters of interest are fitted with a single Gaussian function. If the Gaussian mean differs from zero or the width differs from one, the fitter exhibits a bias. On average, the fit returns $\tau(D^0) = (409.86 \pm 0.03)\,\text{ps}$, $x = (0.517 \pm 0.012)\%$ and $y = (0.520 \pm 0.011)\%$. As can be seen from Fig. 12.5, the fitter exhibits small biases in x and y and a large bias of half a statistical uncertainty σ in $\tau(D^0)$. A possible systematic uncertainty resulting from the observed bias in $\tau(D^0)$ is discussed in Chapt. 13.2.2 together with the uncertainties added due to the small biases in x and y.

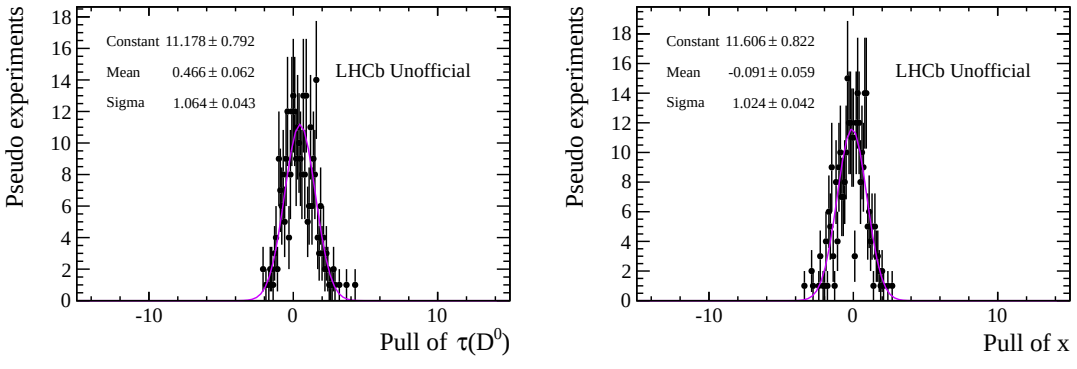

(a) *Pull of* $\tau(D^0)$ **(b)** *Pull of* x

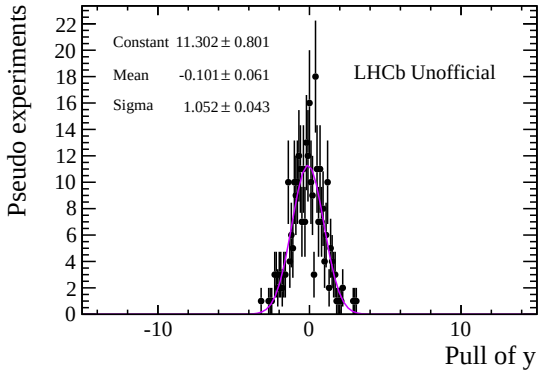

(c) *Pull of* y

Figure 12.5.: *Pull distributions of* $\tau(D^0)$*,* x *and* y *in simulated pseudo-experiments fitted with a single Gaussian function, which is used to assess any biases resulting from the amplitude fit.*

In addition to the ensemble of 300 pseudo-experiments generated with $x = y = 0.5\%$ and $\tau(D^0) = 410.1\,\text{ps}$, simulated data samples were generated with $\tau(D^0) = 410.1\,\text{ps}$ and various sets of x and y. The studied ensembles consist of 100 simulated data samples each reflecting 2011 data-taking conditions for both K^0_S(LL) and K^0_S(DD) types. The results of the amplitude fits to these ensembles are summarised in Table 12.2. The fits to the ensemble generated with $x = 0\%, y = 0\%$ show a potential small bias in x and y but the discrepancy from zero is less than 20% of a statistical uncertainty.

Table 12.2.: *Study of fit bias and sensitivity for simulated pseudo-experiments reflecting 2011 data-taking conditions generated with different values for x and y. The average values for $\tau(D^0)$, x and y are listed as well as the sensitivities on x and y. The distributions of the pulls of $\tau(D^0)$, x and y are fitted with a single Gaussian function. The mean and width of the Gaussian are reported as a measure of the fit bias.*

	$x = 0\%, y = 0\%$	$x = 1\%, y = 1\%$	$x = 0.25\%, y = 0.5\%$
Average fit result			
τ [ps]	409.82 ± 0.13	409.49 ± 0.15	409.82 ± 0.12
x [%]	0.079 ± 0.040	1.000 ± 0.037	0.251 ± 0.036
y [%]	0.077 ± 0.033	0.976 ± 0.032	0.478 ± 0.031
Sensitivity			
$x\,[10^{-2}]$	0.36	0.36	0.36
$y\,[10^{-2}]$	0.32	0.33	0.33
Fit bias assessed with pull distributions			
Mean of τ [ps]	0.555 ± 0.111	0.717 ± 0.121	0.583 ± 0.100
RMS of τ [ps]	1.052 ± 0.078	1.143 ± 0.085	0.948 ± 0.071
Mean of x [%]	-0.210 ± 0.109	0.013 ± 0.102	0.004 ± 0.100
RMS of x [%]	1.038 ± 0.077	0.965 ± 0.072	0.952 ± 0.071
Mean of y [%]	-0.230 ± 0.100	-0.070 ± 0.100	0.072 ± 0.096
RMS of y [%]	0.953 ± 0.071	0.944 ± 0.070	0.908 ± 0.068

	$x = 0.5\%, y = 0.25\%$	$x = 0.5\%, y = 1\%$	$x = 1\%, y = 0.5\%$
Average fit result			
τ [ps]	409.78 ± 0.14	409.82 ± 0.13	409.60 ± 0.14
x [%]	0.567 ± 0.041	0.505 ± 0.037	1.074 ± 0.037
y [%]	0.256 ± 0.029	1.062 ± 0.033	0.500 ± 0.030
Sensitivity			
$x\,[10^{-2}]$	0.36	0.36	0.36
$y\,[10^{-2}]$	0.32	0.33	0.32
Fit bias assessed with pull distributions			
Mean of τ [ps]	0.557 ± 0.1132	0.584 ± 0.110	0.718 ± 0.104
RMS of τ [ps]	1.074 ± 0.080	1.045 ± 0.080	0.990 ± 0.074
Mean of x [%]	-0.185 ± 0.112	-0.018 ± 0.102	-0.202 ± 0.102
RMS of x [%]	1.059 ± 0.079	0.972 ± 0.072	0.969 ± 0.072
Mean of y [%]	-0.144 ± 0.089	-0.189 ± 0.102	0.006 ± 0.093
RMS of y [%]	0.845 ± 0.630	0.969 ± 0.072	0.885 ± 0.066

12.2. *K*-matrix and LASS model

The simulated data samples are generated according to a model with the K-matrix formalism in the production vector approach for the $\pi^+\pi^-$ S-wave and the LASS parameterisation for the $K_0^*(1430)^\pm$ (see Chapt. 11.1.7) under the assumption of no CP violation and with $x = y = 0.5\%$ and $\tau(D^0) = 410.1\,\text{ps}$. The contributions to the model are listed in Table 12.3 and the masses

and widths of the resonances are fixed to the values given in this table. In addition, the parameters listed in Table 12.4 are fixed.

Table 12.3.: *Intermediate resonances contributing to the model with the K-matrix formalism in the production vector approach and LASS parameterisation used in simulated pseudo-experiment studies with their masses, widths and spins. The numbers and the model are taken from the* D0mixDalitz *model implemented in* EvtGen *[78].*

Resonance	Mass [GeV]	Width [GeV]	Spin
	$\pi^+\pi^-$		
$\rho(770)$	0.7758	0.1464	1
ω	0.78259	0.00849	1
$f_2(1270)$	1.2754	0.1851	2
$\pi^+\pi^-$ S-wave			
	$K^0_S\pi^+$		
$K^*(892)^+$	0.893619	0.0466508	1
$K^*_0(1430)^+$	1.46312	0.232393	0
$K^*_2(1430)^+$	1.4256	0.0985	2
	$K^0_S\pi^-$		
$K^*(892)^-$	0.893619	0.0466508	1
$K^*_0(1430)^-$	1.46312	0.232393	0
$K^*_2(1430)^-$	1.4256	0.0985	2
$K^*(1680)^-$	1.677	0.205	1

Table 12.4.: *Parameters of the model with the K-matrix formalism in the production vector approach and LASS parameterisation used in simulated pseudo-experiment studies. The complete list of parameters, including the fixed parameters, can be found in Chapt. 11.1.4. The numbers and the model are taken from the* D0mixDalitz *as in* EvtGen *[78].*

Parameter	
LASS	
s [GeV]	1.07
r	-1.83
B [GeV]	0.80
ϕ_B [rad]	2.33
R	1
ϕ_R [rad]	-5.31
K-matrix	
s_0^{prod} [GeV^2]	-0.07
$f_{12}^{prod'}$	$1.88 - 0.63i$
$f_{13}^{prod'}$	$4.32 - 2.75i$
$f_{14}^{prod'}$	$3.22 - 0.27i$
$f_{15}^{prod'}$	0

12.2.1. Sensitivity and fit validation

The estimated sensitivities are 0.21×10^{-2} and 0.18×10^{-2} to x and y, respectively, for 300 ensembles of pseudo-experiments reflecting 2011 and 2012 data-taking conditions. The uncertainties returned by the amplitude fit are compatible with the spread of x and y as shown in Fig. 12.6. The sensitivity on data is estimated from an amplitude fit, where the central values of x and y are blinded as explained in Chapt. 11.4.

In the amplitude fit to data, the masses and widths of the resonances have been floated around the reference values reported in Ref. [11]. Robustness of the fit is ensured by keeping the mass of the $\rho(770)$, $\omega(782)$, $f_0(980)$ and $f_2(1270)$ as well as the width of the $f_2(1270)$ fixed. The parameters listed in Table 12.4 are floated with exception of R, which is fixed to one, and f_{15}^{prod}, which is set to zero due to the lack of sensitivity. The model contributions are given in Table 11.5. The fit yields 0.21×10^{-2} on x and of 0.18×10^{-2} on y, which are similar to the ones obtained from the study of simulated pseudo-experiments. Figures 12.7, 12.8 and 12.9 illustrate the results of an example amplitude fit to a single pseudo-experiment in the Dalitz plane and in the projections on D^0 decay time and the Dalitz variables, respectively. The pull distribution shown in Fig. 12.7d shows the same feature in the $\omega(782)$ region as Fig. 12.2d, caused by the real part of the $\omega(782)$ amplitude. As discussed previously, the high pulls of the projections shown in Fig. 12.9, especially in the boundary regions, are are plotting effect.

On average, the fit returns $\tau(D^0) = (409.63 \pm 0.03)$ ps, $x = (0.521 \pm 0.012)\%$ and $y = (0.510 \pm 0.010)\%$. As can be seen from Fig. 12.10, the fitter does exhibit a large bias in $\tau(D^0)$, which requires the estimation of a corresponding systematic uncertainty. No bias is observed for x and y.

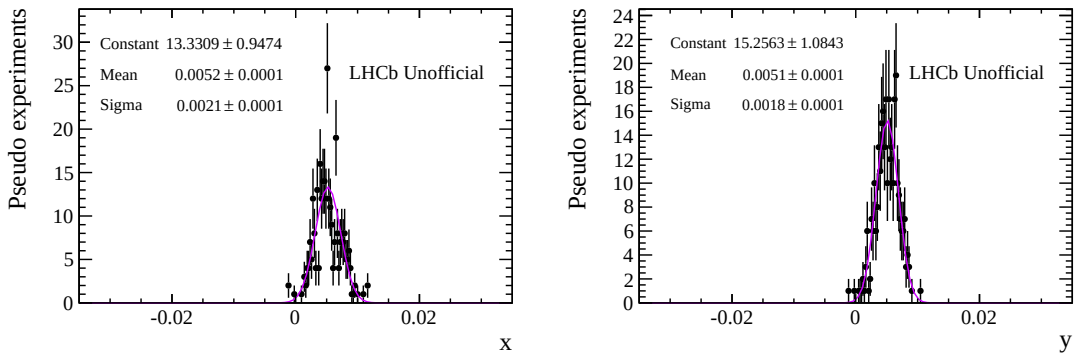

(a) *Distribution of x* **(b)** *Distribution of y*

Figure 12.6.: *Distribution of x and y in simulated pseudo-experiments fitted with a single Gaussian function. The Gaussian widths $\sigma(x) = (0.2067 \pm 0.0085) \times 10^{-2}$ and $\sigma(y) = (0.1806 \pm 0.0074) \times 10^{-2}$ are compatible with the averages of the fitted uncertainties on x and y, $\sigma(x)_{\rm fit} = (0.2097 \pm 0.0001) \times 10^{-2}$ and $\sigma(y)_{\rm fit} = (0.1799 \pm 0.0001) \times 10^{-2}$.*

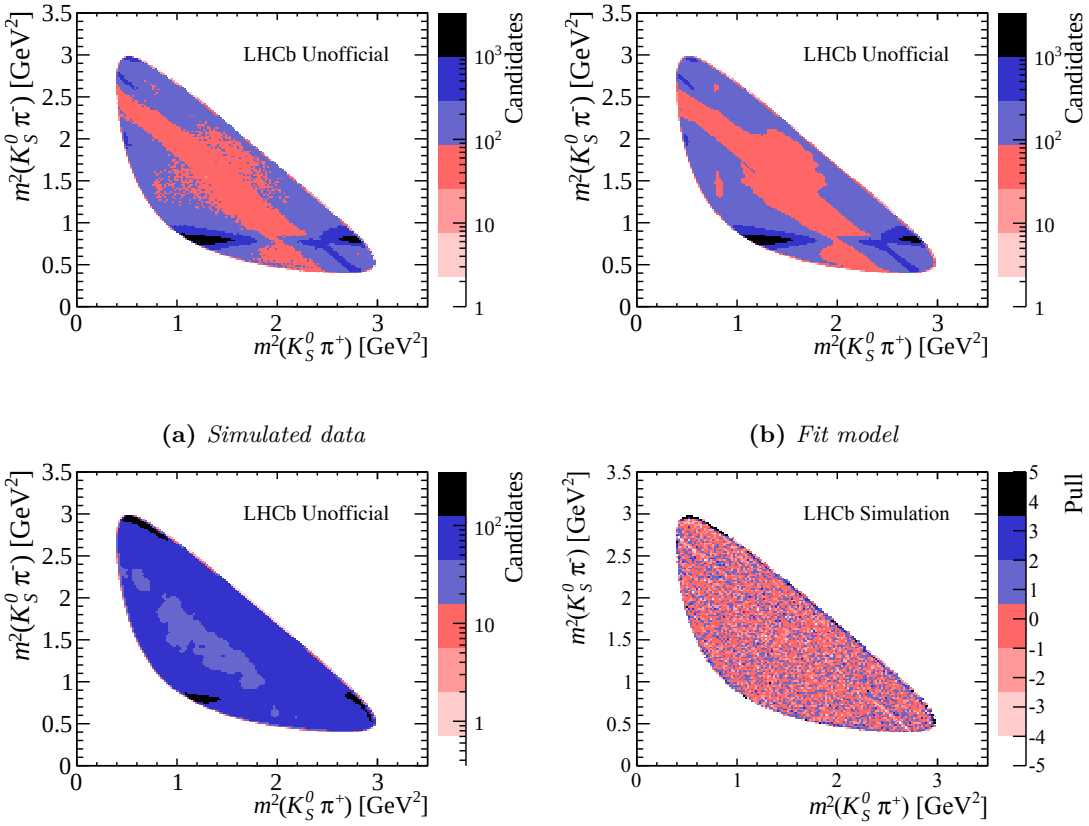

(a) *Simulated data* **(b)** *Fit model*

(c) *Background* **(d)** *Pull*

Figure 12.7.: *Results of an example amplitude fit to a single simulated pseudo-experiment with the K-matrix and LASS model.*

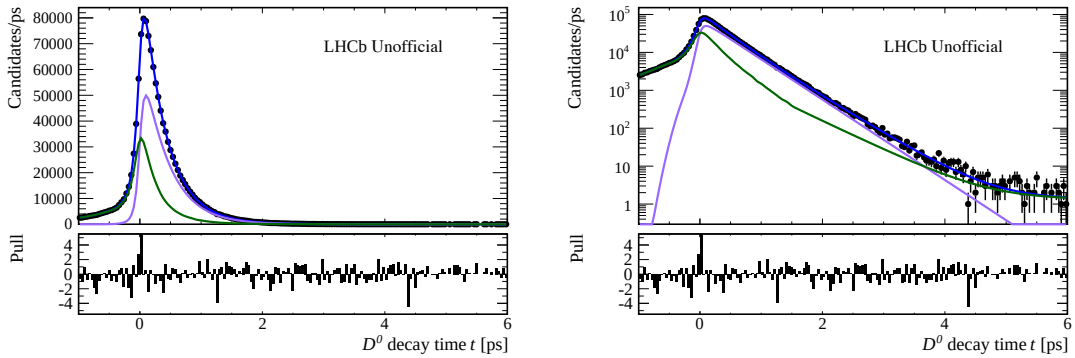

Figure 12.8.: *Projection on D^0 decay time of an example amplitude fit to a single simulated pseudo-experiment with the K-matrix and LASS model. The data points are shown in black, the total PDF in blue, the signal PDF in violet and the background PDF in green. The distributions are shown on a linear (left) and on a log scale (right).*

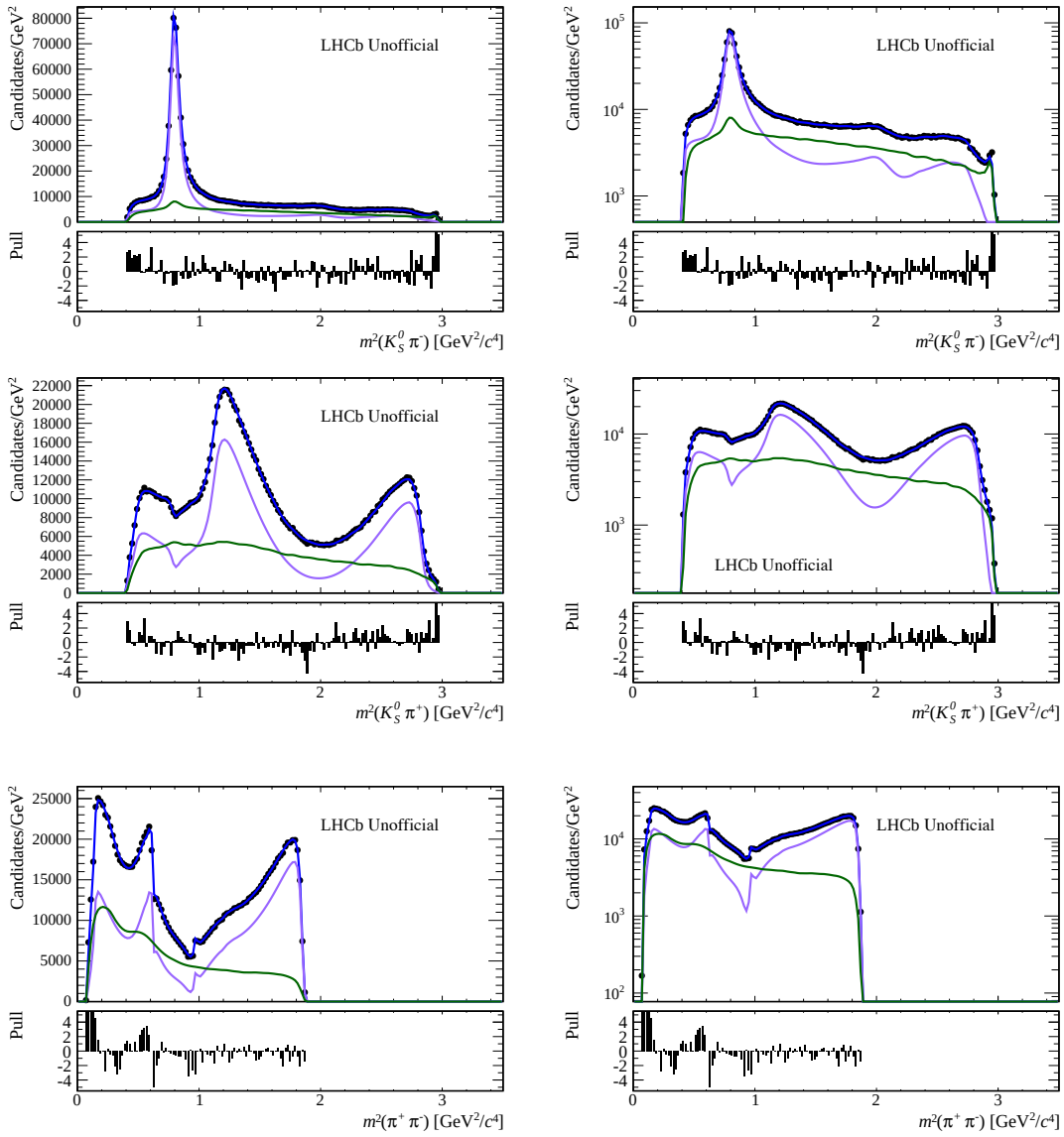

Figure 12.9.: *Phase-space projections of an example amplitude fit to a single simulated pseudo-experiment with the K-matrix and LASS model. The data points are shown in black, the total PDF in blue, the signal PDF in violet and the background PDF in green. The distributions are shown on a linear (left) and on a log scale (right).*

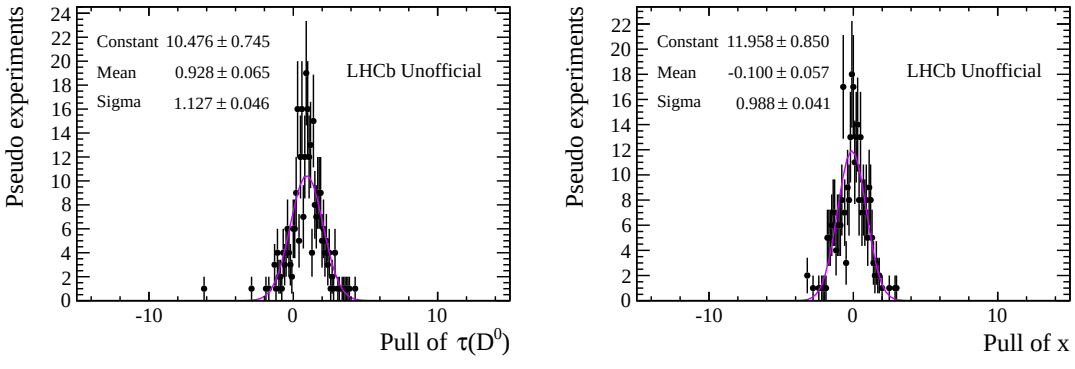

(a) *Pull of* $\tau(D^0)$ **(b)** *Pull of* x

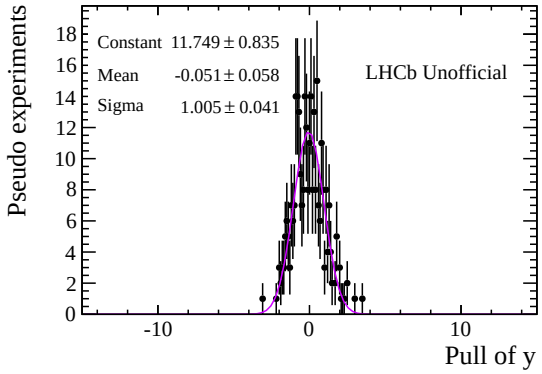

(c) *Pull of* y

Figure 12.10.: *Pull distributions of* $\tau(D^0)$*,* x *and* y *in simulated pseudo-experiments fitted with a single Gaussian function, which is used to assess any biases resulting from the amplitude fit.*

12.3. *CP* violation fit validation

In the Standard Model, direct *CP* violation is expected to be negligibly small in Cabibbo favoured and doubly-Cabibbo suppressed amplitudes, so the amplitude fit includes only the indirect *CP* violating parameter q/p. The simulated data samples are generated according to the isobar model (see Chapt. 11.1.6) including the resonances listed in Table 12.1 with different values of q/p. An ensemble of pseudo-experiments generated with $x = y = 0.5\%$, $\tau(D^0) = 410.1\,\text{ps}$, $|q/p| = 1$ and $\phi = 0$ is studied. Here, the signal probabilities (see Chapt. 8.3) and background distributions (see Chapt. 9.5) are extracted separately for D^0 and $\overline{D}^0$ tags. In the following, studies with the isobar and K-matrix and LASS model are presented.

12.3.1. Isobar model

The simulated data samples are generated according to an isobar model (see Chapt. 11.1.6) including the resonances listed in Table 12.1. In the amplitude fit, the masses and widths of the resonances are fixed to the values given in Table 12.1, whereas the mixing parameters x, y, the D^0 decay time, $|q/p|$, ϕ and the complex coefficients of the amplitudes are floating.

The uncertainties returned by the fit for an ensemble of 100 pseudo-experiments are distributed within a sharp peak but show some outliers, which shift the mean of the uncertainty distribution to higher values. The averages of the uncertainties returned by the fit are $\sigma(x)_{\text{fit}} = (0.22 \pm 0.01) \times 10^{-2}$, $\sigma(y)_{\text{fit}} = (0.20 \pm 0.00) \times 10^{-2}$, $\sigma(|q/p|)_{\text{fit}} = (0.21 \pm 0.01)$, $\sigma(\phi)_{\text{fit}} = (0.18 \pm 0.01)$. The widths of the Gaussian fit to the distributions of x, y, $|q/p|$ and ϕ are $\sigma(x) = (0.22 \pm 0.02) \times 10^{-2}$, $\sigma(y) = (0.18 \pm 0.01) \times 10^{-2}$, $\sigma(|q/p|) = (0.15 \pm 0.01)$, $\sigma(\phi) = (0.18 \pm 0.01)$ as shown in Fig. 12.11. The distributions of the fit uncertainties have a few outliers, especially the distribution of the uncertainty on $|q/p|$ shows a long right tail, which shifts the average to higher values.

On average, the fit returns $\tau(D^0) = (409.653 \pm 0.05)$ ps, $x = (0.530 \pm 0.022)\%$, $y = (0.542 \pm 0.018)\%$, $|q/p| = 1.014 \pm 0.015$ and $\phi = -0.028 \pm 0.019$. As can be seen from Fig. 12.12, slight biases on $\tau(D^0)$, y and ϕ are observed. A corresponding systematic uncertainty is assigned on these parameters to account for the bias caused by the fit as outlined in Chapt. 13.2.2.

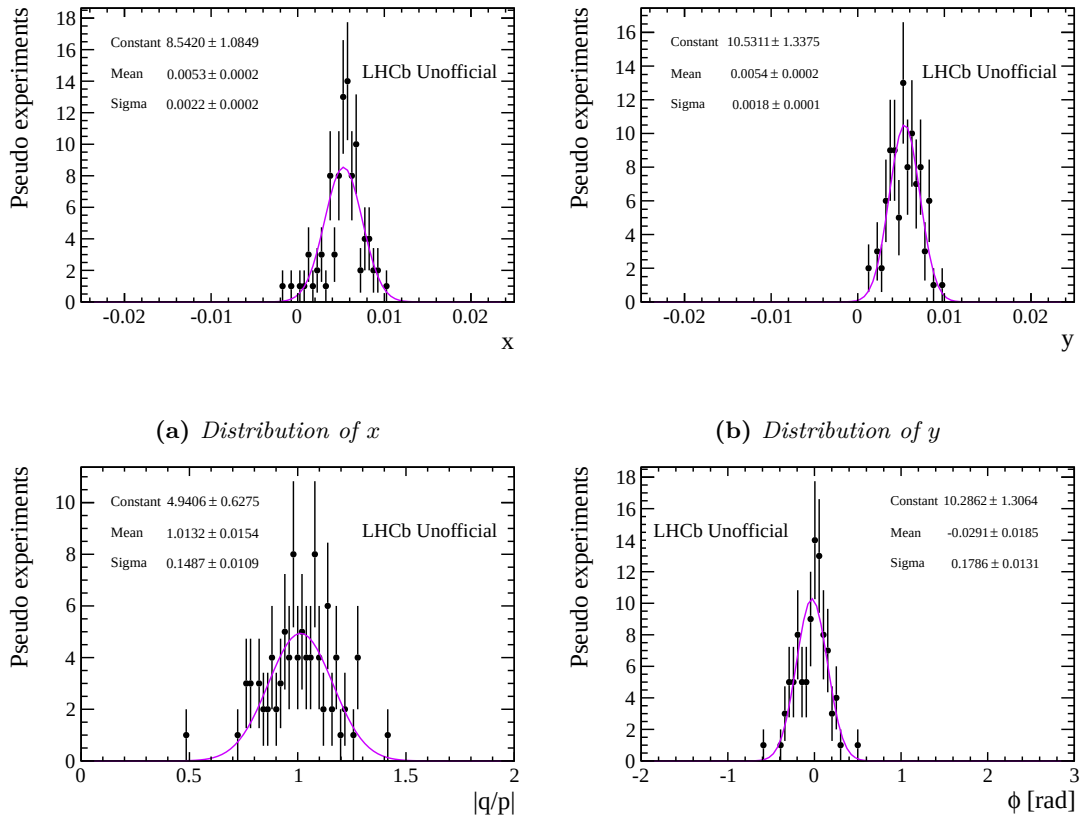

(a) *Distribution of x*

(b) *Distribution of y*

(c) *Distribution of $|q/p|$*

(d) *Distribution of ϕ*

Figure 12.11.: *Distribution of x, y, $|q/p|$ and ϕ in simulated pseudo-experiments fitted with a single Gaussian function.*

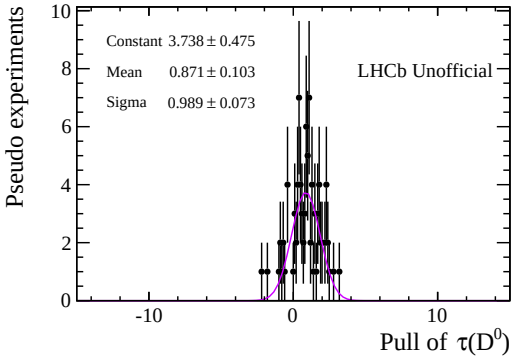

(a) *Pull of* $\tau(D^0)$

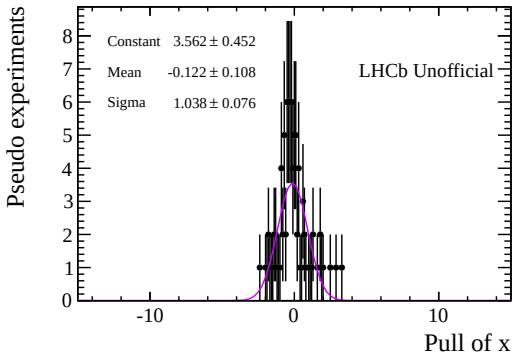

(b) *Pull of* x

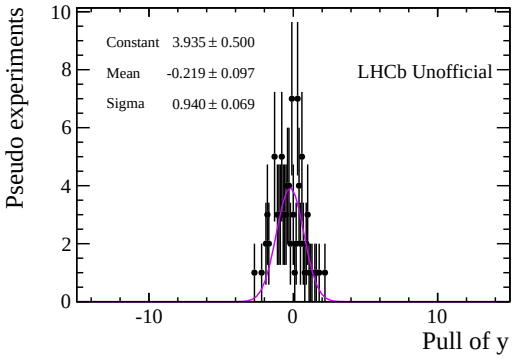

(c) *Pull of* y

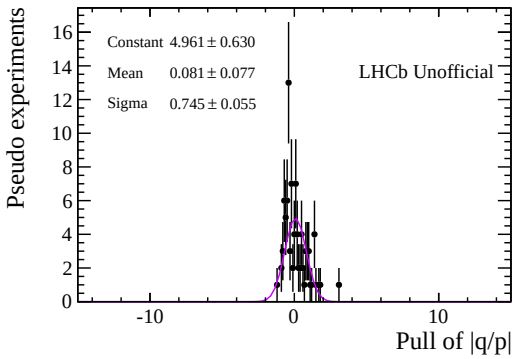

(d) *Pull of* $|q/p|$

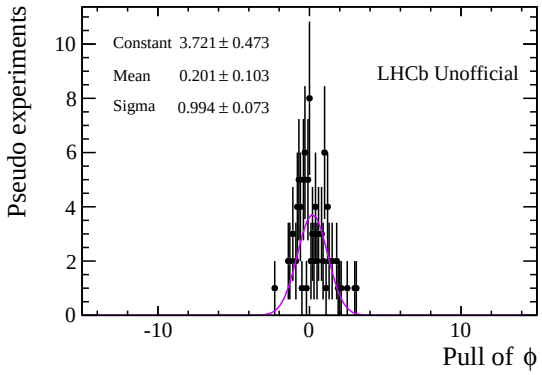

(e) *Pull of* ϕ

Figure 12.12.: *Pull distributions of* $\tau(D^0)$*,* x*,* y*,* $|q/p|$ *and* ϕ *in simulated pseudo-experiments fitted with a single Gaussian function, which is used to assess any biases resulting from the amplitude fit allowing for CP violation.*

For an ensemble of 100 pseudo-experiments reflecting 2011 data-taking conditions and K^0_S(LL) and K^0_S(DD) types generated with $x = y = 0.5\%$ and $\tau(D^0) = 410.1\,\text{ps}$, the $|q/p|, \phi$ parameter space is scanned and the results are summarised in Table 12.5. The values of q/p were chosen according to the superweak constraint [105]

$$\tan\phi = \left(1 - \left|\frac{q}{p}\right|\right)\frac{x}{y}. \tag{12.1}$$

The fits listed in Table 12.5 show clear biases, especially for the samples with extreme values of $|q/p|$ and ϕ. The sample generated with $|q/p| = 1.3$ and $\phi = -0.25$ shows large biases in x, y, $|q/p|$ and ϕ. For $|q/p| = 0.7$ and $\phi = 0.33$, large biases are present in y and $|q/p|$, and a slight bias in ϕ. In the more realistic *CP* scenarios, the size of the biases is reduced and the only significant bias is in $|q/p|$.

Table 12.5.: *Study of fit bias and sensitivity for ensembles of simulated pseudo-experiments reflecting 2011 data taking conditions generated with $x = y = 0.5\%$ and $\tau(D^0) = 410.1\,\text{ps}$ and different values for $|q/p|$ and ϕ. The average values for $\tau(D^0)$, x, y, $|q/p|$ and ϕ are listed as well as the sensitivities on the mixing and CP violation parameters. The distributions of the pulls of $\tau(D^0)$, x, y, $|q/p|$ and ϕ are fitted with a single Gaussian function and the mean and width of the Gaussian function are reported as measure of the fit bias.*

	$\|q/p\| = 0.7$ $\phi = 0.33$	$\|q/p\| = 0.9$ $\phi = 0.11$	$\|q/p\| = 1.1$ $\phi = -0.10$	$\|q/p\| = 1.3$ $\phi = -0.25$
		Average fit result		
τ [ps]	409.50 ± 0.05	409.56 ± 0.05	409.60 ± 0.05	409.53 ± 0.06
x [%]	0.524 ± 0.022	0.517 ± 0.022	0.527 ± 0.022	0.615 ± 0.023
y [%]	0.581 ± 0.021	0.523 ± 0.018	0.500 ± 0.019	0.589 ± 0.027
$\|q/p\|$	0.817 ± 0.015	0.988 ± 0.019	1.160 ± 0.027	1.154 ± 0.018
ϕ [rad]	0.23 ± 0.018	0.029 ± 0.018	-0.112 ± 0.022	-0.262 ± 0.019
		Sensitivity		
$x\,[10^{-2}]$	0.198	0.220	0.235	0.270
$y\,[10^{-2}]$	0.193	0.198	0.214	0.224
$\|q/p\|$	0.148	0.204	0.258	0.271
ϕ [rad]	0.207	0.200	0.218	0.169
		Fit bias assessed with pull distributions		
Mean of τ [ps]	1.173 ± 0.105	1.064 ± 0.103	0.985 ± 0.097	1.116 ± 0.130
RMS of τ [ps]	1.007 ± 0.074	0.957 ± 0.073	0.896 ± 0.068	1.065 ± 0.092
Mean of x [%]	-0.131 ± 0.110	-0.078 ± 0.110	-0.110 ± 0.103	-0.530 ± 0.105
RMS of x [%]	1.050 ± 0.077	1.020 ± 0.078	0.958 ± 0.073	0.856 ± 0.074
Mean of y [%]	-0.444 ± 0.108	-0.129 ± 0.097	0.017 ± 0.100	-0.406 ± 0.134
RMS of y [%]	1.032 ± 0.076	0.900 ± 0.067	0.931 ± 0.071	1.101 ± 0.095
Mean of $\|q/p\|$	1.442 ± 0.111	0.337 ± 0.098	-0.309 ± 0.081	-0.461 ± 0.067
RMS of $\|q/p\|$	1.068 ± 0.079	0.907 ± 0.069	0.753 ± 0.057	0.548 ± 0.047
Mean of ϕ [rad]	-1.173 ± 0.086	-0.116 ± 0.093	0.705 ± 0.103	1.635 ± 0.113
RMS of ϕ [rad]	0.827 ± 0.061	0.859 ± 0.066	0.955 ± 0.073	0.928 ± 0.080

12.3.2. K-matrix and LASS model

The simulated data samples are generated according to a model with the K-matrix formalism in the production vector approach for the $\pi^+\pi^-$ S-wave and the LASS parameterisation for the $K_0^*(1430)^\pm$ (see Chapt. 11.1.7). The masses and widths of the resonances are fixed to the values given in Table 12.3 whereas the mixing parameters x and y, the D^0 decay time $\tau(D^0)$ and the complex coefficients of the amplitudes are floating. In addition, the parameters listed

in Table 12.4 are fixed.

The averages of the uncertainties returned by the fit for 110 pseudo-experiments are $\sigma(x)_{\text{fit}} = (0.26 \pm 0.01) \times 10^{-2}$, $\sigma(y)_{\text{fit}} = (0.22 \pm 0.01) \times 10^{-2}$, $\sigma(|q/p|)_{\text{fit}} = (0.24 \pm 0.01)$, $\sigma(\phi)_{\text{fit}} = (0.19 \pm 0.01)$. The widths of the Gaussian fit to the distributions of x, y, $|q/p|$ and ϕ are $\sigma(x) = (0.19 \pm 0.01) \times 10^{-2}$, $\sigma(y) = (0.18 \pm 0.01) \times 10^{-2}$, $\sigma(|q/p|) = (0.16 \pm 0.01)$, $\sigma(\phi) = (0.18 \pm 0.01)$ as shown in Fig. 12.13. As reported for the studies with the isobar model, the uncertainty on $|q/p|$ has a long right tail, which causes a shift of the averaged uncertainty to higher values. The distributions of the uncertainties on x, y and ϕ have some outliers but this does not introduce a significant shift of the averaged uncertainty compared to the uncertainties returned by the fit.

On average, the fit returns $\tau(D^0) = (409.49 \pm 0.05)$ ps, $x = (0.537 \pm 0.018)\%$, $y = (0.556 \pm 0.018)\%$, $|q/p| = 1.060 \pm 0.015$ and $\phi = -0.086 \pm 0.017$. As can be seen from Fig. 12.14, slight biases on $\tau(D^0)$ and x are present and larger biases on y and ϕ are observed. No bias is found on $|q/p|$. A corresponding systematic uncertainty is assigned on these parameters to account for the bias caused by the fit as outlined in Chapt. 13.2.2.

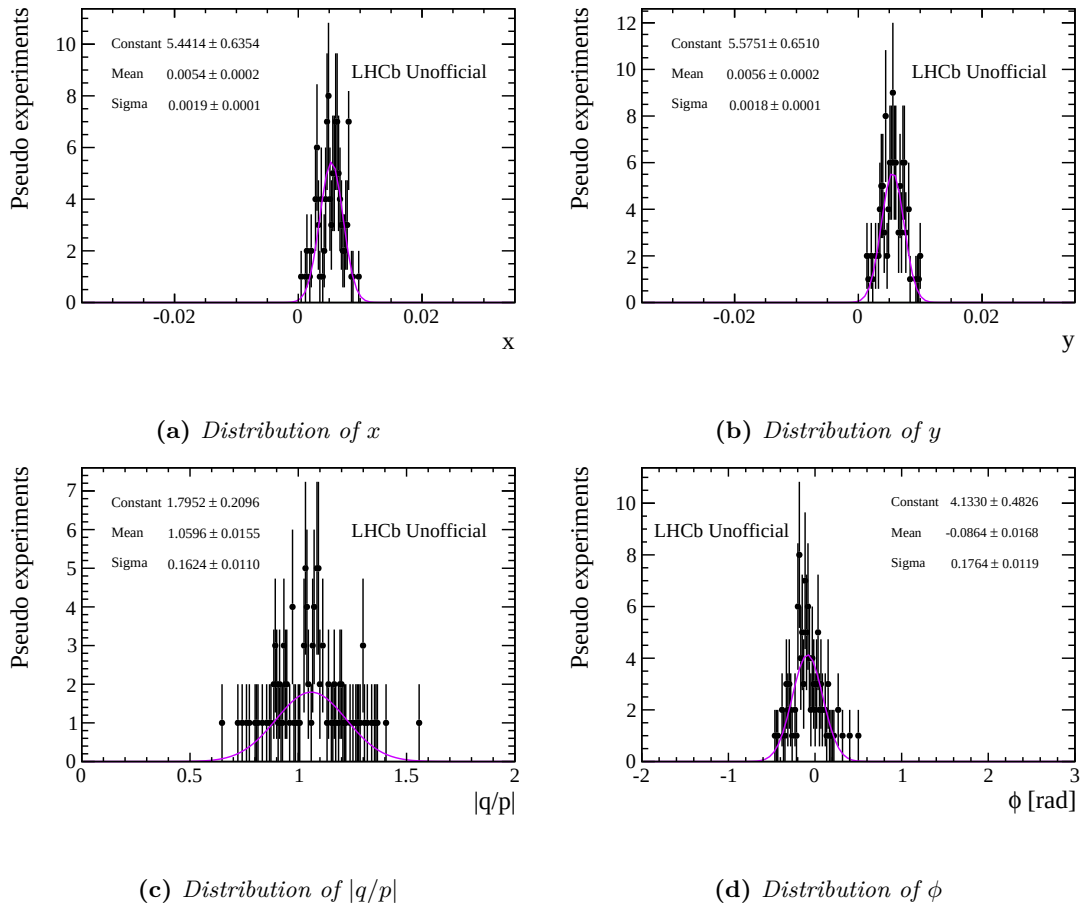

(a) *Distribution of x*

(b) *Distribution of y*

(c) *Distribution of $|q/p|$*

(d) *Distribution of ϕ*

Figure 12.13.: *Distribution of x, y, $|q/p|$ and ϕ fitted with a single Gaussian function.*

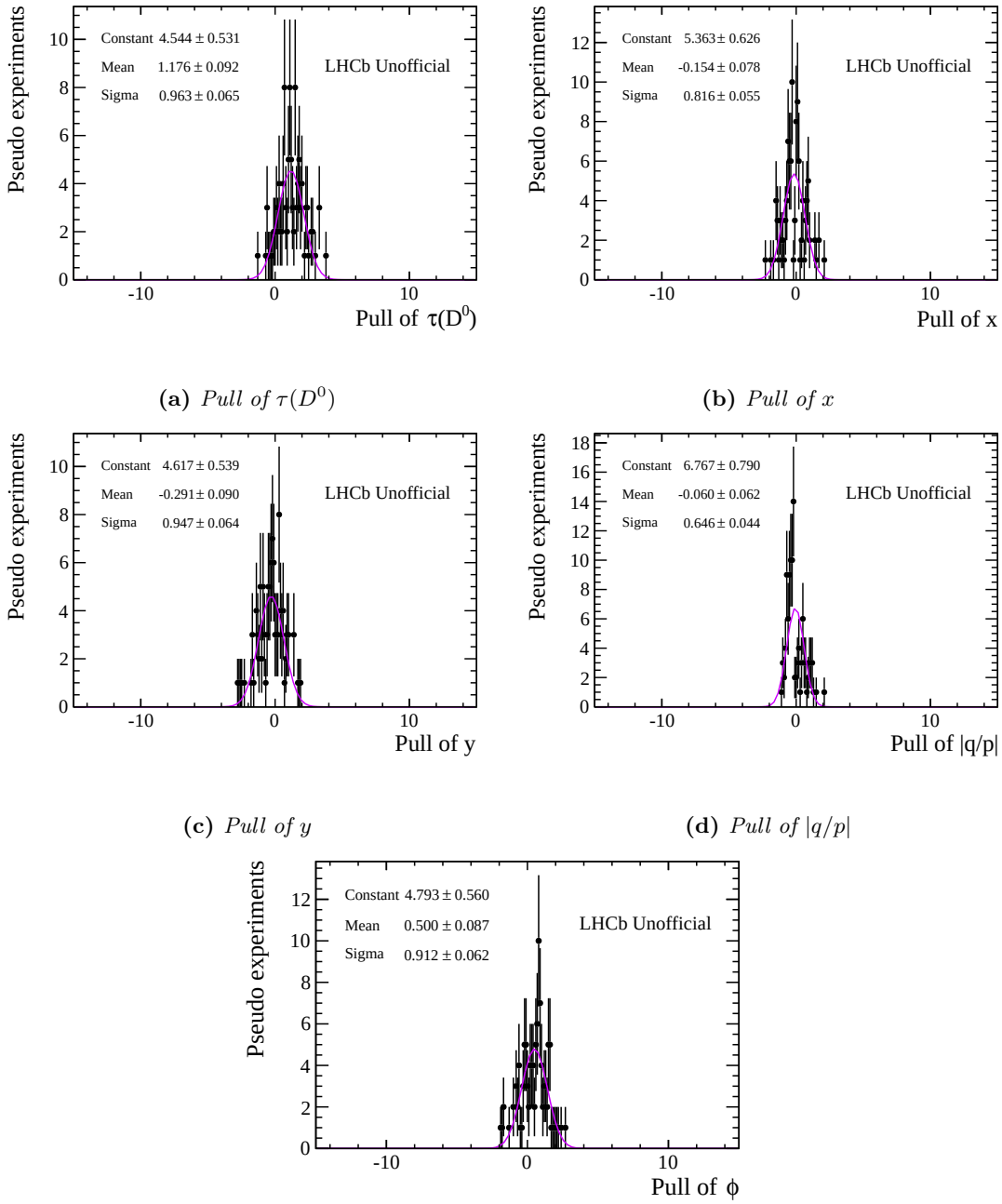

(a) *Pull of* $\tau(D^0)$ **(b)** *Pull of* x

(c) *Pull of* y **(d)** *Pull of* $|q/p|$

(e) *Pull of* ϕ

Figure 12.14.: *Pull distributions of* $\tau(D^0)$*,* x*,* y*,* $|q/p|$ *and* ϕ *in simulated pseudo-experiments fitted with a single Gaussian function, which is used to assess any biases resulting from the amplitude fit allowing for CP violation.*

13. Cross checks and systematic uncertainties

The mixing parameters are measured with a finite statistical precision and systematic uncertainties are assigned for each of these parameters. The measurement is also performed on disjoint subsets of the data to ensure stability of the results. In the following section, these stability tests are detailed and the determination of the systematic uncertainties is discussed.

13.1. Fit stability tests

The amplitude fit is performed on several disjoint subsamples of the dataset. The parameters of interest are extracted separately for data-taking period, K^0_S reconstruction as well as single- (ST) and double-tagged (DT) decays. As can be seen from Fig. 13.1, the mixing parameters are stable.

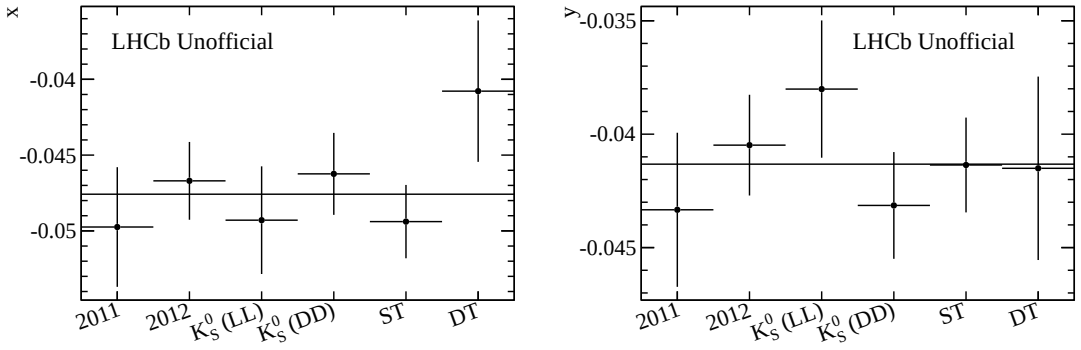

(a) *Results on x* **(b)** *Results on y*

Figure 13.1.: *Comparison of the nominal result for the mixing parameters, which is indicated by the horizontal line, with results obtained on disjoint subsets of the data. The results marked as 2011 and 2012 include data for only these data-taking periods, whereas the results labelled as K^0_S(LL) and K^0_S(DD) are extracted from datasets with K^0_S mesons reconstructed from two long and two downstream pion tracks. The results marked as ST and DT are obtained on datasets containing only single- and double-tagged decays, respectively.*

13.2. Systematic uncertainties

The systematic uncertainties on the mixing parameters are extracted from various sources. The largest uncertainties arise from the phase-space resolution and from the model used in the amplitude fit. A detailed summary of all considered systematic uncertainties is given in the following with the results presented in Table 13.5.

13.2.1. Model uncertainty

The model used in the amplitude fit is a choice and hence the amplitude fit is repeated with several modifications to evaluate the effect of these specific choices on the result. The amplitude of the $D^0 \to K^0_S\pi^+\pi^-$ decay is expressed as in Eqn. 11.8, which is repeated here for convenience

$$A_r = Z_L(\vec{h},\vec{k})B_L^{r\to ab\prime}(|\vec{k}|,|\vec{k_r}|)\mathcal{T}_r(m_{ab})B_L^{D\to rc\prime}(|\vec{h}|,|\vec{h_r}|). \tag{13.1}$$

As outlined in Chapt. 11.1, the spin factors $Z_L(\vec{h},\vec{k})$ are calculated in the Zemach formalism and the Blatt-Weisskopf radius entering the Blatt-Weisskopf factors $B_L^{r\to ab\prime}(|\vec{k}|,|\vec{k_r}|)$ and $B_L^{D\to rc\prime}(|\vec{h}|,|\vec{h_r}|)$ is chosen to be $1.5\,\mathrm{GeV}^{-1}$ for the intermediate resonances and $5.0\,\mathrm{GeV}^{-1}$ for the D^0 meson. In addition, the dynamical function $\mathcal{T}_r$ relies on different resonance lineshapes. Because alternative models can be found, which describe the data as well, the amplitude fit is repeated with a range of different models. The fit model systematic uncertainty is calculated as the sum of the single contributions in quadrature. In case several tests related to the same effect are performed, the largest shift is taken as systematic uncertainty.

13.2.1.1. Blatt-Weisskopf radius

In the nominal amplitude fit, the radius of the Blatt-Weisskopf factors given in Table 11.1 is fixed to $1.5\,\mathrm{GeV}^{-1}$ for intermediate resonances and to $5.0\,\mathrm{GeV}^{-1}$ for the D^0 meson. The radii of the intermediate resonances and the D^0 are varied separately by $\pm 0.5\,\mathrm{GeV}^{-1}$ to evaluate a corresponding systematic uncertainty. The larger shift is quoted as symmetric systematic uncertainty.

The variation of the Blatt-Weisskopf radius of the intermediate resonances leads to a shift of -4.0×10^{-4} on x, which corresponds to 19% of the statistical uncertainty and of 9.0×10^{-5} or 5% of the statistical uncertainty on y.

The shifts caused by the variation of the D^0 Blatt-Weisskopf radius are lower and lie at -3.2×10^{-4} on x and at 6.9×10^{-5} on y.

13.2.1.2. Adding and removing resonances from the nominal model

The nominal model is modified by adding and removing resonances to obtain alternative models, which are used in the amplitude fit. The χ^2 value of the nominal fit is $\chi^2/ndf = 16290/8093 \approx 2.0$. The systematic uncertainty is evaluated in two parts: first, the $K^*(1680)^-$ resonance is added to the nominal model given in Table 11.4, which is expected to have a low fit fraction. Second, the $\rho(1450)$ is removed from the nominal model, as it has a relatively low fit fraction of 2.6%.

The systematic uncertainties arising from the addition of the $K^*(1680)^-$ are 1.4×10^{-5} on x and -4.3×10^{-5} on y, which are small changes. The χ^2 value is reduced to $\chi^2/ndf = 16121/8093 \approx 1.99$, but the fit fractions add up to 1.40 instead of 1.36 for the nominal fit.

When removing the $\rho(1450)$ from the nominal model, the mixing parameters shift by 8.4×10^{-5} for x and by 4.2×10^{-4} for y, which corresponds to 4% and 23% of the corresponding statistical

uncertainty. Hence, the shift on y is significant, but the χ^2 value of the fit is significantly worse as it lies at $\chi^2/ndf = 19023/8093 \approx 2.4$.

These two shifts are added in quadrature and yield a systematic uncertainty of 8.5×10^{-5} on x and of 4.2×10^{-4} on y.

13.2.1.3. Lineshapes

The choice of lineshapes of the resonances entering through the dynamical function $\mathcal{T}_r$ is accounted for by repeating the amplitude fit with different lineshapes. The $\rho(770)$ is modelled with a relativistic Breit-Wigner instead of a Gounaris-Sakurai distribution and the $K_0^*(1430)^\pm$ is described by a LASS parameterisation instead of a relativistic Breit-Wigner function (see Chapt. 11.1.2 and 11.1.3). The shift caused by these changes to the model are 3.0×10^{-5} on x and -1.1×10^{-4} on y, which corresponds to 1.4% and 6.1% of the statistical uncertainties. The χ^2 value changes to $\chi^2/ndf = 16327/8093$; for the nominal model the χ^2 is found to be $\chi^2/ndf = 16290/8093$.

13.2.1.4. Alternative model

The nominal amplitude fit is performed with the isobar model given in Chapt. 11.1.6, where the total $D^0 \to K^0_S\pi^+\pi^-$ decay amplitude is modelled as a linear superposition of Breit-Wigner and Gounaris-Sakurai amplitudes (see Chapt. 11.1.1 and 11.1.2). The alternative model, which is used to extract the mixing and *CP* violation parameters, is summarised in Chapt. 11.1.7. In this alternative model, the $\pi\pi$ S-wave is described by the K-matrix formalism in the P-vector approach given in Chapt. 11.1.4 and the $K^0_S\pi^\pm$ S-wave is modelled by the LASS amplitude detailed in Chapt. 11.1.3.

The shifts on the mixing parameters are 5.3×10^{-4} and 1.6×10^{-4}, which corresponds to 27% and 9% of the statistical uncertainty. As expected, this systematic uncertainty has the largest contribution to the total systematic uncertainty. The χ^2 value improves significantly from $\chi^2/ndf = 16290/8093 \approx 2.0$ for the nominal model to $\chi^2/ndf = 15125/8093 \approx 1.9$ for the alternative model.

Future studies will consider the approach discussed in Ref. [106]. In this approach only fits of comparable quality contribute to the uncertainty, thus preventing this source of systematic to be overestimated through the consideration of poor quality models.

13.2.1.5. Total fit model uncertainty

The contributions to the fit model uncertainty are listed in Table 13.1. As the variation of the lineshapes described in Chapt. 13.2.1.3 and the change to the alternative model discussed in Chapt. 13.2.1.4 are evaluating the same effect, the larger of the two systematic uncertainties, which arises from the use of the alternative model, is quoted as systematic uncertainty. The contributions are added in quadrature to obtain the total fit model uncertainty.

Table 13.1.: *Contributions to the total fit model systematic uncertainty.*

Source	Systematic uncertainty	
	x $[10^{-5}]$	y $[10^{-5}]$
Blatt-Weißkopf radius of r	40	9
Blatt-Weißkopf radius of D^0	32	7
Modified model	9	42
Alternative model	53	16
Fit model	77	47

13.2.2. Fit biases

As outlined in Chapt. 12, the fitter does exhibit a bias in $\tau(D^0)$ of half a statistical uncertainty. The measured D^0 lifetime from the nominal fit is $\tau(D^0) = (410.4 \pm 0.5)\,\text{ps}$, which agrees within uncertainties with the world average of $(410.1 \pm 1.5)\,\text{ps}$ [11]. The bias in D^0 lifetime is accounted for by fixing the D^0 lifetime at 410.2 ps, which corresponds to the nominal result lowered by half a statistical uncertainty. The resulting shifts on the mixing parameters are 1.4×10^{-5} and -3.6×10^{-5}, which corresponds to 0.7% and 2.0% of the statistical uncertainty.

In addition, biases on the parameters of interest occur. The size of these biases is estimated from simulation studies of pseudo-experiments as outlined in Chapt. 12.1.1. The mean of the corresponding pull distribution (or its uncertainty depending on which effect is larger) is added as a systematic uncertainty. Here, the mean of the pull distributions on the mixing parameters show the larger bias.

The bias on x is determined to be -9.1% and on y the bias is -10.1% of the statistical uncertainty. This results in systematic uncertainties of 2.0×10^{-4} on x and of -1.9×10^{-4} on y. Hence, the fit bias is a significant but far from dominant source of systematic uncertainty.

The systematic uncertainty arising from fit biases is computed by adding the two sources in quadrature, which yields 2.0×10^{-4} on x and 1.9×10^{-4} on y.

13.2.3. Signal and background mass model

In the amplitude fit, each candidate is given a signal probability, which is extracted from an extended maximum-likelihood fit to $m(D^0)$ for single-tagged candidates and to δm for double-tagged candidates. The extraction of signal probabilities is discussed in Chapt. 8.3. The background distributions used in the amplitude fit are also extracted from fits to $m(D^0)$ for single-tagged candidates and to δm for double-tagged candidates as is explained in Chapt. 9.5. The mass model, on which the signal probabilities and the background distributions rely, is changed for signal and background models separately. Inaccuracies in the description of the signal shape are accounted for by replacing the Crystal-Ball function in Eqns. 8.3 and 8.7 with a Gaussian function for the $m(D^0)$ fit model

$$
\begin{aligned}
F_{\mathrm{LL}}(m_{D^0};\mu,\sigma,c,f,a) =& N \times \left\{ n_{sig} \left[cG(m(D^0);\mu,\sigma) \right.\right. \\
&+(1-c)G(m(D^0);\mu,\sigma)\left.\right] \\
&\left.+n_{bkg}P_1(m(D^0);a)\right\}, \qquad (13.2)\\
F_{\mathrm{DD}}(m_{D^0};\mu,\sigma,c,f,a) =& N \times \left\{ n_{sig} \left[cG(m(D^0);\mu,\sigma) \right.\right. \\
&+(1-c)G(m(D^0);\mu,\sigma)\left.\right] \\
&\left.+n_{bkg}P_2(m(D^0);a_1,a_2)\right\}, \qquad (13.3)
\end{aligned}
$$

where $P_1(m(D^0);a)1$ and $P_2(m(D^0);a_1,a_2)$ refer to Chebychev polynomials describing the background as introduced in Chapt. 8.1.
A Gaussian function is added to the background model in $m(D^0)$ to account for possible peaking structures seen in Fig. 8.10 in the low D^0 mass sideband, which then is given by

$$
\begin{aligned}
P_1(m(D^0);a_1,a_2,\mu_b,\sigma_b) &= am(D^0)/[\,\mathrm{MeV}] + 1 + G(m(D^0);\mu_b,\sigma_b), \qquad (13.4)\\
P_2(m(D^0);a_1,a_2,\mu_b,\sigma_b) &= a_2\left(2m(D^0)^2/[\,\mathrm{MeV}^2] - 1\right) a_1 m(D^0)/[\,\mathrm{MeV}] + 1 \\
&\quad + G(m(D^0);\mu_b,\sigma_b). \qquad (13.5)
\end{aligned}
$$

The signal part of the fit model in δm given in Eqn. 8.10 is modified to a sum of two Gaussian functions

$$
\begin{aligned}
F(\delta m;\mu,\sigma,f_1,c_1,a_1,g) = n_{sig} &\times [c_1 G(\delta m;\mu,\sigma) + (1-c_1)G(\delta m;\mu,f_1\sigma) \\
&+ n_{bkg} \times \left[g|\delta m - a_1|^{3/2} \right. \\
&\left. +(1-g)\sqrt{|\delta m - a_1|}\right], \qquad (13.6)
\end{aligned}
$$

and a higher order term is included in the background model

$$
\begin{aligned}
F(\delta m;\mu,\sigma,f_1,f_2,c_1,c_2,a_1,g,h) = n_{sig} &\times [c_1 G(\delta m;\mu,\sigma) + c_2 G(\delta m;\mu,f_1\sigma) \\
&+(1-c_1-c_2)G(\delta m;\mu,f_2\sigma)] \\
&+ n_{bkg} \times \left[h|\delta m - a_1|^{5/2} + g|\delta m - a_1|^{3/2} \right. \\
&\left. +(1-g-h)\sqrt{|\delta m - a_1|}\right]. \qquad (13.7)
\end{aligned}
$$

New sets of signal probabilities and background distributions are produced by varying first the signal component and then the background component. The amplitude fit is then repeated with new sets of signal probabilities and background distributions. For the varied signal model, the mixing parameters are shifted by -8.8×10^{-5} and -2.7×10^{-5}, which is about 4% and 1% of the corresponding statistical uncertainty. The effect of the background model is larger and the shifts are 1.4×10^{-4} and 3.1×10^{-4}. These shifts correspond to 6.4% and 16.5% of the statistical uncertainties on x and y, respectively.

13.2.4. Background smearing

In the nominal amplitude fit, a smoothing is applied to the sWeighted background distributions in D^0 decay time and phase-space (see Chapt. 9.5). The effect of this smoothing is evaluated by repeating the amplitude fit with the unsmoothed background distributions. The shifts are 1.0×10^{-5} and 1.1×10^{-4}, which corresponds to 0.5% and to 6% of a statistical uncertainty on x and y, respectively.

13.2.5. Background from wrongly tagged muons

As the implementation of the muon mistag probability in the fit is not yet validated, a muon mistag probability of zero is assumed in the fit. This approach is valid since the measured muon mistag probabilities given in Table 9.4 are small. The effect of neglecting the mistag probability is estimated by studies of simulated pseudo-experiments. Simulated data reflecting the measured levels of the mistag probability are generated and then fitted with the assumption of having a mistag probability of zero.

The shifts in the mean value of the distributions of the mixing parameters are larger than the shifts in the widths and hence, the shifts in the mean are quoted as systematic uncertainty. These shifts are -5×10^{-5} on x, which corresponds to 2.3% of the statistical uncertainty, and -3.6×10^{-4} on y. The uncertainty on y is 19% of the statistical uncertainty and thus contributes significantly to the total systematic uncertainty.

13.2.6. Acceptance and resolution

Systematic uncertainties are evaluated to account for the phase-space acceptance parameterisation, the decay time and the phase-space resolutions.

13.2.6.1. Phase-space acceptance

The systematic uncertainty arising from the acceptance parameterisation (see Chapt. 10.1) is split into two parts: first, an alternative model is used to fit the acceptance variation as a function of phase-space and second, the parameters of the nominal model are varied.

The alternative phase-space acceptance model includes an additional term $q_6 \times m^2(\pi^+\pi^-)\cos(\theta)$, to describe correlations between $m^2(\pi^+\pi^-)$ and $\cos(\theta)$

$$\begin{aligned}\varepsilon(m^2(\pi^+\pi^-), \cos(\theta)) = {} & q_0 \times m^4(\pi^+\pi^-) + q_1 \times m^2(\pi^+\pi^-) \\ & + q_2 \times m^2(\pi^+\pi^-)\cos^2(\theta) + q_3 \times \cos^2(\theta) + q_4 \times \cos(\theta) \\ & + q_5 + q_6 \times m^2(\pi^+\pi^-)\cos(\theta). \end{aligned} \tag{13.8}$$

The quality of this model is slightly worse than of the nominal model. The parameters of the alternative phase-space acceptance parameterisation are summarised in Tables 13.2 and 13.3. The resulting shifts on x and y are -2.3×10^{-5} and -1.0×10^{-5}, which corresponds to 1% and 0.5% of the statistical uncertainties.

Table 13.2.: *Parameters of the alternative single-tagged phase-space acceptance $\varepsilon(m^2(\pi^+\pi^-), \cos(\theta))$ split by year and K^0_S type for a MC sample with tight generator-level cuts after the complete selection chain.*

	2011		2012	
	K^0_S(LL)	K^0_S(DD)	K^0_S(LL)	K^0_S(DD)
$q_0\,[10^{-3}\,\text{GeV}^4]$	3.14 ± 0.21	4.70 ± 0.34	2.70 ± 0.15	3.28 ± 0.25
$q_1\,[10^{-3}\,\text{GeV}^2]$	-2.16 ± 0.40	1.31 ± 0.62	-1.59 ± 0.27	1.99 ± 0.47
$q_2\,[10^{-3}\,\text{GeV}^2]$	2.98 ± 0.32	7.51 ± 0.50	3.18 ± 0.22	8.98 ± 0.37
$q_3\,[10^{-3}]$	-4.11 ± 0.28	-8.98 ± 0.43	-4.20 ± 0.19	-9.58 ± 0.33
$q_4\,[10^{-5}]$	-1.35 ± 34.24	-7.15 ± 11.11	-3.23 ± 9.81	-9.45 ± 8.46
$q_5\,[10^{-2}]$	1.56 ± 0.02	3.59 ± 0.01	1.38 ± 0.01	3.99 ± 0.01
$q_6\,[10^{-4}\,\text{GeV}]$	-1.32 ± 1.57	-1.20 ± 0.19	-0.72 ± 1.14	-2.27 ± 0.14

Table 13.3.: *Parameters of the alternative double-tagged phase-space acceptance $\varepsilon(m^2(\pi^+\pi^-), \cos(\theta))$ split by year and K^0_S type for MC sample with tight generator-level cuts after the complete selection chain.*

	2011		2012	
	K^0_S(LL)	K^0_S(DD)	K^0_S(LL)	K^0_S(DD)
$q_0\,[10^{-3}\,\text{GeV}^4]$	3.11 ± 0.21	5.13 ± 0.35	2.74 ± 0.15	4.02 ± 0.26
$q_1\,[10^{-3}\,\text{GeV}^2]$	-2.16 ± 0.40	0.88 ± 0.64	-1.58 ± 0.27	1.07 ± 0.49
$q_2\,[10^{-3}\,\text{GeV}^2]$	2.97 ± 0.32	8.23 ± 0.51	3.13 ± 0.19	9.80 ± 0.39
$q_3\,[10^{-3}]$	-4.11 ± 0.28	-9.57 ± 0.44	-4.16 ± 0.19	-10.40 ± 0.34
$q_4\,[10^{-5}]$	2.87 ± 14.01	-3.54 ± 11.36	-4.74 ± 9.58	-4.93 ± 8.71
$q_5\,[10^{-2}]$	1.54 ± 0.02	3.77 ± 0.05	1.39 ± 0.02	4.26 ± 0.05
$q_6\,[10^{-4}\,\text{GeV}]$	-1.58 ± 1.62	-0.25 ± 19.03	-0.49 ± 1.12	-0.42 ± 1.42

In addition, a systematic uncertainty arising from the uncertainties of the phase-space acceptance parameterisation is estimated. The parameters of the phase-space acceptance are randomly drawn from the set of parameters, which is varied within the corresponding correlated uncertainties. This procedure is the so-called resampling technique. Here, the uncertainties are inflated to account for data fluctuations observed *e.g.* in Figs. 10.6 and 10.7. The uncertainties are inflated such that the reduced χ^2 of the relative difference between measured and parameterised acceptance is equal to one. This test leads to a systematic uncertainty on x of 2.2×10^{-5} and on y of -3.7×10^{-5} corresponding to 1% and 2% of a statistical uncertainty.

The systematic shifts arising from the alternative model and the resampling technique are added in quadrature.

13.2.6.2. Decay-time acceptance

A systematic uncertainty caused by the decay-time acceptance is evaluated by varying the correction given in Tables 10.3 and 10.4 within its uncertainties and determining the shift in

the parameters of interest. The upper variation of the correction yields larger uncertainties, which are quoted as symmetric errors to give a conservative estimate. The shifts introduced on the mixing parameters are 3.7×10^{-5} and -1.8×10^{-5} on x and y, respectively. These shifts correspond to 2% and 1% of the corresponding statistical uncertainty.

13.2.6.3. Decay-time resolution

The systematic uncertainty arising from the decay-time resolution, which is measured in Chapt. 10.4, is determined by randomly drawing the decay-time resolution parameters from the set of parameters varied within the corresponding correlated uncertainties. The systematic uncertainty of the mixing parameters are of the size of 0.5% of the statistical uncertainty on the mixing parameters. The absolute shifts are -1.2×10^{-5} and 7.7×10^{-6} on x and y, respectively.

13.2.6.4. Phase-space resolution

The nominal amplitude fit to data does not include effects from the phase-space resolution. The effect of this procedure on the mixing parameters is estimated by smearing a single simulated pseudo-experiment randomly a hundred times and then comparing the distribution of the mixing and *CP* violation parameters to the results obtained from the fit to the nominal pseudo-experiment.

For a simulated pseudo-experiment generated with $x = y = 0.5\%$ and no *CP* violation, the nominal values are $x = (0.426 \pm 0.199)\%$ and $y = (0.323 \pm 0.183)\%$. The means of the distribution of the smeared ensemble are $x^{\text{mean}} = (0.396 \pm 0.003)\%$ and $y^{\text{mean}} = (0.279 \pm 0.002)\%$. Hence, the phase-space smearing introduces an absolute shift of 3.0×10^{-4} on x and of 4.4×10^{-4} on y. As the widths of the distributions are smaller than the shifts, the shifts are quoted as systematic uncertainties. This uncertainties are significant as they correspond to 14% and 24% of the statistical uncertainty on x and y, respectively.

13.2.7. K^0 interaction asymmetry

The signal channel $D^0 \to K^0_S \pi^+ \pi^-$ can be affected by the detection asymmetry of the K^0_S meson as found in Ref. [107].
The initial flavour of the K^0 meson is defined at the time of the D^0 decay from the weak decay of the charm quark to a strange quark, so that the D^0 meson produces a $\overline{K}^0$ meson and the $\overline{D}^0$ meson a K^0 meson. The K^0 and $\overline{K}^0$ mesons have different interaction rates with matter, leading to a detection asymmetry. These interaction rates depend on the momentum of the K^0_S meson. The cross-section for interactions between a K^0_S and a nucleon (N) follows

$$\sigma(\overline{K}^0 N) - \sigma(K^0 N) \propto p^{-0.6}. \tag{13.9}$$

Since the K^0_S momentum varies across phase-space, a local asymmetry can be introduced between the phase-space distributions of D^0 and $\overline{D}^0$ mesons, in addition to a global asymmetry.

The Dalitz plane is divided into nine equally-populated bins, whose lower boundaries are listed in Table 13.4. The distribution of the K^0_S lab momentum in these bins varies. The mean

of the K^0_S lab momentum shows a variation of $20 - 28\,\text{GeV}$ for the $K^0_S(\text{LL})$ sample and of $20 - 27\,\text{GeV}$ for the $K^0_S(\text{DD})$ sample. Hence this variation across the Dalitz plane corresponds to $(28/20)^{0.6} - 1 \approx 22\%$. The magnitude of the detection asymmetry depends on the detector material and on the K^0_S decay time. The K^0_S decay time dependence arises from two effects. Firstly, the K^0–$\overline{K}^0$ system undergoes oscillations. In addition, the matter interaction has two effects on the mixing formula: the frequency of the oscillations are affected; the mass eigenstates K^0_S and K^0_L are coupled leading to transitions from one state to the other. The second effect arises from the *CP* violation in the kaon system. The decay of the neutral kaon into $\pi^+\pi^-$ is analysed, thus selecting primarily the K^0_S state. Though, as the *CP* eigenstates of the neutral kaon system are a mixture of K^0_S and K^0_L, *CP* violation in the neutral kaon decay has to be taken into account for a full treatment. Because of the K^0_S decay time dependence, the magnitude of the effect for the $K^0_S(\text{DD})$ sample, where the K^0_S decays outside the VELO, will be significantly larger than in the $K^0_S(\text{LL})$ sample.

The effect was calculated and compared with data in Ref. [107] for $D^+ \to \overline{K}^0\pi^+$, a K^0_S detection asymmetry of 0.6% was observed for $K^0_S(\text{DD})$ decays and 0.08% for $K^0_S(\text{LL})$ decays. The mean K^0_S momenta in the semileptonic $D^0 \to K^0_S\pi^+\pi^-$ sample analysed in this thesis is similar to that of the K^0_S in Ref. [107]. Assuming the K^0_S lifetime acceptance is similar in the analyses, the magnitude of the effect will thus be comparable.

The asymmetry variation across the Dalitz plane will be roughly $0.22 \times 0.6\% = 0.1\%$ for the $K^0_S(\text{DD})$ and $0.22 \times 0.08\% = 0.02\%$ for the $K^0_S(\text{LL})$ sample. Hence, taking into account the total signal sample size of around $750,000$ candidates, an effect of this size is expected to be negligible.

13.2.8. Masses and widths

In the time-dependent amplitude fit, the masses and widths of most resonances are floated with exception of the mass of the $\rho(770)$, $\omega(782)$, $f_0(980)$ and $f_2(1270)$. In addition, the width of the $f_2(1270)$ is fixed. These parameters are well measured and the corresponding systematic uncertainties are estimated by fixing these values at $\pm 1\sigma$ of the reference value reported in Ref. [11]. The larger shift is quoted as a symmetric systematic uncertainty.

The variation of the $f_2(1270)$ width leads to a shift on x of 1.8×10^{-4} and on y of 1.8×10^{-5}, which correspond to 8% and 1% of the statistical uncertainties. The masses lead to systematic uncertainties of -1.6×10^{-4} on x and of 9.2×10^{-5} on y, which are both around 7% of the corresponding statistical uncertainties.

The uncertainties arising from the variation of the masses and the widths are added in quadrature and yield a systematic uncertainty of 2.4×10^{-4} on x and of 9.4×10^{-5} on y.

13.2.9. Summary of systematic uncertainties

A summary of all systematic uncertainties is given in Table 13.5. The largest contributions arise from the fit model and the phase-space resolution. The total systematic uncertainties are

9.0×10^{-4} on x and 8.4×10^{-4} on y, which corresponds to 42% and 45% of the corresponding statistical uncertainties.

Table 13.5.: *Contributions to the total systematic uncertainty*

Source	Systematic uncertainty	
	x $[10^{-5}]$	y $[10^{-5}]$
Fit biases	20	19
Signal mass model	9	3
Background mass model	14	31
Background smearing	1	11
Muon mistag probability	5	36
Acceptance modelling	2	1
Acceptance resampling	2	4
Decay-time acceptance	4	18
Decay time resolution	1	1
Phase-space resolution	30	44
Masses and widths	24	9
Systematic	47	70
Fit model	77	47
Total	90	84

Table 13.4.: *Binning in phase-space split by year and K^0_S type for single-tagged candidates.*

	2011		2012	
	K^0_S(LL)	K^0_S(DD)	K^0_S(LL)	K^0_S(DD)
Bin 0, $m^2(K^0_S\pi^+)$ $[\mathrm{GeV}^2]$	0.41	0.41	0.41	0.41
Bin 1, $m^2(K^0_S\pi^+)$ $[\mathrm{GeV}^2]$	0.41	0.41	0.41	0.41
Bin 2, $m^2(K^0_S\pi^+)$ $[\mathrm{GeV}^2]$	0.41	0.41	0.41	0.41
Bin 3, $m^2(K^0_S\pi^+)$ $[\mathrm{GeV}^2]$	1.20	1.19	1.20	1.19
Bin 4, $m^2(K^0_S\pi^+)$ $[\mathrm{GeV}^2]$	1.20	1.19	1.20	1.19
Bin 5, $m^2(K^0_S\pi^+)$ $[\mathrm{GeV}^2]$	1.20	1.19	1.20	1.19
Bin 6, $m^2(K^0_S\pi^+)$ $[\mathrm{GeV}^2]$	1.82	1.79	1.81	1.82
Bin 7, $m^2(K^0_S\pi^+)$ $[\mathrm{GeV}^2]$	1.82	1.79	1.81	1.82
Bin 8, $m^2(K^0_S\pi^+)$ $[\mathrm{GeV}^2]$	1.82	1.79	1.81	1.82
Bin 0, $m^2(K^0_S\pi^-)$ $[\mathrm{GeV}^2]$	0.41	0.41	0.41	0.41
Bin 1, $m^2(K^0_S\pi^-)$ $[\mathrm{GeV}^2]$	1.26	1.48	1.27	1.53
Bin 2, $m^2(K^0_S\pi^-)$ $[\mathrm{GeV}^2]$	2.09	2.27	2.10	2.30
Bin 3, $m^2(K^0_S\pi^-)$ $[\mathrm{GeV}^2]$	0.41	0.41	0.41	0.41
Bin 4, $m^2(K^0_S\pi^-)$ $[\mathrm{GeV}^2]$	0.80	0.81	0.80	0.81
Bin 5, $m^2(K^0_S\pi^-)$ $[\mathrm{GeV}^2]$	0.92	1.11	0.92	1.16
Bin 6, $m^2(K^0_S\pi^-)$ $[\mathrm{GeV}^2]$	0.41	0.41	0.41	0.41
Bin 7, $m^2(K^0_S\pi^-)$ $[\mathrm{GeV}^2]$	0.74	0.76	0.74	0.76
Bin 8, $m^2(K^0_S\pi^-)$ $[\mathrm{GeV}^2]$	0.85	0.92	0.86	0.92

14. Results

The nominal model for the amplitude fit is the isobar model discussed in Chapt. 11.1.6, where the total $D^0 \to K^0_S\pi^+\pi^-$ decay amplitude is modelled as a linear superposition of Breit-Wigner and Gounaris-Sakurai amplitudes introduced in Chapt. 11.1.1 and 11.1.2. The composition of the amplitude model was determined from a time-integrated fit to a dataset with D^0 decay times below one D^0 lifetime, as the amplitude fit at low lifetimes is only sensitive to the amplitude model and not to mixing effects. The isobar model reported by the Belle Collaboration in Ref. [40] was varied by adding and removing several resonances such as the $f_0(1500)$ [11]. The nominal model was then chosen as the one giving the best χ^2 value leading to the model given in Table 11.4. The results on the amplitude parameters are then used as starting values for the time-dependent fit reported in Chapt. 14.2.

In this analysis, it is assumed that direct *CP* violation is negligible. This assumption is verified in Chapt. 14.1 and hence, the parameters $|q/p|$ and ϕ describing indirect *CP* violation could in principle be extracted from the amplitude fit together with the mixing parameters x and y. The results on the mixing parameters are given in Chapt. 14.2.

14.1. Search for direct *CP* violation

The contribution of direct *CP* violation is expected to be negligible in charm decays and no evidence for direct *CP* violation has been observed [9]. This assumption is verified by performing a time-integrated amplitude fit separately on datasets where the flavour of the D meson at production was either a D^0 or a $\overline{D}^0$. The amplitude fit is performed with the nominal model given in Table 11.4 and the fit results of the real and imaginary parts of the amplitudes are compared for D^0 and $\overline{D}^0$ fits. In the case of no direct *CP* violation, the amplitudes of the decay $D^0 \to K^0_S\pi^+\pi^-$ and the charge-conjugate decay $\overline{D}^0 \to K^0_S\pi^-\pi^+$ agree. In consequence, comparing the results of the real and imaginary parts of the amplitudes contributing to the D^0 and $\overline{D}^0$ model allows to test for direct *CP* violation. Here, the masses and widths of the intermediate resonances are fixed since the amplitudes depend on these values and if the D^0 and $\overline{D}^0$ fits return different masses and widths, then consequently the amplitudes differ.

The *CP* asymmetry of the amplitude model is computed as

$$\mathcal{A}_{CP} \equiv \frac{PDF_{D^0} - PDF_{\overline{D}^0}}{PDF_{D^0} + PDF_{\overline{D}^0}}, \tag{14.1}$$

where PDF_{D^0} ($PDF_{\overline{D}^0}$) refers to the amplitude model obtained from a time-integrated fit to the D^0 ($\overline{D}^0$) dataset. As can be seen from Fig. 14.1a, a significant *CP* asymmetry is present

in the σ_2 region. However, when fixing the real and imaginary parts of the amplitude of the σ_2 resonance to the values obtained from the nominal amplitude fit, no *CP* asymmetry is observed as illustrated in Fig. 14.1b. The remaining structures seen in Fig. 14.1b are caused by statistical fluctuations and hence, the assumption of no direct *CP* violation is justified at the level of precision of this analysis.

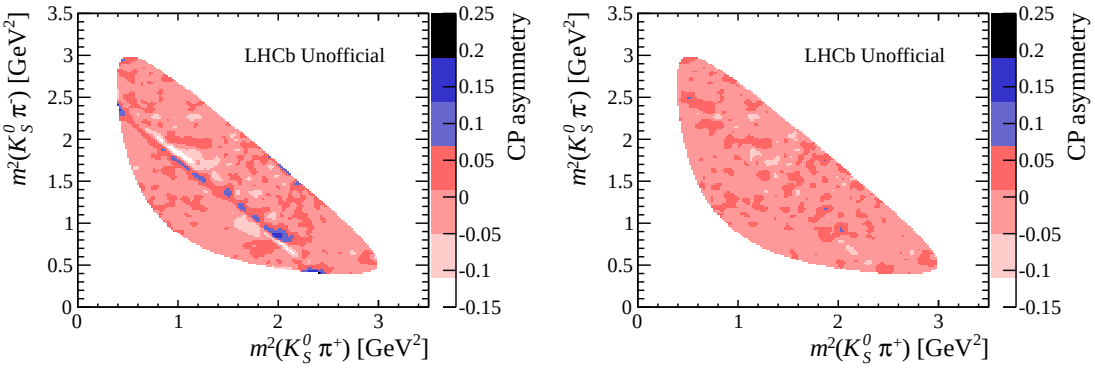

(a) *Amplitude of σ_2 floated* **(b)** *Amplitude of σ_2 fixed*

Figure 14.1.: *Time-integrated CP asymmetry of the amplitude model with the amplitude of the σ_2 resonance being floated (left) and fixed (right). The CP asymmetry observed in the left plot is caused by the mismodelling of the σ_2 resonance and vanishes when the σ_2 amplitude is being fixed.*

14.2. Measurement of the mixing parameters

In the time-dependent amplitude fit, the masses and widths of most resonances are floated with exception of the mass of the $\rho(770)$, $\omega(782)$, $f_0(980)$ and $f_2(1270)$. In addition, the width of the $f_2(1270)$ is fixed. This approach is valid as these masses and widths are well measured and fixing these parameters ensures a better stability of the fit. The results on the mixing parameters are currently blind as is outlined in Chapt. 11.4 due to the pending review of the analysis by the LHCb Collaboration.

The results of the nominal amplitude fit are shown in the Dalitz plane in Fig. 14.2 and the corresponding projections on D^0 decay time and the Dalitz variables are illustrated in Fig. 14.3. Figure 14.2a shows the data, the fitted PDF including signal and background components is illustrated in Fig. 14.2b and the background only distribution is given in Fig. 14.2c. The quality of the fit is assessed in the pull, which is the difference between data and value of the PDF in each bin divided by the uncertainty on the data shown in Fig. 14.2d. As can be seen from Figs. 14.2d and 14.3, the model has some flaws and especially does not describe the interference between the $K^*(892)^\pm$ and the $\rho(770)$ correctly. In addition, the σ_2 resonance description differs between data and the model, which indicates that the σ_2 cannot be modelled with a relativistic Breit-Wigner distribution. In future studies, the $\pi\pi$ S-wave will be described by the K-matrix formalism in the production vector approach as discussed in Chapt. 11.1.4 instead of a superposition of relativistic Breit-Wigner amplitudes.

The isobar model is known not to model the high $m^2(K^0_S\pi^-)$ region well, as has been reported in Ref. [40]. The observed inaccuracies in the model are taken into account in the systematic uncertainties through alternative models considered, which contribute the largest component of the systematic uncertainty (see Chapt. 13.2.1).

The χ^2 value of the fit is $\chi^2/ndf = 16290/8093 \approx 2.0$ and the fit fractions add up to 1.36. This is in good agreement with the quality of the isobar model reported by the Belle Collaboration [40], which had a reduced χ^2 value of 2.1 for 3613 degrees of freedom. The Belle analysis was performed on a dataset containing $534,410 \pm 830$ signal events with a background fraction of $\sim 4\%$ in a $\pm 3\sigma$ window in D^0 mass and δm, whereas the dataset used in this analysis contains $750,270$ signal candidates and $246,777$ background candidates in a $\pm 3\sigma$ window around the $m(D^0)$ and δm peaks for the single- and double-tagged samples, respectively.
The blinded mixing parameters are measured to be

$$x = (-4.76 \pm 0.22_{\,\text{stat.}} \pm 0.05_{\,\text{syst.}} + 0.08_{\,\text{model}})\%, \tag{14.2}$$

$$y = (-4.13 \pm 0.19_{\,\text{stat.}} \pm 0.07_{\,\text{syst.}} + 0.05_{\,\text{model}})\%. \tag{14.3}$$

A complete list of the fit parameters is given in Appendix I.

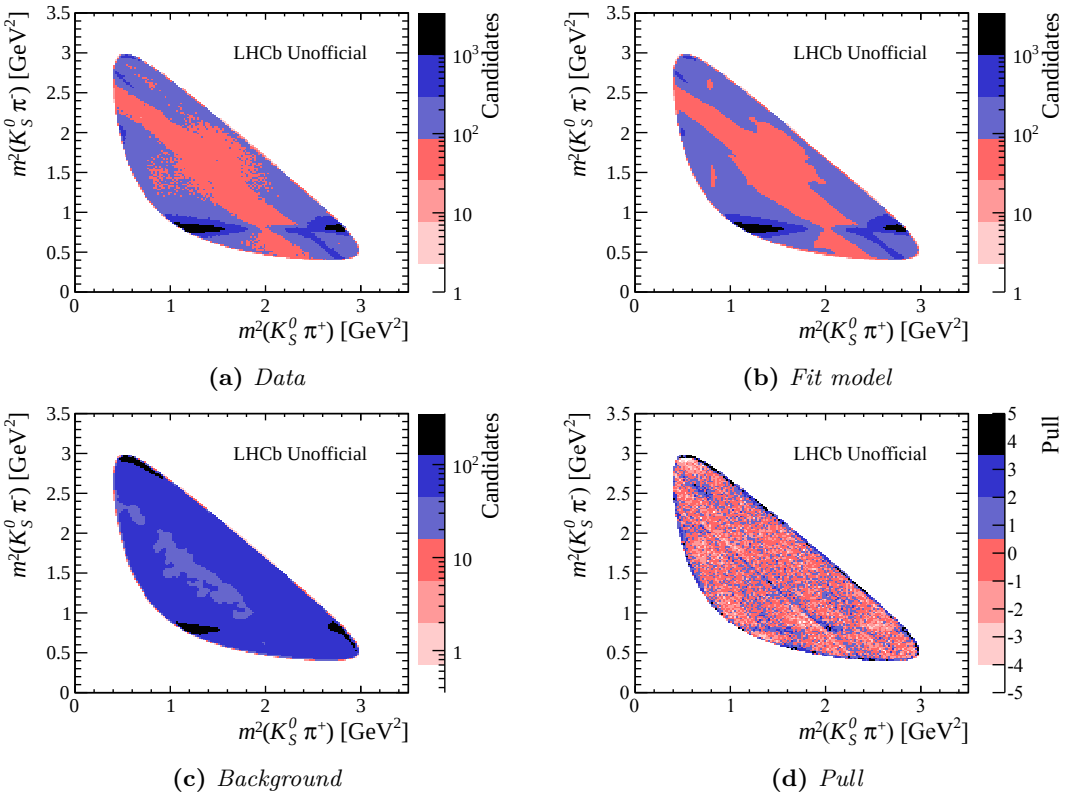

(a) *Data* **(b)** *Fit model* **(c)** *Background* **(d)** *Pull*

Figure 14.2.: *Results of the nominal amplitude fit to data with the isobar model: The data are shown in (a), the fitted model in (b) and the distribution of backgrounds is illustrated in (c). The pull distribution in (d) allows to assess the quality of the fit.*

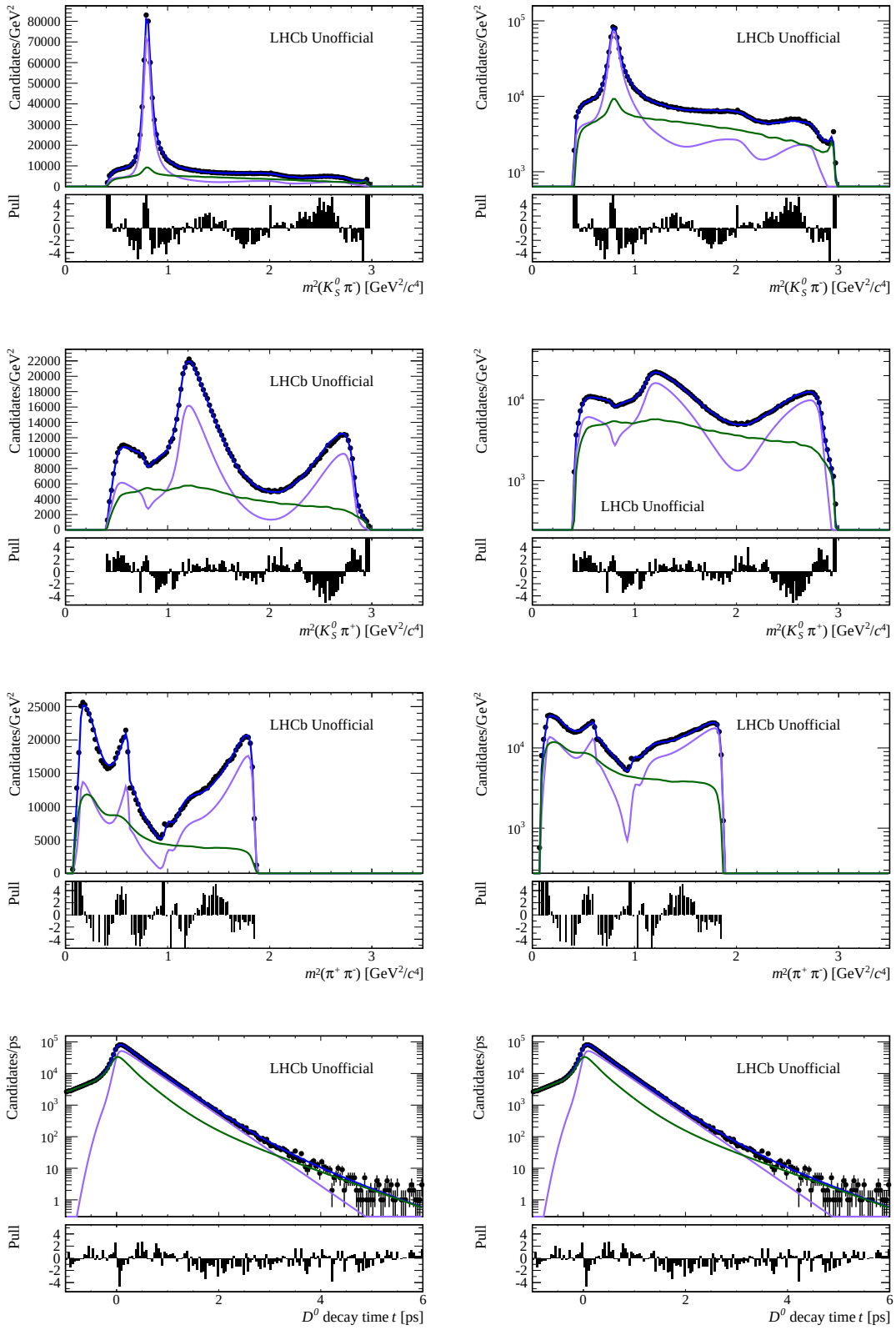

Figure 14.3.: *Projections of the nominal amplitude fit to data with the isobar model. The data points are shown in black, the total PDF in blue, the signal PDF in violet and the background PDF in green. The distributions are shown on a linear (left) and on a log scale (right).*

15. Conclusion and outlook

This thesis reports the measurement of the mixing parameters in the D^0-$\overline{D}^0$ system by analysing semileptonically-tagged $D^0 \to K^0_S\pi^+\pi^-$ decays from LHCb's Run 1 dataset corresponding to an integrated luminosity of $3\,\text{fb}^{-1}$. The work undertaken in this thesis includes the preparation of a search for indirect *CP* violation. The mixing and *CP* violation parameters can be extracted from a time- and model-dependent amplitude fit to D^0 decay time and the Dalitz variables, $m^2(K^0_S\pi^+)$ and $m^2(K^0_S\pi^-)$.

15.1. Conclusion

The blinded D^0-$\overline{D}^0$ mixing parameters are measured to be

$$x = (-4.76 \pm 0.22_{\,\text{stat.}} \pm 0.05_{\,\text{syst.}} + 0.08_{\,\text{model}})\%, \tag{15.1}$$

$$y = (-4.13 \pm 0.19_{\,\text{stat.}} \pm 0.07_{\,\text{syst.}} + 0.05_{\,\text{model}})\%. \tag{15.2}$$

The correlation coefficient of the corresponding statistical uncertainties is 0.01 and the systematic and model-dependent uncertainties are assumed to be uncorrelated.

The current world averages on the mixing and *CP* violation parameters are [9]

$$\begin{aligned} x &= (0.49 \pm 0.15)\%, \\ y &= (0.62 \pm 0.09)\%, \\ |q/p| &= \quad 0.98 \pm 0.09, \\ \phi &= -0.02 \pm 0.13, \end{aligned}$$

as discussed in Chapt. 2.4.5. By combing the result of this thesis with the set of measurements entering the current world average, the mixing and *CP* violation parameters become [44]

$$\begin{aligned} x &= (0.49 \pm 0.13)\%, \\ y &= (0.614 \pm 0.085)\%, \\ |q/p| &= \quad 0.98 \pm 0.09, \\ \phi &= -0.02 \pm 0.13. \end{aligned}$$

As the results reported in this thesis are currently blind, the central values are assumed in the following to agree with the current world averages of $x = 0.49\%$ and $y = 0.61\%$. Figure 15.1 illustrates the world average on the mixing parameters before the measurement presented in this thesis and the averages including the result. In the comparison, it becomes clear that the measurements reported in this thesis lead to a significant improvement of the world average of the mixing parameters.

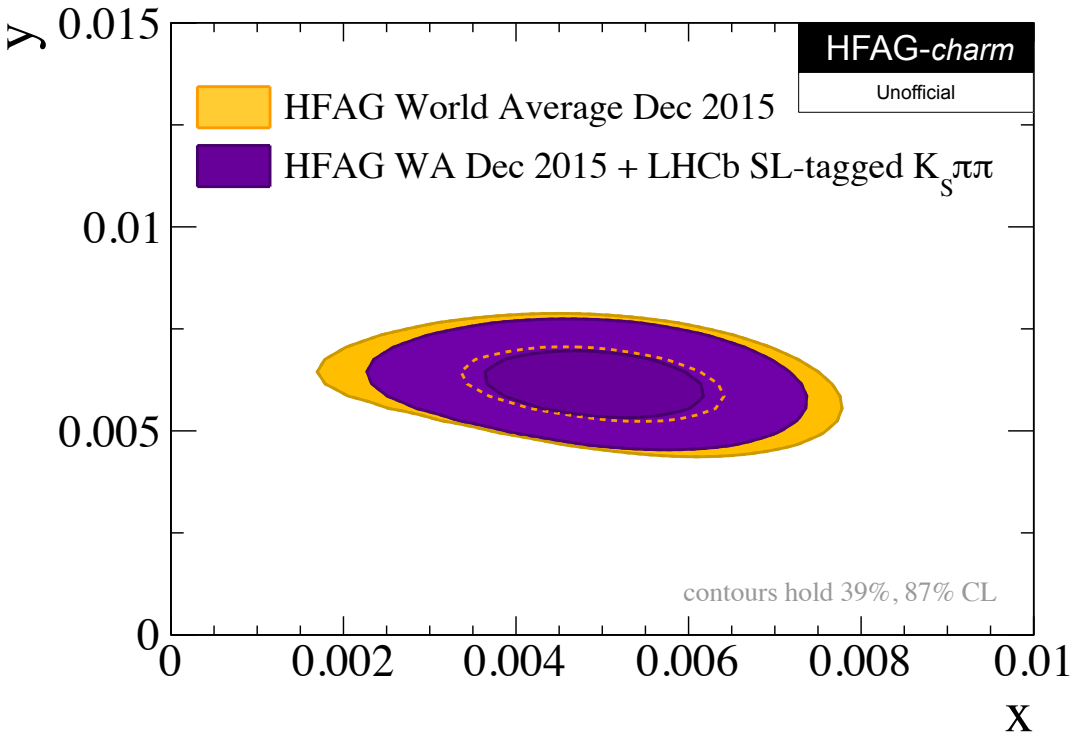

Figure 15.1.: *Current world averages on the mixing parameters excluding (yellow) and including (purple) the results reported in this thesis. The world averages on the mixing parameters including the result reported in this thesis are* $x = (0.49 \pm 0.13)\%$ *and* $y = (0.614 \pm 0.085)\%$ *[44].*

15.2. Future prospects of $D^0 \to K^0_S\pi^+\pi^-$ analyses at LHCb

In addition to the measurement of the mixing parameters reported in this thesis, work has been undertaken to prepare a search for indirect *CP* violation, which is described by the parameters $|q/p|$ and ϕ. Future studies will include a measurement of the *CP* violation parameters and implement changes to the current analysis. The most significant foreseen other changes comprise the change of the nominal amplitude model, which will then use the K-matrix in the production vector approach and the LASS parameterisations detailed in Chapt. 11.1.7. Furthermore, the estimation of the fit model systematic uncertainty will be refined by following the approach discussed in Ref. [106], where only fits of comparable quality contribute to the fit model uncertainty.

In the longer term, a combined analysis of the semileptonically-tagged datasets and $D^0 \to K^0_S\pi^+\pi^-$ decays originating from a prompt $D^{*+} \to D^0\pi^+$ will be performed. The combination will lead

to a higher precision as the prompt $D^0 \to K^0_S\pi^+\pi^-$ dataset is significantly larger and has a very high purity. In addition, the analysis will have access to a wider range of D^0 decay times as can be seen from Fig. 15.2. The sensitivity of the mixing parameters of the combined analysis is expected to be compatible with the precision of the world average [9].

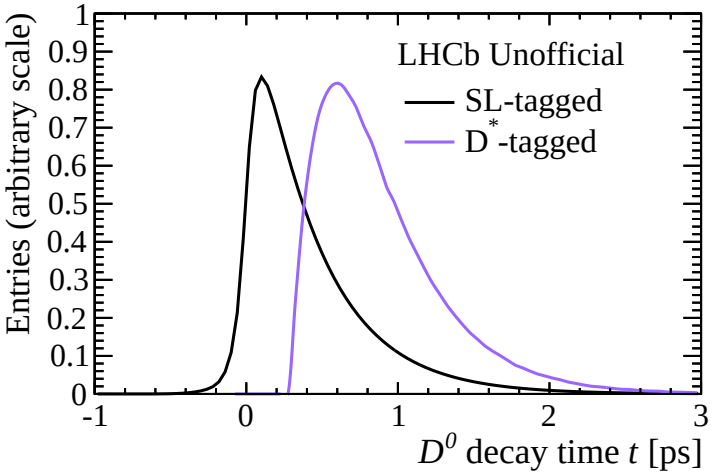

Figure 15.2.: *Decay-time coverage of semileptonically-tagged and prompt $D^0 \to K^0_S\pi^+\pi^-$ decays. The distributions are normalised to the same integral.*

15.3. Impact of $D^0 \to K^0_S\pi^+\pi^-$ analyses on the measurement of the CKM angle γ

The analysis of $D^0 \to K^0_S\pi^+\pi^-$ decay plays also an important role for the extraction of the CKM [26, 27] angle γ, which is defined as [11]

$$\gamma \equiv \arg\left(-\frac{V_{ud}V^*_{ub}}{V_{cd}V^*_{cb}}\right), \tag{15.3}$$

and is the at least well measured angle of the unitarity triangle. The current precision obtained from a combination of LHCb measurements [108] is

$$\gamma = \left(73^{+9}_{-10}\right)^\circ. \tag{15.4}$$

The angle γ can be extracted from tree-level B decays and as such is not expected to be sensitive to physics beyond the Standard Model. Measurements are performed with $B \to D\pi$, $B \to DK$ and $B^0_s \to D^+_s K$ decays. The most precise measurement of γ comes from the GGSZ method [109], which uses $B^\pm \to DK^\pm$ decays followed by a multibody decay, such as $D^0 \to K^0_S\pi^+\pi^-$. In the $D^0 \to K^0_S\pi^+\pi^-$ final state, model-dependent and model-independent measurements of γ have been reported by the LHCb Collaboration. A model-independent GGSZ approach, which uses the strong phase as measured by CLEO [42] as input, finds [110]

$$\gamma = \left(62^{+15}_{-14}\right)^{\circ}. \tag{15.5}$$

The CKM angle γ can also be extracted from a time- and model-dependent analysis of *e.g.* $B^{\pm} \to D(\to K^0_S\pi^{\pm}\pi^{\mp})K^{\pm}$ decays. This approach requires the input of an amplitude model, which is provided by a time- and model-dependent amplitude analysis of $D^0 \to K^0_S\pi^+\pi^-$ decays as performed in this thesis. Following the model-dependent GGSZ method, the LHCb Collaboration has measured [111]

$$\gamma = \left(84^{+49}_{-42}\right)^{\circ}. \tag{15.6}$$

Further methods, such as the GLW [112, 113] and ADS [114, 115] methods, require the knowledge of the mixing parameters x and y to constrain γ. The GLW approach considers D decays to *CP* eigenstates, whereas the ADS method exploits the interference between Cabibbo-favoured $\overline{D}^0$ decays and doubly-Cabibbo suppressed D^0 decays. As these measurements rely on the mixing parameters, an improved measurement of x and y, which is achieved by combining the world average [9] with the results reported in this thesis, also leads to an increased precision on the CKM angle γ.

15.4. Future prospects of mixing measurements at LHCb

The sensitivities on the mixing parameters from the Run 1 analysis presented in this thesis are 0.22% on x and 0.19% on y. With the recent start of Run 2 and the foreseen LHCb upgrade between Run 2 and Run 3, which is discussed in Chapt. 4, the sensitivity on the mixing parameters extracted from semileptonically-tagged $D^0 \to K^0_S\pi^+\pi^-$ decays will improve with the new incoming data.

In Run 2, the LHCb detector is expected to collect a dataset corresponding to an integrated luminosity of $5\,\text{fb}^{-1}$ and in Run 3, an increase in integrated luminosity of further $15\,\text{fb}^{-1}$ is expected [116]. The following estimates assume the same trigger efficiency for Run 2 than in Run 1 and an increase of the trigger efficiency by a factor of two in Run 3. Further taking the increase in cross-section due to the higher centre-of-mass energy of 13 TeV and 14 TeV in Run 2 and Run 3, respectively, into account, the sensitivity on x is expected to be 0.13% after Run 2 and 0.05% after Run 3. The mixing parameter y, which is measured with a higher statistical precision than x, is expected to be measurable with a sensitivity of 0.11% and 0.04% after Run 2 and Run 3, respectively. Beyond the significant improvement on the knowledge of the mixing parameters themselves, these improvements also lead to a better understanding of *CP* violating quantities through measurements such as A_Γ and a more precise extraction of the CKM angle γ.

And all was well.

A. Comparison of BDT input variables for even and odd datasets

The distributions of the variables used in the BDT training (see Chapt. 8.2 are compared for even and odd datasets as some differences in the performance of the BDT selection between even and odd datasets is observed. For this study, the preselection detailed in Chapt. 7 has been applied to these variable distributions, which are split into signal and background contributions by weighting them with the according sWeights. The sWeight extraction is described in detail in Chapt. 8.1. The comparisons for single-tagged datasets are shown in Figs. A.1-A.4 and for the double-tagged datasets in Figs. A.5-A.8.

A. Comparison of BDT input variables for even and odd datasets

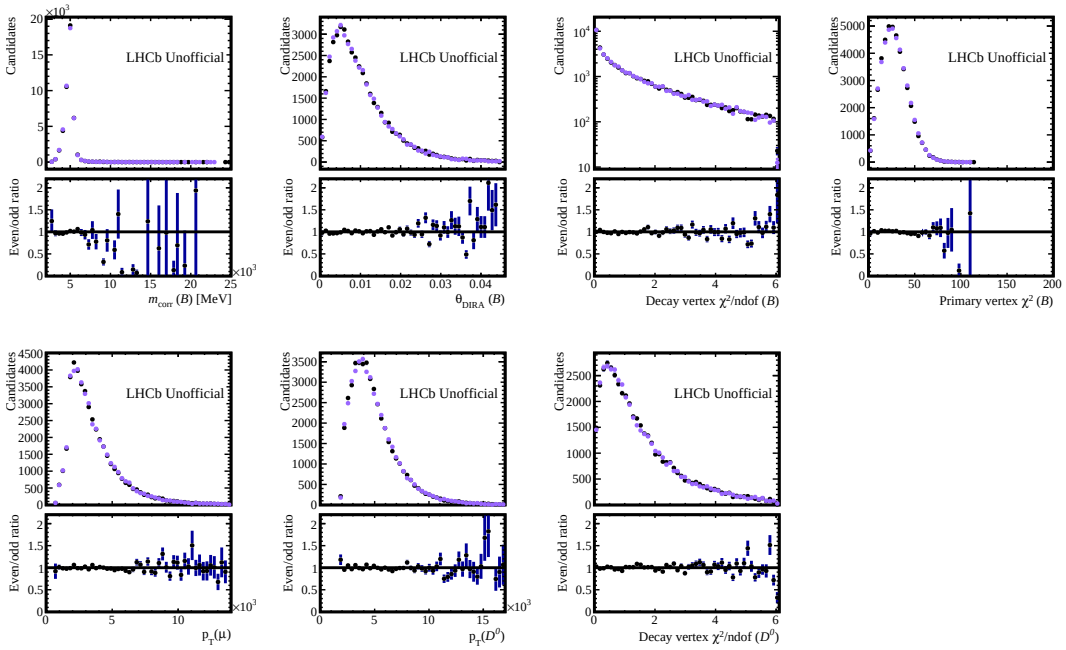

(a) *Signal*

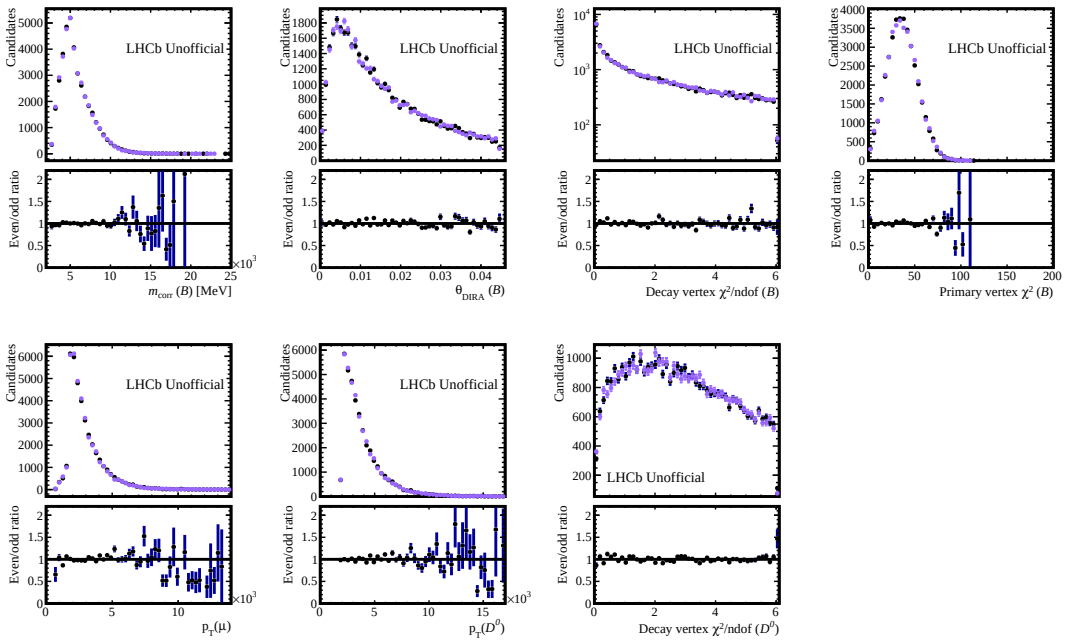

(b) *Background*

Figure A.1.: *Comparison of the BDT input variables for the even (black) and odd (violet) single-tagged 2011 $D^0 \to K^0_S(\mathrm{LL})\pi^+\pi^-$ datasets split into signal and background contributions.*

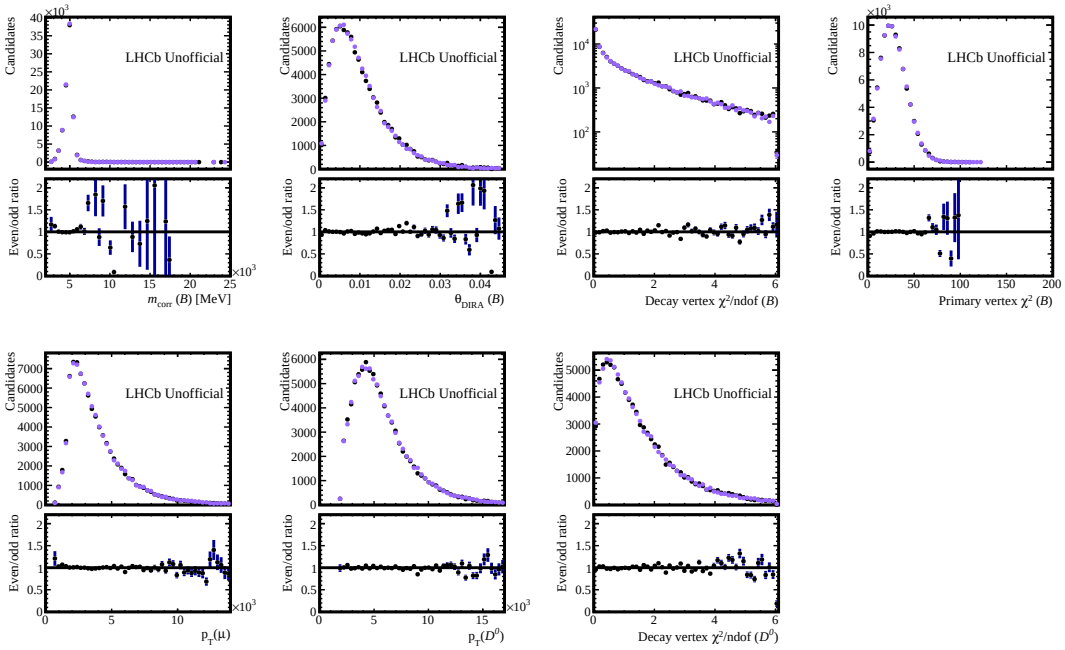

(a) *Signal*

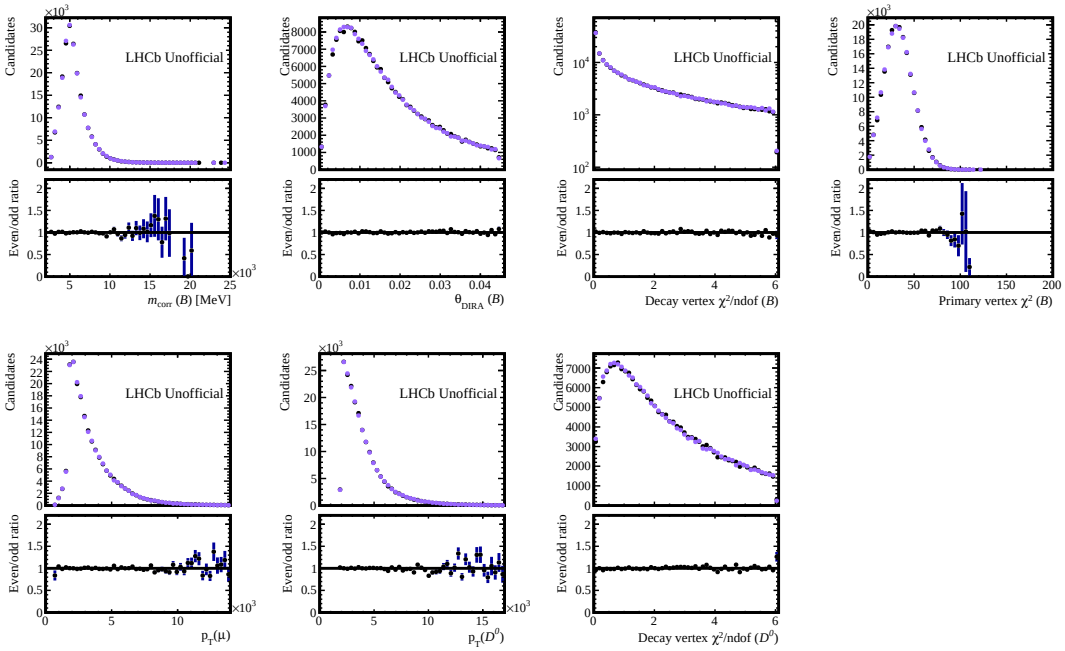

(b) *Background*

Figure A.2.: *Comparison of the BDT input variables for the even (black) and odd (violet) single-tagged 2011 $D^0 \to K^0_S(\mathrm{DD})\pi^+\pi^-$ datasets split into signal and background contributions.*

A. Comparison of BDT input variables for even and odd datasets

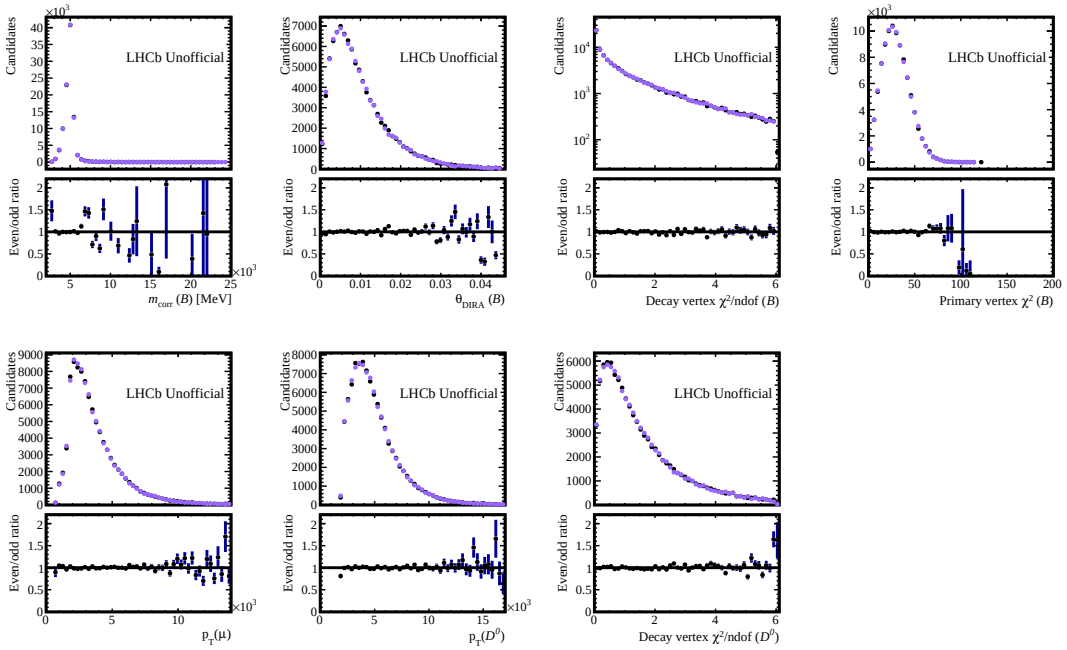

(a) *Signal*

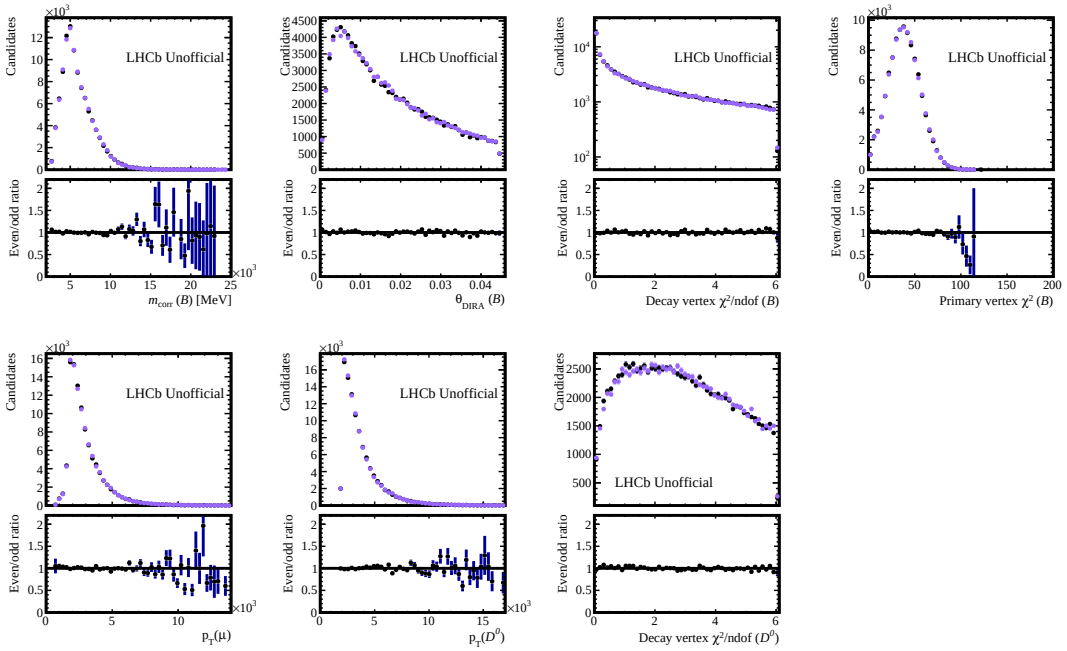

(b) *Background*

Figure A.3.: *Comparison of the BDT input variables for the even (black) and odd (violet) single-tagged 2012 $D^0 \to K^0_S(\mathrm{LL})\pi^+\pi^-$ datasets split into signal and background contributions.*

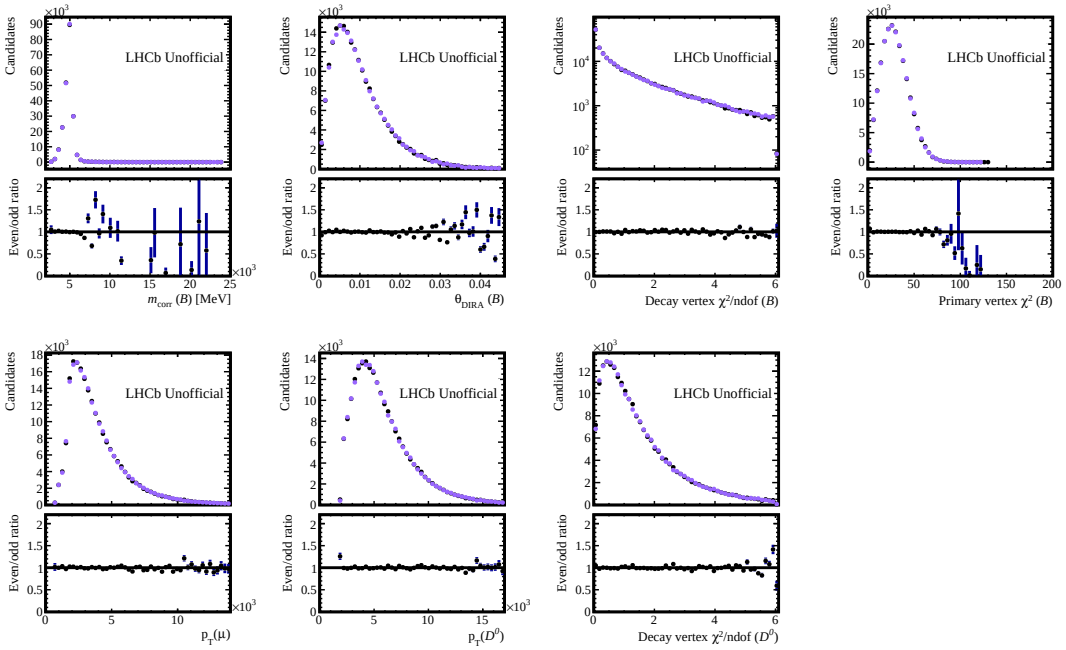

(a) *Signal*

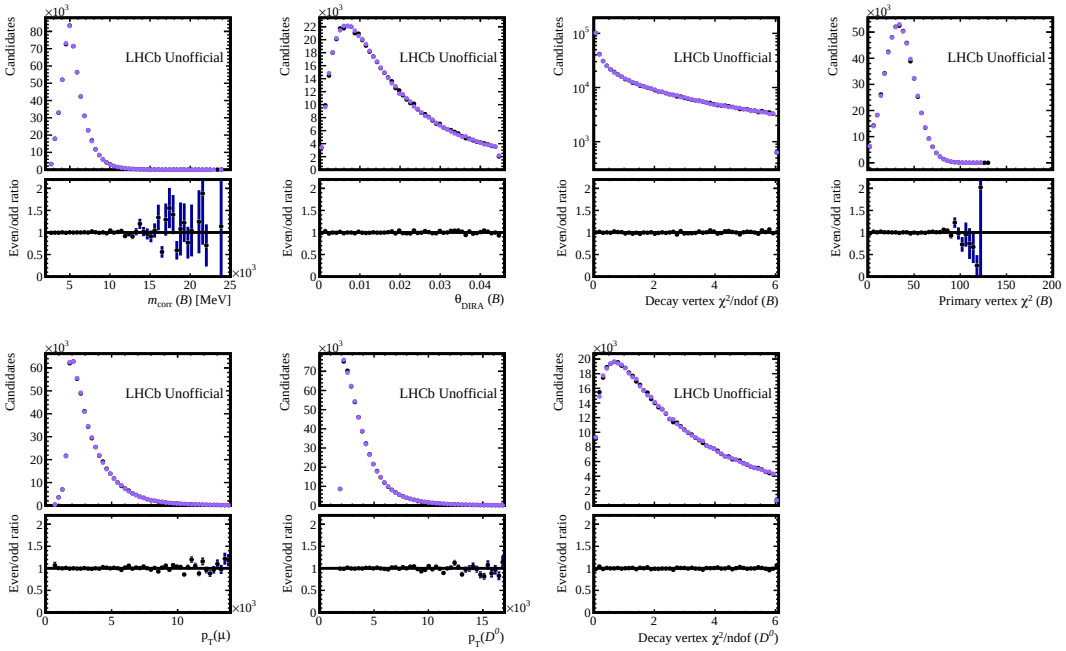

(b) *Background*

Figure A.4.: *Comparison of the BDT input variables for the even (black) and odd (violet) single-tagged 2012 $D^0 \to K^0_S(\mathrm{DD})\pi^+\pi^-$ datasets split into signal and background contributions.*

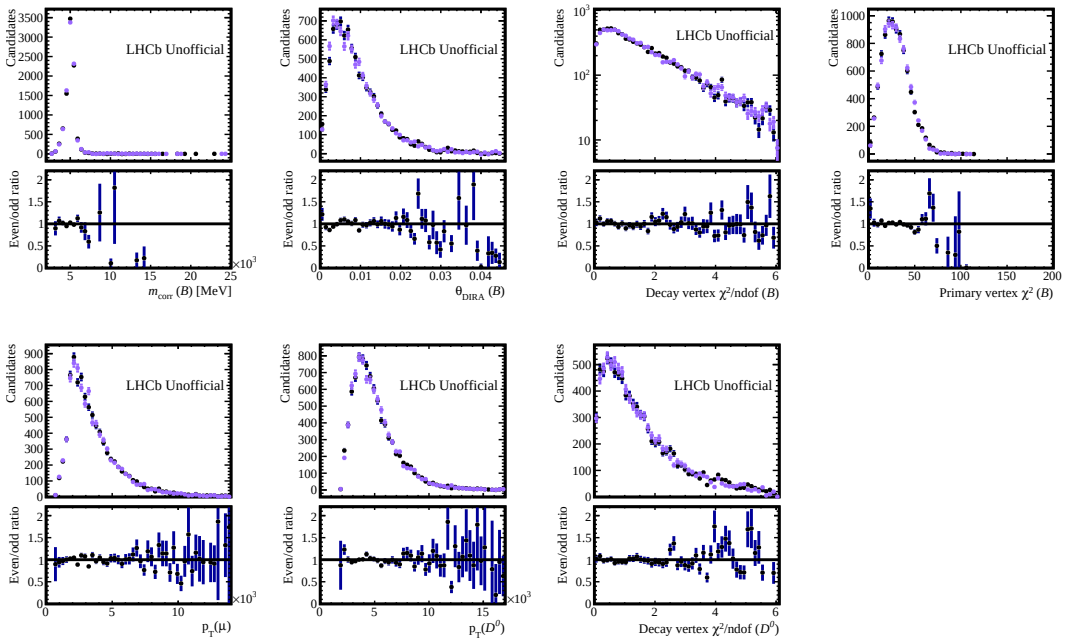

(a) *Signal*

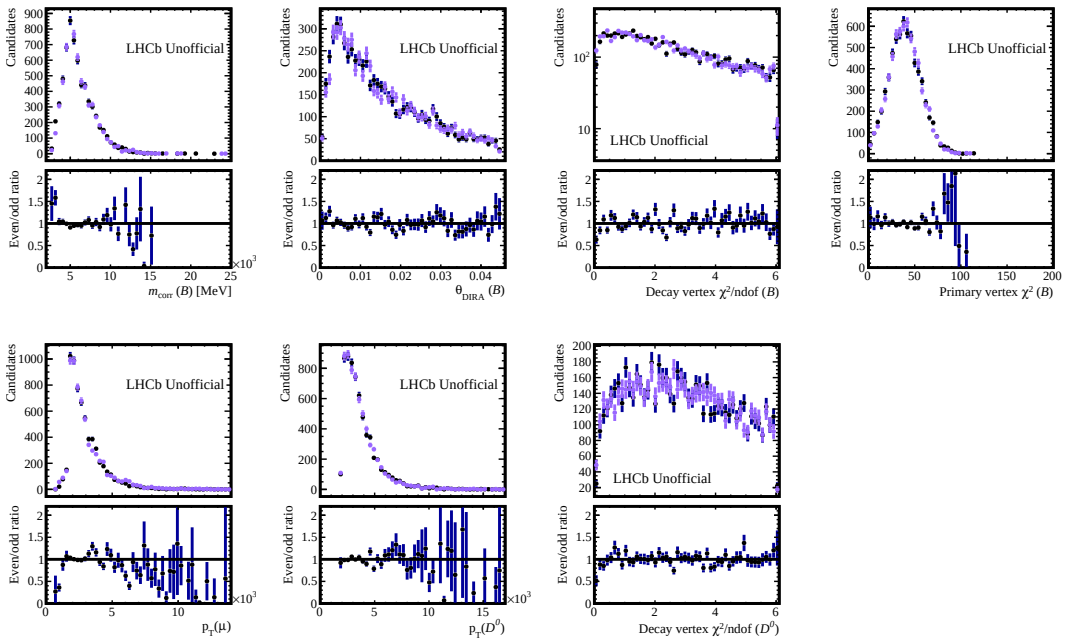

(b) *Background*

Figure A.5.: *Comparison of the BDT input variables for the even (black) and odd (violet) double-tagged 2011 $D^0 \to K^0_S(\mathrm{LL})\pi^+\pi^-$ datasets split into signal and background contributions.*

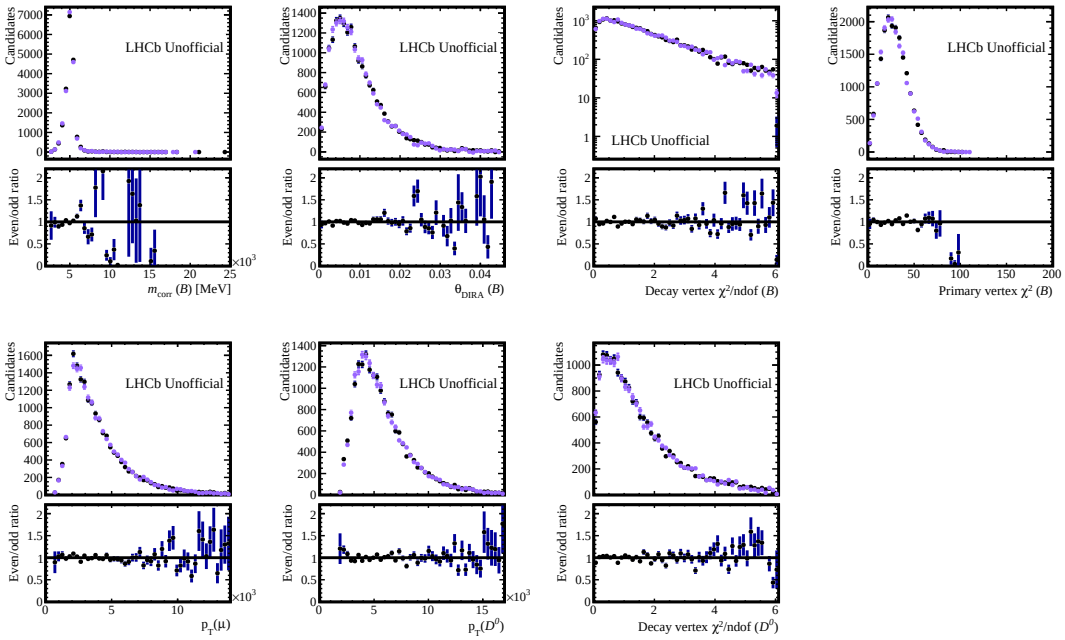

(a) *Signal*

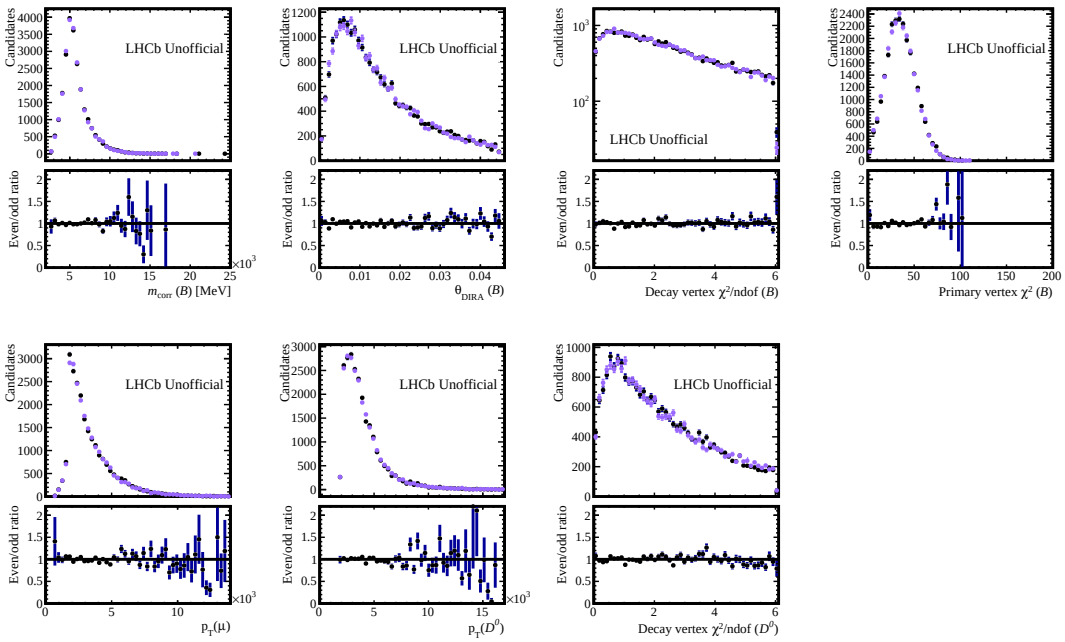

(b) *Background*

Figure A.6.: *Comparison of the BDT input variables for the even (black) and odd (violet) double-tagged 2011 $D^0 \to K^0_S(\mathrm{DD})\pi^+\pi^-$ datasets split into signal and background contributions.*

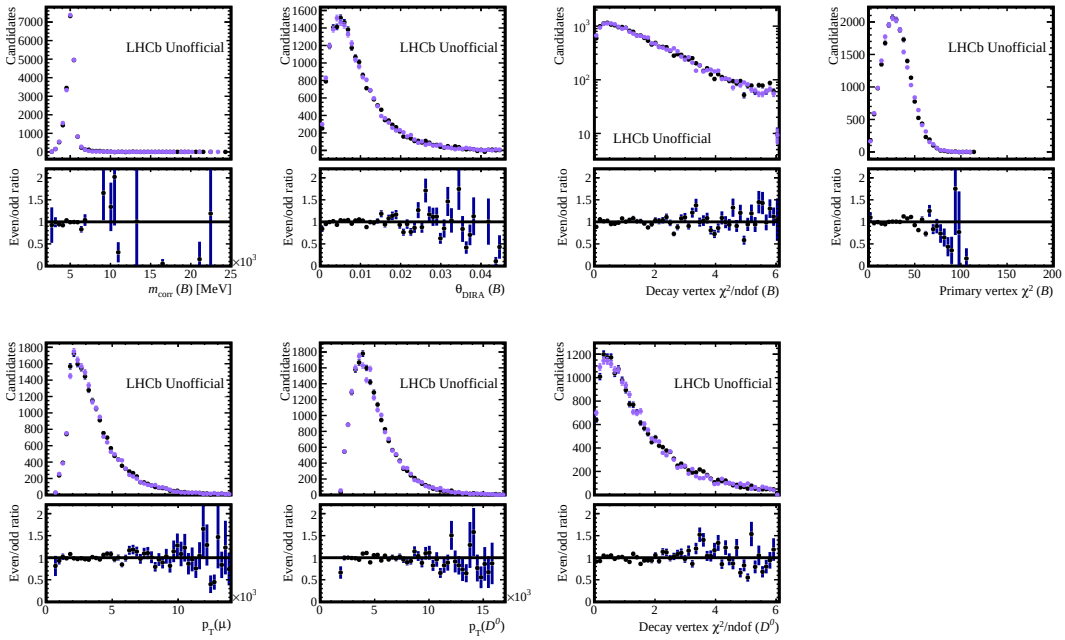

(a) *Signal*

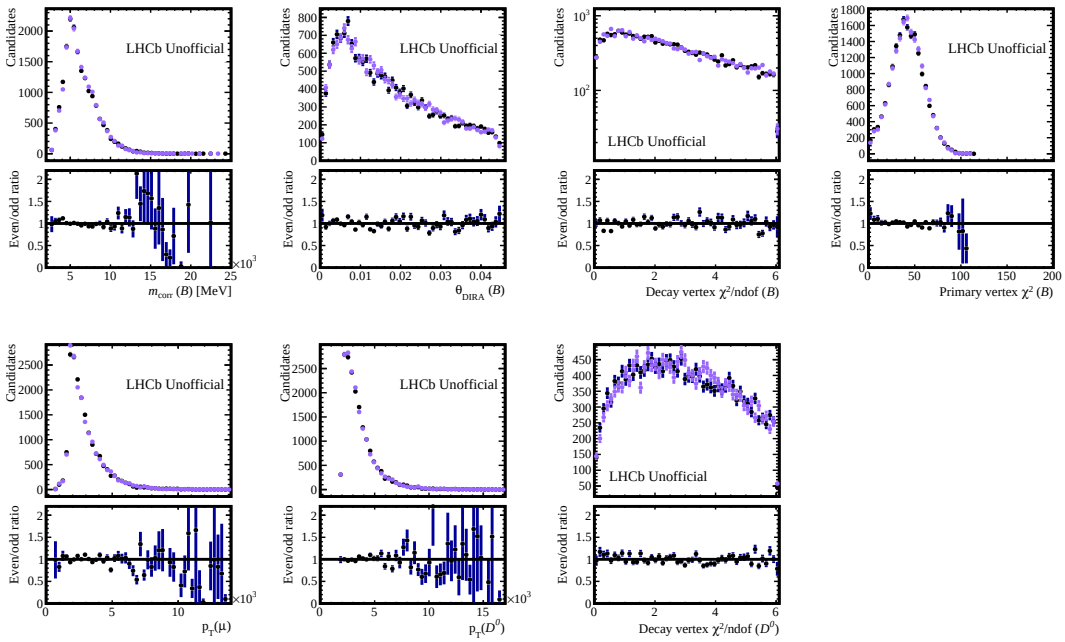

(b) *Background*

Figure A.7.: *Comparison of the BDT input variables for the even (black) and odd (violet) double-tagged 2012 $D^0 \to K^0_S(\mathrm{LL})\pi^+\pi^-$ datasets split into signal and background contributions.*

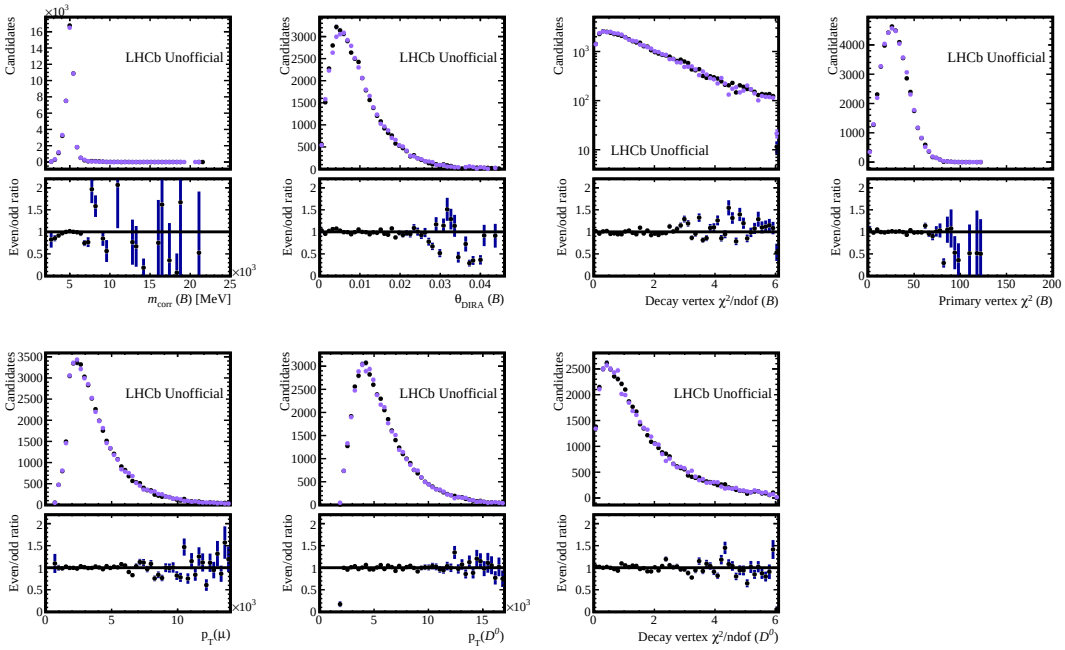

(a) *Signal*

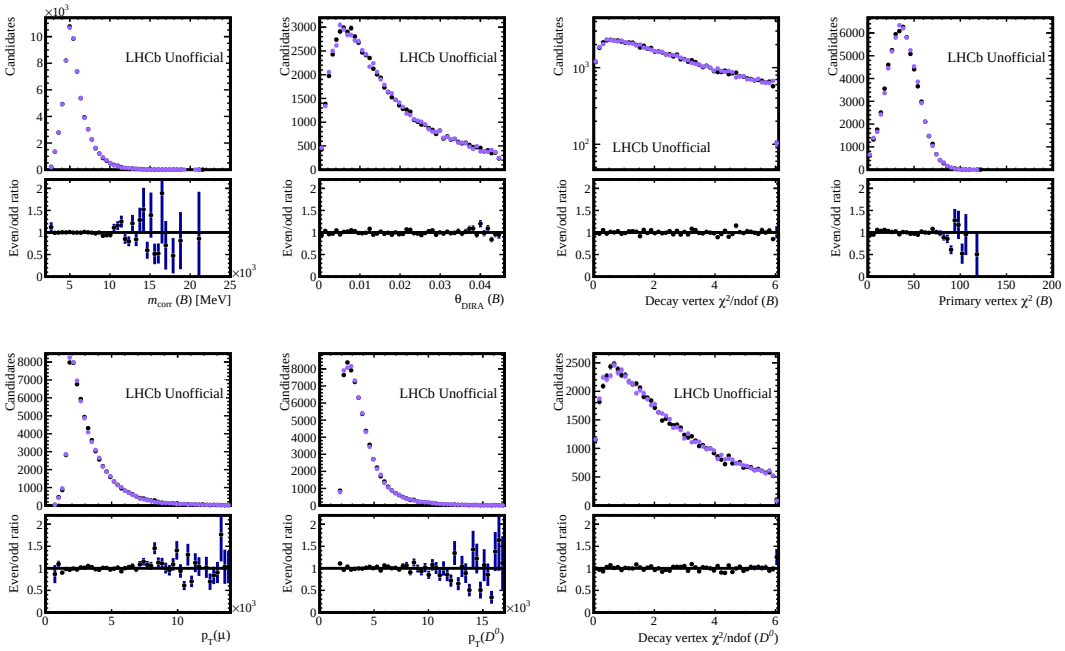

(b) *Background*

Figure A.8.: *Comparison of the BDT input variables for the even (black) and odd (violet) double-tagged 2012 $D^0 \to K^0_S(\mathrm{DD})\pi^+\pi^-$ datasets split into signal and background contributions.*

B. Receiver Operator Characteristics curves

The signal efficiency versus background rejection rate, the so-called ROC or Receiver Operator Characteristics curve is determined by evaluating the signal efficiency and background rejection at various cuts on the BDT response as explained in Chapt. 8.2. Hereby, the background rejection is defined as $1 - \varepsilon(bkg)$ with $\varepsilon(bkg)$ being the background efficiency. Figures B.1 and B.2 show the ROC curves for the single-tagged 2011 and 2012 datasets, respectively. The ROC curves for the double-tagged sample are illustrated in Figs. B.3 and B.4.

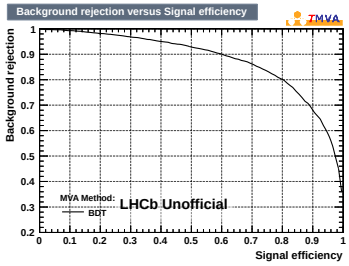

(a) *Even event numbers of* $D^0 \to K^0_S(\mathrm{LL})\pi^+\pi^-$ *sample*

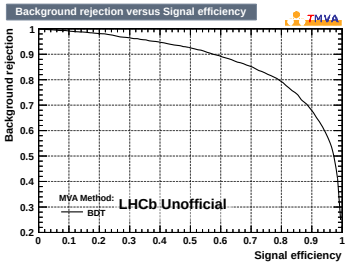

(b) *Odd event numbers of* $D^0 \to K^0_S(\mathrm{LL})\pi^+\pi^-$ *sample*

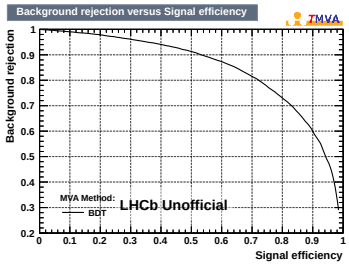

(c) *Even event numbers of* $D^0 \to K^0_S(\mathrm{DD})\pi^+\pi^-$ *sample*

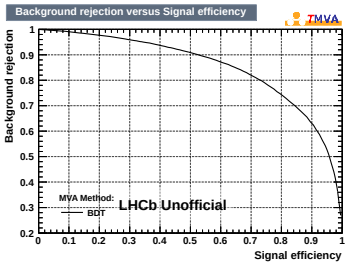

(d) *Odd event numbers of* $D^0 \to K^0_S(\mathrm{DD})\pi^+\pi^-$ *sample*

Figure B.1.: *Signal efficiency versus background rejection calculated for various cuts on the BDT response for the 2011* $B^- \to D^0(\to K^0_S\pi^+\pi^-)\mu^-\overline{\nu}_\mu$ *dataset split by* K^0_S *type and even and odd event numbers.*

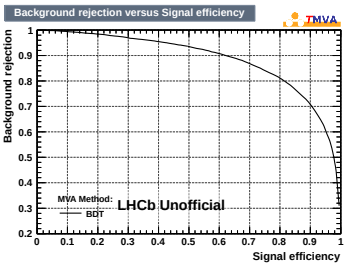

(a) *Even event numbers of* $D^0 \to K^0_S(\mathrm{LL})\pi^+\pi^-$ *sample*

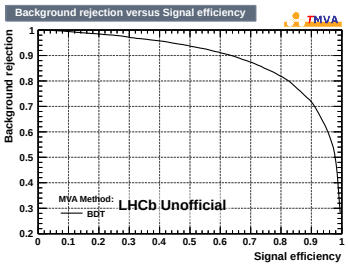

(b) *Odd event numbers of* $D^0 \to K^0_S(\mathrm{LL})\pi^+\pi^-$ *sample*

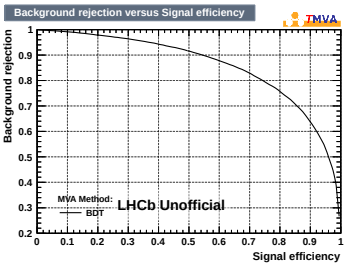

(c) *Even event numbers of* $D^0 \to K^0_S(\mathrm{DD})\pi^+\pi^-$ *sample*

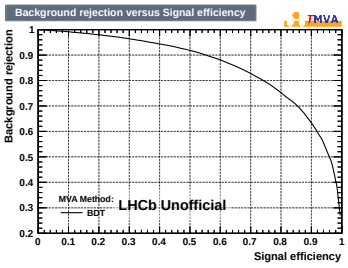

(d) *Odd event numbers of* $D^0 \to K^0_S(\mathrm{DD})\pi^+\pi^-$ *sample*

Figure B.2.: *Signal efficiency versus background rejection calculated for various cuts on the BDT response for the 2012* $B^- \to D^0(\to K^0_S\pi^+\pi^-)\mu^-\overline{\nu}_\mu$ *dataset split by* K^0_S *type and even and odd event numbers.*

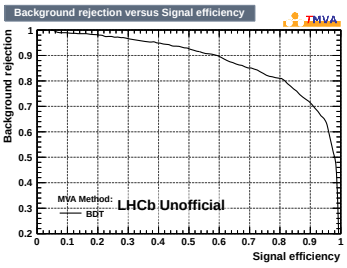

(a) *Even event numbers of* $D^0 \to K^0_S(\mathrm{LL})\pi^+\pi^-$ *sample*

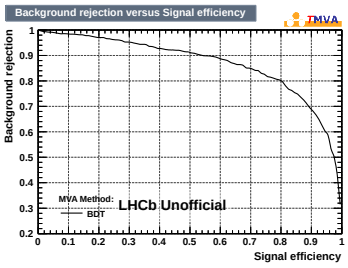

(b) *Odd event numbers of* $D^0 \to K^0_S(\mathrm{LL})\pi^+\pi^-$ *sample*

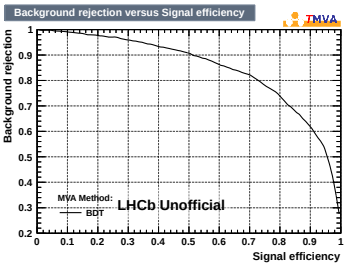

(c) *Even event numbers of* $D^0 \to K^0_S(\mathrm{DD})\pi^+\pi^-$ *sample*

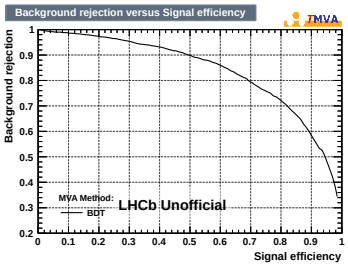

(d) *Odd event numbers of* $D^0 \to K^0_S(\mathrm{DD})\pi^+\pi^-$ *sample*

Figure B.3.: *Signal efficiency versus background rejection calculated for various cuts on the BDT response for the 2011* $\overline{B}^0 \to D^{*+}(\to D^0(\to K^0_S\pi^+\pi^-)\pi^+)\mu^-\overline{\nu}_\mu$ *dataset split by* K^0_S *type and even and odd event numbers.*

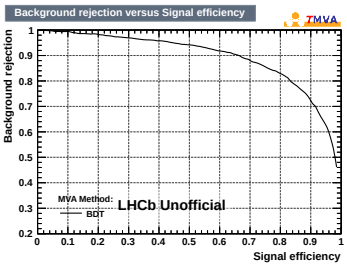

(a) *Even event numbers of* $D^0 \to K^0_S(\mathrm{LL})\pi^+\pi^-$ *sample*

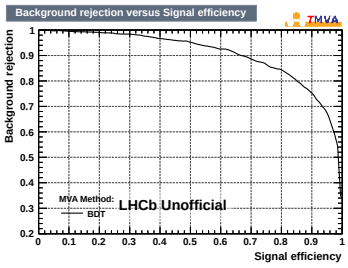

(b) *Odd event numbers of* $D^0 \to K^0_S(\mathrm{LL})\pi^+\pi^-$ *sample*

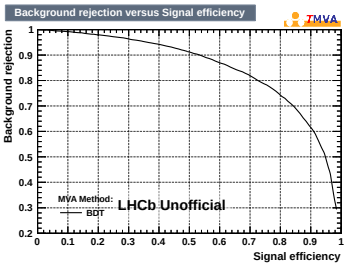

(c) *Even event numbers of* $D^0 \to K^0_S(\mathrm{DD})\pi^+\pi^-$ *sample*

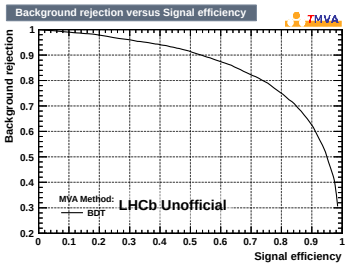

(d) *Odd event numbers of* $D^0 \to K^0_S(\mathrm{DD})\pi^+\pi^-$ *sample*

Figure B.4.: *Signal efficiency versus background rejection calculated for various cuts on the BDT response for the 2012* $\overline{B}^0 \to D^{*+}(\to D^0(\to K^0_S\pi^+\pi^-)\pi^+)\mu^-\overline{\nu}_\mu$ *dataset split by* K^0_S *type and even and odd event numbers.*

C. BDT optimisation

The nominal cut on the BDT output is determined as the cut where the significance between signal S and background B in the training sample $S/\sqrt{S+B}$ reaches its maximum, as detailed in Chapt. 8.2. This figure of merit is optimal for optimising the significance of observing the event sample. However, for this analysis it might not yield the best statistical sensitivity. Hence, the nominal cut is tightened by +0.05, +0.10 and +0.20 to study if the nominal cut yields the optimal statistical sensitivity on x and y. Looser cuts are not considered as tighter cuts will better control the background systematic evaluated in Chapt. 13.2.3. This study relies on pseudo-experiments (see Chapt. 12), which reflect the tightened BDT cut; and thus the reduced signal to background ratio as well as new sets of acceptance and resolution parameters. The results of the amplitude fits to an ensemble of 100 pseudo-experiments each are listed in Table C.1. As can be seen from Table C.1, the nominal BDT cut yields the optimal statistical sensitivity, and hence this is adopted at the chosen working point.

Table C.1.: *Sensitivity on x and y for various BDT cuts split by K^0_S type and year estimated from simulated pseudo-experiments.*

Sample	Nominal cut			
	+0.00	+0.05	+0.10	+0.20
Sensitivity to x				
2011 K^0_S(LL)	0.00537	0.00548	0.00547	0.00571
2011 K^0_S(DD)	0.00437	0.00444	0.00450	0.00472
2012 K^0_S(LL)	0.00374	0.00385	0.00384	0.00396
2012 K^0_S(DD)	0.00295	0.00296	0.00305	0.00317
Sensitivity to y				
2011 K^0_S(LL)	0.00491	0.00498	0.00509	0.00514
2011 K^0_S(DD)	0.00401	0.00405	0.00410	0.00426
2012 K^0_S(LL)	0.00337	0.00341	0.00346	0.00362
2012 K^0_S(DD)	0.00266	0.00268	0.00274	0.00283

D. Phase-space acceptance parameterisation for the single-tagged sample

The fits to D^0 mass in bins of $cos(\theta)$ in the lowest $m^2(\pi^+\pi^-)$ are illustrated in Fig. D.1, which are used to calculate the phase-space acceptance (see Chapt. 10.1). Figures D.2 and D.3 show the acceptance variation as a function of f $m^2(\pi^+\pi^-)$ in different bins of $\cos(\theta)$ and as a function of $\cos(\theta)$ in bins of $m^2(\pi^+\pi^-)$. The p-values of the projections are given in Tables D.1.

Table D.1.: *p-values of the efficiency projections in bins of* $\cos(\theta)$ *and* $m^2(\pi^+\pi^-)$ *for the 2012* K^0_S(LL) *MC sample with tight generator-level cuts after the complete selection chain in bins of* $m^2(\pi^+\pi^-)$ *and* $m^2(\pi^+\pi^-)$*. The lower bin boundaries are increasing with the bin number.*

	p-value	
	in bins of $\cos(\theta)$	in bins of $m^2(\pi^+\pi^-)$
Bin 1	3.3×10^{-5}	6.4×10^{-7}
Bin 2	1.3×10^{-2}	1.2×10^{-1}
Bin 3	1.8×10^{-1}	6.6×10^{-3}
Bin 4	2.7×10^{-4}	3.2×10^{-5}
Bin 5	9.0×10^{-2}	5.6×10^{-4}
Bin 6	1.7×10^{-3}	1.9×10^{-3}
Bin 7	4.5×10^{-2}	1.0×10^{-2}
Bin 8	2.3×10^{-2}	3.1×10^{-1}
Bin 9	8.6×10^{-2}	2.0×10^{-1}
Bin 10	6.2×10^{-3}	3.7×10^{-1}
Bin 11	1.5×10^{-1}	1.6×10^{-3}
Bin 12	5.1×10^{-1}	4.9×10^{-2}
Bin 13	4.3×10^{-1}	1.8×10^{-2}
Bin 14	2.8×10^{-2}	2.9×10^{-1}
Bin 15	3.5×10^{-2}	4.4×10^{-2}
Bin 16	6.6×10^{-3}	1.3×10^{-2}
Bin 17	3.9×10^{-2}	7.7×10^{-1}
Bin 18	6.2×10^{-6}	2.2×10^{-2}

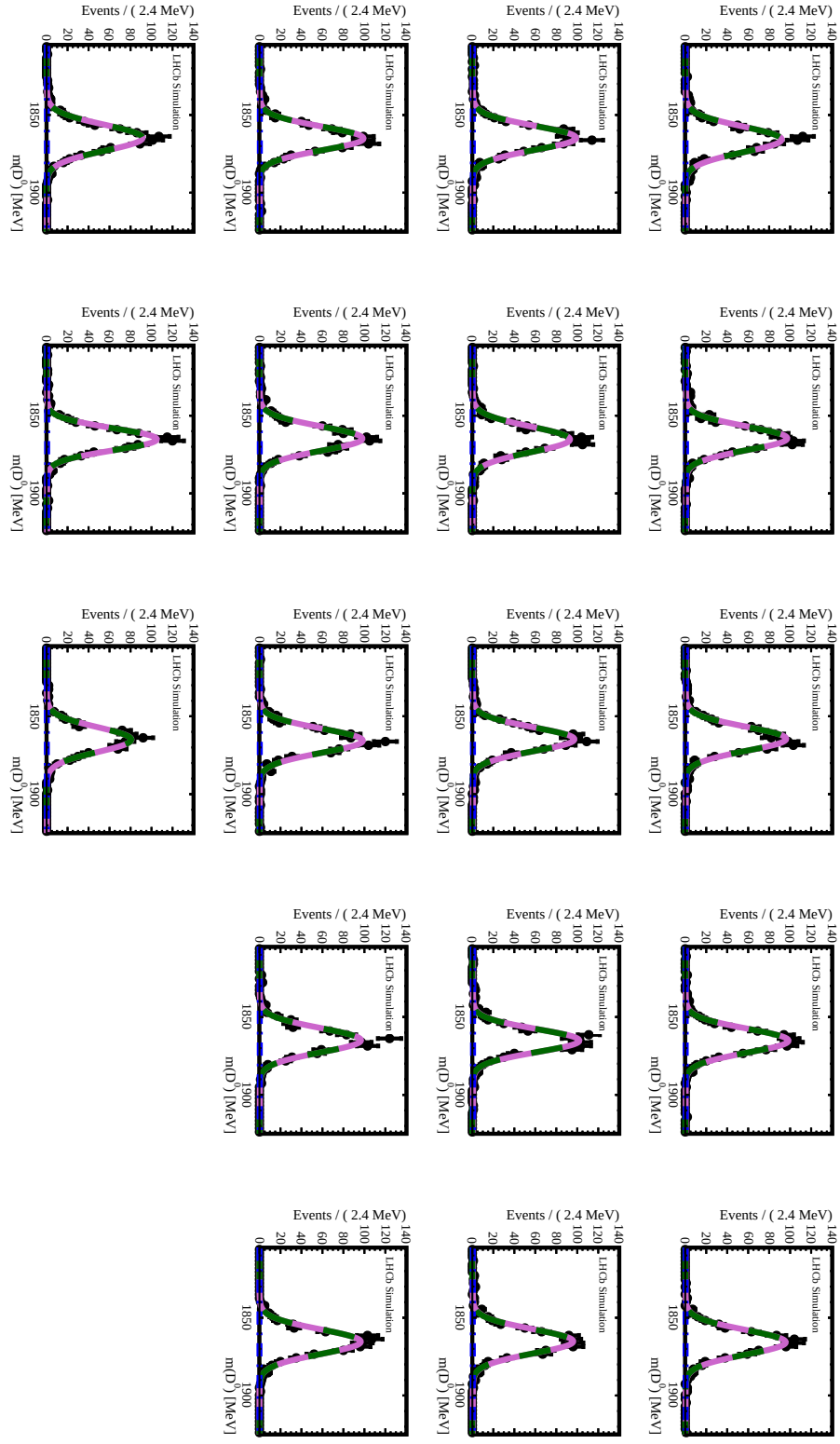

Figure D.1: *$m(D^0)$ distribution of the 2012 K^0_S(LL) single-tagged MC sample with tight generator-level cuts after the complete selection chain in bins of $\cos(\theta)$ in the lowest $m^2(\pi^+\pi^-)$ bin. The lower bin boundaries are increasing from left to right and from top to bottom. The figure depicts the fit (dashed magenta line) to the data (black points) and the fit components. The signal consists of a Gaussian function (dashed green line). The background is modelled by a constant function (solid blue line).*

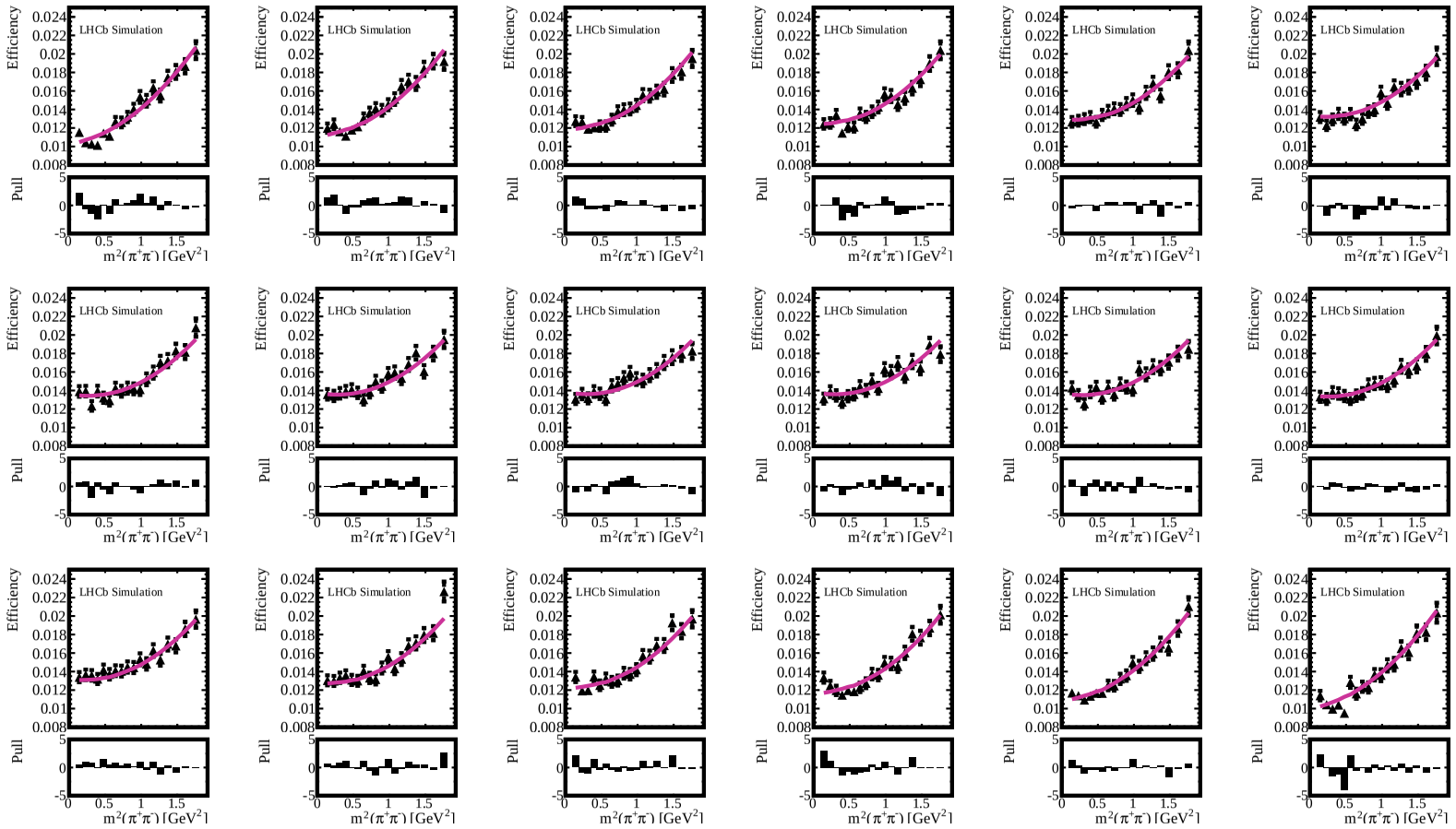

Figure D.2.: *Single-tagged phase-space acceptance as a function of* $m^2(\pi^+\pi^-)$ *in different bins of* $\cos(\theta)$ *for the 2012* K^0_S(LL) *MC sample with tight generator-level cuts after the complete selection chain in bins of* $\cos(\theta)$*. The lower bin boundaries are increasing from left to right and from top to bottom. The black points correspond to the measured acceptance whereas the parameterisation is depicted in pink.*

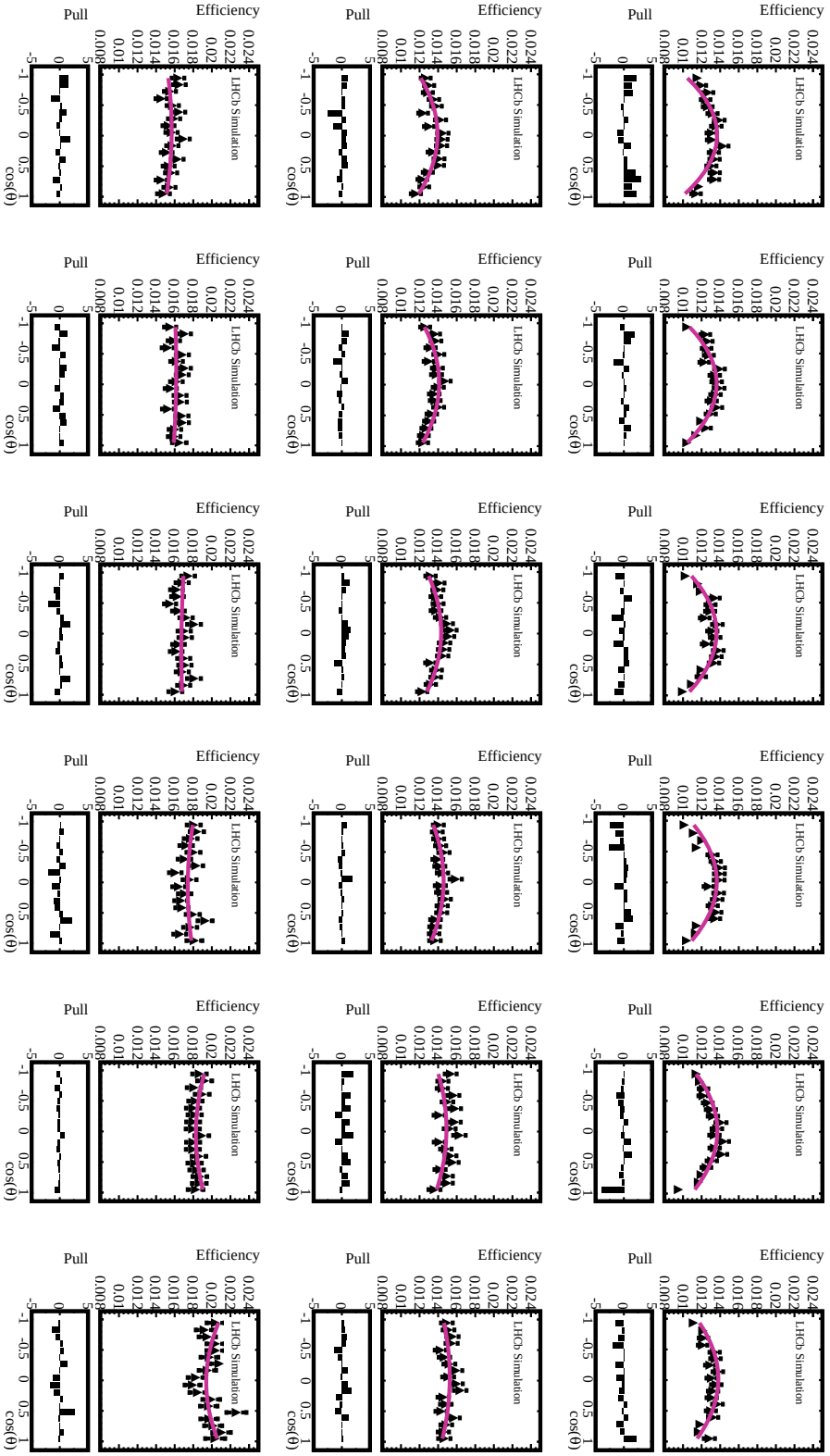

Figure D.3.: *Single-tagged phase-space acceptance as a function of* $\cos(\theta)$ *in different bins of* $m^2(\pi^+\pi^-)$ *for the 2012* K^0_S(LL) *MC sample with tight generator-level cuts after the complete selection chain in bins of* $m^2(\pi^+\pi^-)$*. The lower bin boundaries are increasing from left to right and from top to bottom. The black points correspond to the measured acceptance whereas the parameterisation is depicted in pink.*

E. Comparison of phase-space acceptance variables for single- and double-tagged datasets

The phase-space acceptance is evaluated using Monte Carlo samples of single-tagged decays. The same MC samples are used to calculate the acceptance for double-tagged decays. This approach is valid since the variables entering the computation of $\cos(\theta')$ and $m^2(\pi^+\pi^-)$ are following the same distributions as is shown here for data. For this study, the preselection and BDT selection detailed in Chapt. 7 and 8 criteria are applied. The kinematic variables have been refitted with K^0_S and D^0 mass constraints and all distributions are weighted by the signal sWeights extracted from a $m(D^0)$ fit for the single-tagged and from a δm fit for the double-tagged sample. The comparison is shown for the 2012 K^0_S(LL) and 2012 K^0_S(DD) datasets for the D^0 meson variables illustrated in Fig. E.1, K^0_S meson variables shown in Fig. E.2 and bachelor $\pi^\pm$ variables given in Figs. E.3 and E.4.

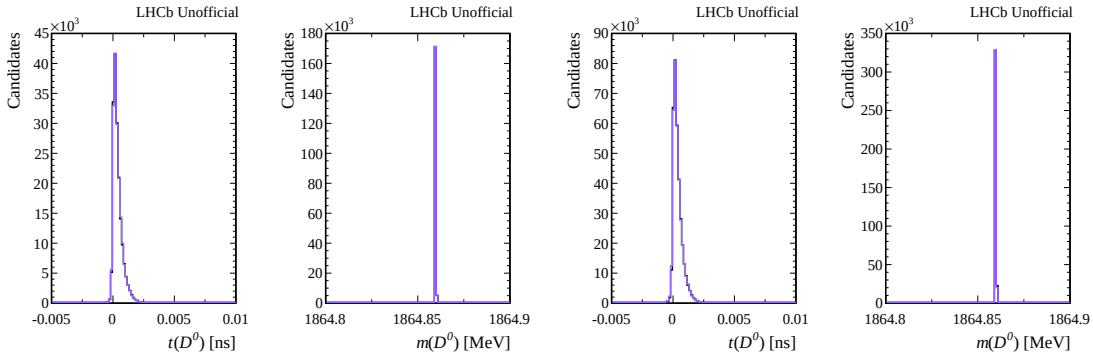

(a) *2012* $D^0 \to K^0_S(\mathrm{LL})\pi^+\pi^-$ *sample* **(b)** *2012* $D^0 \to K^0_S(\mathrm{DD})\pi^+\pi^-$ *sample*

Figure E.1.: *Comparison of the* D^0 *variables entering the phase-space acceptance calculation for single-tagged (black) and double-tagged (violet)* $D^0 \to K^0_S\pi^+\pi^-$ *datasets. The* D^0 *decay time of the double-tagged sample is evaluated with respect to the B vertex instead of the* D^* *vertex.*

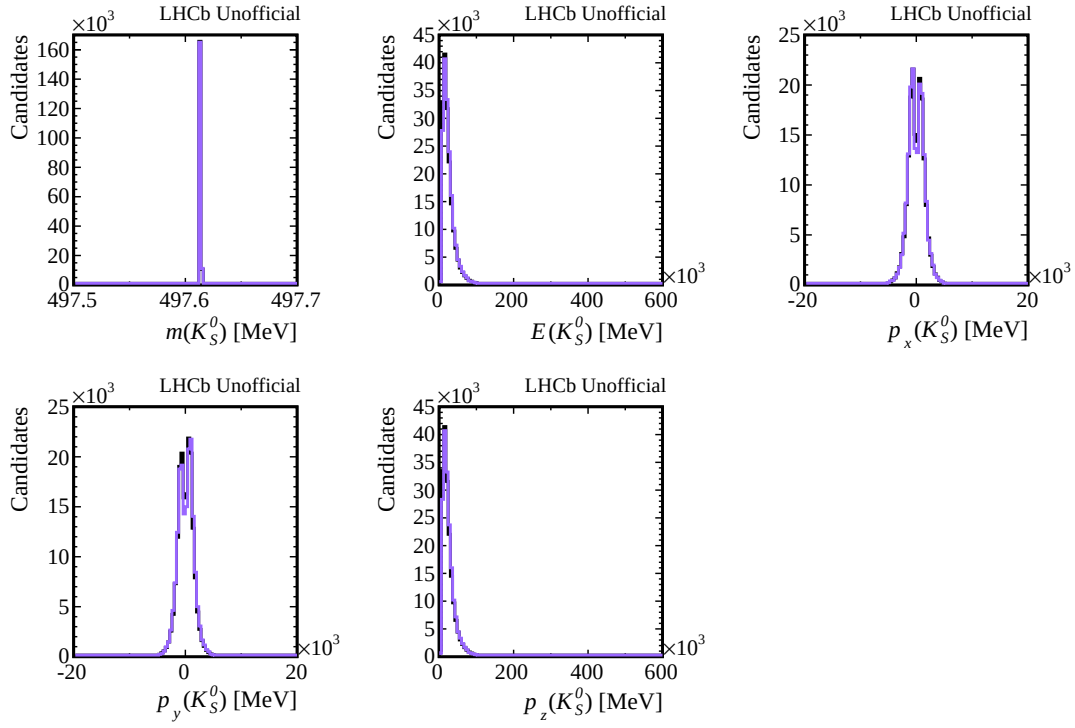

(a) *2012* $D^0 \to K^0_S(\mathrm{LL})\pi^+\pi^-$ *sample*

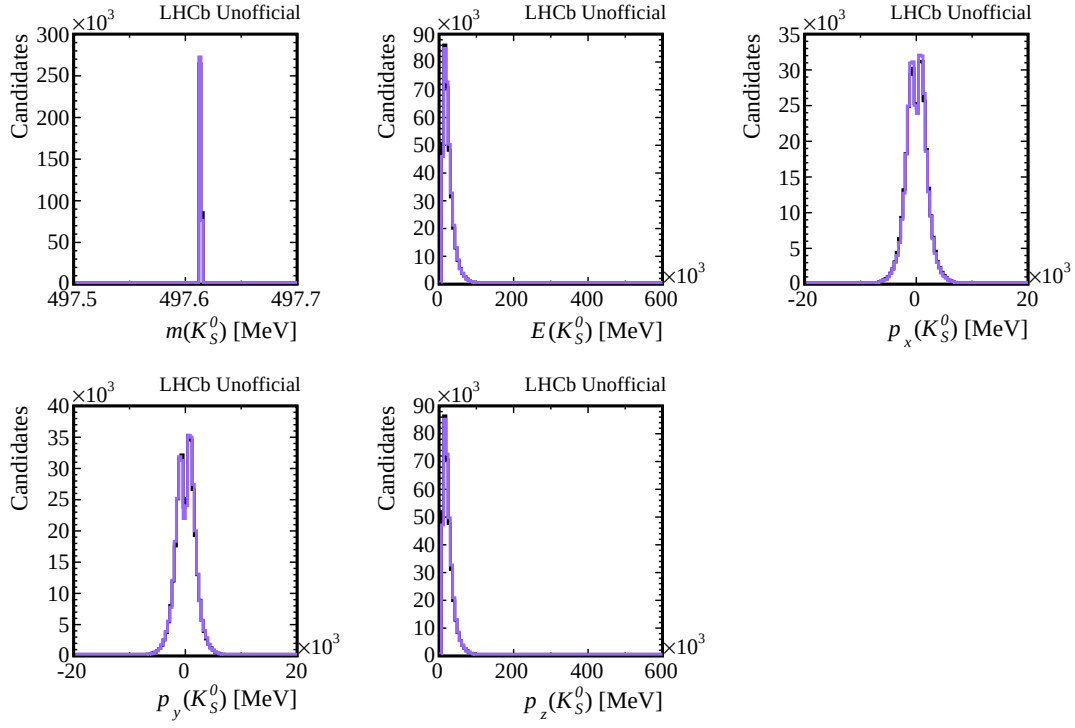

(b) *2012* $D^0 \to K^0_S(\mathrm{DD})\pi^+\pi^-$ *sample*

Figure E.2.: *Comparison of the* K^0_S *variables entering the phase-space acceptance calculation for single-tagged (black) and double-tagged (violet)* $D^0 \to K^0_S\pi^+\pi^-$ *datasets.*

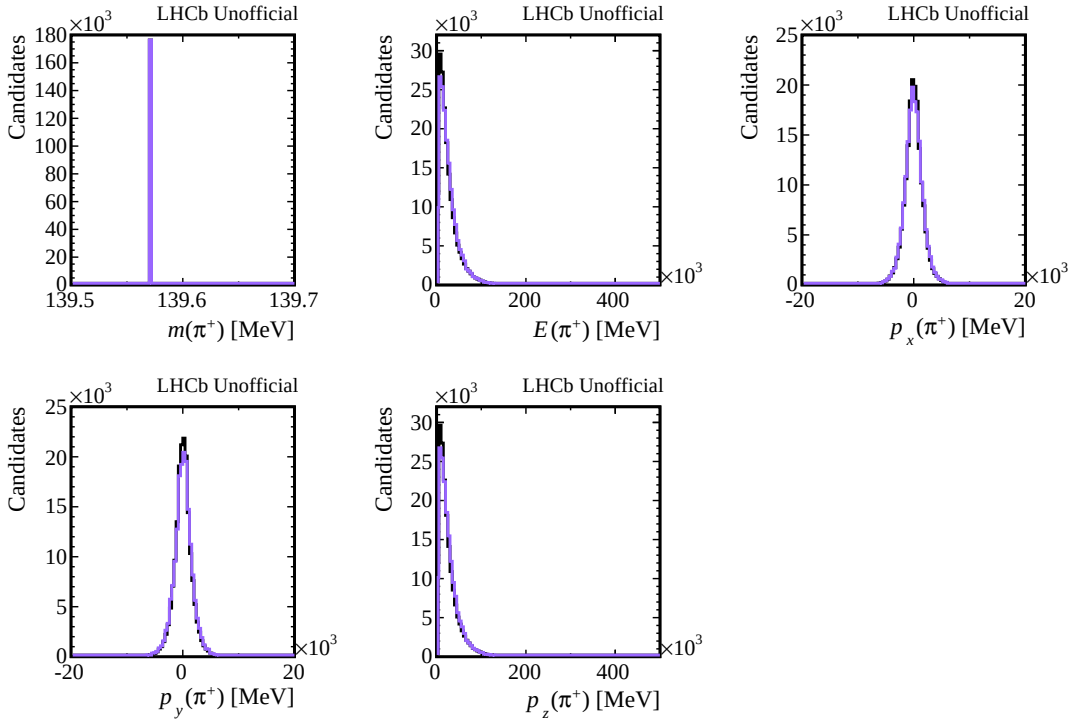

(a) *2012* $D^0 \to K^0_S(\mathrm{LL})\pi^+\pi^-$ *sample*

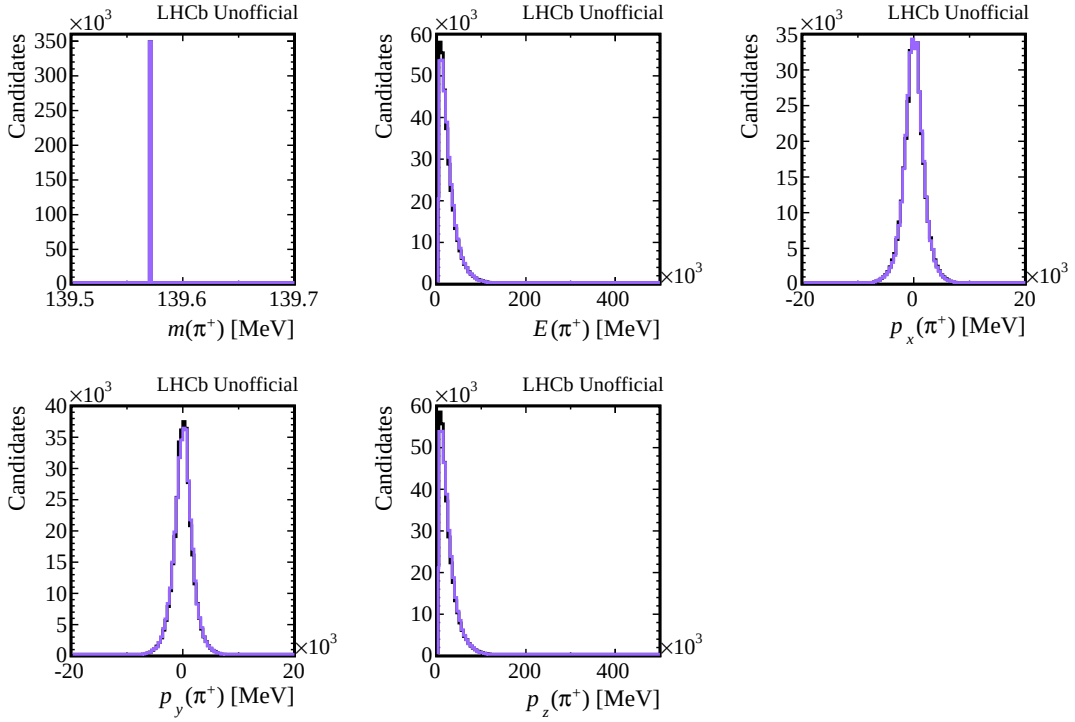

(b) *2012* $D^0 \to K^0_S(\mathrm{DD})\pi^+\pi^-$ *sample*

Figure E.3.: *Comparison of the* π^+ *variables entering the phase-space acceptance calculation for single-tagged (black) and double-tagged (violet)* $D^0 \to K^0_S\pi^+\pi^-$ *datasets.*

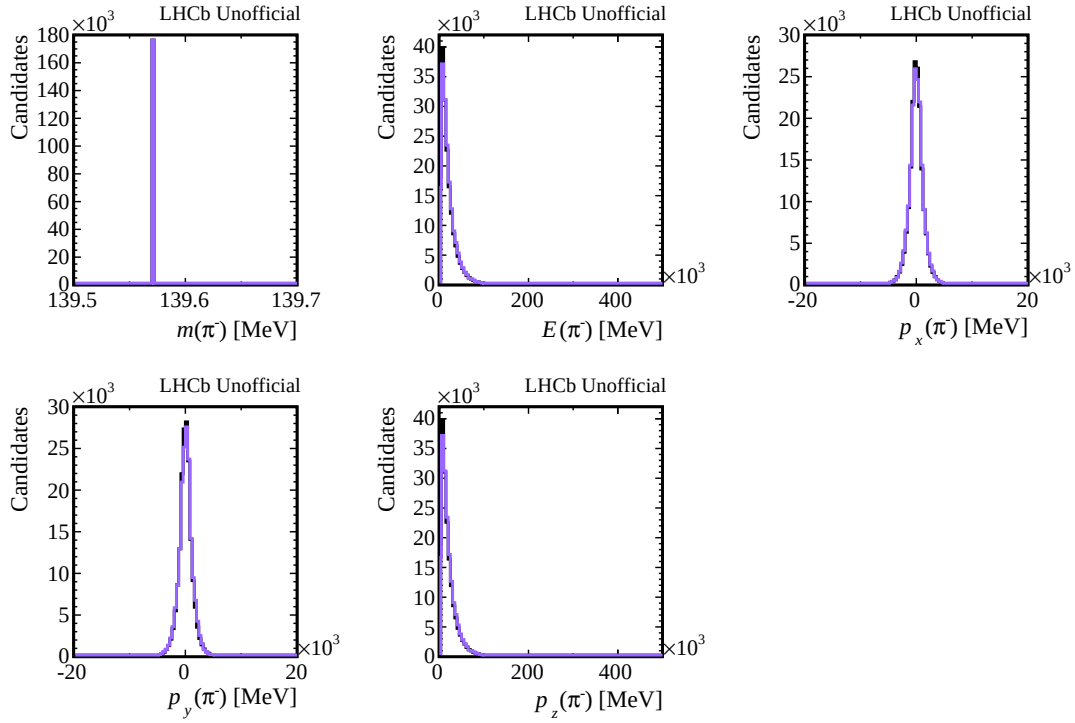

(a) *2012* $D^0 \to K^0_S(\mathrm{LL})\pi^+\pi^-$ *sample*

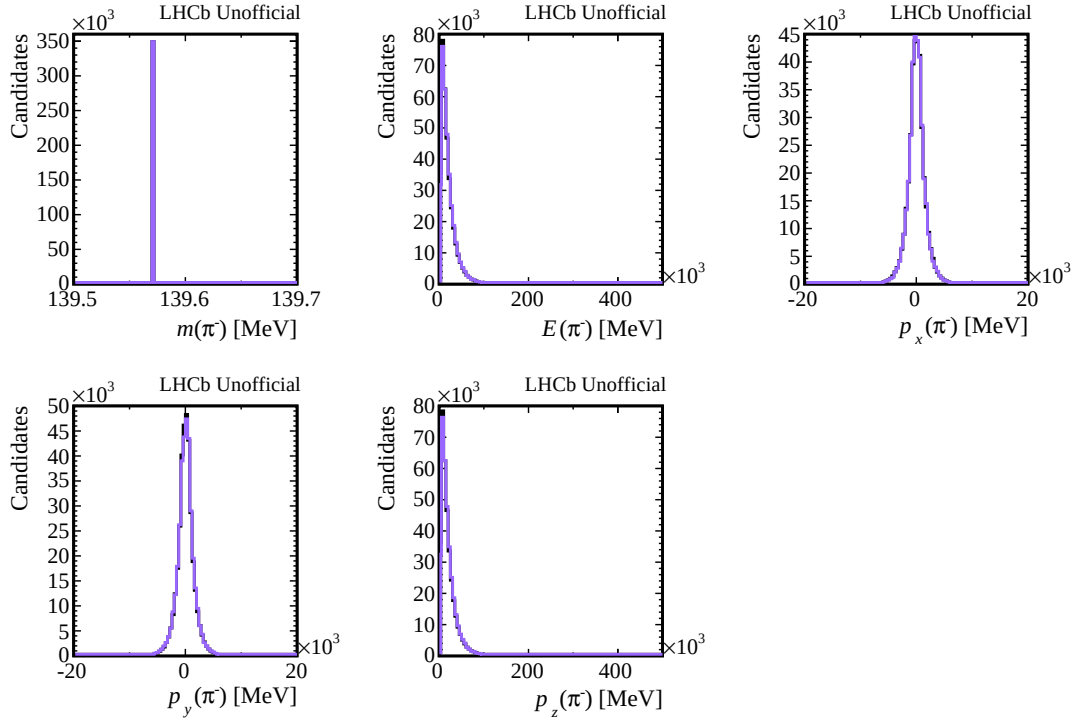

(b) *2012* $D^0 \to K^0_S(\mathrm{DD})\pi^+\pi^-$ *sample*

Figure E.4.: *Comparison of the* π^- *variables entering the phase-space acceptance calculation for single-tagged (black) and double-tagged (violet)* $D^0 \to K^0_S\pi^+\pi^-$ *datasets.*

F. Upper decay-time acceptance

The upper decay-time acceptance discussed in Chapt. 10.3 arises from the clone-killing in the tracking algorithm. Figure F.1 illustrates the tracking acceptance as function of the z-component of the shortest displacement vector between the particle's decay vertex and the nominal beam, d_z. The upper decay-time acceptance $\varepsilon_{\mathrm{UDT}}(t)$ for single-tagged decays is shown in Fig. F.2, and the double-tagged upper decay-time acceptance is illustrated in Fig. F.3.

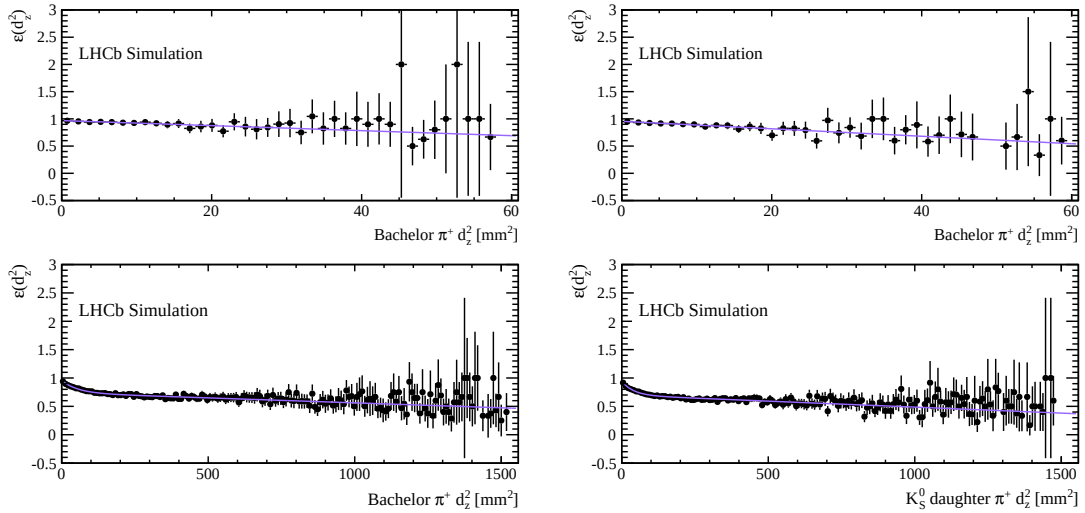

(a) *2011* **(b)** *2012*

Figure F.1.: *Tracking acceptance as a function of d_z^2 for the bachelor and K_S^0 daughter pions. The measured efficiencies (black) are overlaid with a fit according to Eqns. 10.8 and 10.9 (purple).*

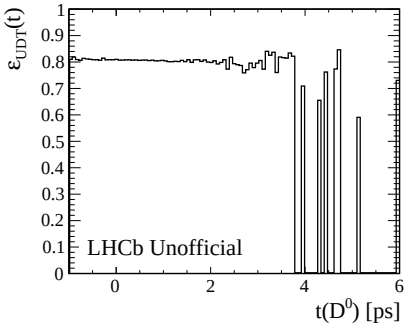

(a) *2011* K^0_S(LL)

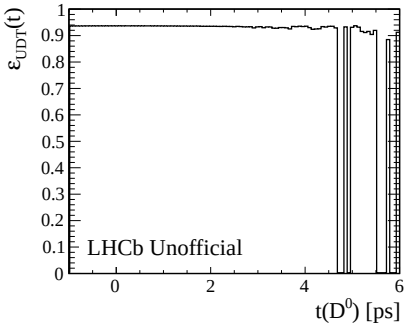

(b) *2011* K^0_S(DD)

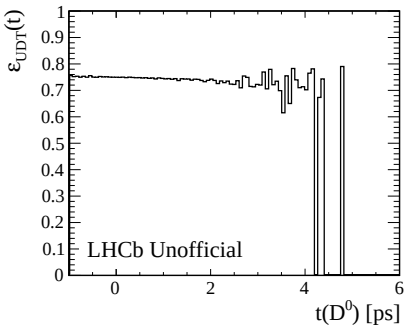

(c) *2012* K^0_S(LL)

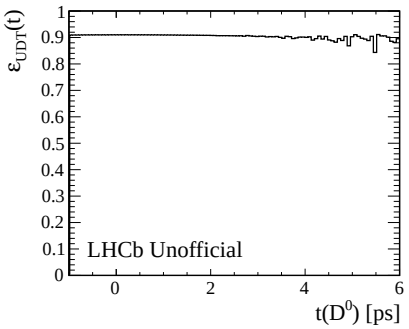

(d) *2012* K^0_S(DD)

Figure F.2.: *Upper decay time acceptance split by year and* K^0_S *type for* $B^- \to D^0(\to K^0_S\pi^+\pi^-)\mu^-\overline{\nu}_\mu$ *decays.*

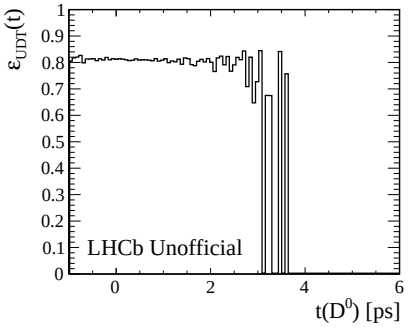

(a) *2011* K^0_S(LL)

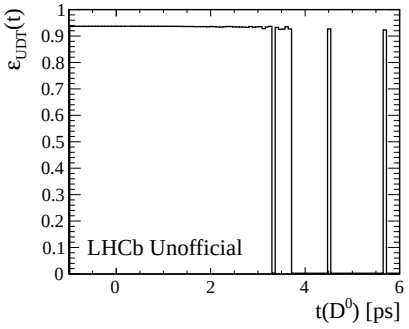

(b) *2011* K^0_S(DD)

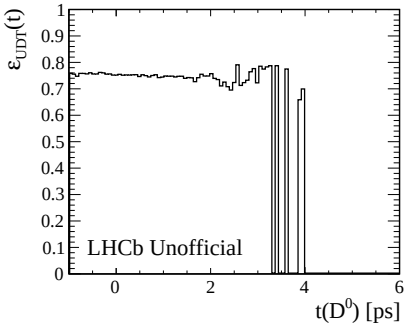

(c) *2012* K^0_S(LL)

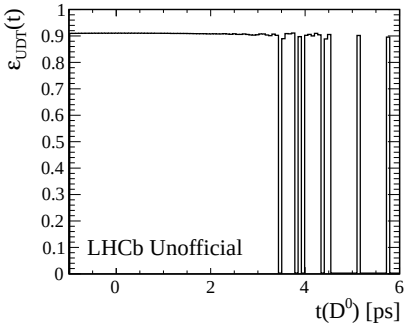

(d) *2012* K^0_S(DD)

Figure F.3.: *Upper decay time acceptance split by year and* K^0_S *type for* $\overline{B}^0 \to D^{*+}(\to D^0(\to K^0_S\pi^+\pi^-)\pi^+)\mu^-\overline{\nu}_\mu$ *decays.*

G. Convolution with decay time resolution

G.1. Convolution with decay time resolution for $T_{0,2}(t;\Gamma,y)\Theta(t)$

The convolution of terms $T_0(t;\Gamma,y) = e^{-\Gamma t}\cosh(y\Gamma t)$ and $T_2(t;\Gamma,y) = e^{-\Gamma t}\sinh(y\Gamma t)$ with a Gaussian resolution function is straightforward.

$$P_{0,2}(t';\Gamma,y,\mu,\sigma) = \int_0^{+\infty} T_{0,2}(t;\Gamma,y)G(t'-t;\mu,\sigma)\,\mathrm{d}t \tag{G.1}$$

$$= \int_0^{+\infty} e^{-\Gamma t}\begin{pmatrix}\cosh(y\Gamma t)\\ \sinh(y\Gamma t)\end{pmatrix} G(t'-t;\mu,\sigma)\,\mathrm{d}t \tag{G.2}$$

$$= \frac{1}{2}\int_0^{+\infty} e^{-\Gamma t}e^{y\Gamma t}G(t'-t;\mu,\sigma)\,\mathrm{d}t$$

$$\pm \frac{1}{2}\int_0^{+\infty} e^{-\Gamma t}e^{-y\Gamma t}G(t'-t;\mu,\sigma)\,\mathrm{d}t \tag{G.3}$$

$$\equiv \frac{1}{\sqrt{2\pi}\sigma}\left(\frac{I_{+y}\pm I_{-y}}{2}\right). \tag{G.4}$$

The integrals $I_{\pm y}$ are given by

$$I_{\pm y} = \int_0^{+\infty} e^{-\Gamma t(1\mp y)}e^{-\left(\frac{(t'-t)-\mu}{\sqrt{2}\sigma}\right)^2}\,\mathrm{d}t, \tag{G.5}$$

$$= \int_0^{+\infty} \exp\left(-\frac{t^2}{2\sigma^2} - t\left[\Gamma(1\mp y) - \frac{(t'-\mu)}{\sigma^2}\right] - \frac{1}{2\sigma^2}(t'-\mu)^2\right)\mathrm{d}t. \tag{G.6}$$

Integrals of the form

$$I(r,p,q) = \int_0^{+\infty} e^{-(rt^2+pt+q)}\,\mathrm{d}t, \tag{G.7}$$

can be simplified by a variable substitution. First, the term rt^2+pt+q is expressed as

$$rt^2+pt+q = \left(\sqrt{r}t + \frac{p}{2\sqrt{r}}\right)^2 + q - \left(\frac{p}{2\sqrt{r}}\right)^2 \tag{G.8}$$

$$\equiv u^2 + q - u_0^2, \tag{G.9}$$

with

$$u_0 \equiv \frac{p}{2\sqrt{r}}, \tag{G.10}$$

$$u \equiv \sqrt{r}t + \frac{p}{2\sqrt{r}} = \sqrt{r}t + u_0. \tag{G.11}$$

By using this substitution, the integral $I(r,q,p)$ becomes

$$I(r,p,q) = \int_0^{+\infty} e^{-(rt^2+pt+q)}\,\mathrm{d}t \tag{G.12}$$

$$= \frac{1}{\sqrt{r}} e^{-q+u_0^2} \int_{u_0}^{+\infty} e^{-u^2}\,\mathrm{d}u \tag{G.13}$$

$$= \frac{1}{\sqrt{r}} e^{-q+u_0^2} \frac{\sqrt{\pi}}{2} \mathrm{erfc}(u_0). \tag{G.14}$$

For the integrals $I_{\pm y}$, the substitutions are

$$r = \frac{1}{2\sigma^2}, \quad p = \Gamma(1 \mp y) - \frac{(t'-\mu)}{\sigma^2}, \quad q = \frac{1}{2\sigma^2}(t'-\mu)^2, \tag{G.15}$$

and lead to

$$u_0^{\pm y} = \frac{\sigma}{\sqrt{2}} \left(\Gamma(1 \mp y) - \frac{(t'-\mu)}{\sigma^2} \right), \tag{G.16}$$

$$u = \frac{t}{\sqrt{2}\sigma} + \frac{\sigma}{\sqrt{2}} \left(\Gamma(1 \mp y) - \frac{(t'-\mu)}{\sigma^2} \right). \tag{G.17}$$

The integrals are then

$$I_{\pm y} = \sigma \sqrt{\frac{\pi}{2}} e^{-q+(u_0^{\pm y})^2} \mathrm{erfc}(u_0^{\pm y}). \tag{G.18}$$

G.2. Convolution with decay time resolution for $T_{1,3}(t;\Gamma,x)\Theta(t)$

The convolution of terms $T_1(t;\Gamma,y) = e^{-\Gamma t}\cos(x\Gamma t)$ and $T_3(t;\Gamma,y) = e^{-\Gamma t}\sin(x\Gamma t)$ with a Gaussian resolution function uses the Taylor expansions

$$\cos(x\Gamma t) = 1 - \frac{(x\Gamma t)^2}{2!} + \mathcal{O}((x\Gamma t)^4), \tag{G.19}$$

$$\sin(x\Gamma t) = (x\Gamma t) - \frac{(x\Gamma t)^3}{3!} + \mathcal{O}((x\Gamma t)^5). \tag{G.20}$$

The convolution integrals are given by

$$P_{1,3}(t';\Gamma,x,\mu,\sigma) = \int_0^{+\infty} T_{1,3}(t;\Gamma,y)G(t'-t;\mu,\sigma)\,\mathrm{d}t \tag{G.21}$$

$$= \int_0^{+\infty} e^{-\Gamma t}\begin{pmatrix}\cos(x\Gamma t)\\ \sin(x\Gamma t)\end{pmatrix} G(t'-t;\mu,\sigma)\,\mathrm{d}t \tag{G.22}$$

$$\approx \frac{1}{\sqrt{2\pi}\sigma}\int_0^{+\infty} e^{-\Gamma t}\begin{pmatrix}1-(x\Gamma t)^2/2\\ x\Gamma t-(x\Gamma t)^3/6\end{pmatrix} e^{-\left(\frac{(t'-t)-\mu}{\sqrt{2}\sigma}\right)^2}\,\mathrm{d}t. \tag{G.23}$$

The integral $P_1(t';\Gamma,x,\mu,\sigma)$ is written as

$$P_1(t';\Gamma,x,\mu,\sigma) = \frac{1}{\sqrt{2\pi}\sigma}\int_0^{+\infty}\left(1-(x\Gamma t)^2/2\right)e^{-\Gamma t}e^{-\left(\frac{(t'-t)-\mu}{\sqrt{2}\sigma}\right)^2}\,\mathrm{d}t \tag{G.24}$$

$$= \frac{1}{\sqrt{2\pi}\sigma}\left(\int_0^{+\infty} e^{-\Gamma t}e^{-\left(\frac{(t'-t)-\mu}{\sqrt{2}\sigma}\right)^2}\,\mathrm{d}t - \frac{1}{2}\int_0^{+\infty}(x\Gamma t)^2 e^{-\Gamma t}e^{-\left(\frac{(t'-t)-\mu}{\sqrt{2}\sigma}\right)^2}\,\mathrm{d}t\right) \tag{G.25}$$

$$= \frac{1}{\sqrt{2\pi}\sigma}\left(I_{t0}-\frac{1}{2}I_{t2}\right), \tag{G.26}$$

and $P_3(t';\Gamma,x,\mu,\sigma)$ as

$$P_3(t';\Gamma,x,\mu,\sigma) = \frac{1}{\sqrt{2\pi}\sigma}\int_0^{+\infty}\left(x\Gamma t-(x\Gamma t)^3/6\right)e^{-\Gamma t}e^{-\left(\frac{(t'-t)-\mu}{\sqrt{2}\sigma}\right)^2}\,\mathrm{d}t \tag{G.27}$$

$$= \frac{1}{\sqrt{2\pi}\sigma}\left(\int_0^{+\infty} x\Gamma t e^{-\Gamma t}e^{-\left(\frac{(t'-t)-\mu}{\sqrt{2}\sigma}\right)^2}\,\mathrm{d}t - \frac{1}{6}\int_0^{+\infty}(x\Gamma t)^3 e^{-\Gamma t}e^{-\left(\frac{(t'-t)-\mu}{\sqrt{2}\sigma}\right)^2}\,\mathrm{d}t\right) \tag{G.28}$$

$$= \frac{1}{\sqrt{2\pi}\sigma}\left(I_{t1}-\frac{1}{6}I_{t3}\right), \tag{G.29}$$

where

$$I_{tn} = \int_0^{+\infty}(x\Gamma t)^n e^{-\Gamma t}e^{-\left(\frac{(t'-t)-\mu}{\sqrt{2}\sigma}\right)^2}\,\mathrm{d}t. \tag{G.30}$$

As previously, I_{tn} can be rewritten in the form

$$I_{tn}(r,p,q) = \int_0^{+\infty}(x\Gamma t)^n e^{-(rt^2+pt+q)}\,\mathrm{d}t. \tag{G.31}$$

The variables are substituted again by

$$rt^2 + pt + q = \left(\sqrt{r}t + \frac{p}{2\sqrt{r}}\right)^2 + q - \left(\frac{p}{2\sqrt{r}}\right)^2 \tag{G.32}$$

$$\equiv u^2 + q - u_0^2, \tag{G.33}$$

with

$$u_0 \equiv \frac{p}{2\sqrt{r}} \quad \text{and} \quad u \equiv \sqrt{r}t + \frac{p}{2\sqrt{r}} = \sqrt{r}t + u_0. \tag{G.34}$$

By using this substitution, the integral $I_{tn}(r,p,q)$ becomes

$$I_{tn}(r,p,q) = \int_0^{+\infty} (x\Gamma t)^n e^{-(rt^2+pt+q)}\,\mathrm{d}t \tag{G.35}$$

$$= \left(\frac{x\Gamma}{\sqrt{r}}\right)^n \frac{1}{\sqrt{r}} e^{-q+u_0^2} \int_{u_0}^{+\infty} (u-u_0)^n e^{-u^2}\,\mathrm{d}u. \tag{G.36}$$

The coefficients are

$$r = \frac{1}{2\sigma^2}, \quad p = \Gamma - \frac{(t'-\mu)}{\sigma^2}, \quad q = \frac{1}{2\sigma^2}(t'-\mu)^2. \tag{G.37}$$

In a next step, the integrals I_{tn} are written as

$$I_{t0} = \frac{1}{\sqrt{r}} e^{-q+u_0^2} \int_{u_0}^{+\infty} e^{-u^2}\,\mathrm{d}u, \tag{G.38}$$

$$I_{t1} = \left(\frac{x\Gamma}{\sqrt{r}}\right) \frac{1}{\sqrt{r}} e^{-q+u_0^2} \int_{u_0}^{+\infty} (u-u_0) e^{-u^2}\,\mathrm{d}u, \tag{G.39}$$

$$I_{t2} = \left(\frac{x\Gamma}{\sqrt{r}}\right)^2 \frac{1}{\sqrt{r}} e^{-q+u_0^2} \int_{u_0}^{+\infty} (u-u_0)^2 e^{-u^2}\,\mathrm{d}u, \tag{G.40}$$

$$I_{t3} = \left(\frac{x\Gamma}{\sqrt{r}}\right)^3 \frac{1}{\sqrt{r}} e^{-q+u_0^2} \int_{u_0}^{+\infty} (u-u_0)^3 e^{-u^2}\,\mathrm{d}u. \tag{G.41}$$

The terms $(u-u_0)^n$ are multiplied out and the integrals are split into sums, *e.g.*

$$I_{t0} = \frac{1}{\sqrt{r}} e^{-q+u_0^2} \int_{u_0}^{+\infty} e^{-u^2}\,\mathrm{d}u, \tag{G.42}$$

$$I_{t1} = \left(\frac{x\Gamma}{\sqrt{r}}\right) \frac{1}{\sqrt{r}} e^{-q+u_0^2} \left[\int_{u_0}^{+\infty} u e^{-u^2}\,\mathrm{d}u - u_0 \int_{u_0}^{+\infty} e^{-u^2}\,\mathrm{d}u\right], \tag{G.43}$$

$$I_{t2} = \left(\frac{x\Gamma}{\sqrt{r}}\right)^2 \frac{1}{\sqrt{r}} e^{-q+u_0^2} \left[\int_{u_0}^{+\infty} u^2 e^{-u^2}\,\mathrm{d}u \right.$$
$$\left. -2u_0 \int_{u_0}^{+\infty} u e^{-u^2}\,\mathrm{d}u + u_0^2 \int_{u_0}^{+\infty} e^{-u^2}\,\mathrm{d}u\right], \tag{G.44}$$

$$I_{t3} = \left(\frac{x\Gamma}{\sqrt{r}}\right)^3 \frac{1}{\sqrt{r}} e^{-q+u_0^2} \left[\int_{u_0}^{+\infty} u^3 e^{-u^2}\,\mathrm{d}u - 3u_0 \int_{u_0}^{+\infty} u^2 e^{-u^2}\,\mathrm{d}u\right. \tag{G.45}$$
$$\left. +3u_0^2 \int_{u_0}^{+\infty} u e^{-u^2}\,\mathrm{d}u - u_0^3 \int_{u_0}^{+\infty} e^{-u^2}\,\mathrm{d}u\right]. \tag{G.46}$$

The remaining integrals are all integrals of moments of the Gaussian function given by

$$I_{g0}(u_0) = \int_{u_0}^{+\infty} e^{-u^2}\,\mathrm{d}u = \frac{\sqrt{\pi}}{2}\mathrm{erfc}(u_0), \tag{G.47}$$

$$I_{g1}(u_0) = \int_{u_0}^{+\infty} u e^{-u^2}\,\mathrm{d}u = \frac{1}{2} e^{-u_0^2}, \tag{G.48}$$

$$I_{g2}(u_0) = \int_{u_0}^{+\infty} u^2 e^{-u^2}\,\mathrm{d}u = \frac{1}{2}\left(u_0 e^{-u_0^2} + \frac{\sqrt{\pi}}{2}\mathrm{erfc}(u_0)\right), \tag{G.49}$$

$$I_{g3}(u_0) = \int_{u_0}^{+\infty} u^3 e^{-u^2}\,\mathrm{d}u = \frac{1}{2} e^{-u_0^2}(u_0^2+1), \tag{G.50}$$

and thus, the integrals I_{tn} are

$$I_{t0} = \frac{1}{\sqrt{r}} e^{-q+u_0^2} I_{g0}(u_0), \tag{G.51}$$

$$I_{t1} = \left(\frac{x\Gamma}{\sqrt{r}}\right) \frac{1}{\sqrt{r}} e^{-q+u_0^2} \left[I_{g1}(u_0) - u_0 I_{g0}(u_0)\right], \tag{G.52}$$

$$I_{t2} = \left(\frac{x\Gamma}{\sqrt{r}}\right)^2 \frac{1}{\sqrt{r}} e^{-q+u_0^2} \left[I_{g2}(u_0) - 2u_0 I_{g1}(u_0) + u_0^2 I_{g0}(u_0)\right], \tag{G.53}$$

$$I_{t3} = \left(\frac{x\Gamma}{\sqrt{r}}\right)^3 \frac{1}{\sqrt{r}} e^{-q+u_0^2} \left[I_{g3}(u_0) - 3u_0 I_{g2}(u_0) + 3u_0^2 I_{g1}(u_0) - u_0^3 I_{g0}(u_0)\right]. \tag{G.54}$$

H. Comparison of the amplitudes for the direct CP violation search

The real and imaginary parts of the amplitudes obtained from separate time-integrated fits to D^0 and $\overline{D}^0$ data are listed in Table H.1. As can be seen from Table H.1, significant disagreement between some of the amplitudes is observed. A study presented in Chapt. 14.1 shows that the disagreement is cause by the σ_2 resonance and that by fixing the amplitude of this resonance, no evidence for direct CP violation is observed.

Table H.1.: *Results of a time-integrated fit on the amplitude model for D^0 and $\overline{D}^0$ decays to test for direct CP violation.*

Fit parameter	D^0 dataset	$\overline{D}^0$ dataset
$\mathcal{R}e[\rho(770)]$	1	1
$\mathcal{I}m[\rho(770)]$	0	0
$\mathcal{R}e[\sigma_1]$	-2.050 ± 0.033	-1.839 ± 0.032
$\mathcal{I}m[\sigma_1]$	-1.354 ± 0.042	-1.394 ± 0.040
$\mathcal{R}e[\omega(782)]$	-0.031 ± 0.002	-0.035 ± 0.002
$\mathcal{I}m[\omega(782)]$	0.065 ± 0.001	0.065 ± 0.001
$\mathcal{R}e[f_0(980)]$	-0.364 ± 0.015	0.137 ± 0.011
$\mathcal{I}m[f_0(980)]$	-0.802 ± 0.012	-0.385 ± 0.012
$\mathcal{R}e[\sigma_2]$	-0.555 ± 0.016	-0.420 ± 0.014
$\mathcal{I}m[\sigma_2]$	-0.110 ± 0.015	-0.190 ± 0.015
$\mathcal{R}e[f_2(1270)]$	0.435 ± 0.011	0.443 ± 0.013
$\mathcal{I}m[f_2(1270)]$	0.046 ± 0.012	0.182 ± 0.013
$\mathcal{R}e[f_0(1370)]$	1.422 ± 0.164	3.214 ± 0.165
$\mathcal{I}m[f_0(1370)]$	1.672 ± 0.140	1.600 ± 0.136
$\mathcal{R}e[\rho(1450)]$	-1.410 ± 0.035	-1.535 ± 0.037
$\mathcal{I}m[\rho(1450)]$	1.064 ± 0.048	1.070 ± 0.046
$\mathcal{R}e[f_0(1500)]$	-3.985 ± 0.320	-4.594 ± 0.311
$\mathcal{I}m[f_0(1500)]$	1.746 ± 0.346	-0.966 ± 0.355
$\mathcal{R}e[K^*(892)^+]$	0.163 ± 0.005	0.168 ± 0.005
$\mathcal{I}m[K^*(892)^+]$	-0.092 ± 0.004	-0.081 ± 0.004
$\mathcal{R}e[K_0^*(1430)^+]$	0.181 ± 0.030	0.475 ± 0.032
$\mathcal{I}m[K_0^*(1430)^+]$	-0.001 ± 0.033	0.155 ± 0.038
$\mathcal{R}e[K_2^*(1430)^+]$	0.045 ± 0.018	0.133 ± 0.019
$\mathcal{I}m[K_2^*(1430)^+]$	0.185 ± 0.019	-0.121 ± 0.018
$\mathcal{R}e[K^*(892)^-]$	-1.616 ± 0.014	-1.662 ± 0.013
$\mathcal{I}m[K^*(892)^-]$	1.018 ± 0.014	0.979 ± 0.015

$\mathcal{R}e[K_0^*(1430)^-]$	3.326 ± 0.042	3.389 ± 0.039
$\mathcal{I}m[K_0^*(1430)^-]$	0.613 ± 0.043	1.070 ± 0.045
$\mathcal{R}e[K_2^*(1430)^-]$	1.040 ± 0.022	1.204 ± 0.020
$\mathcal{I}m[K_2^*(1430)^-]$	-0.617 ± 0.025	-4.637 ± 0.026
$\mathcal{R}e$[non-resonant]	-2.878 ± 0.233	-4.289 ± 0.243
$\mathcal{I}m$[non-resonant]	0.483 ± 0.221	0.199 ± 0.216

I. Parameters of the nominal amplitude model

The parameters of the nominal amplitude fit, which is used to extract the mixing parameters reported in Chapt. 14.2, are listed in Table I.1.

Table I.1.: *Results of the nominal amplitude fit. For each contribution to the isobar model given in Table 11.4, the results of the real and imaginary parts of the resonance as well as their masses and widths are listed. The masses of the $\rho(770)$, $\omega(782)$, $f_0(980)$, $f_2(1270)$, and the width of the $f_2(1270)$ are fixed to the reference values reported in [11].*

Contribution	$\mathcal{R}e$	$\mathcal{I}m$	$m\,[\,\mathrm{GeV}]$	$\Gamma\,[\,\mathrm{GeV}]$
$\rho(770)$	1	0	0.775	0.142 ± 0.002
σ_1	-1.89 ± 0.02	-1.43 ± 0.03	0.528 ± 0.003	0.503 ± 0.007
$\omega(782)$	-0.021 ± 0.001	0.056 ± 0.001	0.783	0.016 ± 0.001
$f_0(980)$	0.10 ± 0.01	-0.05 ± 0.01	0.990	0.058 ± 0.003
σ_2	-0.48 ± 0.01	-1.64 ± 0.01	1.028 ± 0.002	0.083 ± 0.004
$f_2(1270)$	0.50 ± 0.01	0.23 ± 0.01	1.275	0.185
$f_0(1370)$	1.85 ± 0.15	1.6 ± 0.1	1.345 ± 0.007	0.32 ± 0.02
$\rho(1450)$	-1.53 ± 0.03	1.31 ± 0.04	1.55 ± 0.02	0.43 ± 0.05
$f_0(1500)]$	-4.5 ± 0.2	2.1 ± 0.2	1.53 ± 0.01	0.12 ± 0.02
$K^*(892)^+$	0.184 ± 0.004	-0.078 ± 0.003	0.8943 ± 0.0002	0.0484 ± 0.0004
$K_0^*(1430)^+$	0.57 ± 0.02	0.425 ± 0.029	1.425 ± 0.002	0.259 ± 0.004
$K_2^*(1430)^+$	1.69 ± 0.01	-0.07 ± 0.01	1.43 ± 0.01	0.092 ± 0.005
$K^*(892)^-$	-1.68 ± 0.01	1.02 ± 0.01	0.8943 ± 0.0002	0.0484 ± 0.0004
$K_0^*(1430)^-$	3.69 ± 0.03	1.02 ± 0.03	1.425 ± 0.002	0.259 ± 0.004
$K_2^*(1430)^-$	1.08 ± 0.01	-0.51 ± 0.02	1.43 ± 0.01	0.092 ± 0.005
non-resonant	-2.9 ± 0.2	-1.5 ± 0.2	$\times$	$\times$

Bibliography

[1] Muller, F. and others, "Regeneration and mass difference of neutral K mesons," *Phys. Rev. Lett.* **4** (1960) 418–421.

[2] **The ARGUS Collaboration**, Albrecht, H. and others, "Observation of B^0- $\overline{B}^0$ mixing," *Phys. Lett. B* **192** (1987) 245–252.

[3] **The CDF Collaboration**, Abulencia, A. and others, "Observation of B_s^0-$\overline{B}_s^0$ oscillation," *Phys. Rev. Lett.* **97** (2006) 242003.

[4] **The BaBar Collaboration**, Aubert, B. and others, "Evidence for D^0-$\overline{D}^0$ mixing," *Phys. Rev. Lett.* **98** (2007) 211802.

[5] **The Belle Collaboration**, Staric, M. and others, "Evidence for D^0-$\overline{D}^0$ mixing," *Phys. Rev. Lett.* **98** (2007) 211803.

[6] Bianco, S. and Fabbri, F. L., "A cicerone for the physics of charm," *Riv. Nuovo Cim.* **26N7** (2003) 1–200.

[7] Bobrowski, M., Lenz, A., Riedl, J. and Rohrwild, J., "How large can the SM contribution to *CP* violation in D^0-$\overline{D}^0$ mixing be?," *JHEP* **03** (2010) 009.

[8] Manohar, A. V. and Wise, M. B., *Heavy quark physics*. Cambridge University Press, 2000.

[9] **Heavy Flavor Averaging Group**, Amhis, Y. and others, "Averages of b-hadron, c-hadron, and τ-lepton properties as of summer 2014," `arXiv:1412.7515 [hep-ex]`. Updated results and plots available at `http://www.slac.stanford.edu/xorg/hfag/`.

[10] Halzen, F. and Martin, A. D., *Quarks and leptons: an introductory course in modern particle physics*. John Wiley & Sons, 1984.

[11] **Particle Data Group**, Olive, K. A. and others, "2014 review of particle physics," *Chin. Phys.* **C38** (2014) 090001.

[12] Glashow, S. L., "Partial symmetries of weak interactions," *Nucl. Phys.* **22** (1961) 579–588.

[13] Salam, A., "Renormalizability of gauge theories," *Phys. Rev.* **127** (1962) 331–334.

[14] Weinberg, S., "A model of leptons," *Phys. Rev. Lett.* **19** (1967) 1264–1266.

[15] Englert, F. and Brout, R., "Broken symmetry and the mass of gauge vector mesons," *Phys. Rev. Lett.* **1964** (13) 321–323.

[16] Higgs, P. W., "Broken symmetries and the masses of gauge bosons," *Phys. Rev. Lett.* **1964** (13) 508–509.

[17] **The ATLAS Collaboration**, Aad G. and others, "Observation of a new particle in the search for the Standard Model Higgs boson with the ATLAS detector at the LHC," *Phys. Lett. B* **716** (2012) 1–29.

[18] **The CMS Collaboration**, Chatrchyan S. and others, "Observation of a new boson at a mass of 125 GeV with the CMS experiment at the LHC," *Phys. Lett. B* **716** (2012) 30.

[19] **The ATLAS and CMS Collaborations**, Aad G. and others, "Combined measurement of the Higgs boson mass in pp collisions at $\sqrt{s} = 7$ and 8 TeV with the ATLAS and CMS experiments," *Phys. Rev. Lett.* **114** (2015) 191803.

[20] Maki, Z., Nakagawa, M. and Sakata, S., "Remarks on the unified model of elementary particles," *Prog. Theor. Phys.* **28** (1962) 870–880.

[21] Pontecorvo, B., "Mesonium and anti-mesonium," *Sov. Phys. JETP* **6** (1957) 429.

[22] Pontecorvo, B., "Inverse beta processes and nonconservation of lepton charge," *Sov. Phys. JETP* **7** (1958) 172–173.

[23] Fukuda, Y. and others, "Evidence for oscillation of atmospheric neutrinos," *Phys. Rev. Lett.* **81** (1998) 1562–1567.

[24] **The SNO Collaboration**, Ahmad, Q. R. and others, "Measurement of the rate of $\nu_e + d \rightarrow p + p + e^-$ interactions produced by ^8B solar neutrinos at the Sudbury Neutrino Observatory," *Phys. Rev. Lett.* **87** (2001) 071301.

[25] **The SNO Collaboration**, Ahmad, Q. R. and others, "Direct evidence for neutrino flavor transformation from neutral-current interactions in the Sudbury Neutrino Observatory," *Phys. Rev. Lett.* **89** (2002) 011301.

[26] Cabibbo, N., "Unitary symmetry and leptonic decays," *Phys. Rev. Lett.* **10** (1963) 531–533.

[27] Kobayashi, M. and Maskawa, T., "*CP* violation in the renormalizable theory of weak interaction," *Prog. Theo. Phys.* **49** (1973) 652 – 657.

[28] Glashow, S. L., Iliopoulos, J. and Maiani, L., "Weak interactions with lepton-hadron symmetry," *Phys. Rev. D* **2** (1970) 1285.

[29] Wolfenstein, L., "Parametrization of the Kobayashi-Maskawa Matrix," *Phys. Rev. Lett.* **51** (1983) 1945.

[30] **The LHCb Collaboration**, Aaij, R. and others, "Observation of the resonant character of the $Z(4430)^-$ state," *Phys. Rev. Lett.* **112** (2014) 222002.

[31] **The Belle Collaboration**, Choi, S. K. and others, "Observation of a resonance-like structure in the $\pi^\pm\psi'$ mass distribution in exclusive $B \rightarrow K\pi^\pm\psi'$ decays," *Phys. Rev. Lett.* **100** (2008) 142001.

[32] **The LHCb Collaboration**, Aaij, R. and others, "Observation of $J/\psi p$ resonances consistent with pentaquark states in $\Lambda_b^0 \to J/\psi K^- p$ decays," *Phys. Rev. Lett.* **115** (2015) 072001.

[33] Sozzi, M. S., *Discrete symmetries and CP violation: from experiment to theory*. Oxford University Press, 2008.

[34] Bevan, A. J., "C, P, and CP asymmetry observables based on triple product asymmetries," 2014.

[35] Durieux, G. and Grossman, Y., "Probing CP violation systematically in differential distributions," *Phys. Rev. D* **92** (2015) 076013.

[36] **The CDF Collaboration**, Aaltonen, T. and others, "Measurement of CP-violation asymmetries in $D^0 \to K^0_S \pi^+ \pi^-$," *Phys. Rev. D* **86** (2012) 032007.

[37] **The LHCb Collaboration**, Aaij, R. and others, "Model-independent measurement of mixing parameters in $D^0 \to K^0_S \pi^+ \pi^-$ decays," *Submitted to JHEP* (2015) , `arXiv:1510.01664 [hep-ex]`.

[38] **The CLEO Collaboration**, Asner, D. M. and others, "Search for D^0-$\overline{D}^0$ mixing in the Dalitz plot analysis of $D^0 \to K^0_S \pi^+ \pi^-$," *Phys. Rev. D* **72** no. 012001, (2005) .

[39] **The BaBar Collaboration**, del Amo Sanchez, P. and others, "Measurement of D^0-$\overline{D}^0$ mixing parameters using $D^0 \to K^0_S \pi^+ \pi^-$ and $D^0 \to K^0_S K^+ K^-$ decays," *Phys. Rev. Lett.* **105** (2010) 081803.

[40] **The Belle Collaboration**, Zhang, L. M. and others, "Measurement of D^0-$\overline{D}^0$ mixing in $D^0 \to K^0_S \pi^+ \pi^-$ decays," *Phys. Rev. Lett.* **99** (2007) 131803.

[41] **The Belle Collaboration**, Peng, T. and others, "Measurement of D^0-$\overline{D}^0$ mixing and search for indirect CP violation using $D^0 \to K^0_S \pi^+ \pi^-$ decays," *Phys. Rev. D* **89** (2014) 091103.

[42] **The CLEO Collaboration**, Libby, J. and others, "Model-independent determination of the strong-phase difference between D^0 and $\overline{D}^0 \to K^0_{S,L} h^+ h^-$ ($h = \pi, K$) and its impact on the measurement of the CKM angle γ/ϕ_3," *Phys. Rev. D* **82** (2010) 112006.

[43] Global fit for D^0-$\overline{D}^0$ mixing allowing for CP violation, "`http://www.slac.stanford.edu/xorg/hfag/charm/CHARM15/results_mix_cpv.html`.".

[44] Gersabeck, M. Private communication.

[45] Brüning, O. S. and others, "LHC design report: the LHC main ring," , CERN, DOI: 10.5170/CERN-2004-003-V-1, 2004.

[46] Brüning, O. S. and others, "LHC design report: the LHC infrastructure and general services," , CERN, DOI: 10.5170/CERN-2004-003-V-2, 2004.

[47] Benedikt, M. and others, "LHC design report: the LHC injector chain," , CERN, DOI: 10.5170/CERN-2004-003-V-3, 2004.

[48] Evans, L. and Bryant, P. (editors), "LHC machine," *JINST* **3** (2008) S08001.

[49] **The TOTEM Collaboration**, Anelli, G. and others, "The TOTEM experiment at the CERN Large Hadron Collider," *JINST* **3** (2008) S08007.

[50] **The LHCf Collaboration**, Adriani, O. and others, "The LHCf detector at the CERN Large Hadron Collider," *JINST* **3** (2008) S08006.

[51] Pinfold, J. L., "The MoEDAL experiment - a new light on LHC physics," *EPJ Web Conf.* **95** (2015) .

[52] The CERN accelerator complex, "`http://cds.cern.ch/record/1260465`.".

[53] Schematic diagram of the LHC sectors, "`https://cds.cern.ch/record/1706606`.".

[54] **The LHCb Collaboration**, Aaij, R. and others, "LHCb detector performance," *Int. J. Mod. Phys. A* **30** (2015) 1530022.

[55] **The LHCb Collaboration**, Alves Jr., A. A. and others, "The LHCb detector at the LHC," *JINST* **3** (2008) S08005.

[56] The LHCb detector, "`https://cds.cern.ch/record/1087860`.".

[57] **The LHCb VELO Group**, Aaij, R. and others, "Performance of the LHCb Vertex Locator," *JINST* **9** (2014) P09007.

[58] VELO conference plots,
"`https://lbtwiki.cern.ch/pub/VELO/VELOConferencePlots/`.".

[59] **The LHCb Silicon Tracker Group**, Elsasser, C. and others, "The LHCb Silicon Tracker," *JINST* **9** no. 01, (2014) C01009.

[60] **The LHCb Outer Tracker Group**, Arink, R. and others, "Performance of the LHCb Outer Tracker," *JINST* **9** (2014) P01002.

[61] **The LHCb RICH Group**, Adolfini, M. and others, "Performance of the LHCb RICH detector at the LHC," *Eur. Phys. J.* **C 73** (2013) 2431.

[62] RICH pictures and figures,
"`https://twiki.cern.ch/twiki/bin/view/LHCb/RICHPicturesAndFigures`.".

[63] Machikhiliyan, I. on behalf of the LHCb Collaboration, "The LHCb electromagnetic calorimeter," *J. Phys. Conf. Ser.* **160** (2009) 012047.

[64] Perret, P. and Vilasís-Cardona, X. on behalf of the LHCb Collaboration, "Performance of the LHCb calorimeters during the period 2010-2012," *Journal of Physics: Conference Series* **587** no. 1, (2015) 012012.

[65] **The LHCb MuonID Group**, Archilli, F. and others, "Performance of the muon identification at LHCb," *JINST* **8** (2013) P10020.

[66] LHCb trigger schemes,
"`http://lhcb.web.cern.ch/lhcb/speakersbureau/html/TriggerScheme.html`.".

[67] **The LHCb Collaboration**, Aaij, R. and others, "Letter of Intent for the LHCb Upgrade," *CERN-LHCC-2011-001* (2011) .

[68] **The LHCb Collaboration**, Alves Jr., A. A. and others, "LHCb Tracker upgrade technical design report," *CERN-LHCC-2014-001* (2014) .

[69] **The LHCb Collaboration**, Aaij, R. and others, "LHCb VELO Upgrade Technical Design Report," *CERN-LHCC-2013-021* (2013) .

[70] Hulsbergen, W. D., "The VELO upgrade RF shield," in *Forum on Tracking Detector Mechanics*. 2015.

[71] Cid Vidal, X., "Radiation hard pixel development for the LHCb VELO upgrade," in 10^{th} *International Hiroshima Symposium on the Development and Application of Semiconductor Tracking Detectors*. 2015.

[72] Illustration of the parallel bubblesort algorithm, "`http://www.massey.ac.nz/~mjjohnso/notes/59735/myslides8.pdf`.".

[73] Pivk, M. and Le Diberder, F. R., "sPlot: a statistical tool to unfold data distributions," *Nucl.Instrum.Meth.* **A555** (2005) 356–369.

[74] Hulsbergen, W. D., "Decay chain fitting with a Kalman filter," *Nucl.Instrum.Meth.* **A552** (2005) 566–575.

[75] Clemencic, M and others, "The LHCb simulation application, Gauss: design, evolution and experience," *J. Phys. Conf. Ser.* **331** (2011) 032023.

[76] Sjöstrand, T., Mrenna, S. and Skands, P., "PYTHIA 6.4 physics and manual," *JHEP* **05** (2006) 026.

[77] Sjöstrand, T., Mrenna, S. and Skands, P., "A brief introduction to PYTHIA 8.1," *Comput.Phys.Commun.* **178** (2008) 852–867.

[78] Lange, D. J., "The EvtGen particle decay simulation package," *Nucl. Instrum. Meth.* **A462** (2001) 152–155.

[79] Golonka, P. and Was, Z., "PHOTOS Monte Carlo: a precision tool for QED corrections in Z and W decays," *Eur.Phys.J.* **C45** (2006) 97–107.

[80] **Geant4 collaboration**, Agostinelli, S. and others, "Geant4: a simulation toolkit," *Nucl. Instrum. Meth.* **A506** (2003) 250.

[81] **Geant4 collaboration**, Allison, J., Amako, K., Apostolakis, J., Araujo, H., Dubois, P. A. and others, "Geant4 developments and applications," SLAC-PUB-11870, *IEEE Trans.Nucl.Sci.* **53** (2006) 270.

[82] Gligorov, V. V. and Williams, M., "Efficient, reliable and fast high-level triggering using a bonsai boosted decision tree," *JINST* **8** (2013) P02013.

[83] Puig, A., "The LHCb trigger in 2011 and 2012," LHCb-PUB-2014-046. CERN-LHCb-PUB-2014-046, CERN, 2014.

[84] Van Tilburg, J., *Track simulation and reconstruction in LHCb.* PhD thesis, University of Amsterdam, 2005.

[85] Hocker, A., Stelzer, J., Tegenfeldt, F., Voss, H., Voss, K. and others, "TMVA - Toolkit for Multivariate Data Analysis," CERN-OPEN-2007-007, *PoS* **ACAT** (2007) 040, `arXiv:physics/0703039 [PHYSICS]`.

[86] Skwarnicki, T., *A study of the radiative CASCADE transitions between the Upsilon-Prime and Upsilon resonances.* PhD thesis, Cracow, INP, 1986.

[87] Justel, A., Pen~na, D. and Zamar, R., "A multivariate Kolmogorov-Smirnov test of goodness of fit," *Statistics and Probability Letters* **35** (1997) 3.

[88] **The LHCb Collaboration**, Aaij, R. and others, "Prompt charm production in pp collisions at $\sqrt{s} = 7\,\text{TeV}$," *Nucl. Phys. B* **871** (2013) 1–20.

[89] **The LHCb Collaboration**, Aaij, R. and others, "B meson production cross-sections in proton-proton collisions at $\sqrt{s} = 7\,\text{TeV}$," *JHEP* **08** (2013) 117.

[90] **The LHCb Collaboration**, Aaij, R. and others, "Search for the lepton flavour violating decay $decay\tau^-\mu^-\mu^+\mu^-$," *JHEP* **02** (2014) 121.

[91] Poluektov, A., "Kernel density estimation of a multidimensional efficiency profile," *JINST* **10** (2015) P02011.

[92] Definition of reconstructed and reconstructible tracks, "`https://lhcb-comp.web.cern.ch/lhcb-comp/Analysis/DaVinci/v8/recrecdefinition.htm`.".

[93] **Particle Data Group**, Beringer, J. and others, "Review of particle physics," *Phys. Rev. D* **86** (2012) 010001. And 2013 partial update for the 2014 edition.

[94] **The CLEO Collaboration**, Kopp, S. and others, "Dalitz analysis of the decay $D^0 \to K^-\pi^+\pi^0$," *Phys. Rev. D* **83** (2001) 092001.

[95] Blatt, J. M. and Weisskopf, V. F., *Theoretical nuclear physics.* John Wiley & Sons, 1952.

[96] Von Hippel, F. and Quigg, C., "Centrifugal-barrier effects in resonance partial decay widths, shapes, and production amplitudes," *Phys. Rev. D* **5** (1972) 624.

[97] Pilkuhn, H., *The interactions of hadrons.* North-Holland, Amsterdam, 1967.

[98] Gounaris, G. J. and Sakurai, J. J., "Finite-width corrections to the vector-meson-dominance prediction for $\rho \to e^+e^-$," *Phys. Rev. Lett.* **21** (1968) 244.

[99] Aston, D. and others, "A study of $K^-\pi^+$ scattering in the reaction $K^-p \to K^-\pi^+n$ at $11\,\text{GeV}/c$," *Nuclear Physics* **B296** (1988) 493.

[100] Anisovich, V. V. and Sarantsev, A. V., "K-matrix analysis of the $(IJ^{PC} = 00^{++})$-wave in the mass region below $1900\,\text{MeV}$," *Eur. Phys. J.* **A16** (2003) 229–258.

[101] Klempt, E., Matveev, M. and Sarantsev, A. V., "Further study of D_s^+ decays into $\pi^-\pi^+\pi^+$," *Eur. Phys. J.* **C55** (2008) 39–50.

[102] The GooFit package, "`https://github.com/GooFit/GooFit`.".

[103] Andreassen, R.E. and others, "Implementation of a thread-parallel, GPU-friendly function evaluation library," *IEEE Access* **2** (2014) . `10.1109/ACCESS.2014.2306895`.

[104] Andreassen, R., Meadows, B. T., de Silva, M., Sokoloff, M. D. and Tomko, K., "GooFit: A library for massively parallelising maximum-likelihood fits," *Journal of Physics: Conference Series* **513** no. 5, (2014) 052003. `http://stacks.iop.org/1742-6596/513/i=5/a=052003`.

[105] Kagan, A. L. and Sokoloff, M. D., "On indirect *CP* violation and implications for D^0-$\overline{D}^0$ and B_s^0-$\overline{B}_s^0$ mixing," *Phys. Rev. D* **871** (2009) 076008.

[106] Dauncey, P. D., Kenzie, M., Wardle, N. and Davies, G. J., "Handling uncertainties in background shapes: the discrete profiling method," *JINST* **10** (2015) P04015.

[107] Stahl, S., van Tilburg, J., Gersabeck, E., Dijkstra, H., Ruf, T. and Vesterinen, M., "Search for *CP* violation in $D^0 \to K^-K^+\pi^+\pi^-$ using semileptonic B decays on 3 fb^{-1}," LHCb-ANA-2013-055. `https://cds.cern.ch/record/1556318`.

[108] The LHCb Collaboration, "Improved constraints on γ: CKM2014 update," *LHCB-CONF-2014-004* (2014) .

[109] Giri, A., Grossman, Y., Soffer, A. and Zupan, J., "Determining γ using $B^\pm \to DK^\pm$ with multibody D decays," *Phys. Rev. D* **68** (2003) 054018.

[110] **The LHCb Collaboration**, Aaij, R. and others, "Measurement of the CKM angle γ using $B^\pm \to DK^\pm$ with $D \to K^0_S\pi^+\pi^-, K^0_S K^+K^-$ decays," *JHEP* **10** (2014) 097.

[111] **The LHCb Collaboration**, Aaij, R. and others, "Measurement of *CP* violation and constraints on the CKM angle γ using $B^\pm \to DK^\pm$ with $D \to K^0_S\pi^+\pi^-, K^0_S K^+K^-$ decays," *Nucl. Phys. B* **888** (2014) 69 – 193.

[112] Gronau, M. and London, D., "How to determine all the angles of the unitarity triangle from $B^0 \to DK^0_S$ and $B^0_s \to D\phi$," *Phys. Lett. B* **253** (1991) 483.

[113] Gronau, M. and Wyler, D., "On determining a weak phase from charged B decay asymmetries," *Phys. Lett. B* **265** (1991) 172.

[114] Atwood, D., Dunietz, I. and Soni, A., "Enhanced *CP* Violation with $B \to KD^0(\overline{D}^0)$ modes and extraction of the CKM angle γ," *Phys. Rev. Lett.* **78** (1997) 3257.

[115] Atwood, D., Dunietz, I. and Soni, A., "Improved methods for observing *CP* violation in $B^\pm \to K^\pm D^0$ and measuring the CKM phase γ," *Phys. Rev. D.* **63** (2001) 036005.

[116] Gershon, T. and others, "Updated sensitivity projections for the LHCb Upgrade.".